

Fabrication and applications of suspended graphene membranes

A thesis submitted to the University of Manchester for the degree of

Doctor of Philosophy

in the Faculty of Engineering and Physical Sciences

2016

Nicholas J Clark

School of Materials

Table of Contents

Table of figures	9
Table of tables	13
Table of Acronyms	15
Abstract	17
Declaration	19
Copyright Statement	19
1 Introduction	21
<i>1.1 Rationale for submitting thesis in alternative format</i>	<i>21</i>
<i>1.2 Outline of the thesis</i>	<i>21</i>
<i>1.3 Author Contribution</i>	<i>22</i>
2 Thesis aim	23
3 Existing literature	27
<i>3.1 Graphene and other two dimensional materials</i>	<i>27</i>
3.1.1 Introduction to graphene	27
3.1.2 Formal structure of graphene and its reciprocal lattice	29
3.1.3 Other two dimensional materials and stacking	30
<i>3.2 Electrical properties</i>	<i>32</i>
3.2.1 Band structure	32
3.2.2 Dirac cone at the K/K' point	33
3.2.3 Van Hove singularities at the M-point	34
3.2.4 Electronic properties of bilayer graphene (AB stacked).....	35
<i>3.3 Optical properties</i>	<i>37</i>
3.3.1 Basic optical behaviour	37
3.3.2 Raman spectra of graphene	39
G band @ $\sim 1580\text{ cm}^{-1}$	43

2D or G' band @ $\sim 2700\text{ cm}^{-1}$	44
D band @ $\sim 1350\text{ cm}^{-1}$	44
3.4 Mechanical properties	46
3.4.1 Predicted strength	46
3.4.2 Quasi-static means of measurement	48
3.4.2.1 Approximate solutions	49
3.4.2.2 Measurements of Young's Modulus	52
3.4.2.3 Measuring ultimate strength	54
3.4.5 Dynamic behaviour of graphene membranes	54
3.5 Production of graphene	56
3.5.1 'Top down' production	56
3.5.2 'Bottom up' production	57
3.5.3 Epitaxial graphene on SiC	58
3.6 Twisted bilayer graphene	59
3.6.1 Physical structure of twisted bilayer graphene	59
3.6.2 Electronic structure of twisted bilayer graphene	62
3.6.3 Optical properties of tBLG	66
3.6.4 Probing tBLG with resonance <i>Raman</i> spectroscopy	68
3.7 Graphene on waveguides	70
3.7.1 Silicon photonics	70
3.7.2 Ring/ racetrack cavity resonators	71
3.7.3 Graphene integrated on optical waveguides	74
3.8 Transmission electron microscopy	77
3.8.1 Energy Dispersive X-ray Spectroscopy (EDXS)	77
3.8.2 Electron Energy Loss Spectroscopy (EELS)	78
4 Experimental techniques review	81
4.1 Graphene/h-BN flake preparation, characterisation and transfer	81
4.1.1 Mechanical exfoliation onto silicon oxide	81
4.1.1.1 Mechanical exfoliation of graphene	82
4.1.1.2 Mechanical exfoliation of hexagonal boron nitride	82
4.1.2 Characterising flakes	82

4.1.2.1 Optical microscopy	83
4.1.2.2 Scanning Probe Microscopy.....	83
4.1.2.4 Raman Spectroscopy.....	84
4.1.3 Graphene transfer techniques.....	85
4.1.3.1 CVD graphene transfer	85
4.1.3.2 Flake transfer techniques	87
4.1.3.3 Aligned crystalline axis transfer.....	89
4.1.3.4 Removing polymer after transfer	90
<i>4.2 Microfabrication techniques.....</i>	<i>91</i>
4.2.1 Lithography for nanostructures	91
4.2.1.1 Maskless/ scanning optical lithography	91
4.2.1.2 Electron beam lithography	92
4.2.2 Evaporation and lift off.....	92
4.2.3 Etching.....	93
4.2.3.1 Wet etching	94
4.2.3.2 Dry etching.....	95
<i>4.3 Nanomechanical characterisation with AFM.....</i>	<i>97</i>
4.3.1 Nano indentation	97
4.3.2 Force calibration.....	99
4.3.2 Mapping / spatial variation.....	100
<i>4.4 Ultraresolution patterning in graphene.....</i>	<i>101</i>
4.4.1 Resist based patterning	101
4.4.2 Direct write patterning.....	101
5 Experimental procedures	103
<i>5.1 Microfabrication of silicon structures</i>	<i>103</i>
5.1.1 Wafers and preparation	104
5.1.2 Resist coating and patterning	105
5.1.3 KOH etching of silicon	107
5.1.4 Bosch etching of silicon nitride	109
<i>5.2 2D material exfoliation, identification, and transfer.....</i>	<i>112</i>
5.2.1 Micromechanical exfoliation procedure for graphene	112

5.2.2 Micromechanical exfoliation of hexagonal boron nitride.....	115
5.2.3 Wet transfer processes	116
5.2.4 Dry transfer process.....	119
5.2.5 CVD transfer process.....	121
5.2.6 Graphene annealing procedure.....	123
<i>5.3 Selective patterning of graphene.....</i>	<i>124</i>
<i>5.4 Optimised TEM sample fabrication procedure.....</i>	<i>126</i>
<i>5.5 EELS spectra; fitting and quantification</i>	<i>132</i>
<i>5.6 Mechanical measurements on graphene membranes – 1st Paper.....</i>	<i>134</i>
<i>5.8 Selectively graphene coating SOI ring resonator waveguides – 2nd Paper.....</i>	<i>136</i>
<i>5.7 Fabrication of large area suspended tBLG – 3rd Paper.....</i>	<i>137</i>
<i>5.9 Fabrication and TEM patterning of suspended 2D materials - 4th paper.....</i>	<i>141</i>
6 1st paper	143
6.1 Introduction to 1 st paper.....	145
6.2 Summary of 1 st paper.....	145
6.3 Author contribution to 1 st paper	145
7 2nd paper	147
7.1 Introduction to 2 nd paper	149
7.2 Summary of 2 nd paper.....	149
7.3 Author contribution to 2 nd paper	149
8 3rd paper.....	151
8.1 Introduction to 3 rd paper.....	153
8.2 Summary of 3 rd paper	153
8.3 Further work related to 3 rd paper	153
8.4 Author contribution to 3 rd paper.....	153
9 4th paper.....	155

<i>4.1 Introduction to 4th paper</i>	157
<i>4.2 Summary of 4th paper</i>	157
<i>4.3 Author Contribution</i>	157
10 Conclusions and outlook	159
1 st Paper	159
2 nd Paper	160
3 rd Paper.....	161
4 th Paper	161
List of publications	163
References	165

Table of figures

Figure 1 The 3 forms of nano-Carbon	28
Figure 2 Diagram showing the lattice structure and first Brillouin zone of a graphene monolayer	30
Figure 3 The band structure of monolayer graphene	33
Figure 4 Atomic arrangements and simplified electronic structure of Bernal stacked bilayer graphene	35
Figure 5 Perpendicular optical absorption of graphene and few-layer graphene flakes ..	38
Figure 6 Gate variable optical transitions in graphene	39
Figure 7 Feynman diagrams comparing 3 possible optical scattering paths	41
Figure 8 Evolution of the Raman spectra with thickness from monolayer graphene to bulk graphite	42
Figure 9 Raman scattering modes in monolayer graphene	43
Figure 10 Extraordinary stiffness of graphene supported on one edge	47
Figure 11 Bulge testing of graphene membranes	48
Figure 12 Illustration of deformed graphene membranes	49
Figure 13 Frequency response of a circular clamped graphene resonator	55
Figure 14 Methods of graphene production arranged by relative quality and price	56
Figure 15 Brillouin zones of twisted bilayer graphene samples	60
Figure 16 Moiré patterns in rotated graphene	61
Figure 17 Illustrative band structure of tBLG	62
Figure 18 Calculated band structure and density of states of a tBLG structure with a twist angle of $\theta = 3.89^\circ$	63

Figure 19 Scanning tunnelling spectroscopy of a twisted bilayer graphene on graphite sample with a rotation angle $\theta = 1.79^\circ$	64
Figure 20 Energy dependence of van Hove singularities in twisted bilayer graphene.....	65
Figure 21 Full optical spectra of tBLG samples with differing interlayer rotations	67
Figure 22 Summary of literature values for energy of the optical excitation linked to the presence of extra van Hove singularities in twisted bilayer graphene as a function of the twisting angle.....	69
Figure 23 Schematic showing 2 basic racetrack cavity resonator setups	72
Figure 24 Spectral response of a silicon microring photonic resonator	73
Figure 25 Optical spectra of graphene integrated silicon waveguide in a Mach-Zehnder interferometer setup	75
Figure 26 Representative energy dispersive x-ray spectrum of nickel nanowires	78
Figure 27 Representative electron energy loss spectra of manganese containing carbon nanotubes.....	79
Figure 28 Diagram illustrating 3 graphene transfer methodologies.....	85
Figure 29 Outline of wet and dry graphene flake transfer techniques onto hexagonal boron nitride substrates	88
Figure 30 Crystallographic edges in exfoliated graphene flakes.....	89
Figure 31 Schematic illustrating the steps in the lift off process using a bilayer resist	93
Figure 32 Deep reactive ion etching (DRIE) of silicon during the Bosch process.....	96
Figure 33 Schematic illustrating the process of taking a force displacement curve in an AFM	98
Figure 34 Fabrication steps involved in the manufacture of patterned silicon nitride membranes	104

Figure 35 Illustration of the simultaneous double sided spin coating process	106
Figure 36 A schematic view of an anisotropic KOH Si etch with an etch stop layer from the (001) plane	107
Figure 37 KOH etching of silicon	108
Figure 38 Optical images showing the progression of the wet etching of 500 μm thick silicon wafers using KOH	109
Figure 39 Micron scale holes patterned into silicon nitride membranes using maskless optical lithography and a DRIE process	111
Figure 40 Optical images of thin graphene flakes on oxide coated silicon wafers produced using two micromechanical exfoliation techniques	114
Figure 41 Optical and AFM images of a representative mechanically exfoliated hexagonal boron nitride flake	115
Figure 42 Optical and AFM images showing various steps in a wet transfer process	117
Figure 43 Schematic illustrating the dry transfer process	120
Figure 44 Optical images showing the dry transfer process	121
Figure 45 Schematic illustrating the 3-layer resist technique for clean patterning of graphene flakes	125
Figure 46 Old method of segmenting wafers into TEM compatible samples	127
Figure 47 Etch mask and produced structure dimensions in the improved TEM sample fabrication process	128
Figure 48 Series of diagrams showing the steps in the improved TEM sample fabrication process using a top down view of the sample array, and a side view of an individual sample in the array	129
Figure 49 New method of fabricating TEM samples	131
Figure 50 Least squares fitting of EELS spectra using Hyperspy	132

Figure 51 Optical images of SOI ring resonators before and after selective patterning with CVD graphene	136
Figure 52 Sequence of optical images showing stages in the tBLG suspended membrane fabrication process	138
Figure 53 AFM images of graphene flakes with straight, crystalline edges on the smaller scale, but a messy appearance at scales observable using optical microscopy	139
Figure 54 AFM images of large (11 μm diameter) suspended tBLG membranes	140
Figure 55 2 layer membrane patterned in 4th paper	141

Table of tables

Table 1 Summary of measured and calculated values of the two dimensional Young's modulus of monolayer graphene reported in the literature record, adapted from a table in ⁷⁵ . Black text shows experimental studies and grey text shows theoretical studies.....	53
Table 2 Literature values for the linear absorption coefficient of graphene obtained via its integration on silicon waveguides. The result from a paper forming part of this work (Crowe et al., 2014) is included for comparison.	76
Table 3 Annealing procedures for removing polymer (typically PMMA) residue from graphene sheets after transfer and patterning procedures. The atmosphere is 10% hydrogen with argon as a carrier gas. The final step provides no power to the heater and simply allows the furnace to cool at its natural rate. The maximum temperature of 280°C is the maximum found not to degrade the electronic behaviour of graphene devices after prolonged exposure.	123

Table of Acronyms

AFM	Atomic Force Microscope/ Microscopy
CMOS	Complementary Metal Oxide Semiconductor
CPD	Critical Point Dryer
CTEM	Conventional Transmission Electron Microscope
CVD	Chemical/ Catalytic Vapour Deposition
DFT	Density Functional Theory
DI	De-Ionised
DOS	Density Of States
DRIE	Deep Reactive Ion Etching
EELS	Electron Energy Loss Spectroscopy
EDXS	Energy Dispersive X-ray spectroscopy
HAADF	High Angle Annular Dark Field
hBN	hexagonal Boron Nitride
HOPG	Highly Oriented Pyrolytic Graphite
IR	InfraRed
NEMS	Nano Electro-Mechanical Systems
Nd:YAG	Neodymium doped Yttrium Aluminium Garnet
NMP	n-Methyl-pyrrolidone
PMMA	Poly Methyl MethAcrylate
QNM	Quantitative Nanomechanical Mapping
RMS	Root Mean Squared
SEM	Scanning Electron Microscope/ Microscopy
SOI	Silicon On Insulator
STEM	Scanning Tunnelling Electron Microscopy
tBLG	twisted BiLayer Graphene
TEM	Transmission Electron Microscope/ Microscopy
TE/TM	Transverse Electric / Transverse Magnetic
UHV	Ultra High Vacuum
vHS	van Hove Singularity
ZDP	Zero Deflection Point
ZLP	Zero Loss Peak

Abstract

FABRICATION AND APPLICATIONS OF SUSPENDED GRAPHENE MEMBRANES

NICK CLARK

DOCTOR OF PHILOSOPHY

THE UNIVERSITY OF MANCHESTER

27/09/2016

This thesis reports research activity on suspended graphene membranes. Scientific results in the form of peer-reviewed publications are presented, along with supporting information to provide context, detailed experimental procedures, and recommendations of future work. The four papers cover a wide variety of topics, but are linked by common experimental sample fabrication techniques.

Understanding the mechanical properties of suspended graphene membranes is crucial to the development of graphene nano-electromechanical devices. In the first presented paper, PeakForce QNM (quantitative nanomechanical mapping) atomic force microscopy imaging was used to rapidly map the nanomechanical properties of a range of suspended graphene membranes. The force–displacement behaviour of monolayer graphene extracted from the peak force imaging map was found to be comparable to that taken using standard nanoindentation. By fitting to a simple elastic model, the two-dimensional elastic modulus was measured at around 350Nm^{-1} , corresponding to a Young's modulus of around 1 TPa.

The second paper examines the near-IR light-matter interaction for graphene integrated cavity ring resonators based on silicon-on-insulator (SOI) racetrack waveguides. Fitting of the cavity resonances from the predicted transmission spectra reveal the real part of the effective refractive index for graphene, $n_{\text{eff}} = 2.23 \pm 0.02$ and linear absorption coefficient, $\alpha_{\text{gTE}} = 0.11 \pm 0.01\text{dB } \mu\text{m}^{-1}$. The evanescent nature of the guided mode coupling to graphene at resonance depends strongly on the height of the graphene above the cavity, which places limits on the cavity length for optical sensing applications.

Twisted-bilayer graphene (tBLG) exhibits van Hove singularities in the density of states that can be tuned by changing the twisting angle θ . In the third paper, θ -defined tBLG was produced and characterized using optical reflectivity and resonance Raman scattering. This represents the first reported fabrication of a rationally designed (twist engineered) tBLG structure. The θ -engineered optical response is shown to be consistent with persistent saddle-point excitons. Separate resonances with Stokes and anti-Stokes Raman scattering components can be achieved due to the sharpness of the two-dimensional saddle-point excitons, similar to what has been previously observed for one-dimensional carbon nanotubes. The excitation power dependence for the Stokes and anti-Stokes emissions indicate that the two processes are correlated and that they share the same phonon.

Nano-patterned and suspended graphene membranes find applications in electronic devices, filtration and nano-pore DNA sequencing. However, the fabrication of suspended graphene structures with nanoscale features is challenging. In the fourth and final paper, the direct patterning of suspended membranes consisting of a graphene layer on top of a thin layer of hexagonal boron nitride which acts as a mechanical support is demonstrated for the first time, using a highly focused electron beam to fabricate structures with extremely high resolution within the scanning transmission electron microscope. The boron nitride support enables the fabrication of stable graphene geometries which would otherwise be unachievable, by preventing intrinsic strain in graphene membranes from distorting the patterned features after areas are mechanically separated. Line cuts with widths below 2 nm are reported. It is also demonstrated that the cutting can be monitored in-situ utilising electron energy loss spectroscopy (EELS).

Declaration

I declare that no portion of the work referred to in the thesis has been submitted in support of an application for another degree or qualification of this or any other university or other institute of learning.

Copyright Statement

The author of this thesis (including any appendices and/or schedules to this thesis) owns certain copyright or related rights in it (the “Copyright”) and he has given The University of Manchester certain rights to use such Copyright, including for administrative purposes.

Copies of this thesis, either in full or in extracts and whether in hard or electronic copy, may be made only in accordance with the Copyright, Designs and Patents Act 1988 (as amended) and regulations issued under it or, where appropriate, in accordance with licensing agreements which the University has from time to time. This page must form part of any such copies made.

The ownership of certain Copyright, patents, designs, trademarks and other intellectual property (the “Intellectual Property”) and any reproductions of copyright works in the thesis, for example graphs and tables (“Reproductions”), which may be described in this thesis, may not be owned by the author and may be owned by third parties. Such Intellectual Property and Reproductions cannot and must not be made available for use without the prior written permission of the owner(s) of the relevant Intellectual Property and/or Reproductions.

Further information on the conditions under which disclosure, publication and commercialisation of this thesis, the Copyright and any Intellectual Property and/or Reproductions described in it may take place is available in the University IP Policy (see <http://documents.manchester.ac.uk/DocuInfo.aspx?DocID=487>), in any relevant Thesis restriction declarations deposited in the University Library, The University Library’s regulations (see <http://www.manchester.ac.uk/library/aboutus/regulations>) and in The University’s policy on Presentation of Theses.

1 Introduction

This thesis documents work carried out by the author between 2012 and 2015 at the University of Manchester. Experimental work was undertaken principally in the Centre for Mesoscience and Nanotechnology, a suite of class 100/1000 cleanrooms. This chapter acts as an introduction to the document, outlining the reasoning for presenting it in alternative format, outlining the structure of the thesis, and reviewing the author's contribution to the peer reviewed papers presented as part of the work.

1.1 Rationale for submitting thesis in alternative format

The author of the presented thesis has been in the fortunate position of having been able to publish the results of his research in peer reviewed journals. The emerging study of graphene and the multifaceted skillset required to fabricate and characterise graphene devices allowed the author to contribute to a number of different related areas of graphene research. The many applications that graphene can be put to means that any novel device fabrication technique must be put into the context of its intended destination. Throughout the course of the author's PhD studies a body of work has been generated linked commonly throughout by the novel fabrication techniques the author has developed to realise a variety of graphene experimental systems. The author has chosen to present a set of four papers that represent the novel fabrication techniques that best represent the innovative methods that have been developed during the course of the authors PhD studies.

1.2 Outline of the thesis

Chapter 1 acts as an introduction to the thesis, setting out its format and structure, and describing the thesis author's contribution to each piece of previously published work contained within it. **Chapter 2** describes the aims of the thesis, and of the individual pieces of work. **Chapter 3** is a literature review which attempts to provide context for the research questions which are tackled in the results chapters. **Chapter 4** reviews relevant reported experimental techniques. **Chapter 5** describes the experimental procedures developed and used in this work. **Chapters 6-9** present the results in the form of peer reviewed publications and manuscripts submitted for peer review. Finally, **Chapter 10** discusses the presented results and makes suggestions for possible future research directions.

1.3 Author Contribution

Chapter 6, 1st Paper, entitled “*Ultrafast quantitative nanomechanical mapping of suspended graphene*” is a peer reviewed research paper. The patterned silicon nitride membranes were fabricated by the author. The optimisation of the plasma etching step was carried out by the author and Antonios Oikonomou. Graphene flakes were exfoliated and transferred over the membranes by the author. Mechanical measurements were carried out by the author. The author assisted in the design of the experiment, interpretation of the data and preparation of the manuscript along with Aravind Vijayaraghavan.

Chapter 7, 2nd Paper, entitled “*Determination of the quasi-TE mode (in-plane) graphene linear absorption coefficient via integration with silicon-on-insulator racetrack cavity resonators*” is a peer reviewed research paper. The SOI ring resonator waveguides and surface gratings were designed and fabricated by Milan Milosevic, Frederic Gardes, and Goran Mashanovich. A CVD graphene sheet was transferred onto the sample, and patterned such that it only remained over the required ring optical cavities by the author. The author also confirmed the configuration of membrane and waveguide using AFM. The author assisted with the design of the sample, interpretation of the results, and the editing of the manuscript.

Chapter 8, 3rd Paper, entitled “*Optical-phonon resonances with saddle-point excitons in twisted-bilayer graphene*” is a peer reviewed research paper. The suspended tBLG sample, and the processes required to fabricate it, were designed by the author to meet the optical specification. This included the design and fabrication of custom patterned silicon nitride membranes, exfoliation and optical selection of large ‘aligned’ graphene flakes, and their transfer and alignment. The author assisted with the editing of the manuscript.

Chapter 9, 4th Paper, entitled “*Nanometre electron beam sculpting of suspended graphene and hexagonal boron nitride heterostructures*” is a manuscript in preparation. The design and fabrication of the experimental system was carried out by the author. TEM imaging, patterning and spectroscopy were performed by Edward Lewis and Sarah Haigh. The interpretation of the images, EELS spectra, and EDS spectra were performed by the author. The design of the experiment, interpretation of the results, and the preparation of the manuscript were performed primarily by the author.

2 Thesis aim

The previously published work presented as part of this thesis consists of four research papers in diverse areas, linked by common experimental techniques. Throughout the programme of work, the author developed a number of novel experimental techniques and optimised processes related to graphene device fabrication, particularly suspended graphene structures. These fabrication procedures could then be used to generate samples for a wide variety of experimental studies, in areas as diverse as optics, nanomechanics, and electrochemistry. The four topics selected for presentation as part of this thesis are representative of this wider body of work. This section outlines background to each area of work, and the research objectives posed, and summarises the work carried out to achieve them.

Suspended graphene membranes are a useful experimental testbed in a wide range of areas, but are challenging to characterise due to their extreme optical and electronic transparency. Atomic force microscopy (AFM) nanoindentation experiments on circular suspended graphene are the primary method in which the mechanical properties of graphene can be measured. Tapping mode AFM has been previously used to image graphene membranes, but the high interaction forces between the AFM probe and graphene induce large high frequency oscillations in the graphene membrane. This limits the size of membranes that can be measured using this technique, and makes it hard to assess the membrane geometry at low forces. PeakForce QNM (quantitative nanomechanical mapping) AFM mode allows the spatial mapping of the nanomechanical properties of a surface at high speed by capturing a force curve per pixel; the time taken for a full nanomechanical map is comparable to the time taken for a standard AFM tapping mode image showing topography only. This method had not been previously employed to characterise graphene, or graphene membranes. We aimed to test the force curves obtained using this technique on graphene membranes against those obtained by indentation and modelling, and assess the utility of the off-resonance imaging technique for general suspended membranes. The experimental method and resulting findings are presented in Chapter 6. Here it is shown that it was possible to demonstrate that peak-force imaging allows topographic and nanomechanical data to be captured on large soft graphene membranes, of 3 – 10 μm scale, with a high dynamic vertical range at known deformations, as opposed to tapping mode. The force distance behaviour of the central area of the membrane was compared to mechanical measurements performed using conventional

nanoindentation techniques, and found to be in good agreement. Using the force displacement behaviour at the centre of the membrane and a semi-empirical model, a ‘derived’ Young’s modulus for graphene of 1 TPa was measured on the large scale graphene membranes fabricated, which agreed with values found in the literature.

Along with graphene’s unique mechanical properties, its ability to absorb light over an extremely wide wavelength and its high carrier mobility make a variety of graphene based photonic devices possible. The large surface area of graphene, as well as its chemical purity, reactivity and simplicity of functionalisation, make it an ideal sensing platform, potentially leading to ultra-sensitive devices that detect biological or gas molecules. Understanding the nature of light’s interaction with graphene is critical if graphene integrated silicon photonic devices of this type are to be realised. To investigate light’s interaction with graphene in photonic devices a method of transferring and patterning graphene onto a racetrack type silicon cavity resonator was developed. The methods developed are described in Chapter 7. Analysis of this device showed that the transmission spectra for a cavity resonator with graphene displayed a strong quenching of the resonance signal as light-graphene interaction length is increased. The linear attenuation due to graphene (as a function of its length) was measured using both a cutback method (as had been performed previously) and as a fitting parameter in the ring resonator transmission spectrum. At the time, this figure was a matter of dispute despite earlier measurements. From this work a model of cavity resonance attenuation with respect to graphene length and height over said cavity was developed, which should provide future design rules for developing graphene integrated silicon photonic devices for chemical sensing and optoelectronic applications.

Graphene and other 2D materials are also unique in that their properties are highly dependent on their environment. This can how they are stacked, with respect to their order and angular geometry. Twisting bilayer graphene layers generates a peak in the dynamic optical conductivity, related to the angle that one layer is misrotated relative to the other. If this angle can be controlled a twisted bilayer graphene can be engineered to have a large peak in the optical conductivity spectrum. A method of controlling the angle between each layer of graphene was developed, which is presented in Chapter 8. A method to control the twist angle between layers of graphene had not previously been successfully developed prior to this work, and all studies were performed on ‘randomly’ oriented twisted samples. This

demonstrated the possibility of mode-engineering twisted graphene systems to control their optical behaviour in the suspended regime. The large area suspended samples allowed highly sensitive transmission Raman measurements. By positioning the peak energy, we were able to greatly favour anti-Stokes inelastic scattering processes when under illumination using a laboratory standard 532nm laser.

Patterning graphene with nanoscale features in the sub 10 *nm* range is of interest for creating structures such as nanoribbons, nanopores, quantum dots, and nanogap electrodes. Typically, graphene is patterned by using oxygen plasma etching to remove graphene not protected by a polymer mask defined by electron beam lithography (EBL), but this is typically only able to create patterns with feature sizes down to 10 – 20 *nm*, although in special cases this has been reduced to around 5 *nm*. Patterning suspended graphene by ablating areas with the tightly confined electron beam in a scanning tunnelling electron microscope (STEM) is able to create features on nanometre scales. However this process is not ideal as the graphene is self-supporting, and loses its mechanical integrity as it is patterned. This limits the utility of the technique. Manufacturing only one nanoribbon per membrane is possible, as they cannot be electrically isolated without being mechanically separated. Intrinsic tension in suspended graphene sheets distorts features after they are cut, so line cuts tend to bow outwards. This makes it completely unsuitable for patterning nanogap electrodes. We aimed to develop a new strategy which would enable working around these drawbacks, based on a graphene membrane supported by a thin insulating boron nitride membrane, and investigate the required STEM patterning parameters. This would have 2 effects. Firstly, the graphene could be pre-patterned using conventional EBL and plasma etching without affecting the structural integrity of the boron nitride support. Secondly, it would prevent the distortion of the membrane when patterning using subsequent direct write ablation in a STEM system, as long as areas are not completely mechanically separated. This would enable the creation of linear arrays of nanoribbons or nanogap electrodes; thin strips of graphene defined using EBL could be narrowed or cut using STEM. It also solves a number of fabrication issues relating to experiments with nanopores, where maintaining a physical barrier around the nanopore is useful, and can also be used to affect the depth of the pore (which influences translocation speed) whilst maintaining the sensing advantages of using thin graphene.

We fabricated a hexagonal boron nitride (hBN) supported graphene membrane on a TEM support using a newly developed technique, and then investigated patterning parameters for this membrane using STEM direct write. The published results are included as chapter 9 of this work. We performed analysis while patterning using energy dispersive x-ray spectroscopy (EDXS) and electron energy loss spectroscopy (EELS) to investigate the patterning process, and help us to choose a useful general patterning strategy. We were successful in producing long (hundreds of nm) cuts with widths as low as 1.5 *nm* along their length. This provides a proof of principle for a technique which enables the fabrication of a variety of novel nanoscale graphene structures.

3 Existing literature

This chapter presents an overview of the physical properties of graphene, providing context to the research questions which are examined in the results chapters. Firstly, it reviews the unique electronic and optical properties of monolayer graphene. Then, graphene's mechanical properties are introduced and discussed, with a focus on how they can be investigated experimentally. The different forms of graphene obtained from different production methods, and their distinct properties are outlined and compared. Following this, the peculiar properties of twisted bilayer graphene (tBLG), which are very different from the 'vanilla' system, are reviewed. Then, this chapter introduces silicon photonics and the 'ring resonator' optical modulator, and reviews experimental results on progress towards the integration of graphene with photonic waveguides. Finally, it introduces two spectroscopic techniques used for elemental analysis in scanning transmission electron microscope (STEM) systems; an X-ray emission spectroscopy technique known as energy dispersive x-ray spectroscopy (EDX/S), and an absorption spectroscopy technique using the transmitted electron beam known as electron energy loss spectroscopy.

3.1 Graphene and other two dimensional materials

Graphene¹, a two dimensional 'honeycomb' lattice of carbon atoms, was the first 2D crystal to be discovered, but there is now a whole family of other 2D structures which have been isolated in the same manner². The material parameters of graphene in particular are supreme when compared to bulk materials, and it has been predicted that graphene will replace many materials in existing technological applications as well as enabling new device functionalities in the near future³. The 2D nature of these materials means that it is feasible to effectively create new materials⁴ merely by creatively stacking and twisting the various layers. This section introduces graphene and describes its history and its formal structure in real space and reciprocal space, before briefly introducing a variety of other 2 dimensional materials, including hexagonal Boron Nitride.

3.1.1 Introduction to graphene

Carbon is one of the most abundant elements in the universe, and perhaps the most interesting. It has 6 electrons, of which two sit in a closed $1s^2$ shell, with 4 in $2s$ and $2p$ shells.

However, when atoms bond into molecules or crystals, the total energy is decreased by the overlap of the wavefunctions⁵ of these states into *molecular orbitals* (for molecules) or *energy bands* (for bulk solids). For carbon molecules, mixed states labelled as sp^3 and sp^2 are generated. Carbon atoms in sp^3 materials bond with 4 other C atoms, in a tetragonal arrangement. This is the arrangement of the atoms in crystalline diamond. In the sp^2 state, three hybrid sp covalent bonds are formed, with one p orbital extending across the molecule or solid. Carbon with sp^2 hybridization forms three bonds in a plane, separated by angles of 120° .

Two dimensional graphene forms part of a wider family of sp^2 hybridized Carbon nanomaterials. Carbon nanotubes⁶ are the one-dimensional analogues, and fullerenes⁷ or ‘buckyballs’ are ‘zero dimensional’, completing the set. An illustrative example of all three forms is shown in figure 1. They are all primarily composed of the hexagonal lattice characteristic of sp^2 hybridization.

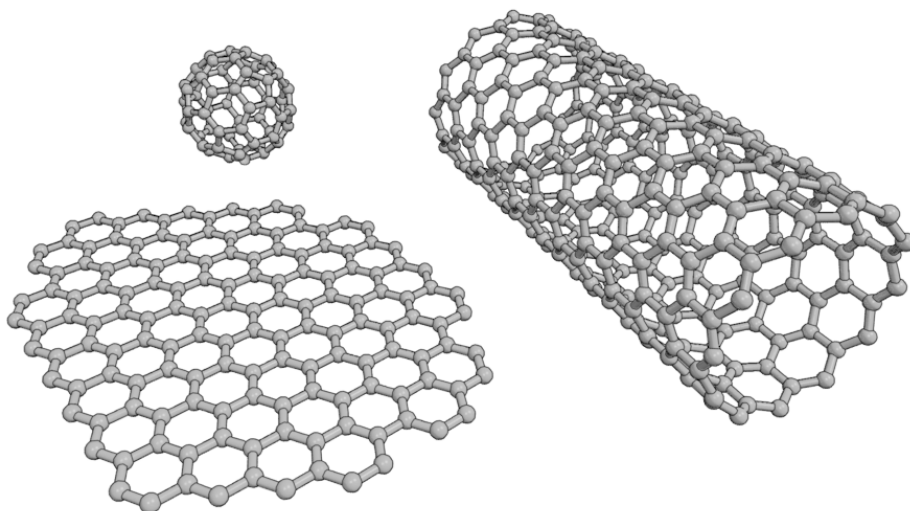


Figure 1 The 3 forms of nano-Carbon. Schematic showing the carbon atomic arrangement in 0D fullerenes (top left), 1D nanotubes (right), and 2D graphene (bottom left).

As graphene is an inherently two dimensional material, it therefore was thought to be unstable, until first isolated in 2004¹. Previously to this, it was long assumed that completely

2D crystals would be thermodynamically unstable^{8,9} and would break apart at finite temperatures. Experimental evidence seemed to support this view; thin film melting temperatures drop rapidly with thickness, and thin films were seen to segregate or decompose when thicknesses corresponding to tens of atomic layers were reached¹⁰. Now, its existence can be reconciled with these predictions by including the stabilising effect of microscopic crumpling in the 3rd dimension¹¹.

Graphene was studied theoretically before its isolation, as a building block for both bulk graphite^{12,13} (a material of particular interest during the mid-20th century due to its use in nuclear reactors), and the other nano-carbons^{14,15}. Since graphene was isolated via mechanical exfoliation using sticky tape¹, it has become a focus of research worldwide¹⁶ due to its superlative electrical, optical, thermal and mechanical properties, and because its planar nature makes integration into devices relatively simple³. It is a zero-bandgap semiconductor with a linear dispersion relation¹⁷, and a constant (and remarkably high) optical absorption across the whole visible region. It also exhibits unparalleled mechanical strength, thermal conductivity and specific surface area.

3.1.2 Formal structure of graphene and its reciprocal lattice

Graphene is an sp^2 carbon structure, where each atom bonds to three others in a plane with angles separated by 120° . The resulting ‘honeycomb’ structure can be described as a triangular lattice with a basis of 2 atoms per unit cell, or as two superimposed triangular sublattices. The lattice vectors are given by:

$$\vec{a}_1 = \frac{L_{C=C}}{2}(3, \sqrt{3}) \quad \text{and} \quad \vec{a}_2 = \frac{L_{C=C}}{2}(3, -\sqrt{3}) \quad (1)$$

where $L_{C=C} \approx 1.42 \text{ \AA}$ is the carbon-carbon bond length, or nearest neighbour distance. The size of the lattice vector is $a = |\vec{a}| = \sqrt{3}L_{C=C} \approx 2.46 \text{ \AA}$. The reciprocal lattice vectors are therefore

$$\vec{b}_1 = \frac{2\pi}{3L_{C=C}} (1, \sqrt{3}) \quad \text{and} \quad \vec{b}_2 = \frac{2\pi}{3L_{C=C}} (1, -\sqrt{3}) \quad (2)$$

The sublattices are shown along with the lattice vectors in real and reciprocal space in figure 2. Two key locations on the Brillouin zone are highlighted as the K/K' point and the M point. These are the locations of the Dirac cone and the van Hove singularities respectively, which are introduced in section 3.2.

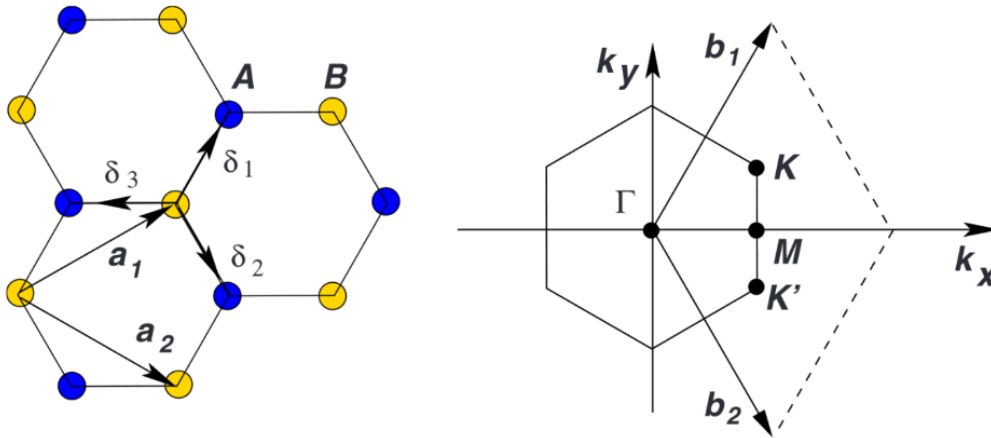


Figure 2 Diagram showing the lattice structure and first Brillouin zone of a graphene monolayer. The left part shows the lattice structure, where the two sublattices are denoted A (blue) and B (yellow). The two lattice vectors are shown as a_1 and a_2 . The nearest neighbour vectors are denoted δ_1 , δ_2 and δ_3 . The right part shows the first Brillouin zone, with the reciprocal lattice vectors b_1 and b_2 . Dirac cones in the band structure correspond to the K and K' points, and hyperbolic saddle points in the band structure to the M point. Reprinted with permission from reference¹⁷. Copyright (2009) by the American Physical Society.

The atomic lattice of sp^2 carbon materials has 3 degrees of rotational symmetry around 2 sets of axes. These axes are termed the *zigzag* and *armchair* directions, in reference to their edge shapes. Graphene sheets, under certain conditions, preferentially tear along these directions, creating so called zigzag and armchair edges, as discussed in section 4.1.3.3.

3.1.3 Other two dimensional materials and stacking

Graphene's isolation from bulk graphite caused a new focus on atomically layered three dimensional materials¹⁸ held together by *van der Waals* interactions, and it was found that many other materials could be exfoliated in a similar way to generate new two dimensional

systems. Transition metal dichalcogenides (MX_2) consist of a hexagonal layer of atoms of transition metal M (often Mo, W, Nb) sandwiched between layers of chalcogen atoms X (often S, Se, Te), and over 40 have been isolated. MoS_2 is a direct bandgap semiconductor, and has been demonstrated as an ideal channel material for next generation transistors^{19,20}. Hexagonal boron nitride (hBN) is an insulator (with a band gap of 6 eV)²¹ with the same structure as graphene, with the two sublattices filled with boron and nitrogen atoms respectively.

Stacking these 2D materials can alter or enhance their properties. ‘Normal’ bilayer graphene exhibits a small band gap, but by adding a twist between the two layers its electronic structure and derived quantities can be radically altered. This is discussed in section 3.6. Graphene on reasonably thick hBN substrates shows electron mobility similar to that of freely suspended graphene due to its atomically flat surface and lack of charged surface sites²². By creatively stacking various 2D materials, *van der Waals heterostructures*⁴ may reveal extreme properties or new physical phenomena.

3.2 Electronic properties

This section explores the electronic properties of monolayer graphene. First the main features of the band structure are described, then two features are described in detail; the Dirac cone at the K point and the saddle point at the M point. The linear dispersion relation and its consequences are introduced. The van Hove singularities that are generated by the saddle points are introduced and discussed. Finally, the electronic structure of bilayer graphene is described.

3.2.1 Band structure

The electronic structure of graphene was first considered in 1946 by Wallace¹², as the first step of the calculation of the band structure of graphite. The possibility of a two dimensional material being isolated was not considered at this point^{8,23}. A tight binding approximation was used to calculate the band structure as

$$E_{\pm}(\vec{k}) = \pm t \sqrt{3 + f(\vec{k})} - t' f(\vec{k}) \quad (3)$$

where E_{\pm} is the energy of the valence and conduction band at wavevector \vec{k} , and t and t' are the nearest neighbour (between sublattices) and next nearest neighbour (within sublattices) hopping energies respectively. This equation can be extended to include a t'' term related to third nearest neighbour hopping, and so on. f is a function of the wavevector given by

$$f(\vec{k}) = 2 \cos(k_y a) + 4 \cos\left(\frac{1}{2} k_y a\right) \cos\left(\frac{\sqrt{3}}{2} k_x a\right) \quad (4)$$

where $a \approx 2.46\text{\AA}$ is the modulus of the lattice vectors as shown in figure 2. The values of the hopping parameters $t, t', t'' \dots$ have to be estimated by fitting the results of this tight-binding model to those of first principles electronic structure calculations. Reich¹⁴ *et al.* calculate values of $t = -2.97\text{eV}$, $t' = -0.073\text{eV}$ and $t'' = -0.33\text{eV}$. The band structure shown in equations (3) and (4) is plotted in figure 3.

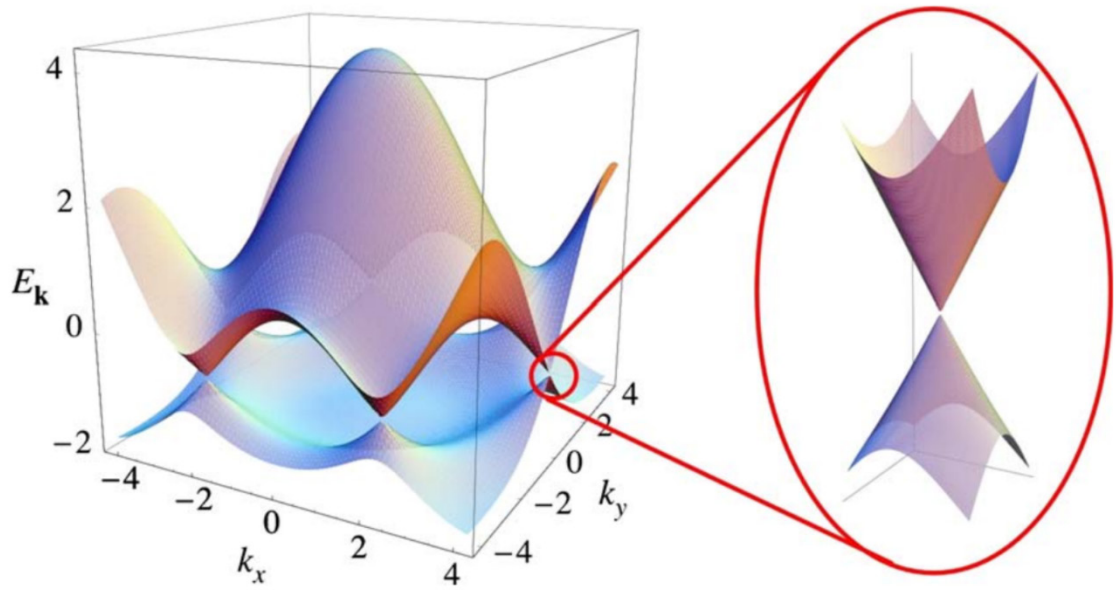


Figure 3 The band structure of monolayer graphene. The left image is the calculated band structure with an energy scale in units of $E_k = 2.7$ eV. The right image is a close-up of a Dirac cone at the K point, showing the local linear dispersion relation. Hyperbolic saddle points occur in both bands directly between adjacent Dirac cones. Reprinted with permission from reference¹⁷. Copyright (2009) by the American Physical Society.

A more representative dispersion relation can be obtained by accounting for more nearest neighbour terms (t'' , t''' , ...) in a tight binding model²⁴, or using *ab initio* methods^{25,26}.

3.2.2 Dirac cone at the K/K' point

The dispersion relation given by equations (3) and (4) has minima at the K and K' points, where the energy bands are close to the intrinsic Fermi level. By expanding the full structure close to \vec{K} as $\vec{k} = \vec{K} + \vec{q}$ where $|\vec{q}| \ll |\vec{K}|$, it is found that¹⁷

$$E_{\pm}(q) = \pm v_F |\vec{q}| + O\left[\left(\frac{q}{K}\right)^2\right] \quad (5)$$

where the final term denotes higher order terms of q/K , which can be neglected close to K , and the Fermi velocity v_F is a constant given by

$$v_F = \frac{3}{2} ta \approx 10^6 \text{ ms}^{-1}. \quad (6)$$

It is this remarkable result which is responsible for many of graphene's superlative properties. The reduced Hamiltonian that produces the linear dispersion relation²⁷ is formally analogous to the two-dimensional Dirac equation, with the constant speed of light c replaced by the constant Fermi velocity v_F . This is why the linear conical structures in the band structure around the K points, described by equation (5), are known as *Dirac cones*, and the K points referred to as *Dirac points*.

3.2.3 Van Hove singularities at the M-point

At the M point in the Brillouin zone, a saddle-point in both the valence and conduction bands (visible half way between the Dirac cones in figure 3) generates a logarithmic singularity in the density of states (DOS) known as a *van Hove singularity* (vHS).

These logarithmic infinities were first described by Smollett²⁸, who calculated the 'spectral density' (analogous to the density of states) of a two-dimensional ionic crystal, and found that the hyperbolic nature of saddle points in the 'frequency contour map' (band structure) caused the infinite logarithmic discontinuities in the density of states.

Van Hove extended this analysis, showing that the existence of these saddle points in the band structure was general to all 2D crystals. With reference to Morse theory²⁹, he stated³⁰:

“Any function of more than one independent variable which, as $v(\vec{q})$, is periodic in all its variables has at least a certain number of saddle points; this number is determined only by topological considerations and depends only on the number of independent variables”

Here, $v(\vec{q})$ is van Hove's nomenclature for the frequency of a plane wave as a function of its wave-vector. He then showed that the generation of the singularities was general to all two dimensional lattices but not in three dimensional solids, as Smollett had predicted (three dimensional lattices exhibit discontinuities only in the first derivative of the density of states).

Graphene's M points generate such van Hove singularities, although they are so far from the Dirac point ($E_{vHS} \approx \pm 3 \text{ eV}$) that they are outside the range of the Fermi energy which can

be achieved using doping or gating³¹. However, they are important when considering its optical properties, as discussed in sections 3.3 and 3.6.

3.2.4 Electronic properties of bilayer graphene (AB stacked)

Within natural graphite, layers are normally stacked in an *AB* pattern, also known as *Bernal stacking*, where atoms from sublattice *A* from one layer are on top of those from sublattice *B* from adjacent layers. The atomic arrangement of bilayer graphene in this stacking arrangement is shown in figure 4.

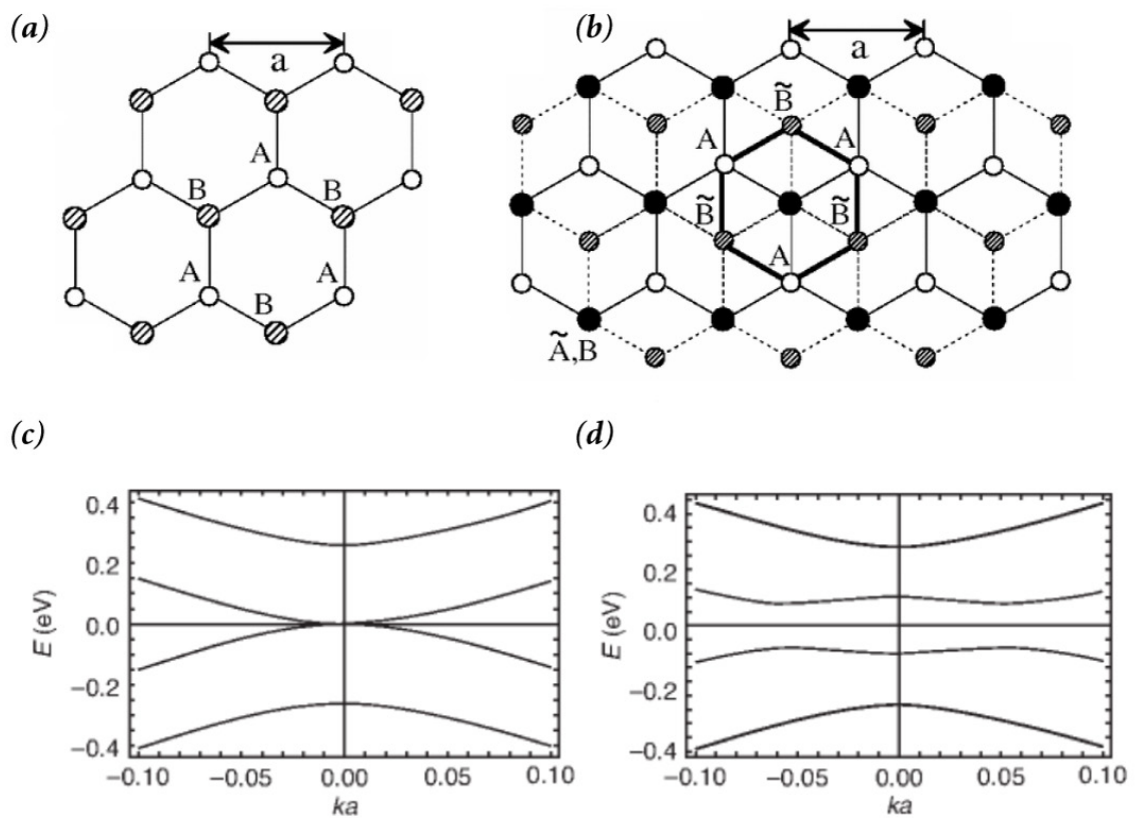


Figure 4 Atomic arrangements and simplified electronic structure of Bernal stacked bilayer graphene. (a) shows a graphene monolayer composed of two sublattices, labelled **A** and **B**. (b) shows the monolayer from (a), with bonds drawn in solid lines, stacked in a Bernal stacking configuration with a second layer with bonds drawn using dashed lines, containing sublattices $\tilde{\mathbf{A}}$ and $\tilde{\mathbf{B}}$. The larger dark sites indicate where there are atoms from both layers. The thick black hexagon is a unit cell containing 4 sites: $1\tilde{\mathbf{A}} + 1\mathbf{B} + 3(\frac{1}{3}\mathbf{A}) + 3(\frac{1}{3}\mathbf{B})$. (c) shows the simplified (nearest neighbour only approximation) electronic structure of Bernal stacked bilayer graphene near the K point as a function of the distance from the K point as described in equation 7. (d) shows the modified electronic structure due to a voltage being applied perpendicularly across the layers, with the formation of a clear band gap. Image adapted with permission from reference^{32,33}. Copyright (2006) by the American Physical Society.

Using a simple tight binding model^{32,33}, the energy and conduction bands in bilayer graphene stacked in this way around the K-point (and writing \vec{k} as $\vec{k} = \vec{K} + \vec{q}$ where $|\vec{q}| \ll |\vec{K}|$) can be approximated (for intermediate energies) as

$$E_{c,v}(q) = \pm \frac{\gamma_1}{2} \left(\sqrt{1 + \frac{4v^2 q^2}{\gamma_1^2}} - 1 \right) \quad (7)$$

where v is a *band velocity* characterised by $v = \sqrt{3}a\gamma_0/2\hbar$. Here, γ_0 is a coupling parameter related to nearest neighbour hopping between sublattices A and B within one layer, and γ_1 is a coupling parameter related to interlayer hopping between the sublattices in the same stacking site, \tilde{A} and B . At large momenta, this can be simplified to a linear expression $E \approx \pm vq$, and at small momenta to a quadratic $E \approx \pm p^2 q^2 / \gamma_1$. Interestingly, the application of a voltage perpendicular to the bilayer results in the shifting of these levels³⁴ and the opening of a bandgap between the 2 bands. This is shown in panel (d) in figure 4. At very low energies around the K point, the inclusion of a γ_3 coupling term related to next nearest neighbour interlayer hopping¹³ (corresponding to hopping between A and \tilde{B} sublattices in figure 4(b)) causes *trigonal warping*^{17,32} and a *Lifshitz transition*³³, generating 4 mini Dirac-like cones separated by a low energy saddle point³⁵.

3.3 Optical properties

This section reviews the optical properties of graphene. Firstly, the constant dynamic conductivity approximation and its resulting constant wideband absorption is introduced, along with the conditions under which the approximation breaks down. The Pauli blocking mechanism which modifies the optical absorption as the Fermi level is shifted is described. Finally, Raman scattering is introduced, and the Stokes and anti-Stokes light scattering signals are discussed. Raman active phonon modes which are particularly useful for characterising graphene and other sp_2 bonded carbon structures are also outlined.

3.3.1 Basic optical behaviour

The optical properties of thin films can be specified using their dynamic conductivity G . For a purely conical Dirac spectrum, neglecting higher order terms from equation (5), as $E_{\pm} = v_F |\vec{k}|$, the dynamic conductivity is predicted³⁶ to be

$$G \equiv G_0 \equiv \frac{e^2}{4\hbar} \approx 6.08 \times 10^{-5} \Omega^{-1} \quad (8)$$

Here e is the fundamental charge, and \hbar is the reduced Planck constant. As monolayer graphene is purely two-dimensional, derived properties such as transmittance T , absorption A , and reflection R are directly proportional³⁷ to the dynamic conductivity and therefore also constant. Transmittance (and absorbance) are given by

$$T = 1 - A = \frac{1}{\left(1 + \frac{2\pi G_0}{c}\right)^2} \approx 1 - \pi\alpha \quad (9)$$

where α is the fine structure constant, equal to $\alpha = e^2/\hbar c$. The reflectivity is neglected here as $R < 0.1\%$. The conical Dirac cone approximation which gives the constant dynamic conductivity in equation (8) is valid when the energy of the incident photon is much larger than the thermal energy and the Fermi level shift ΔE_F (the shift of the Fermi level from that of the intrinsic crystal due to doping or gating), which holds for visible light at room

temperature^{38,39}. An experimentally measured transmittance spectrum is shown in figure 5. The absorbance combines additively with the number of graphene layers, as can be seen from the inset on the right hand plot.

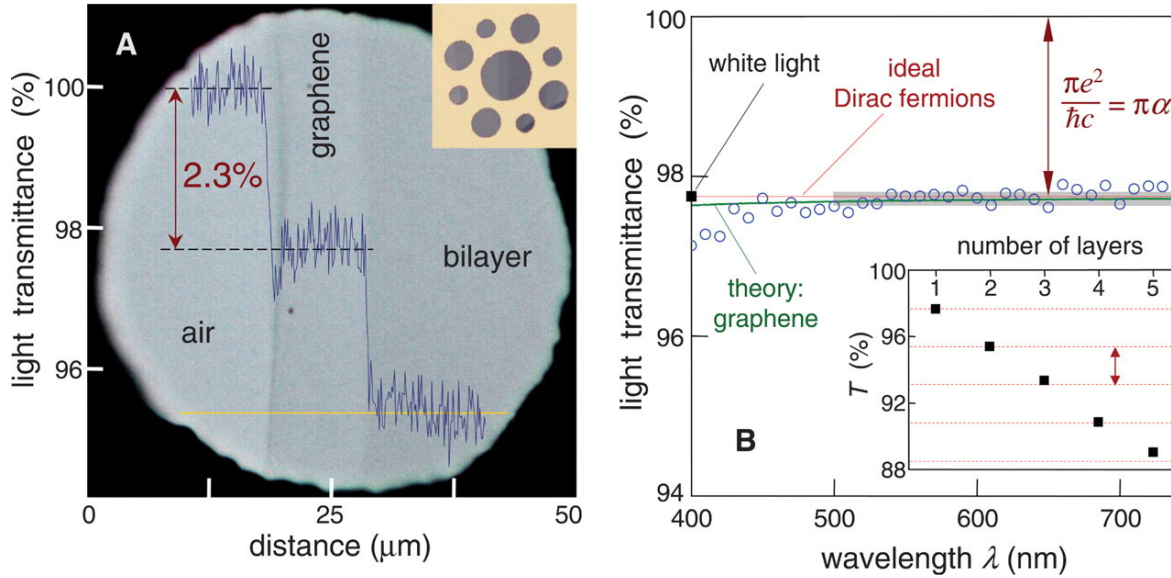


Figure 5 Perpendicular optical absorption of graphene and few-layer graphene flakes. The left image shows a flake with monolayer and bilayer graphene regions covering a 50μm aperture in a metal TEM support grid. The transmitted light intensity profile along the yellow line in the image is overlaid. The inset shows an image of a larger area of the flake over various apertures. The central hole is that shown in the larger image. The right panel is the measured transmittance spectra of monolayer graphene. The blue circles are a measured spectra, the red line is the constant transmittance of ideal 2D Dirac fermions, and the green line is a more complicated theoretical graphene model. The grey box represents the experimental error. The inset shows white light transmittance of few layer graphene as a function of layer number. Image from reference³⁷. Reprinted with permission from AAAS.

More advanced treatments, such as taking extra terms in the tight binding approximation into account or deriving from first principles³⁹ give a slightly modified dynamical conductivity, as shown by the green plot in figure 5, but the correction is very small for visible light. There is, however, a large peak in dynamic conductivity in the ultraviolet region associated with the van Hove singularities at the M point, at $E_{vHS} \approx 4.6 \text{ eV}$ (corresponding to a wavelength of $\lambda_{vHS} \approx 270 \text{ nm}$). It's energy is slightly redshifted from the energy of the vHS due to excitonic effects⁴⁰. In the other direction, the spectrum becomes dominated by intraband absorption beyond mid-IR wavelengths^{41,42}.

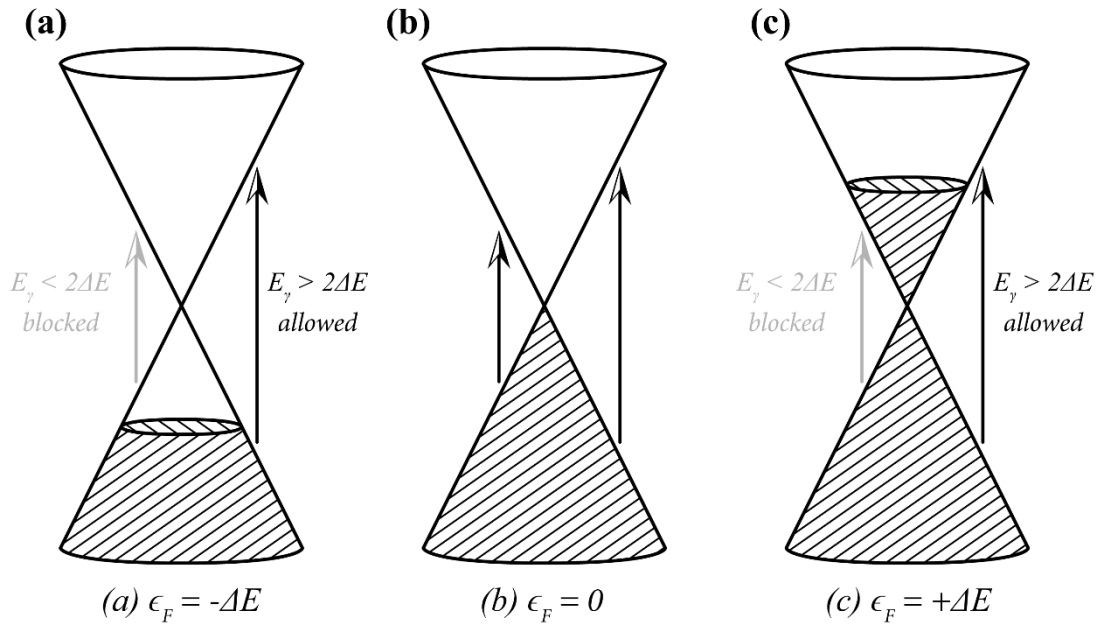


Figure 6 Gate variable optical transitions in graphene. Schematic illustrating the Pauli blocking process in three cases: (a) ϵ_F negatively shifted by ΔE , (b) ϵ_F not shifted and (c) ϵ_F positively shifted by ΔE . In case (b), all interband transitions are possible and the constant wideband absorption spectrum is preserved. In cases (a) and (c), transitions with energies less than roughly $2\Delta E$ are suppressed due to the lack of a state to promote from and to respectively. This cut off is broadened out by finite temperature and finite carrier lifetime.

Changing the Fermi level via chemical doping or electrostatic gating can be used to controllably alter the optical properties of graphene⁴³. When the Fermi energy is shifted by ΔE , optical transitions with energies below $2\Delta E$ are suppressed, due to a lack of promotable electrons, as in case (a), or *Pauli blocking*, as in case (c). This process is illustrated in figure 6. This effect offers interesting possibilities for new technological applications of graphene^{44,45}, and allows the determination of the Fermi energy in a particular graphene sample without needing to make electrical contact.

3.3.2 Raman spectra of graphene

Raman scattering is the term given to the inelastic scattering of light by materials. When light interacts with a material, most is elastically scattered by the atoms and molecules *i.e.* with no change in energy. However, a small percentage will lose or gain energy via interaction with an excited state in the material. If an incident photon with energy E_{laser} and momentum k_{laser} is inelastically scattered to one with energy E_{Raman} and momentum k_{Raman} , then using energy and momentum conservation we can write

$$E_{Raman} = E_{laser} \pm E_q \quad \text{and} \quad k_{Raman} = k_{laser} \pm q \quad (10)$$

where E_q and q are the energy and momentum transferred during the scattering event. Most typically, this is the energy and momentum of a phonon which is created (or destroyed) during the scattering process, although it can be any other exciton, such as plasmons⁴⁶ or polaritons⁴⁷. The positive and negative signs in equation (10) refer to the fact that energy can be added to the photon by the annihilation of a phonon, or subtracted from the photon by the creation of one. These are labelled, respectively as *Stokes* and *anti-Stokes* scattering processes. The expected ratio of intensities of Stokes and anti-Stokes processes is dependent on the thermal population of these phonon states, as in

$$\frac{I_S}{I_{aS}} \propto e^{E_q/k_B T} \quad (11)$$

where I_S and I_{aS} are the intensities of the Stokes and anti-Stokes processes, k_B is Boltzmann's constant, and T is the temperature. A Raman spectrum is the plot of the intensity of light scattered from a medium as a function of E_{Raman} . The spectrum will show peaks at photon energies $E_{Laser} \pm E_q$, corresponding to the energies of excitations within the medium. The linewidth of the peak is related to the lifetime of the related phonon⁴⁸. By convention, the Stokes signal is plotted at positive energies whilst the anti-Stokes signal is plotted at negative energies. As the anti-Stokes signal is usually much weaker, it is not usually discussed. Under certain special conditions, a third two photon process can become significant, where a phonon is simultaneously created by a Stokes process and annihilated in an anti-Stokes process, as shown in figure 7. This creates a pair of correlated photons⁴⁹, but has so far only been observed in diamond under a femtosecond pumping regime generating a very high photon flux⁵⁰.

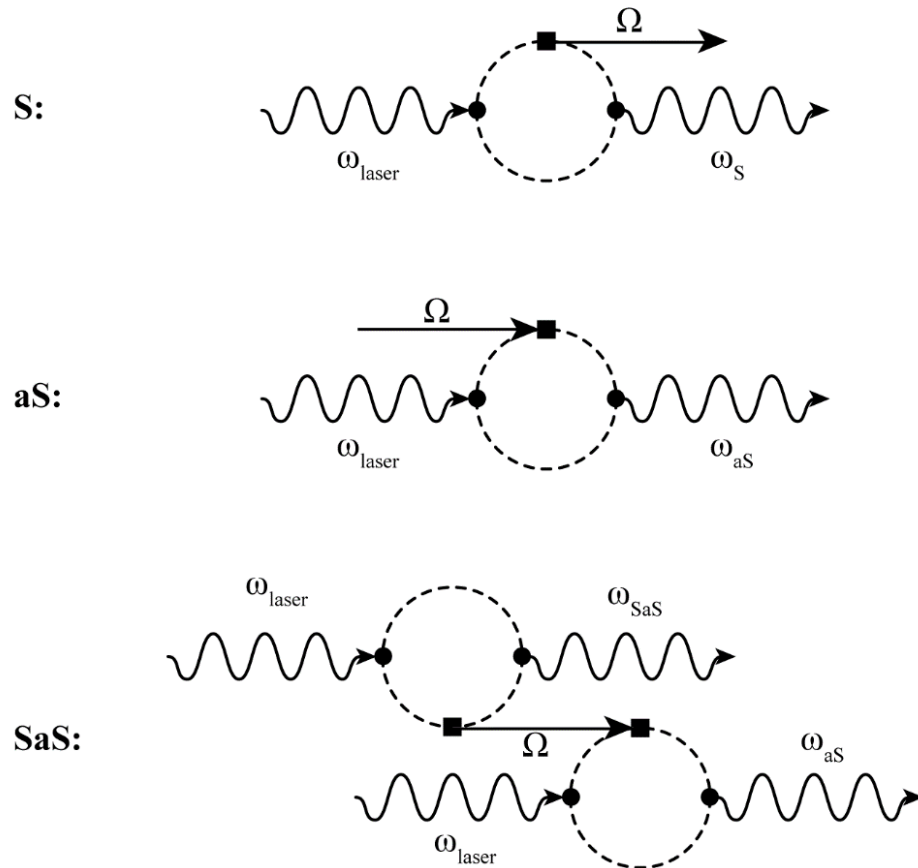


Figure 7 Feynman diagrams comparing 3 possible optical scattering paths. The top, middle, and bottom diagrams represent the Stokes process, the anti-Stokes process, and the correlated Stokes/anti-Stokes process respectively. Wavy and straight arrows represent photons and phonons respectively, and the dotted loop represents electron hole pairs. Black squares and circles represent electron phonon interactions and electron photon interactions respectively. Adapted from reference⁵¹ under Creative Commons (CC-BY) license.

Raman spectroscopy has long been used to characterize graphitic materials⁵², including graphite⁵³ and carbon nanotubes⁵⁴. Representative spectra of graphite and graphene are shown in figure 8. The main features seen in the Raman spectra occur in the region between 1250 cm^{-1} and 3400 cm^{-1} . The dominant (Raman-active) vibrations arise from the transverse optical (TO) and longitudinal optical (LO) phonon branches. At the centre of the first Brillouin zone (known as the Γ point and shown in figure 2), they form a doubly degenerate mode with $\vec{q} = 0$. A Kohn anomaly (discontinuity in the first derivative of the phonon dispersion relation) at this point⁵⁵ means that the electron phonon coupling is particularly strong. There is a second Kohn anomaly in the TO branch, near the K point ($\vec{q} \approx \vec{K}$).

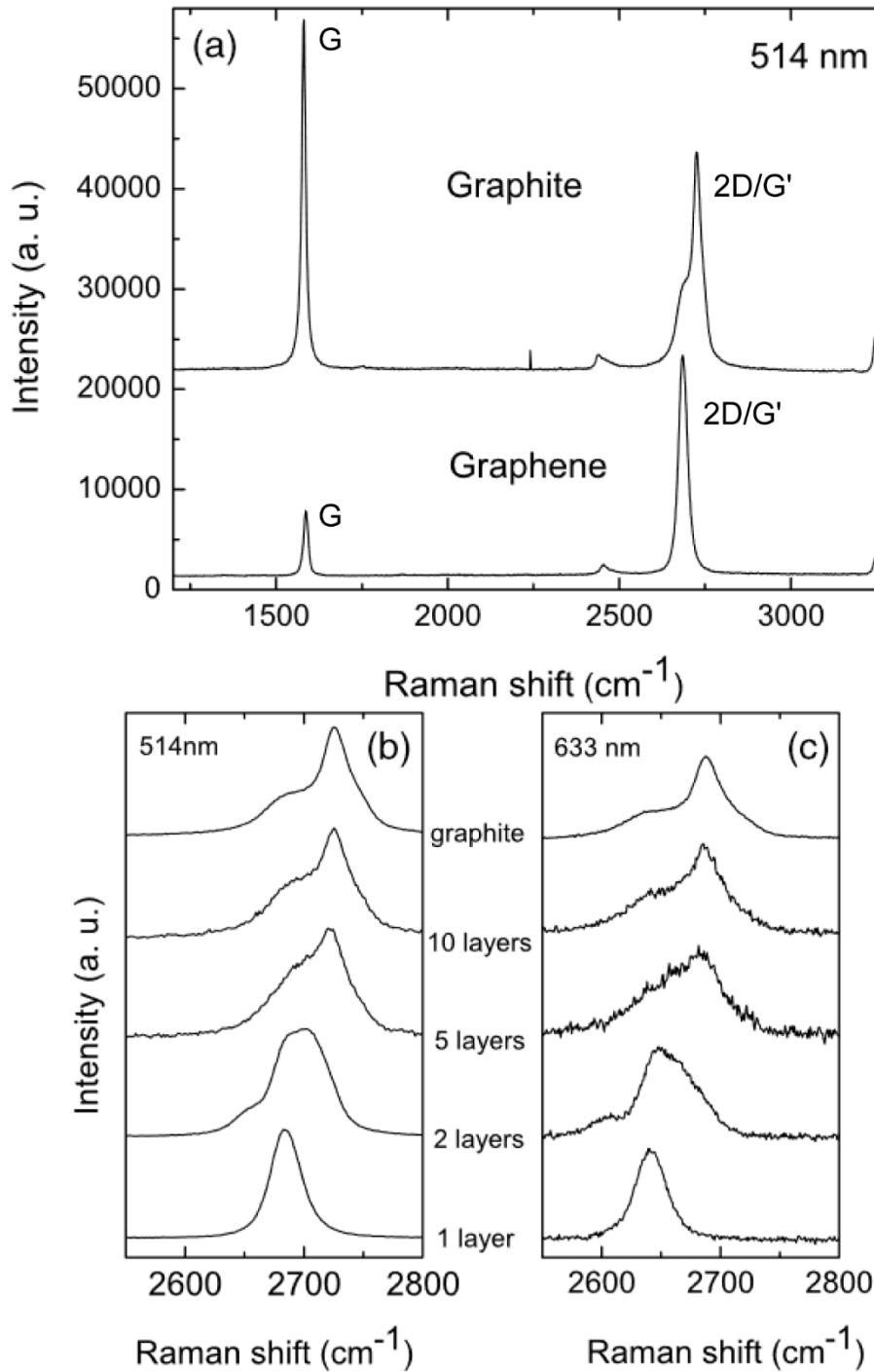


Figure 8 Evolution of the Raman spectra with thickness from monolayer graphene to bulk graphite. (a) Comparison of the Raman spectra (with $\lambda_{\text{Laser}} = 514 \text{ nm}$) of monolayer graphene and bulk graphite. The spectra have been rescaled such that their 2D/G' peak heights are equivalent. The 'Raman shift' refers to the change in wavenumber of Raman scattered photons due to the Stokes process. The G peak at $\sim 1580 \text{ cm}^{-1}$ and the 2D or G' peak at $\sim 2700 \text{ cm}^{-1}$ are the two prominent peaks. No D peak (at $\sim 1350 \text{ cm}^{-1}$) is visible demonstrating the absence of defects in the sample. (b) and (c) show the evolution of the 2D/G' peak at excitations of $\lambda_L = 514 \text{ nm}$ and $\lambda_L = 633 \text{ nm}$ respectively. Image adapted with permission from reference⁵⁶. Copyright (2006) by the American Physical Society.

A simplified picture of the various Raman scattering channels in monolayer graphene is shown in figure 9, categorised by their resonance conditions. The individual processes are discussed in the following section.

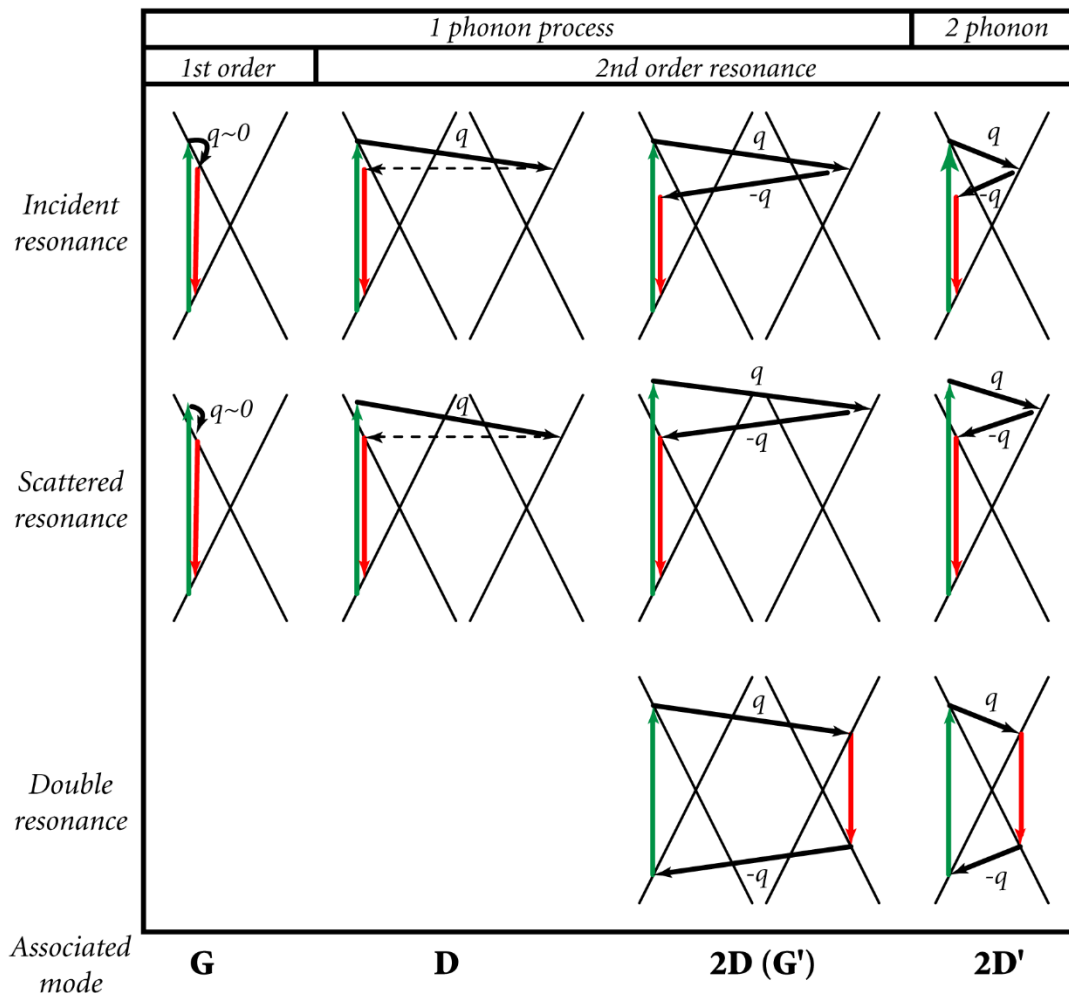


Figure 9 Raman scattering modes in monolayer graphene. The black crosses represent the Dirac cones of monolayer graphene at the k -point in energy-momentum space. Green arrows represent transitions due to photon absorption, and red lines represent transitions due to photon emission. Black arrows represent transitions due to phonon coupling events, and dotted arrows represent momentum transfer due to elastic scattering by a defect. The G and $2D'$ modes show intervalley scattering ($K \leftrightarrow K'$), and the D and $2D$ modes show scattering within one Dirac cone.

G band @ $\sim 1580 \text{ cm}^{-1}$

The *G band* corresponds to the doubly degenerate (LO and TO) phonon modes at the Γ point in the centre of the first Brillouin zone, which is the only Raman-active phonon with $\vec{q} = 0$. It has an intrinsically high Raman intensity due to the presence of the Kohn anomaly. It

corresponds to an in-plane vibration of the sp^2 bonds, and is particularly sensitive to strain⁵⁷, as the change in bond angles and lengths breaks the hexagonal symmetry of the graphene.

D band @ $\sim 1350\text{ cm}^{-1}$

The phonon involved in the D-mode comes from the TO branch close to the K point, and is a one-phonon, second order process. The scattering occurs between valleys. As $\vec{q} \approx \vec{K} \neq 0$, it does not conserve momentum and is generally forbidden. However, the presence of a defect in the graphene lattice allows the provision of the necessary momentum through an elastic scattering process. Similarly to the G mode, it has an intrinsically high Raman intensity due to the presence of the Kohn anomaly. The presence of a D-peak is therefore related to disorder in sp^2 systems, and is not seen in pristine graphene/ graphite layers. The amount of defects in a graphene monolayer can be estimated by looking at the relative heights of the D and G peak. A D peak is also observed for armchair terminated edges, and absent for zigzag terminated edges⁵⁸ in ‘crystallographic’ graphene flakes.

2D (or G') band @ $\sim 2700\text{ cm}^{-1}$

This doubly resonant band⁵⁹ is known as both the *G' band* (with G denoting Graphite) and, more commonly, the *2D band* (due to its doubly resonant nature). It is a second order two-phonon process which exhibits a strong dependence on the incident energy E_{laser} . It involves the same phonon as the D peak (meaning that there is strong coupling due to the presence of the Kohn anomaly), but the second phonon provides the necessary momentum transfer rather than scattering from a defect site. It therefore involves twice the energy/wavenumber shift as the D-mode. As the number of graphene layers increases, the 2D peak is split into 4 components due to the changes in the electronic band structure^{56,60}, as discussed in section 3.2.4. The evolution of the 2D peak shape with increasing layer number is shown in the lower part of figure 8 for two different incident laser energies. This characteristic shape, along with the G:2D intensity ratio (1:4 for monolayer graphene, decreasing with increasing layer number), means that Raman spectroscopy can be used to accurately specify the number of layers in a graphene sample.

2D' band @ 3250 cm⁻¹

The 2D' band is a doubly resonant, two phonon second order scattering process, but unlike the 2D band it is an intravalley rather than intervalley process. It is associated with LO-mode phonons near the Γ point. It is less intense than the other scattering processes, as there is no associated Kohn anomaly in the phonon dispersion at this point. There is an equivalent intervalley one phonon scattering process corresponding to the D mode, where the extra momentum is provided by defect scattering known as the D' mode, which generates a peak at $\sim 1620 \text{ cm}^{-1}$ (close to the G-peak).

3.4 Mechanical properties

The mechanical properties of graphene are perhaps the hardest to explore. Its 2 dimensional nature means it is simple to make good electrical contact to defined pristine areas when exploring its electronic properties. Its remarkably strong optical interaction per layer means that optical experiments are feasible with conventional equipment. However graphene's planar nature and fragility at large sizes makes it difficult to interface with mechanically. Nevertheless, its simple structure gives it extraordinary strength at μm length scales. This section outlines how various metrology techniques have been applied to quantify its mechanical behaviour. Firstly, theoretical predictions of graphene's strength are reviewed. Then quasi-static means of measurement, specifically central point indentation and pressure differential bulge testing, are introduced. Approximate solutions for the force displacement behaviour of circular graphene membranes, and the stress maxima under spherical indentation are discussed. Measurements of the elastic modulus and intrinsic strength are reviewed. Finally, dynamic measurements on the vibrational resonances of suspended graphene membranes are discussed.

3.4.1 Predicted strength

The principle that as the size of a material is reduced, its relative strength is increased is well-known. In 1921, Griffith proposed a theory for the failure of brittle materials⁶¹. As a result, he showed that the failure strength of a brittle material is dominated by flaws and defects within the material, rather than the strength of its chemical bonds. Extending this to the ultimate limit, he wrote:

“In the limit, a fibre consisting of a single line of molecules must possess the theoretical molecular (maximum) tensile strength... Fine wires are stronger than thicker ones, but the present view suggests that in sufficiently thin wires the effect should be enormously greater”

The strength of graphene was theoretically predicted to be higher than that of any other material⁶² before its isolation, when considering it as a theoretical building block for carbon nanotubes in an *ab initio* study.

The earliest indication for the extraordinary stiffness of the 2D membrane was the observation that it could support its own weight over very large distances, rather than rolling or scrolling⁶³. Graphene supported only by one edge with a length to thickness ratio of 10^6 has been observed⁶³ in transmission electron microscope (TEM) samples. One such flake is shown in figure 10.

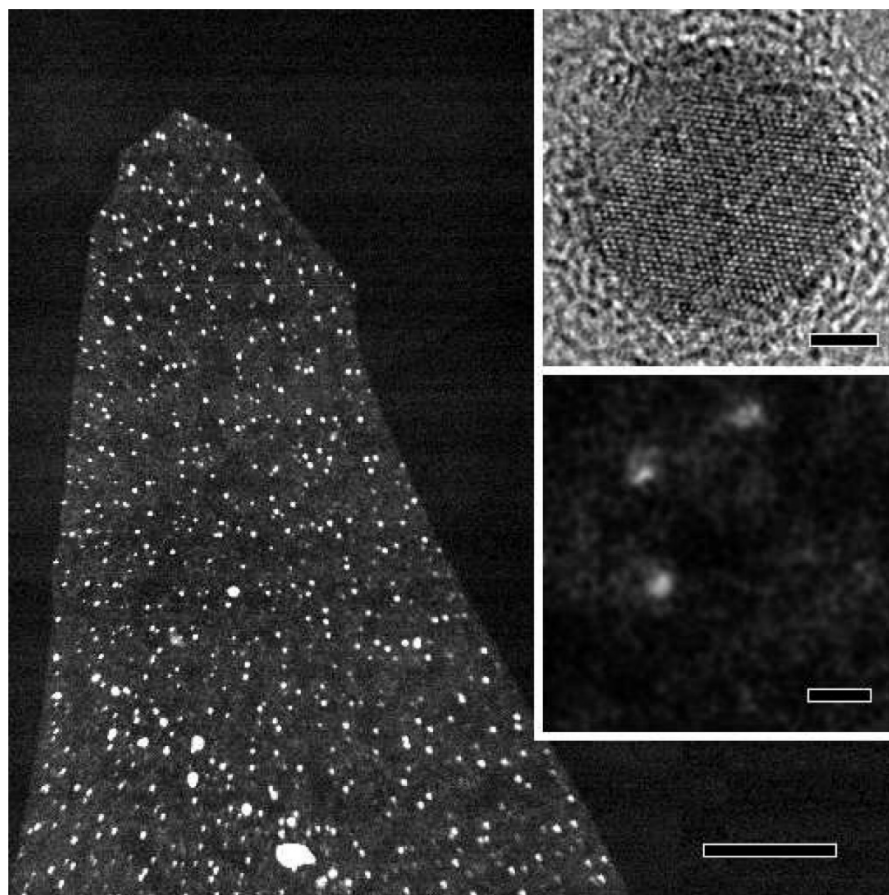


Figure 10 Extraordinary stiffness of graphene supported on one edge. The main image shows a HAADF TEM image of a graphene fragment left after a membrane ruptured during annealing. The fragment is supported only from one edge (the bottom edge in the figure). The scale bar is $1\ \mu\text{m}$. The white dots are Cu nanoparticles. The upper inset shows a bright field STEM image of one of the Cu nanoparticles, with a scale bar of $2\ \text{nm}$. The lower inset shows a HAADF image of individual ad-atoms on the graphene surface, with a scale bar of $2\ \text{\AA}$. Image reprinted with permission from reference⁶³. Copyright (2008) American Chemical Society.

Generally, meaningful mechanical parameters of graphene cannot be extracted using conventional techniques developed for three dimensional materials. The experimental approaches used to study this can be divided into two main categories: quasi-static and dynamic. Quasi-static techniques examine the controlled deformation of a membrane by an applied pressure or mechanical force. Measured deformations can then be compared to

membrane models to estimate the model parameters. Dynamic measurements investigate the vibrational resonance modes in suspended membranes.

3.4.2 Quasi-static means of measurement

Quasi-static techniques can be split into two main branches. The first involves applying a pressure differential across a sealed graphene membrane and measuring the resulting deflection, typically using atomic force microscopy (AFM). In the second, a known mechanical deformation is applied to a membrane by a mechanical probe, which is used to measure the resulting deformation due to a range of applied forces. In general, this involves using an AFM cantilever or specialised nanoindentation system to centrally indent a clamped circular membrane. An example of the first kind of investigation, colloquially known as a *bulge test*, is shown in figure 11.

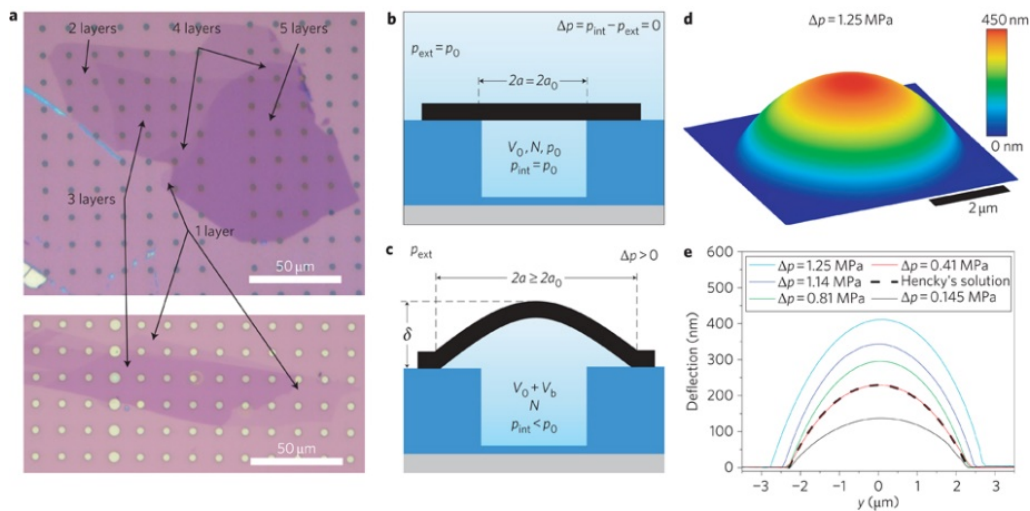


Figure 11 Bulge testing of graphene membranes. (a) shows optical images of graphene flakes exfoliated onto a SiO_2 coated silicon substrate pre patterned with cylindrical cavities. (b) shows a schematic of a circular membrane without a pressure differential across it. (c) shows a similar membrane with an internal pressure p_{int} greater than the external pressure p_{ext} such that the membrane bulges outwards due to a pressure differential $\Delta p = p_{\text{int}} - p_{\text{ext}} > 0$. The membrane is partially delaminated from the substrate around the edges of the holes, increasing the footprint of the bubble. (d) shows a height image taken with an AFM of a membrane with a differential in pressure of $\Delta p = 1.25 \text{ MPa}$. (e) shows height profiles of a membrane with various differential pressures. The black line is Hencky's solution⁶⁴ for a differential pressure $\Delta p = 0.41 \text{ MPa}$, which shows a very good fit to the experimental data. Reprinted by permission from Macmillan Publishers Ltd: *Nature Nanotechnology*⁶⁵, copyright (2011).

These techniques do not directly measure any intrinsic parameters of graphene, rather they probe the behaviour of the specific membrane under test; a model of the membrane is

required. The simple models used are those where the graphene membrane is considered a clamped, circular, two dimensional, uniform elastic film under a uniform pressure differential, or centrally indented by a point like probe. Such solutions are referred to as Hencky's solutions after the author of a 1915 paper⁶⁶ on the deformation of such membranes. These solutions are introduced and discussed in the following subsection.

3.4.2.1 Approximate solutions

A convenient way to study the mechanical response of graphene using commonly available equipment is via the indentation of a suspended membrane using an AFM or specialised nano-indenter. A model of the graphene membrane as a (circular) two dimensional elastic film is then required to extract meaningful information from the experimental force displacement data. However, even for a clamped, circular membrane under central point indentation (*i.e.* with zero tip radius), there is no closed-form analytical solution which allows for both finite deformations as well as intrinsic (zero deflection) tension⁶⁷⁻⁶⁹. A schematic of this system is shown in panel (a) of figure 12.

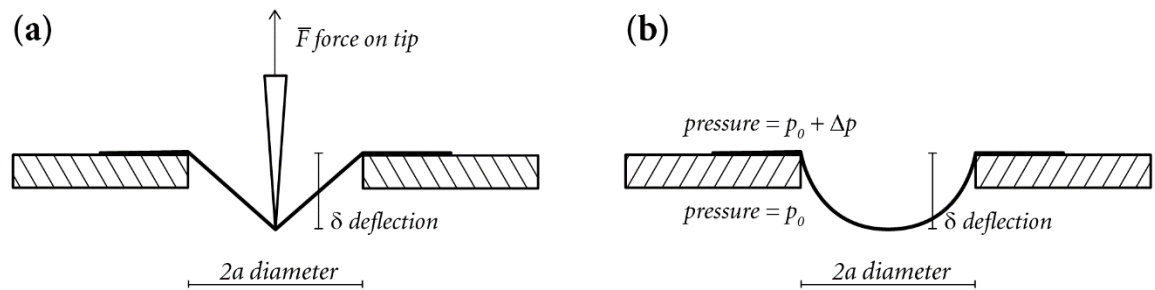


Figure 12 Illustration of deformed graphene membranes. Parameters referred to in this section are indicated on the diagram. (a) shows a membrane under central point loading, and its resultant deformation. (b) shows a membrane deformed by a pressure differential across it.

Lee *et al.*⁷⁰ combined approximate solutions for two special cases to give a force-displacement relationship which was found to correspond to the results of numerical simulations to within the level of experimental uncertainties. The two cases are that of a membrane with very high pre-tension relative to the stress induced by very small indentation depths, and that of large deflections and corresponding stresses relative to the initial pre tension. These produce a linear and a cubic relationship respectively, and their sum is then employed to analyse force-displacement curves obtained from experiment.

High pretension relative to induced stress

In the case of a clamped suspended circular elastic thin membrane under point load, with zero bending stiffness and at low displacement, Wan *et al.*⁶⁹ showed that the force displacement behaviour due to the intrinsic pretension in the membrane can be approximately expressed as a linear relationship:

$$F = (\pi T)\delta \quad (12)$$

where F is the applied central perpendicular point force magnitude, T is the pre-tension in the membrane and δ is the central point perpendicular deformation.

Low pretension relative to induced stress

In the opposite case, at large deflections and with stresses far greater than the initial pretension, Komaragiri *et al.*⁶⁸ give an approximate value for the force-displacement behaviour as:

$$\left(\frac{\delta}{a}\right) = \frac{1}{q} \left(\frac{F}{E_{2D}a}\right)^{\frac{1}{3}} \quad (13)$$

where F is the central perpendicular point force magnitude applied, δ is the central point perpendicular deformation, a is the membrane radius, E^{2D} is a ‘two-dimensional Young’s modulus’ with units of N/m . The constant q is given by:

$$q = \frac{1}{(1.049 - 0.15\nu - 0.16\nu^2)} \quad (14)$$

where ν is the Poisson’s ratio of the membrane material.

Combined solution

Summing the two terms described previously, in equations (12) and (13), allows us to write an approximate solution for the force displacement behaviour:

$$F = (\pi T)\delta + E_{2D} \left(\frac{q^3}{a^2} \right) \delta^3 \quad (15)$$

This is the basic model generally used for examining the inelastic deformation of graphene and other 2D materials via indentation using atomic force microscopy.

Central stress under spherical tip

In the point loading case, there is an assumed stress singularity at the centre of the membrane. Since this is clearly nonphysical, a finite tip shape must be assumed. The simplest case is that of a spherical tip, as it preserves the circular symmetry of the problem. Bhatia *et al.* derived⁷¹ the maximum stress in the centre of a thin clamped circular membrane under central indentation by a spherical tip as

$$\sigma_{max}^{2D} = \sqrt{\frac{F E_{2D}}{4\pi R_{tip}}} \quad (16)$$

where R_{tip} is the radius of the spherical indenter. This implies that the force at which the membrane fails (at a force corresponding to the maximum stress) is a function of the tip radius. This approximation slightly overestimates the maximum stress at high membrane deformations as it fails to account for nonlinear elasticity.

Uniform pressure differential solution

A similar method can be used^{64,72} to generate an alternative solution for the case where the (circular) membrane is deformed by a pressure differential:

$$\Delta p = \left(\frac{4T}{a^2}\right)\delta + \left(\frac{8E_{2D}}{3a^4(1-\nu)}\right)\delta^3 \quad (17)$$

where Δp is the pressure differential across the membrane, δ the perpendicular deformation of the central area of the membrane, a is the membrane radius, T the membrane pre-tension, E_{2D} is the 2D modulus, and ν is the Poisson's ratio of the membrane material. This arrangement is shown in part (b) of figure 12.

3.4.2.2 Measurements of Young's Modulus

A summary of measured and calculated values for the two dimensional Young's modulus of monolayer graphene reported in the literature is contained in table 1. Further experimental measurements, including those on other 2D materials are tabulated by Castellanos-Gomez et al⁷³. Reported values generally range around 300 – 350 N/m . Measurements made using central point loading and bulge testing give equivalent answers, although bulge testing can also be used to measure graphene-substrate adhesion in the absence of adequate clamping⁷⁴. In the central point loading technique, a force curve in the centre of the membrane is recorded using an AFM and a sharp tip (see section 4.3) corresponding to $F(\delta)$ from equation (15). A fit is then used to estimate E_{2D} , although there is a large potential error⁷⁵ due to incorrectly specifying the zero deflection point (ZDP), where $F = \delta = 0$. This is discussed in detail in section 5.6. Although equation (15) is a quasi-empirical approximation, *ab initio* calculations⁷⁶ have shown it captures the elastic behaviour well.

Table 1 Summary of measured and calculated values of the two dimensional Young's modulus of monolayer graphene reported in the literature record, adapted from a table in⁷⁷. Black text shows experimental studies and grey text shows theoretical studies.

<i>Experimental (HREELS), graphene on multiple substrates, graphite</i> ⁷⁷	$E_{2D} = 342 \text{ N/m}$
<i>Experimental (HREELS), graphene on Ni(111)</i> ⁷⁷	$E_{2D} = 310 \text{ N/m}$
<i>Experimental (AFM) on graphene/copper foils</i> ⁷⁸	$E_{2D} = 339 \pm 17$
<i>Experimental (AFM) on graphene membranes</i> ⁷⁰	$E_{2D} = 340 \pm 50$
<i>Experimental (AFM) on graphene membranes</i> ⁷⁹	$E_{2D} = 350 \pm 50^*$
<i>Tersoff-Brenner potential</i> ⁸⁰	$E_{2D} = 235 \text{ N/m}$
<i>Energetic model</i> ⁸¹	$E_{2D} = 307 \text{ N/m}$
<i>Continuum elasticity theory + tight-binding atomistic simulations</i> ⁸²	$E_{2D} = 312 \text{ N/m}$
<i>Density Functional Theory (DFT)</i> ⁸³	$E_{2D} = 330 \text{ N/m}$
<i>Brenner's potential</i> ⁸⁴	$E_{2D} = 336 \text{ N/m}$
<i>First-principles energy calculations, to continuum elasticity</i> ⁸⁵	$E_{2D} = 344 \text{ N/m}$
<i>Tersoff-Brenner potential</i> ⁸⁶	$E_{2D} = 345 \text{ N/m}$
<i>Ab initio</i> ⁸⁷	$E_{2D} = 350 \text{ N/m}$
<i>Atomistic Monte Carlo</i> ⁸⁸	$E_{2D} = 353 \text{ N/m}$
<i>Density functional theory</i> ⁸⁹	$E_{2D} = 356 \text{ N/m}$
<i>Empirical force-constant calculations</i> ⁹⁰	$E_{2D} = 384 \text{ N/m}$
<i>Experimental (AFM) on graphene/copper foils</i> ⁹¹	$E_{2D} = 55 \text{ N/m}^{**}$

*This paper is included as part of this work **Refers to wrinkled regions where substrate adhesion is poor

By dividing the measured two dimensional Young's modulus by a nominal graphene thickness (usually taken to be the interlayer spacing in graphite $h = 0.335 \text{ nm}$), we can generate a conventional three dimensional Young's modulus with units of pressure. This results in a modulus of around 1 TPa , which matches the in-plane Young's modulus of bulk graphite⁹². It is worth noting that the thickness for monolayer graphene⁶³ calculated using elasticity theory⁹³ is $h = 0.23 \text{ nm}$. Though this derived, thickness dependent, bulk value is useful for comparison with other materials, it is not an intrinsic property of the graphene sheet, and cannot be used to estimate other mechanical properties.

3.4.2.3 Measuring ultimate strength

Measuring the ultimate strength of graphene monolayers is particularly tricky. Central point indentation using an atomic force microscope (AFM) is an ideal way to measure this, but the forces which need to be applied to the AFM tip are of the order of a few μN , which is enough to shatter conventional silicon tips. This tip damage is discussed in section 6. Nevertheless, this is the only way in which the ultimate strength of a graphene monolayer has been measured. The breaking force for membranes is actually independent of the membrane geometry, but merely a function of the tip radius. This is because even when the membrane is stretched to its maximum extent, the stress is concentrated in the area immediately around the tip.

Averaged measurements of the maximum stress at failure obtained using the breaking force and equation (16) (it is nontrivial to vary the tip radius and plot a gradient!) give results ranging up to^{70,78,94} around $50 Nm^{-1}$. In a similar manner to the two dimensional Young's modulus, this can be converted to a derived intrinsic strength by defining a finite graphene monolayer thickness, giving a value of $\sigma_{int} \approx 120 - 130 GPa$ using the interlayer spacing in graphite. Full *ab initio* modelling⁷⁶ shows that equation (16) slightly overestimates the maximum stress, but finite element modelling⁹⁵ of indentation with a realistic tip accurately predicts the experimental breaking strain. There is also a large degree of uncertainty due to the real tip geometry; as they are generally crystalline diamond a spherical approximation is not ideal. Nevertheless, these properties make monolayer graphene the strongest material ever measured. It is thought that these extreme mechanical properties will find applications in a wide array of nanoelectromechanical systems^{96,97}, as well as eventually in bulk composites³.

3.4.5 Dynamic behaviour of graphene membranes

The dynamic behaviour of 2D materials is typically investigated⁷³ by measuring the oscillation amplitude of suspended membranes subject to a controlled actuation at or near the resonance of the membrane⁹⁸. Large resonance peaks are observed in the frequency spectra when the actuation frequency matches the membrane resonance⁹⁹. The positions of the resonance peaks are determined by both the membranes geometry and on the mechanical properties of the membrane material. As the geometry is well known, this approach allows

for the extraction of the mechanical properties. The widths of the resonances is controlled by Q , the *quality factor*, which is related to the resonator damping. An example of a resonance curve of an oscillating graphene membrane (on axes of both logarithmic amplitude and power) is shown in figure 13.

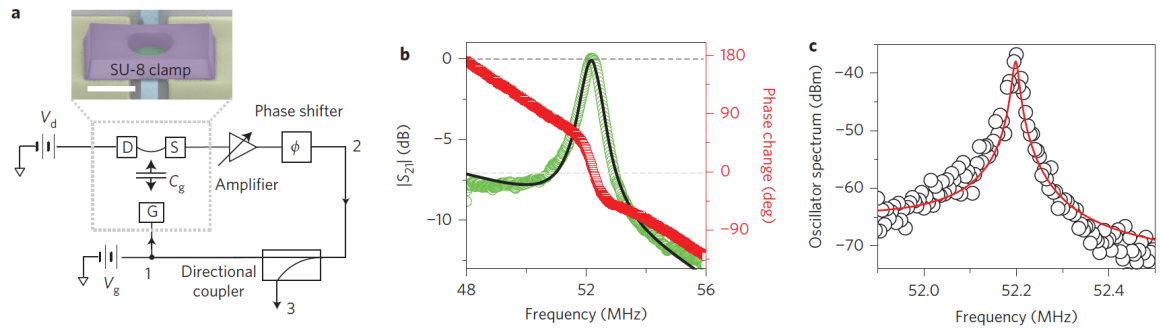


Figure 13 Frequency response of a circular clamped graphene resonator. (a) shows a simplified circuit diagram, with the inset showing a false-colour SEM image of a resonator. The scale bar shown is $3 \mu\text{m}$. (b) shows signal transmission through the resonator (with a diameter of $4 \mu\text{m}$). The green data (left axis) shows the transmitted magnitude, and the red data (right axis) shows the corresponding phase change. The black line is a Lorentzian fit, with a resonant frequency of 52.19 MHz and a quality factor of 55 . (c) shows the power spectrum of the same oscillator. The red line is a forced Lorentzian fit. All measurements were at room temperature. Reprinted by permission from Macmillan Publishers Ltd: *Nature Nanotechnology*¹⁰⁰, copyright (2013).

The most common way of actuating the membranes is via electrostatic deflection¹⁰¹ from a back gate, but they can also be driven optically¹⁰², or purely driven by thermal fluctuations¹⁰³. The resultant oscillations are then detected by electrical readout¹⁰⁴, optical interferometry¹⁰⁵ or scanning probe techniques¹⁰⁶. The mechanical properties of a wide range of 2D material mechanical resonators are tabulated by Castellanos-Gomez et al⁷³. Graphene based resonators have exhibited resonance frequencies from 1-200MHz, with quality factors as high as $Q \approx 2.2 \times 10^5$ at cryogenic temperatures. These properties make graphene a strong candidate for use in on-chip nano electro mechanical system (NEMS) oscillators for communications applications, such as frequency modulators and timing references¹⁰⁰. As graphene has such a high surface area relative to its mass, even a small amount of material adsorbed on the surface can dramatically alter its mode frequencies. It has been theorised that graphene resonators could function as mass sensors with a resolution¹⁰⁷ down to $10^{-6} fg$, and their large scale integration is relatively simple¹⁰⁸ when compared with ultrasensitive carbon nanotube resonators¹⁰⁹.

3.5 Production of graphene

In light of the novel applications that graphene promises, efforts were directed towards investigating alternative ways to produce the material, at increased scales^{3,110}. This section reviews all the ways in which graphene can be produced, and discusses the quality of the resulting materials. All of the major proposed production methods are shown on a plot of relative quality against relative price in figure 14.

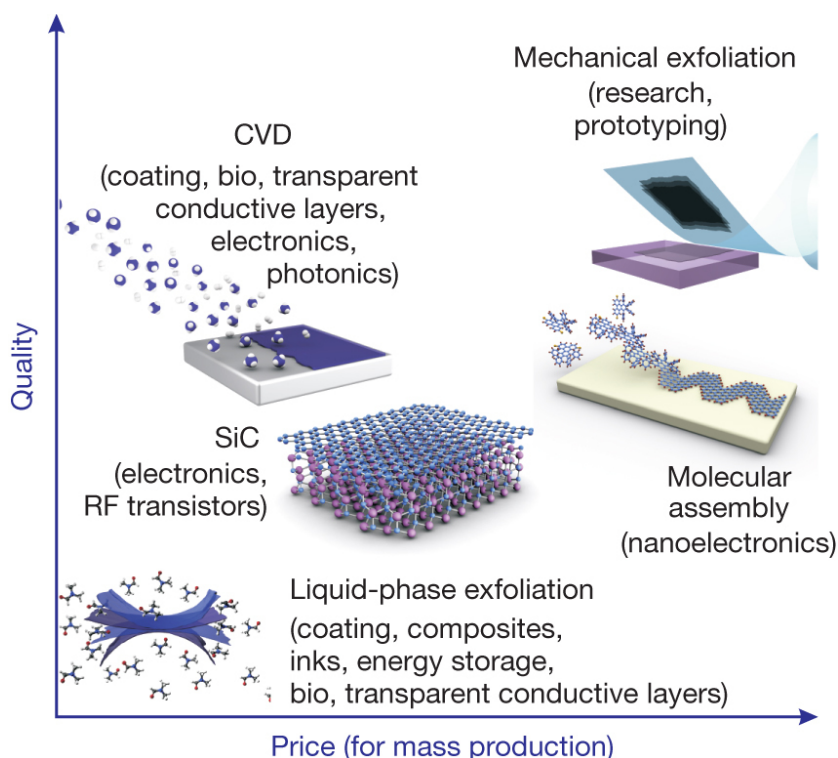


Figure 14 Methods of graphene production arranged by relative quality and price. Included are liquid phase exfoliated (LPE) graphene (low quality, low price), CVD graphene (relatively high quality, relatively low price), epitaxial graphene grown on SiC (relatively high price, medium quality), Graphene assembled from molecular components (very high price, medium quality), and mechanically cleaved graphite (highest quality, highest price). Reprinted by permission from Macmillan Publishers Ltd: Nature³, copyright (2012).

3.5.1 'Top down' production

The technique used in the discovery of monolayer graphene, micromechanical cleavage from bulk crystals using adhesive tape, still results in the highest quality resulting flakes, however with limited size (typically $\sim 10 - 100 \mu\text{m}$ with optimised processing, and occasionally up to $\sim 1 \text{ mm}$ on clean SiO_2). This technique is also incredibly time consuming for the relative amount of graphene that is produced, but allows skilled researchers to exfoliate flakes with

very high crystalline quality onto a variety of materials, from silicon dioxide to polymers (useful in 'dry' transfer processes) and even atomically flat substrates such as Mica¹¹¹.

Liquid exfoliation of graphene is conceptually similar to manual exfoliation in that it involves the separation of bulk graphite into its component layers. However it takes place in solution and is inherently scalable and therefore of great interest for applications despite the relatively low quality of the resultant films. It is possible to directly exfoliate graphene from graphite via sonication¹¹² in a solvent that favours an increase in the total surface area of graphite, such as *n-methyl pyrrolidone* (NMP) or *dimethyl sulfoxide* (DMSO), but the resultant flake sizes are extremely small. A more common and industrially relevant technique is the exfoliation and subsequent reduction of Graphite oxide to form so-called reduced Graphene Oxide (rGO) films. Here, graphite pellets are oxidised, then exfoliated in aqueous solutions, often containing surfactants to prevent aggregation. Cleaning steps (often using bases) then follow to remove the oxidised graphitic debris. The GO can then be deposited on almost any substrate via spin coating, spraying, dip coating, or Langmuir-Blodgett deposition, and annealed in a reducing atmosphere (normally hydrazine) to partially remove the remaining oxidation¹¹³, producing slightly oxidised graphene films. Alternatively, it is possible to reduce the flakes while still in solution that can subsequently be deposited. Graphene produced via liquid phase exfoliation (LPE) is already produced on the tonne scale¹¹⁰ for applications in composites and coatings.

3.5.2 'Bottom up' production

In contrast to the other two techniques discussed so far, *chemical/catalytic vapour deposition* (CVD) is a bottom-up technique, where a graphene layer is synthesised from its component parts, in this case carbon atoms in gaseous form. It forms on a metal surface, which acts as both a catalyst for the activation of the gaseous species and a substrate for deposition. The most common metal surfaces used are Ni and Cu, with Cu having the edge due to the very low permeability of Carbon atoms inside Cu¹¹⁴. Cu also tends to self-limit growth after a complete layer is formed¹¹⁵, which makes it simpler to produce large area monolayer areas. More exotic substrates have been investigated, with growth on Ge (110) wafer shown to be single crystal¹¹⁶, although their cost precludes their use in large scale production as they are damaged or destroyed during most transfer processes currently used. The films are first

heated in a reducing atmosphere to clean and reduce the surface, before precursor gases containing carbon, such as methane (CH_4) are introduced. Different gas mixtures, temperatures and pressures have all been investigated, using both one step and many step 'recipes'^{114,115}. Clean transfer of CVD graphene onto insulating subjects is an area of intense focus^{117,118}, with research into non-destructive transfer processes ongoing. The main advantage of the CVD process is that the size of the graphene area produced is limited only by the size of the substrate/furnace, so it is very scalable. Roll-to-roll production and transfer has been reported¹¹⁸.

Alternatively, small, defined graphene sheets can be synthesised from polyaromatic hydrocarbon (PAH) molecules in solution in the molecular nano assembly process^{119,120}. While only very small molecules can be produced, their defined size and geometry makes them potentially useful for next generation nanoelectronic devices. As the electronic properties of very small graphene flakes (dimension below $\sim 20\text{nm}$) are dominated by their size and edge termination (armchair or zigzag), the ability to produce defined geometries is potentially extremely useful¹¹⁰.

3.5.3 Epitaxial graphene on SiC

A third way of producing graphene is via the high temperature graphitization of certain faces of Silicon Carbide crystals¹²¹. The quality of graphene produced in this manner can be very high¹²², however the high cost of SiC wafers and the temperatures required (well over 1000°C) make this probably the most expensive way to produce graphene. Despite this high cost, it has been suggested that so called epitaxial graphene may be used in high frequency transistors for communications¹²³, or in developing a new standard resistance¹²⁴.

3.6 Twisted bilayer graphene

In section 3.2.3, the van Hove singularities present in the density of states of monolayer graphene were introduced. In many cases, new material systems with desirable properties are formed when the Fermi energy is close to a vHS^{125,126}. Their large distance from the Dirac point in monolayer graphene means that they are hard to interact with by manipulating the Fermi energy through gating or chemical doping. However, by introducing a rotation between two monolayer graphene sheets in a so called twisted bilayer graphene (or tBLG) system, it is possible to introduce a new set of van Hove singularities close to the Fermi level which can have a profound effect on the electronic properties of the system. Furthermore, the positions of the singularities are dependent on the twist angle, meaning that it is possible to engineer a new phase of matter with controlled properties if we can control the twist angle.

In this section, the moiré superlattice generated by the rotation between the two layers in a tBLG system is introduced. Then the electronic structure and optical properties of tBLG, and their dependence on the twist angle is discussed. Finally, resonance Raman spectroscopy studies on tBLG systems are discussed.

3.6.1 Physical structure of twisted bilayer graphene

When two hexagonal lattices are twisted in relation to one another, a moiré pattern is generated with a wavelength given by¹²⁷

$$\lambda_{\text{moiré}} = \left(\frac{a}{2 \sin\left(\frac{\theta}{2}\right)} \right) \quad (18)$$

where $\lambda_{\text{moiré}}$ is the moiré wavelength, a is the lattice constant, and θ is the twist angle from AB stacked graphene (see section 3.2.4). As the hexagonal lattice has 3 fold rotational symmetry, this is only valid when $-60^\circ \leq \theta \leq 60^\circ$. A schematic showing these twist induced moiré patterns is shown in figure 15.

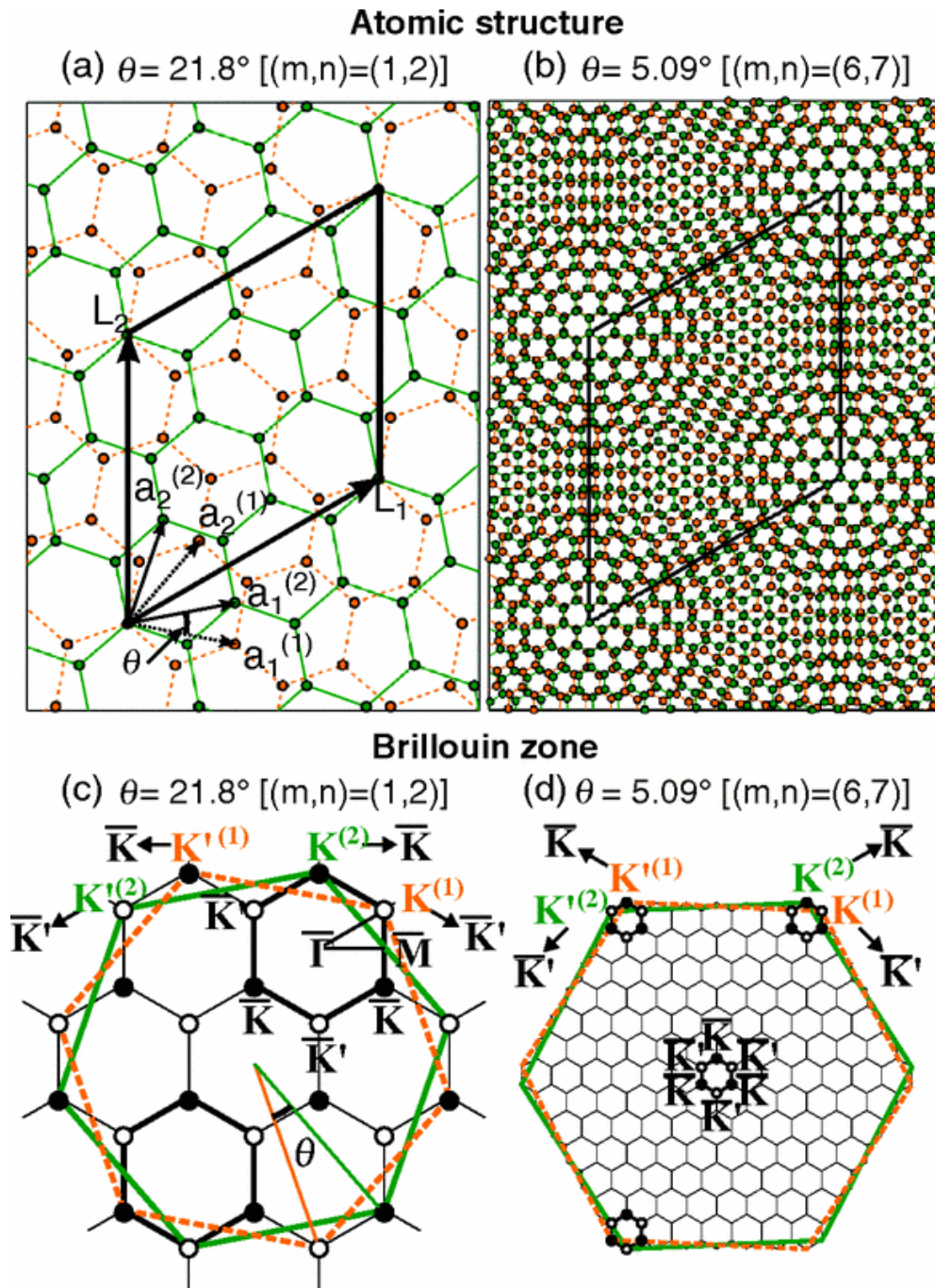


Figure 15 Brillouin zones of twisted bilayer graphene samples. (a) and (b) show the atomic arrangements of tBLG samples with rotation angles of $\theta = 21.8^\circ$ and $\theta = 5.09^\circ$ respectively. The dashed (orange) and solid (green) lines represent the atomic lattices in layers 1 and 2 respectively. (c) and (d) show the Brillouin zones of the arrangements in (a) and (b) respectively. The dashed (orange) and solid (green) lines show the first Brillouin zones of layers 1 and 2 respectively. The thick black (small) hexagon represents the folded Brillouin zone of the tBLG in both cases. Reprinted with permission from reference¹²⁸. Copyright (2013) by the American Physical Society.

Such moiré patterns are observed at cleaved surfaces in samples of highly oriented pyrolytic graphite (HOPG), where the top layer is misorientated with AB stacked graphite underneath. Due to minute differences between the interlayer couplings between the two layers across the moiré pattern, the pattern can be visualised by STM. A range of STM height images at

different magnifications of such a moiré pattern found after cleaving an HOPG sample are shown in figure 16. Areas of twisted bilayer graphene are also commonly formed during CVD growth processes¹²⁹, and are readily observable using transmission electron microscopy¹³⁰.

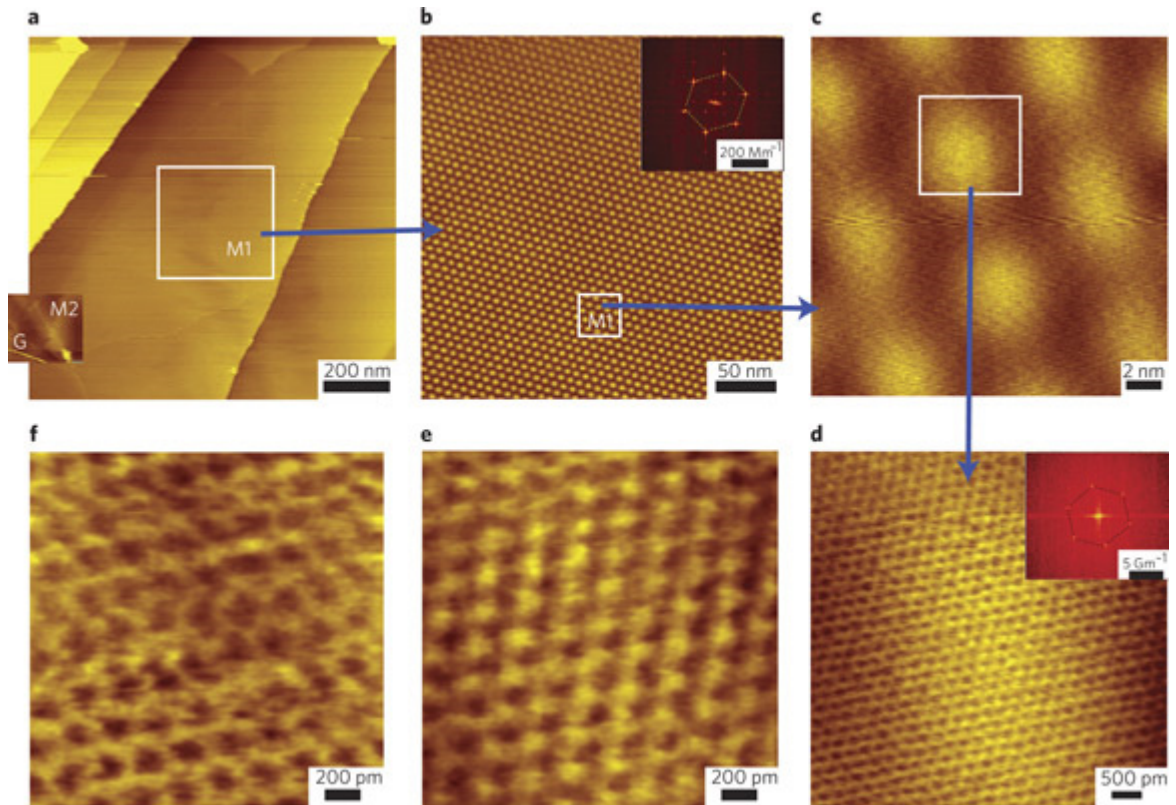


Figure 16 Moiré patterns in rotated graphene. STM images of a moiré pattern observed in a freshly cleaved HOPG sample. (a) shows a large area overview, while (b) is a zoomed in region showing the moiré pattern with a periodicity of ~ 7.7 nm, corresponding to a twist angle of $\theta = 1.79^\circ$. (c) shows a further zoom in to the area marked in (b), while (d) is a blow-up of the bright area highlighted in (c). (e) and (f) show atomic resolution images of a bright and dark region respectively. Reprinted by permission from Macmillan Publishers Ltd: *Nature Physics*³¹, copyright (2010).

Similar moiré patterns are generated by other 2D materials, and even by the combination of two. The moiré pattern formed when graphene is placed on hexagonal boron nitride is particularly well studied, as it is commonly used as an ultra-flat substrate. The patterns do not have the exact same form as those in tBLG due to a mismatch in the lattice constant of the two materials. However such patterns can be visualised using room temperature AFM¹³¹.

3.6.2 Electronic structure of twisted bilayer graphene

The superlattice generated by the moiré pattern profoundly affects the electronic structure of twisted bilayer graphene systems. As shown in the lower part of figure 15, the rotation of one of the layers in real space leads to the rotation of one of the individual layers Brillouin zones. The schematic individual band structures of the two layers are shown in figure 17. Although this is not a complete picture, it highlights the origins of the 3 new saddle points. Within the K and K' region, the pairs of Dirac cones hybridise to form a new saddle point between them at (i). (ii) is also a hybridised saddle point, corresponding to the symmetrical pair of that indicated by (i). The original saddle point remains at (iii), but is perturbed by the presence of the second layer.

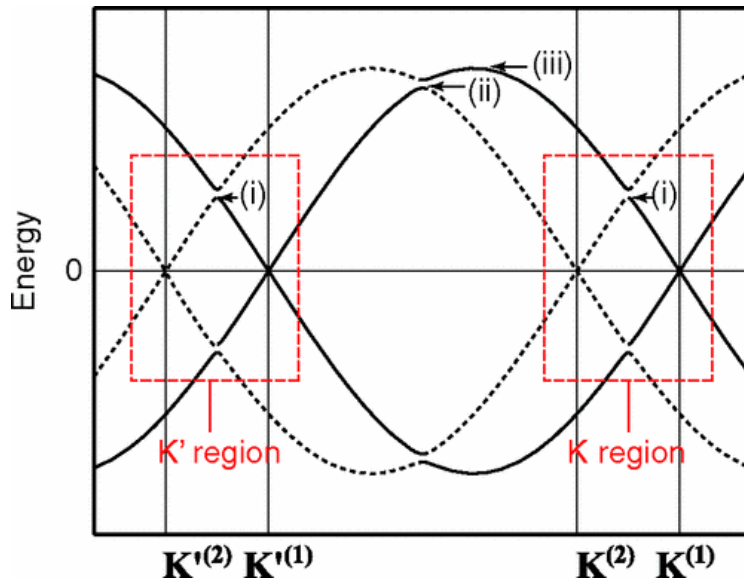


Figure 17 **Illustrative band structure of tBLG.** The band structure of the two individual layers (1) and (2) from Figure 15 (c) and (d) is shown around the line $K^{(2)} \rightarrow K^{(1)} \rightarrow K^{(2)} \rightarrow K^{(1)}$. (i), (ii), and (iii) highlight likely saddle points in the tBLG band structure. Reprinted with permission from reference¹²⁸. Copyright (2013) by the American Physical Society.

A full tight-binding calculation¹³²⁻¹³⁴ gives a better representation of the real band structure of the hybrid system. The calculated band structure of a tBLG system with a rotation angle of $\theta = 3.89^\circ$ is shown in figure 18. The lowest energy van Hove singularities in the density of states, at $E_{vHS} \approx \pm 150 \text{ meV}$, resulting from the new saddle points, are also highlighted.

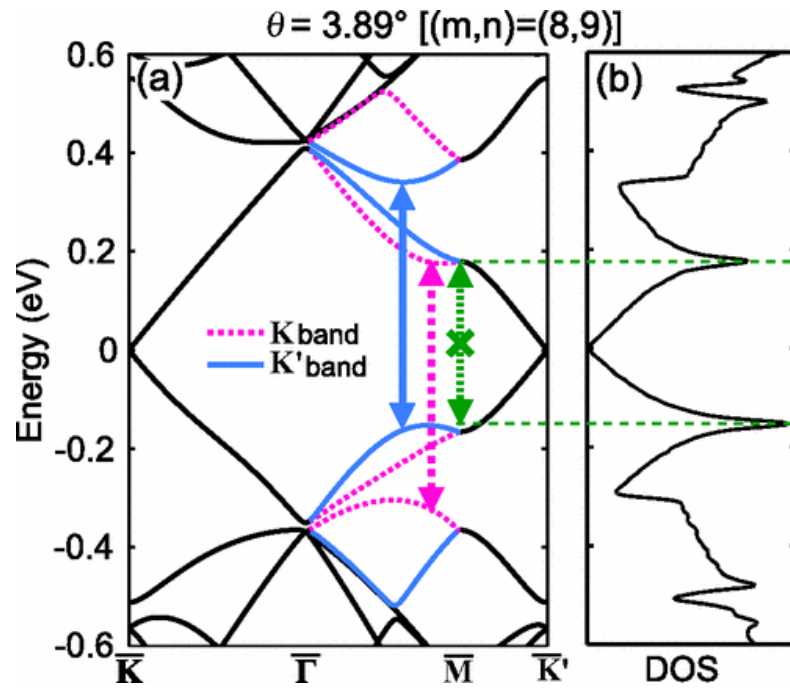


Figure 18 Calculated band structure and density of states of a tBLG structure with a twist angle of $\theta = 3.89^\circ$. (a) shows the band structure and (b) shows the density of states. The solid (blue) arrow and dashed (blue) arrow represent excitations corresponding to the major peaks in the optical spectrum. The dotted (green) arrow shows an optically forbidden process. The thick black (small) hexagon represents the folded Brillouin zone of the tBLG in both cases. Reprinted with permission from reference¹²⁸. Copyright (2013) by the American Physical Society.

The peaks in the density of states are readily observable using scanning tunnelling spectroscopy¹²⁹. An example is shown in figure 19. The observed asymmetry in the density of states is caused by the underlying Bernal stacked graphite. The panel in figure 19(c) shows how the signal changes when moving across the moiré pattern between the bright and dark regions along the line in panel (a). The vHS are clearly visible in the ‘bright’ region, but are not observable in the darker region, where the signal looks like that of graphite, despite the moiré pattern being visible. This is because the singularities form only in the presence of finite interlayer coupling. Often graphene flakes on graphite will become completely decoupled from the surface, exhibiting the properties of monolayer graphene. This highlights the importance of generating a clean and uniform interface between the two layers in a tBLG system when attempting to control its behaviour through ‘twist engineering’.

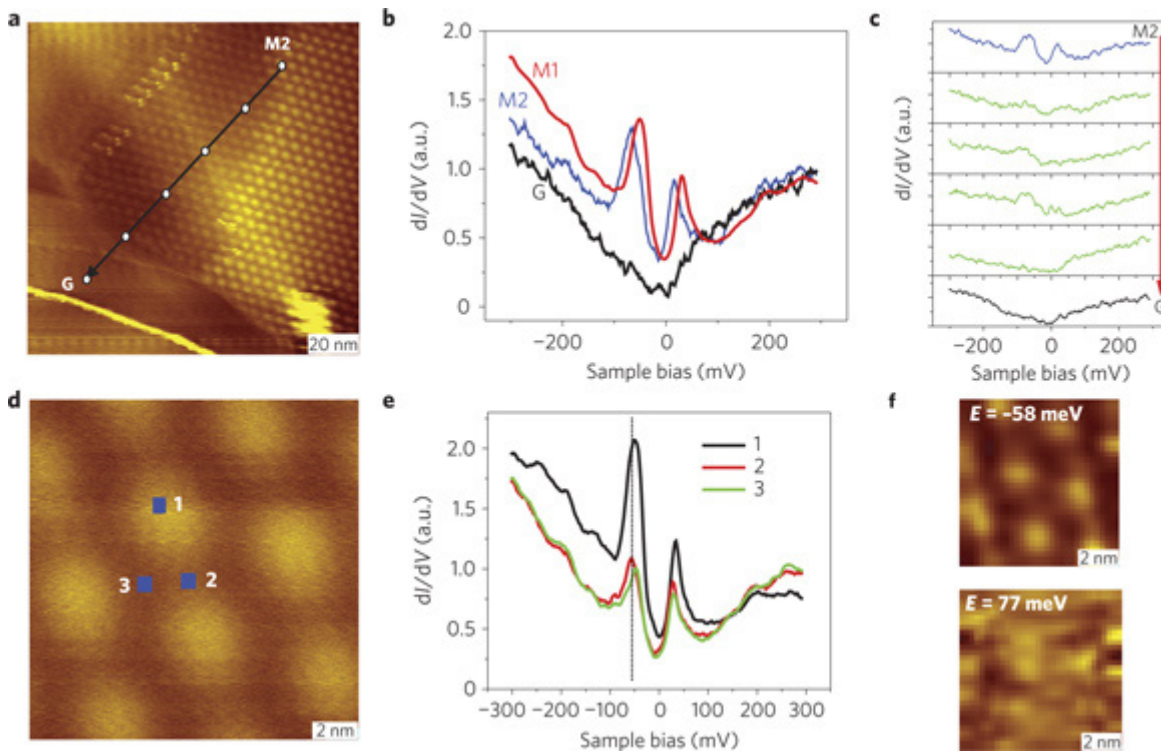


Figure 19 Scanning tunnelling spectroscopy of a twisted bilayer graphene on graphite sample with a rotation angle $\theta = 1.79^\circ$. (a) shows the STM topography of the moiré pattern caused by the rotation. (b) shows the tunnelling spectra in the centre of the moiré pattern (M1), at the edge of the twisted region (M2), and on a bare graphite region (G). Two sharp peaks corresponding to van Hove singularities appear flanking the Dirac point at energies $\Delta E_{\text{vHS}} = \pm 82 \text{ meV}$ in the twisted region. (c) shows the spatial dependence of the tunnelling spectra along the line shown in (a). (d) shows the topography of the moiré pattern at higher magnification, and (e) compares the tunnelling spectra at three positions in the moiré pattern shown in (d). (f) shows dI/dV maps of the region from (d), with the top taken at a Fermi energy close to the lower energy van Hove singularity, and the bottom map further from it. Reprinted by permission from Macmillan Publishers Ltd: *Nature Physics*³¹, copyright (2010).

A simple tight binding model can be used^{31,128,132} to calculate the relation between the twisting angle and the energy of 1st van Hove singularity to a good agreement with experiment. The calculated relation is shown in figure 20, along with calculated DOS for tBLG systems with various interlayer coupling terms. It also shows the dispersion relation for low energy states, showing the hybridised Dirac cones separated by the saddle point (marked 'sp') generating the singularities.

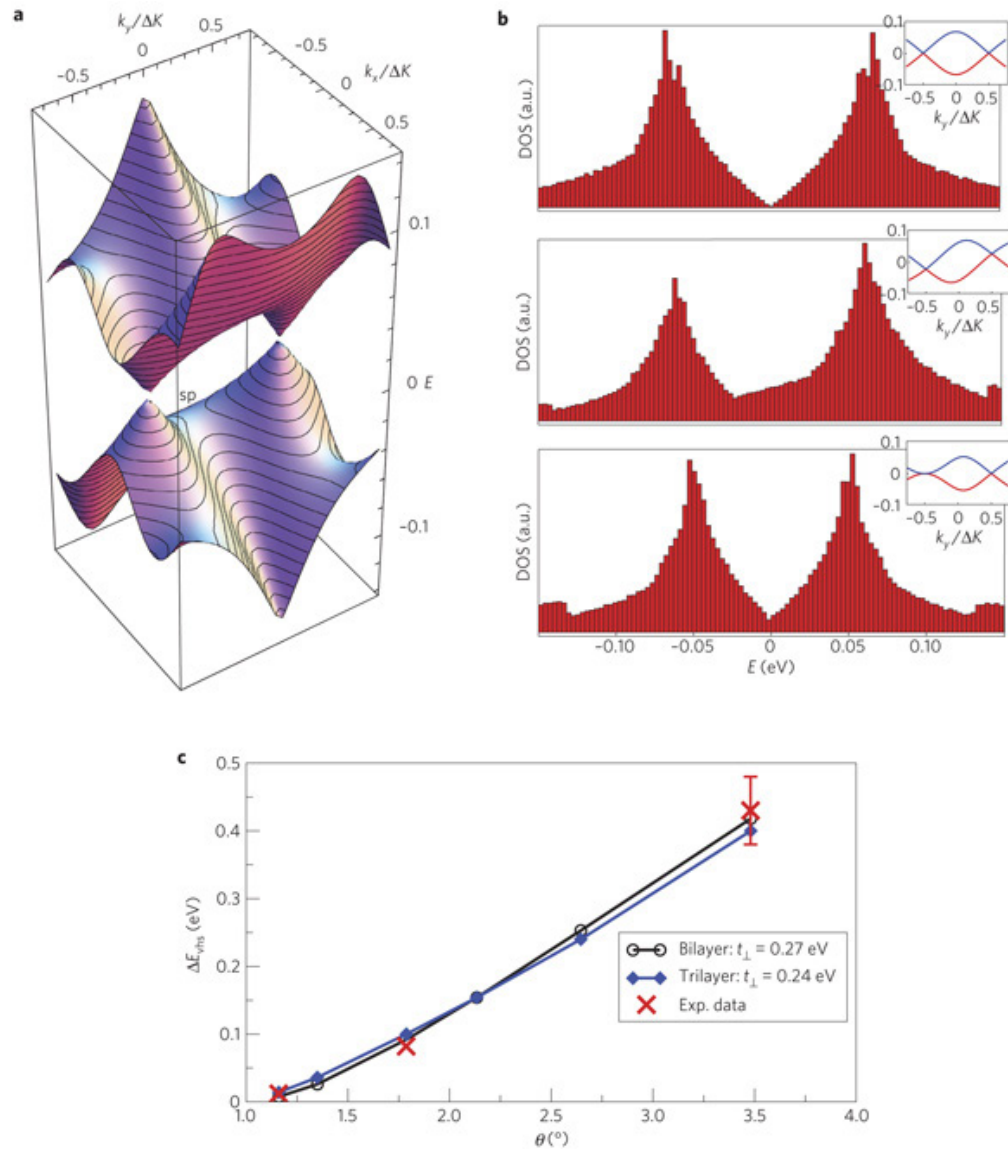


Figure 20 Energy dependence of van Hove singularities in twisted bilayer graphene. (a) shows the calculated dispersion relation for low energy states for a tBLG with a rotation angle of $\theta = 1.79^\circ$. One of the saddle-points which lead to the van Hove singularities is marked by a 'sp' in the negative energy band; there is an equivalent saddle point in the positive band. (b) shows the calculated density of states for three cases. Top: bilayer with a twist angle of $\theta = 1.79^\circ$, an interlayer coupling of $t_{\perp} = 0.24$ eV and no interlayer bias. Middle: same case as the top plot but with an interlayer bias of 0.15 V. Bottom: a trilayer sample, as that shown on top but with an AB stacked bottom bilayer graphene sheet. (c) shows the angular dependence of the energy gap between the van Hove singularities via experiment (crosses) and by calculation with a free parameter for the interlayer coupling. Reprinted by permission from Macmillan Publishers Ltd: *Nature Physics*³¹, copyright (2010).

Calculating the dispersion relation further from the hybridised Dirac cones requires excitonic corrections to the tight bonding model^{128,129,135}, the use of density functional theory^{136,137}, or continuum methods^{132,138}.

3.6.3 Optical properties of tBLG

The optical properties of tBLG¹³⁹ are closely related to the twist angle θ . There is a large peak in the optical joint density of states associated with the lowest energy van Hove singularities, labelled *(i)* in figure 17. The transitions between states in the singularities themselves are forbidden due to selection rules¹⁴⁰, but occur between the bands indicated in figure 18. As the transition energy is dependent on the energy of the singularities, the position of this optical peak E_A is dependent on the twist angle, and ranges through infrared, optical, and ultraviolet wavelengths. There are two other peaks in the optical spectra; E_B associated with the secondary twist singularities indicated by *(ii)* in figure 17, and E_M associated with the M-point singularity in monolayer graphene, indicated by *(iii)* in figure 17.

The experimentally measured real part of the optical conductivity spectra at various twist angles is shown in panel (a) in figure 21, but the twist dependent features are obscured by the large peak in the UV from the individual monolayers. In panels (c) and (d), the spectra from Bernal-stacked bilayer graphene has been subtracted from the tBLG spectra obtained experimentally, and through tight binding calculations respectively. The peak at E_A ranges throughout the optical spectrum in a manner that is completely controlled by the twist angle. This means that tBLG actually looks coloured under optical microscopy¹⁴¹.

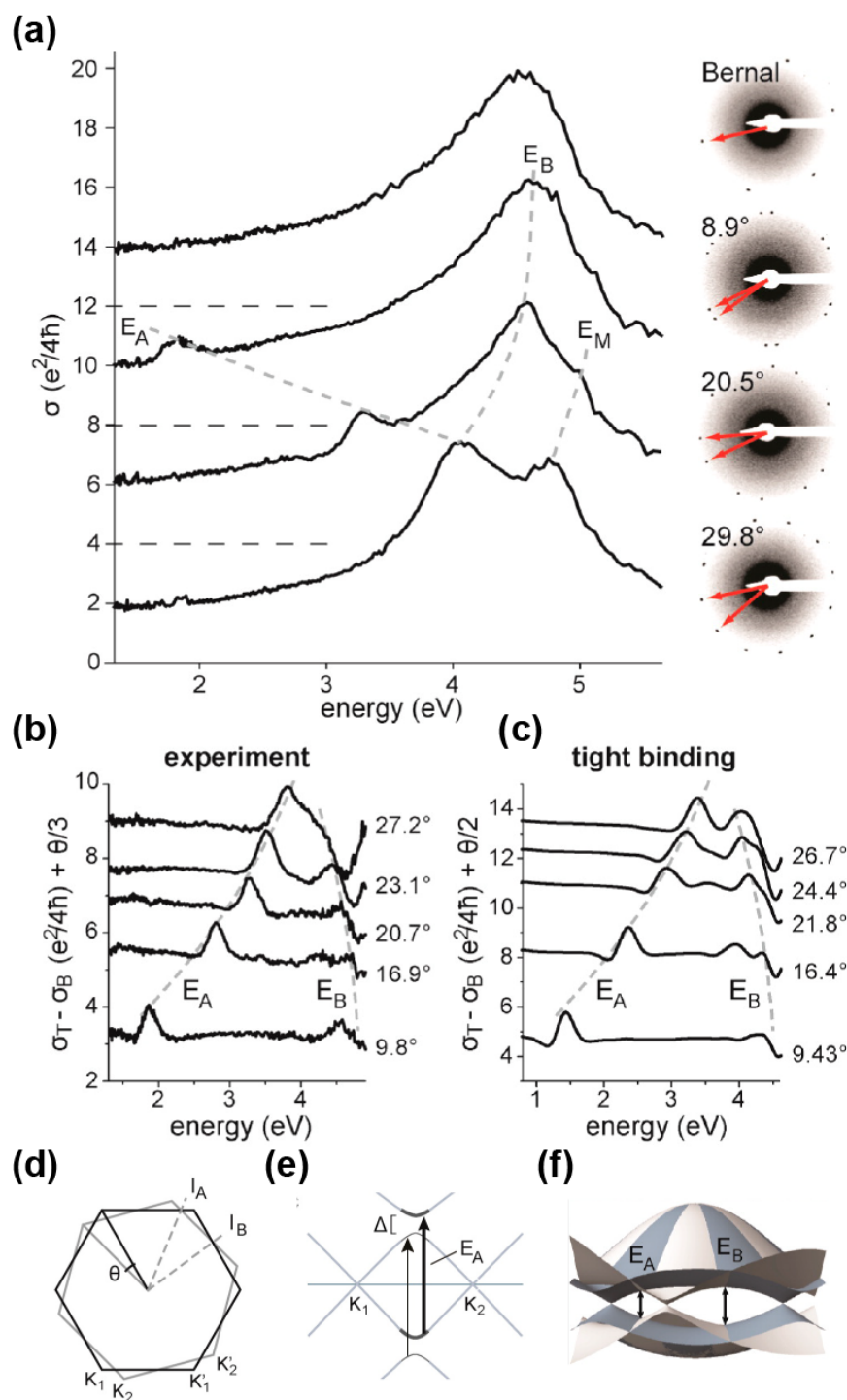


Figure 21 Full optical spectra of tBLG samples with differing interlayer rotations. (a) shows the experimental evolution of the real part of the optical conductivity with increasing twist angle from Bernal-stacked graphene. (b) shows a similar dataset, except here it shows the difference between the measured spectra σ_T and that of Bernal-stacked graphene σ_B which is plotted as the upper trace in (a). (c) shows equivalent spectra to that in (b) calculated using a tight binding method. (d), (e), and (f) show the Brillouin zone, local band structure, and a 3D representation of the band structure of a general tBLG. The energies E_A and E_B correspond to the 2 new van Hove singularities generated by the saddle points indicated in (f). If E_A corresponds to a rotation of θ , E_B corresponds to the equivalent rotation of $60^\circ - \theta$. E_M corresponds to the M-point vHS in single layer graphene, although it is perturbed in tBLG due to the 2 new twist induced vHS as well as excitonic effects. Adapted with permission from reference¹³⁵. Copyright (2014) American Chemical Society.

At higher energies, the spectra calculated using the tight binding model does not match the experimentally measured spectra. This deviation can be accounted for by including excitonic e-h interactions in the model^{40,135}.

Using the Dirac dispersion relation of monolayer graphene (and a small angle approximation), an estimate for the critical angle at which the energy between the conduction and valence Hove singularities is equal to the energy of the incoming laser, and Raman enhancement is maximised, can be expressed¹⁴² as

$$\theta_c = \frac{\Delta k}{K} = \frac{3aE_A}{\hbar v_F 4\pi} \quad (19)$$

where a and v_F are, respectively, the lattice parameter (2.46 Å) and Fermi velocity (10^6 m/s) of monolayer graphene, and θ_c is the critical angle expressed in radians. This corresponds to an angle $\theta_c = 10.0^\circ$ for an excitation corresponding to a 633 nm (1.96 eV) laser and an angle of $\theta_c = 11.8^\circ$ for excitation corresponding to a 532 nm (2.32 eV) laser.

3.6.4 Probing tBLG with resonance *Raman* spectroscopy

The presence of low energy van Hove singularities in the DOS of twisted bilayer graphene systems induces very strong enhancement of the G-band Raman intensity for specific incident laser wavelengths¹⁴³, which are dependent on the twist angle θ . Various measurements of the laser energy at which G-band enhancement was maximised in tBLG systems with known twist angles have been performed^{135,142-145}. They are summarised in a plot of maximum enhancement energy against twist angle in figure 22.

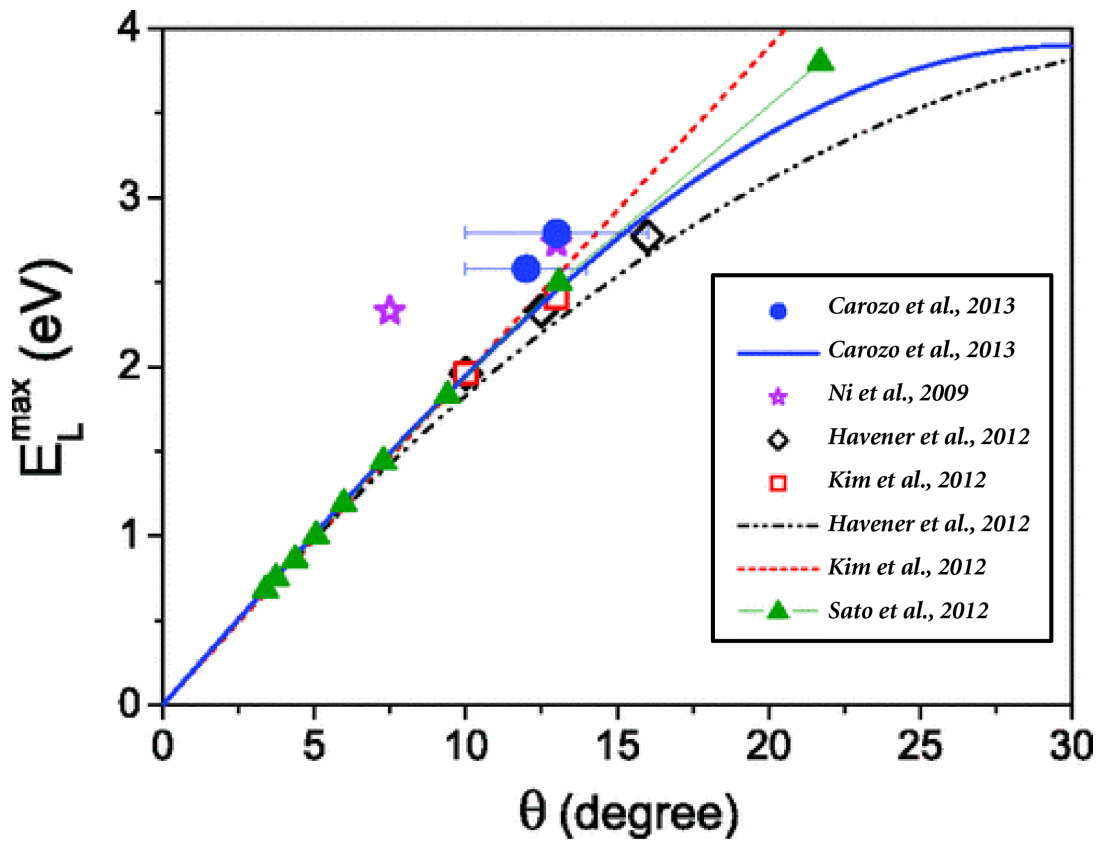


Figure 22 Summary of literature values for energy of the optical excitation linked to the presence of extra van Hove singularities in twisted bilayer graphene as a function of the twisting angle. E_L^{\max} is the laser excitation energy at which the Raman G-band enhancement is maximised. This energy is the energy of the optical excitation caused by the extra van Hove singularities present in tBLG ($E_L^{\max} = E_{vHs}$). The red and blue fits correspond to equations (19) and (20). Reprinted figure with permission from reference¹⁴⁴. Copyright (2013) by the American Physical Society. Data points are from (Carozo et al., 2013)¹⁴⁴, (Ni et al., 2009)¹⁴³, (Havener et al., 2012)¹³⁵, (Kim et al., 2012)¹⁴² and (Sato et al., 2012)¹⁴⁵.

A fit of the angle dependence to a sinusoidal function with the correct periodicity (to account for the threefold rotational symmetry of the hexagonal lattice¹⁴⁶) yields¹⁴⁴

$$E_{Max} \equiv E_0 |\sin(3\theta)| = 3.9 |\sin(3\theta)| \text{ eV} \quad (20)$$

where E_{Max} is the position of the optical absorption maxima, θ is the tBLG twist angle, and $E_0 = 3.9 \text{ eV}$ is the fitting parameter. This is shown as the blue curve in figure 22. A variety of other twist generated features in the Raman spectra are observed^{146,147}, including an array of new peaks caused by the superlattice modulation that enables activation of phonons in the interior of the Brillouin zone^{52,141,148}, including inter layer breathing modes¹⁴⁴.

3.7 Graphene on waveguides

This section introduces the use of silicon waveguides for photonic applications. It then discusses one photonic system in particular, that of looped waveguides acting as optical cavity resonators, and describes the transmission spectra of a straight waveguide coupled to such a *racetrack resonator*. Their application as sensing systems is also discussed.

Finally, it reviews the integration of graphene with silicon waveguides and optical fibres to act as an optical modulator. Literature measurements of the in-plane linear absorption coefficient are discussed and tabulated.

3.7.1 Silicon photonics

Silicon photonics is a focus of research because of its potential in ultra-wide bandwidth communications systems and next generation interconnects for complementary metal oxide semiconductor (CMOS) chips^{149,150} with reduced power consumption. Silicon waveguides are preferred due to their high refractive index contrast and the wide availability of CMOS fabrication technology, as well as the ease of potential integration with other CMOS devices¹⁵¹. Silicon optical modulators include *Mach-Zehnder interferometers*¹⁵², ring resonators¹⁵³, and electroabsorption¹⁵⁴ devices based on modulation via interference, resonance and bandgap absorption respectively.

The *modes of propagation* in a waveguide¹⁵⁵ can be categorised using their polarizations: TE modes refers to those where the electric field vector is transverse to the direction of propagation, in TM modes the magnetic field vector is transverse, and in TEM modes both the field vectors are transverse to the direction of propagation. The modes which a waveguide can support are restricted by its geometry; at least two separate conductors are needed to support propagation of TEM modes. Silicon waveguides are generally too small to support propagation of higher order TE/TM modes and can only support the *dominant mode*. Typically the aspect ratio of the waveguide defines whether TE mode or TM mode propagation is preferred.

3.7.2 Ring/ racetrack cavity resonators

Ring and racetrack cavity resonators consist of looped optical waveguides with some kind of coupling to the outside world, typically another waveguide. When the optical path length of the cavity is equal to an integer number of the wavelength of light travelling around it, the cavity is in resonance. Although ‘ring resonator’ is a general term, often it is used to refer to circular waveguides, whereas ‘racetrack’ is used to describe those with extended straight sections. In the simplest case, they are positioned next to a straight single waveguide in an *all pass* configuration, although they are often coupled to two waveguides in an *add drop* configuration. Silicon microring resonators have been widely discussed in the literature record^{156,157}, particularly in relation to their use as spectral filters in nanophotonic circuits¹⁵⁸, as delay lines¹⁵⁹, and for sensing applications (particularly label free biosensing¹⁶⁰).

All pass racetrack cavity resonators are described by their radius of curvature r and coupling length L_C . The total length of the racetrack cavity L is then given by $L = 2L_C + 2\pi r$. Evanescent coupling between the waveguide and the loop occurs when the length of the racetrack is equal to an integer multiple of the excitation wavelength, *i.e.* when the laser wavelength matches the condition

$$L = n\lambda_{Laser} \quad \text{where } n = 1, 2, 3 \dots \quad (21)$$

A schematic of a basic racetrack resonator coupled using both *all pass* and *add drop* configurations is shown in figure 23.

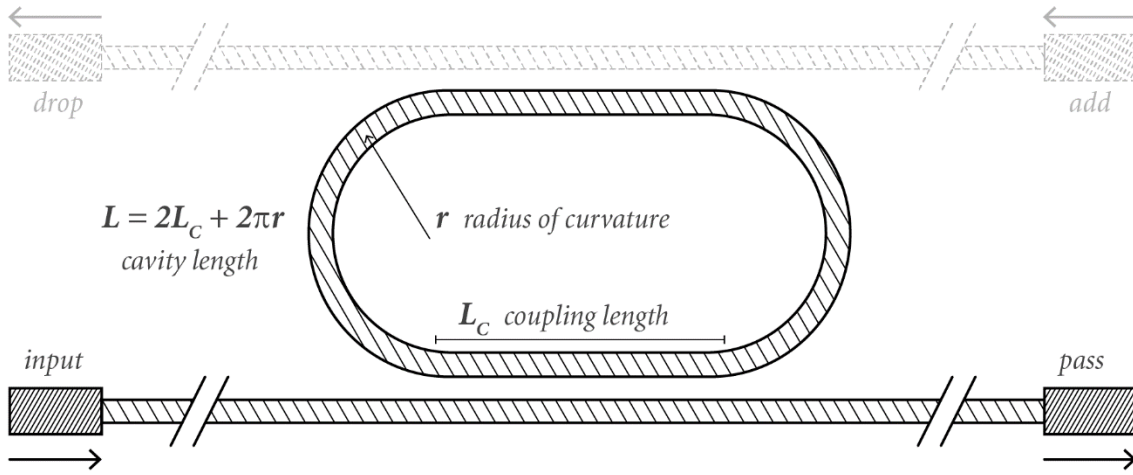


Figure 23 Schematic showing 2 basic racetrack cavity resonator setups. The solid (black) lines show the waveguide coupled in an 'all pass' configuration. The solid (black) and dashed (grey) lines together show a racetrack resonator in an 'add drop' configuration. The coupling length L_C and radius of curvature r are highlighted.

The transmission spectrum of such a configuration is well described¹⁶¹⁻¹⁶³ by the expression

$$T = (1 - \gamma) \left[\frac{(\sqrt{1 - \kappa}) - (\sqrt{1 - \gamma}) \exp\left(-\frac{\alpha n_{eff}}{2} L - i\Phi\right)}{1 - (\sqrt{1 - \kappa})(\sqrt{1 - \gamma}) \exp\left(-\frac{\alpha n_{eff}}{2} L - i\Phi\right)} \right]^2 \quad (22)$$

where, i is the imaginary unit defined by $i^2 = -1$, and Φ is a phase factor is given by

$$\Phi = 2\pi n_{eff}^2 \frac{L}{\lambda}. \quad (23)$$

Here λ is the wavelength of the incident light, and L is the total round trip length of the ring/racetrack cavity resonator. α is the ring's loss coefficient, including contributions from both scattering and absorption, and n_{eff} is the effective refractive index at the waveguide interface. γ and κ are coupling coefficients related to the intensity loss of the coupler and the power coupling factor between the cavity and the bus waveguide respectively.

The spectra consists of a series of a series of narrow negative peaks in the transmission spectra corresponding to the resonances. A measured transmission spectra of a typical silicon microring resonator along with a fit to the above relation is shown in figure 24.

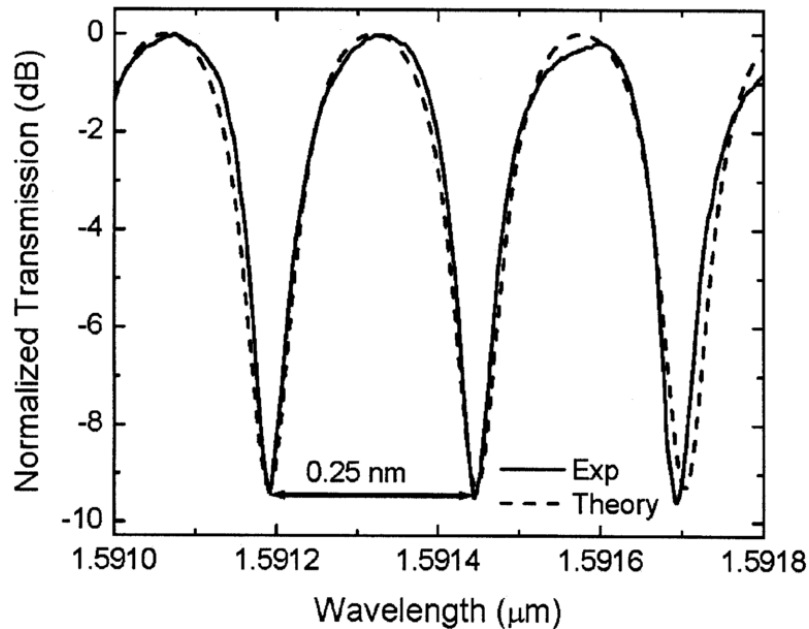


Figure 24 Spectral response of a silicon microring photonic resonator. The solid line shows part of an experimentally measured spectra for a typical device, whilst the dashed line is a fit to equations (22) and (23) with the fit parameters $\gamma = 0.3$, $\kappa = 0.4$, $n_{eff} = 3.194$ and $L = 3020 \mu\text{m}$. Reprinted from reference¹⁶¹. © 2014 IEEE.

The waveguide surface produces a tightly confined and intense evanescent field which can interact with molecules near the surface. The extremely narrow resonances have a spectral position which is highly sensitive to changes in the local (surface and local few nm) refractive index, meaning that ring resonator systems can be used for extremely sensitive label free biosensing if the surface can be appropriately functionalized. Immobilisation and detection of ssDNA by peptide nucleic acid functionalisation¹⁶⁴, streptavidin by biotin functionalization¹⁶⁵, and glucose detection via glucose oxidase functionalization¹⁶⁶ have been reported. However, silicon has limited reactivity, so many functionalization routines such as ‘click chemistry’¹⁶⁷ are not possible directly on it. Due to the evanescent decay of the sensing field away from the surface, techniques to improve the reactivity of silicon surfaces leaving ‘thick’ (more than a few tens of nm) coatings such as poly-p-xylylenes¹⁶⁸ are limited in their usefulness in bio sensing setups. Racetrack resonators are also particularly sensitive to

changes in the cavity length/strain, and have been implemented in optical NEMS devices¹⁶⁹ as pressure sensors.

3.7.3 Graphene integrated on optical waveguides

Many optical properties observed in graphene, such as its wideband absorption^{36,37} across the visible and infra-red part of the spectrum, gate controlled optical transitions⁴⁵, high electron/hole mobility¹⁷⁰ and saturable absorption¹⁷¹ are particularly desirable in photonic systems¹⁷², and not observed in any CMOS process compatible materials. This motivates its integration with silicon photonics¹⁷³ as a means to develop high speed and low power photonic systems such as photodetectors¹⁷⁴ and optical modulators¹⁷⁵.

Graphene's inherent thinness means its planar integration with optical waveguides via evanescent coupling is often needed in order to increase the light matter interaction length. In the more typical normal incidence configuration, this is limited to a few nm at most. On a waveguide, the graphene-light interaction length is limited only by the length of the waveguide. Optical and scanning electron microscope (SEM) images of a silicon Mach Zehnder interferometer with both arms partially coated with graphene are shown in figure 25.

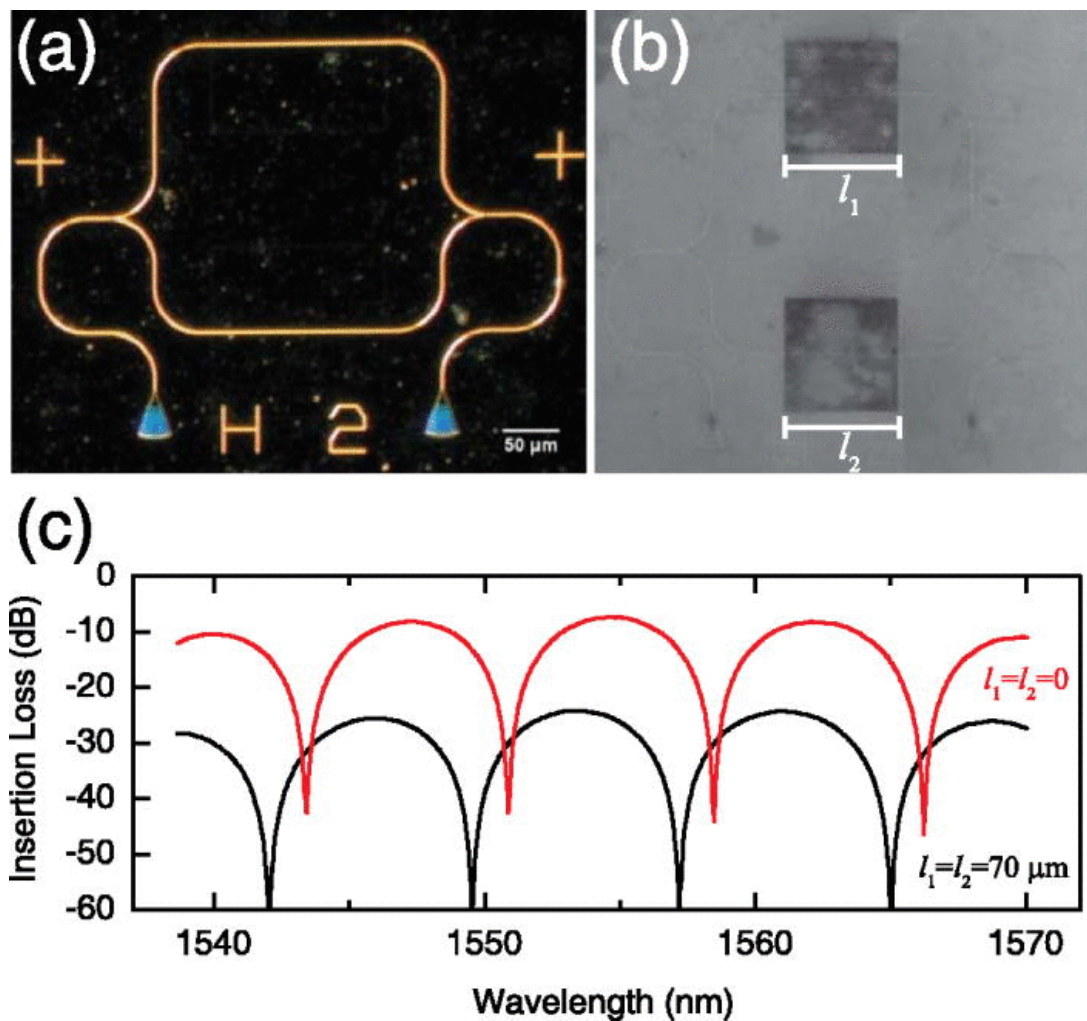


Figure 25 Graphene integrated silicon waveguide in a Mach-Zehnder interferometer setup. (a) shows an optical image of the whole waveguide taken using dark-field microscopy. (b) shows an SEM image of the device after the transfer and subsequent patterning of the graphene layer. The MZI is barely visible as a fainter line in the same location as in image (a). The graphene squares are visible as dark areas as the graphene is more efficient at discharging electrons than the surrounding SiO_2 . (c) shows sections of the transmission spectra for (red) unmodified MZI interferometers and for (black) an interferometer where both lines are covered with lengths of graphene equal to $l_1 = l_2 = 70 \mu\text{m}$. Reprinted from reference¹⁷⁶, with the permission of AIP Publishing.

Multiple studies are reported, including proof of concept demonstrations of devices such as fibre based polarizers using graphene's ability to support TE mode surface waves¹⁷⁷, mode locked fibre lasers based on saturable absorption¹⁷⁸, and a broadband electro absorption modulator¹⁷⁵ based on graphene's gate-variable optical transitions (as illustrated in figure 6). Graphene has also been integrated on waveguides as a means of probing its optical absorption properties. A *linear absorption coefficient* is a measure of how much light is absorbed by a finite length of a material, typically in $\text{dB}/\mu\text{m}$. Typically this is measured using a *cutback method*, where absorption of several devices is plotted as a function of graphene length, and the gradient is taken as the absorption coefficient. Measurements of graphene's

linear absorption coefficient reported in the literature, along with the number of devices included in the cutback method fit, are tabulated in table 2.

Table 2 Literature values for the linear absorption coefficient of graphene obtained via its integration on silicon waveguides. The result from a paper forming part of this work (Crowe et al., 2014) is included for comparison.

<i>Liu et al., 2011¹⁷⁵</i>	<i>TE Mode: 0.1 dB/μm</i>	<i>1 device</i>
<i>Li et al., 2012¹⁷⁶</i>	<i>TE Mode: \sim0.2 dB/μm</i>	<i>16 devices</i>
<i>Kou et al., 2013¹⁷⁹</i>	<i>TE Mode: 0.09 dB/μm, TM Mode: 0.09 dB/μm</i>	<i>40 devices</i>
<i>Crowe et al., 2014¹⁸⁰</i>	<i>TE Mode: 0.11 dB/μm</i>	<i>4 devices^{**}</i>

***In this study the absorption coefficient was obtained independently using a cutback method and via the fit of the transmission spectra to equations (22) and (23), and found to agree within experimental error.*

3.8 Transmission electron microscopy

Transmission electron microscopy^{181,182} (TEM) is a high resolution imaging technique where a beam of electrons is transmitted through a thin specimen, and the interactions of the electron beam with the sample are used to form an image. The two variants of TEM differ in the way in which they address the sample. Conventional TEM (CTEM) uses a wide beam to interact with the sample, and an image is formed on a pixel array using an objective lens after the sample. In scanning TEM (STEM), a tightly focussed beam is rastered across the sample, with the transmission value according to each pixel being measured sequentially. Often to increase contrast, high angle annular dark field (HAADF) imaging is used, where only high angle scattered electrons are collected by an annular detector around the main transmitted beam. CTEM resolution is limited by the aberrations in the objective lens, and STEM resolution is limited by the beam diameter. Both require carefully prepared thin samples.

The beam electrons can interact with the sample, which can be used to perform chemical analysis^{183,184}. Electron energy loss spectroscopy (EELS) is an *absorption* technique where the energy lost by transmitted electrons is measured directly. Energy dispersive x-ray spectroscopy (EDX) is a complementary *emission* technique where the energies of x-rays produced due to the electrons interaction with the sample are recorded. Used in STEM mode, they can provide spatial mapping of the chemical composition of the sample. They are outlined and discussed in the following sections.

3.8.1 Energy Dispersive X-ray Spectroscopy (EDXS)

EDX is an emission spectroscopy technique, where the energies of emitted X-rays produced by the interaction of the electron beam and the sample. If the beam excites an electron within the test material to a higher energy state, when the electron configuration returns to its ground state, the difference in energy between the two states can be emitted as a photon. This process is dominant for heavier atoms, but for lighter ones there is a competing process known as *Auger electron emission*, where the excess energy is transferred to a higher shell electron which is ejected. A representative EDX spectra showing a series of X-ray peaks from a Ni nanowire sample is shown in figure 26.

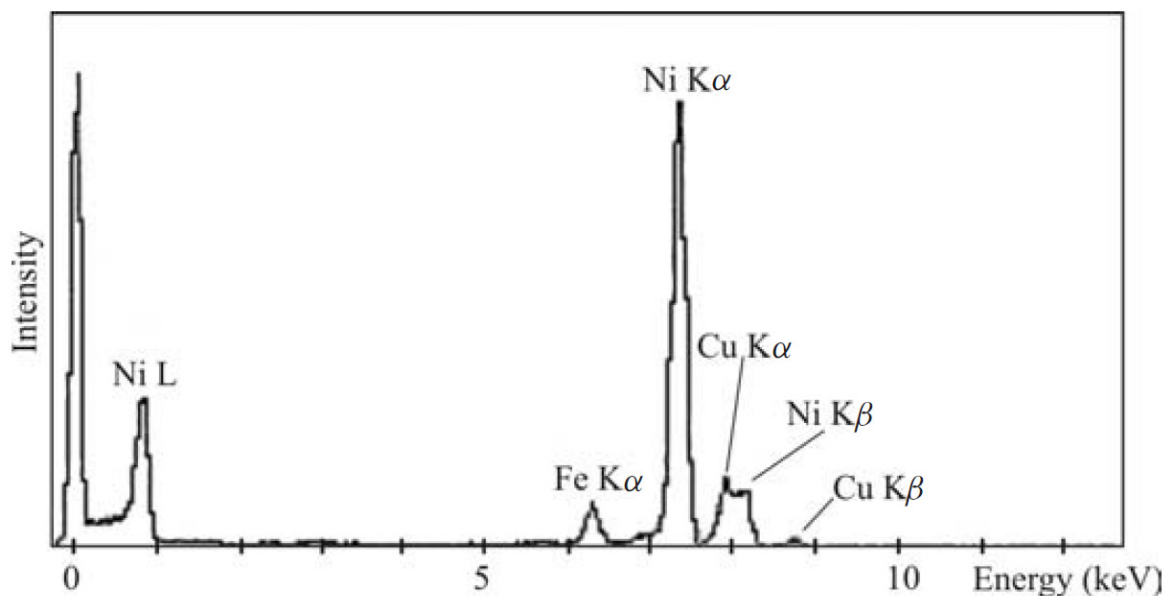


Figure 26 Representative energy dispersive x-ray spectrum of nickel nanowires. The iron peak is due to contamination, and the copper signal is from the TEM holder and support grid. Reprinted with permission from reference¹⁸⁴. Copyright (2011) Wiley Materials.

Standard notation for X-ray spectroscopy labels transitions to $n=1$ states, where n is the *principle quantum number*, as K shell transitions, and transitions to $n=2$ states L shell transitions. These are further subdivided, with $K\alpha$ and $K\beta$ x-rays associated with transitions from $n=2$ and $n=3$ states respectively. Typically $K\alpha$ edges are the dominant feature in each elemental spectrum, although there are exceptions for heavy atoms.

3.8.2 Electron Energy Loss Spectroscopy (EELS)

EELS is an absorption spectroscopy technique, where the part of the transmitted beam which is scattered inelastically by the sample is used to interpret the composition of the sample. An energy loss spectra gives the energy lost by each electron from the initial beam energy. A representative energy loss spectra, showing the main features typically seen is shown in figure 27.

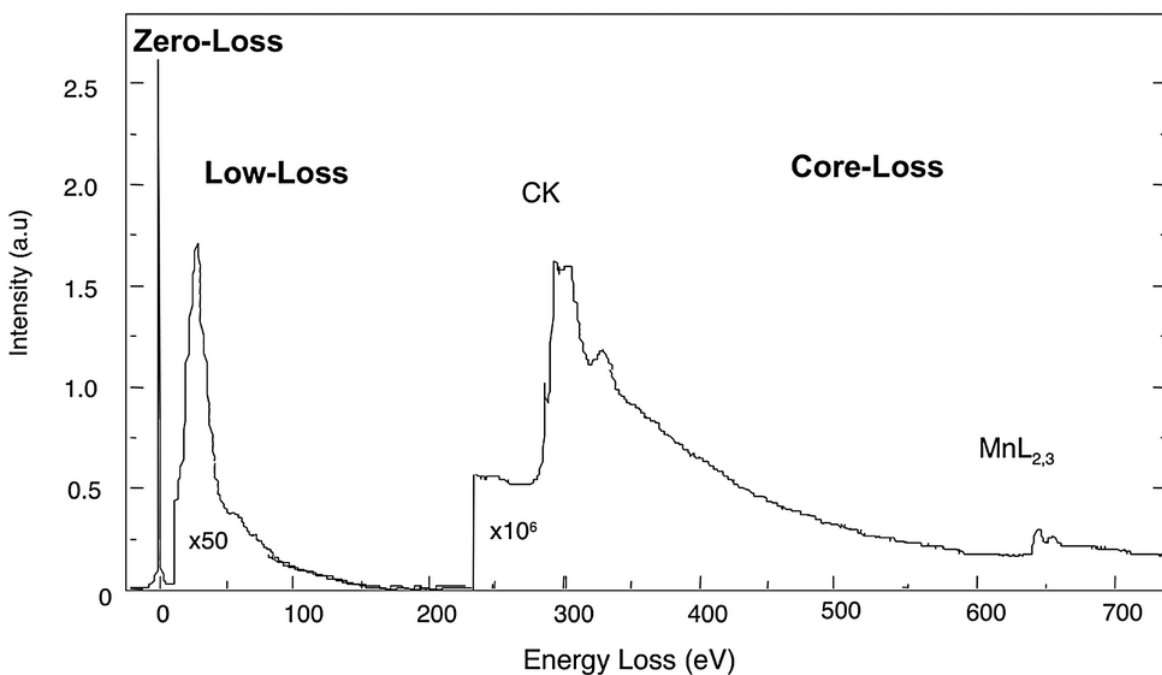


Figure 27 **Representative electron energy loss spectra of manganese containing carbon nanotubes.** Core-loss peaks corresponding to the carbon K-edge and the manganese $L_{2,3}$ edge are marked. The low loss region and core-loss region are shown multiplied by factors of 50 and 10^6 respectively to show the full dynamic range on the same scale. Reproduced from reference¹⁸⁵ with permission of The Royal Society of Chemistry.

The zero loss peak (or ZLP) is the sum of all the electrons scattered elastically, or inelastically with a very small ΔE . Unless the sample is extremely thick it is usually many orders of magnitude stronger than any other feature in the spectrum. The *low loss* spectra covers the area from the edge of the ZLP to an energy around 50-100 eV. Features in this region arise from collective electron excitations in the outer atomic orbitals, such as plasmon oscillations and interband transitions. The *high loss* (also called *core loss*) region covers energies higher than 50-100 eV, and is dominated by ionisation edges corresponding to the excitation of inner shell electrons to above the Fermi level. Peaks are labelled according to spectroscopic notation, with ground state transitions corresponding to K edges, and so on. For a thin sample (where multiple scattering is insignificant), the relative edge strengths can be normalised by a calculated elemental cross section for the experimental conditions to give a measure of the relative ratio of atomic species present in the sample¹⁸⁶. By comparison with an experimentally measured spectra where the sample is not present, an absolute areal density for each elemental species can be obtained¹⁸⁷.

4 Experimental techniques review

This section presents a literature review of experimental techniques related to those used and developed for the work presented as part of this thesis. Firstly, techniques used for the exfoliation, characterisation, and transfer of graphene and hexagonal boron flakes, and the transfer of graphene grown via chemical vapour deposition (CVD) are described. Then, microfabrication techniques used to pattern silicon materials at the microscale are introduced. Following this, atomic force microscope (AFM) based techniques used to measure and map surface material properties are reviewed, with a focus on the acquisition of force-displacement curves and how they can be interpreted. Subsequently, techniques for patterning graphene at sub 10 *nm* length scales using both optimised resist exposure and direct write techniques are reviewed.

4.1 Graphene/h-BN flake preparation, characterisation and transfer

Although other scalable production methods exist, micromechanical exfoliation is still the ‘gold-standard’ production method for high quality flakes of graphene and other two dimensional materials. CVD graphene growth (which is outlined in section 3.5.2) is not discussed here as it does not relate to the work included in this thesis, but transfers of CVD graphene from the growth substrate are.

4.1.1 Mechanical exfoliation onto silicon oxide

Micromechanical exfoliation aims to separate individual 2D layers from bulk layered materials held together by van der Waals interactions by the use of successively peeling away layers using adhesive tape. Using adhesive tape to thin and clean samples has long been a familiar technique¹⁸⁸ in crystallography. Mechanically rubbing highly oriented pyrolytic graphite (HOPG) samples on silicon surfaces using an AFM tip was investigated in 1999 with the explicit aim of producing single layer graphene¹⁸⁹, but only relatively thick flakes were observed. The first identification of an exfoliated monolayer¹ occurred in 2004.

4.1.1.1 Mechanical exfoliation of graphene

In the usual technique, adhesive tape is used to lift a graphite film from the surface of an HOPG or natural graphite sample. The tape is used to repeatedly cleave the film apart, thinning and spreading it. Then, it is pressed down onto a target substrate, which is typically a thin silicon dioxide film on a silicon wafer, in order to make identifying thin flakes¹⁹⁰ simpler. The tape is then removed, either mechanically or by being dissolved or detached in a suitable solvent. This leaves a distribution of graphene and graphite flakes of varying thickness on the substrate. Often a second ‘final peel’ is used, where a fresh piece of tape is used to remove graphitic material from the substrate. This will destroy any pre-existing graphene layers, but typically exposes new graphene areas as thicker material is removed. Flake sizes are typically below $\sim 100 \mu\text{m}$, but *mm* scale monolayer flakes¹⁶ are occasionally observed. Although this makes it almost useless for large scale applications, produced flakes are large enough such that the vast majority of basic studies and prototype devices based on graphene are performed using mechanically exfoliated samples¹⁹¹ due to their high quality.

4.1.1.2 Mechanical exfoliation of hexagonal boron nitride

Hexagonal Boron Nitride flakes can be exfoliated in the same manner as graphene, although it is typically more challenging to produce large thin flakes. Originally, highly oriented pyrolytic boron nitride¹⁹² was exfoliated, which tended to produce thick flakes with strongly terraced edges and no monolayers¹⁹³. However the move towards the growth of single crystal hexagonal boron nitride (hBN) flakes¹⁹⁴ allowed the exfoliation of flat thin flakes down to monolayers. Because of its large band gap²¹ thin BN exhibits almost no opacity, and is only observable because of the thin substrate interference effect. A maximum contrast¹⁹⁵ of $\sim 2.5\%$ per layer is seen when using an oxide thickness of $80\text{nm} \pm 10\text{nm}$. It can be transferred using exactly the same techniques as are used for graphene, as discussed in the previous section.

4.1.2 Characterising flakes

Identifying the thickness of a graphene layer is more challenging than it might seem. Often, a combination of techniques is required to unambiguously tag a flake as monolayer or bilayer. Characterisation of flake thicknesses using the three most commonly used techniques is discussed here. These techniques are optical microscopy, atomic force

microscopy (AFM) and Raman spectroscopy. The discussion is limited to techniques which can be used to characterise flakes prior to their incorporation into devices. SEM is not discussed here, as it is not only extremely challenging to identify flake thickness, it also causes beam induced contamination which makes it unsuitable for characterisation prior to other measurements. TEM is not discussed due to the onerous sample fabrication requirements. It is not practical to transfer a flake to a TEM compatible substrate, before imaging and transferring it to a 3rd location.

4.1.2.1 Optical microscopy

The visibility of graphene on thin films is governed by an interference effect¹⁹⁰. Typically flakes are mechanically exfoliated onto thin thermal oxide films on silicon wafers. Under white light illumination, the contrast is maximised at an oxide thickness of around 90nm, with a second maxima at around 300nm. Graphene flakes with thicknesses below a few nm are invisible under white light illumination, but detectable using a blue narrow-pass filter. Indeed, the use of narrow pass filters can make monolayer graphene visible on almost any thin film, including silicon nitride and polymer films.

Unambiguous determination of the number of layers in a flake using optical microscopy is very difficult, but experienced researchers can establish the number of layers in thin flakes with very high accuracy on silicon dioxide films (often using the typical morphology of natural graphite crystals as a guide). This is much harder on other substrates, particularly spun polymer films due to the variable thickness due to flow around thick flakes and relatively rough surface.

4.1.2.2 Scanning Probe Microscopy

Atomic force microscopy should be perfectly capable of identifying flake thicknesses unambiguously, but in fact this is not always possible. Although steps in graphite flakes typically show the spacing of interlayer graphite ($h = 0.335 \text{ nm}$), the height of known monolayer flakes exfoliated onto silicon oxide varies between 0.35 – 1 nm. This may be partly attributable to measurement error due to incorrect setting of the tip free amplitude¹⁹⁶, but also reflects a variable height due to the underlying oxide roughness and wetting effects.

In practice, distinguishing between 1 and 2 layer graphene from a step height on silicon oxide is impossible, although if wrinkles or torn regions are present they can be used to specify the layer number. On atomically flat substrates such as thick hBN, graphite, or mica, the interlayer graphite spacing step height is restored, and unambiguous specification of layer number from thickness is possible.

4.1.2.4 Raman Spectroscopy

Characterising graphene flakes using Raman spectroscopy is fast, non-destructive, offers μm scale resolution, and can be used to determine both structural⁵⁷ and electronic information^{52,197}. It can unambiguously determine the number of layers⁵⁶ in a thin graphene flake on almost any substrate⁶⁰. It can also provide information on adsorbed contaminants, defects, and functional groups introduced into the graphene lattice during processing¹⁹¹. However the generated spectra do not yield much information by visual inspection, requiring sophisticated fitting and data analysis to extract the desired properties. Monolayer graphene flakes can be distinguished from bilayer flakes, and ‘few layer’ flakes^{54,56,60,198} by comparing the G peak position, the 2D/G’ peak shape and symmetry (single Lorentzian for monolayer, combination of Lorentzians for bilayer and above), and the 2D:G integrated peak area ratio. However it is hard to distinguish the thickness of thicker flakes.

4.1.3 Graphene transfer techniques

The transfer of 2D materials onto arbitrary substrates is essential for their characterisation and use in almost any possible application. This section outlines common transfer processes for CVD grown graphene and mechanically exfoliated flakes. It then discusses aligned transfers, where the crystalline lattice rotation match between layers of 2D materials is controlled. Finally, it discusses commonly used cleaning techniques to remove polymer residue from surfaces after transfer and processing.

4.1.3.1 CVD graphene transfer

The most widely used laboratory scale process for transferring CVD grown graphene to arbitrary substrates is polymer supported metal etching and transfer. 3 related methods are shown in figure 28. In all 3 cases the graphene is supported by a polymer layer while the metallic growth substrate is etched away in a wet chemical process. The polymer film is then used to transfer the graphene layer to a target substrate, where the polymer layer is removed.

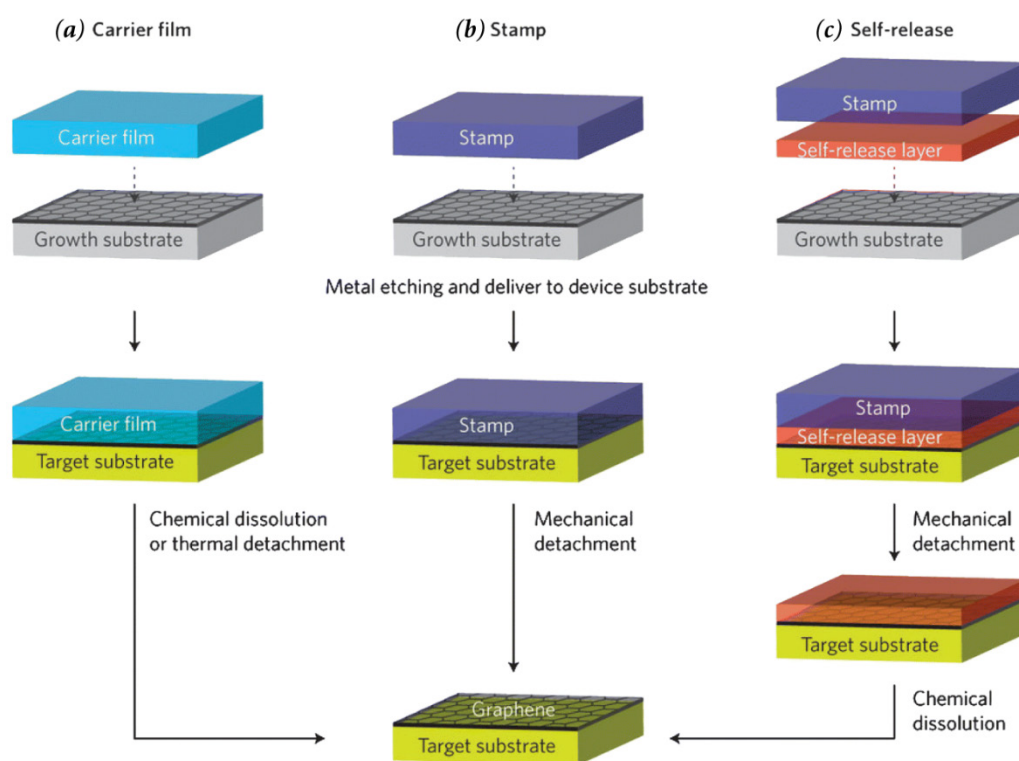


Figure 28 Diagram illustrating 3 graphene transfer methodologies. The growth substrate can be silicon dioxide onto which flakes have been mechanically exfoliated, which can be alkaline etched away. The techniques also apply to other 2D materials such as hexagonal boron nitride. Adapted from reference¹⁹⁹. Copyright (2014) Royal Society of Chemistry.

Panel (a) from figure 28 shows the carrier film technique¹³⁰, where a transfer polymer is deposited, typically *poly (methyl methacrylate)* (PMMA). After the metal is removed and the graphene transferred, the carrier film is dissolved using organic solvents. It has been suggested that this transfers the ripples and folds in graphene from the growth substrate to the target, which causes rips and tears²⁰⁰ when the PMMA is removed. It was found that, after the transfer, depositing a second layer of PMMA before removing it partially dissolves and relaxes the original film, reducing this effect²⁰¹. Panel (b) shows a stamp technique, where a thick polymer stamp (typically PDMS) is affixed to the graphene prior to etching away the substrate²⁰². It is then transferred to the required substrate by stamping and peeling away the polymer stamp. Panel (c) shows the use of a self-release layer in between a PDMS stamp to prevent the graphene from being contaminated by coming into contact with the PDMS. This layer can consist of materials including *polystyrene*, *poly (isobutylene)*, *poly (butadiene)*, *Teflon AF* or *poly (L-lactic acid)*²⁰³⁻²⁰⁵, and is dissolved after the graphene has been transferred. Metal etchants used include *hydrochloric acid (HCl)*¹³⁰ to dissolve Ni substrates, and *ferric chloride (FeCl₃)* and, more recently *ammonium persulfate (APS)* [(NH₄)₂S₂O₈] to dissolve Cu. APS is preferred as it avoids the Fe contamination observed when etching using ferric chloride^{206,207}, and avoids mechanical weakening of the graphene at the grain boundaries⁷⁸.

Other techniques have been developed aiming to make the process more industrially viable^{117,191}. A roll to roll transfer using thermal release tape to support the graphene while the growth substrate was etched away by APS, before the graphene was 'rolled' onto a flexible PET substrate and the tape peeled away after heating has been reported¹¹⁸. This enabled the transfer of essentially continuous films of graphene. A similar method for rigid substrates affixed thermal release tape supported graphene to the substrate by pressing them between two heated plates²⁰⁸ before peeling the tape away. It increased the quality of transferred graphene compared to the roll to roll process by reducing the mechanical stress on the graphene whilst the tape was removed. In so called *bubble transfer*²⁰⁹, the polymer supported graphene film is detached from the metallic growth substrate by electrochemical delamination. This allows the metallic substrate to be reused, and allows the use of metals that are impractical to remove via wet etching such as Pt²¹⁰.

4.1.3.2 Flake transfer techniques

Exfoliated flakes can be transferred from silicon dioxide coated wafers using all of the methods identified in the previous section, although the carrier film technique is the most common. After the polymer layer is deposited, the oxide layer is etched away using an alkaline solution, typically *sodium hydroxide* (NaOH) or *potassium hydroxide* (KOH). The film can then be used to transfer the graphene to an arbitrary substrate¹⁹⁸, and subsequently dissolved. To reduce the amount of contamination trapped under the flake after transfer, an alternative method termed *dry transfer*²² has been developed. This method aims to avoid contact between one side of the exfoliated flake (the side which will face the target substrate) and any liquid or polymer. These ‘wet’ and ‘dry’ transfer schemes are illustrated and compared in figure 29.

In the dry transfer scheme, the graphene is exfoliated directly onto a polymer carrier film which sits on a release layer. This film is then detached from its substrate via the dissolution of the release layer. The sample is floated on top of the solvent so that the flake is never submerged, as shown in panels (i) and (j). Finally, it is removed and pressed on to the target substrate. The polymer is then dissolved. Dry transfer drastically improves the interfacial cleanliness as compared to wet transfer. Graphene transferred onto²², or ideally encapsulated within²¹¹, hexagonal boron nitride flakes using dry transfer techniques shows electronic properties²¹² close to that of suspended graphene. In so called *peel and lift transfer*²¹³, a thick hBN is stamped onto flakes, and then peeled away carrying the flake with it. Successive flakes can be picked up, enabling the creation of heterostructures with large numbers of layers²¹⁴ without any polymer. Even graphene transferred using dry transfer techniques onto freshly cleaved hexagonal boron nitride exhibits bubbles²¹⁵ of trapped contamination on scales greater than a few microns, although there are atomically clean regions due to the graphene substrate interaction forcing the adhering molecules into highly pressurized bubbles during heating. Cross sectional TEM chemical analysis of such heterostructures reveals they are composed of adsorbed hydrocarbons²¹⁶.

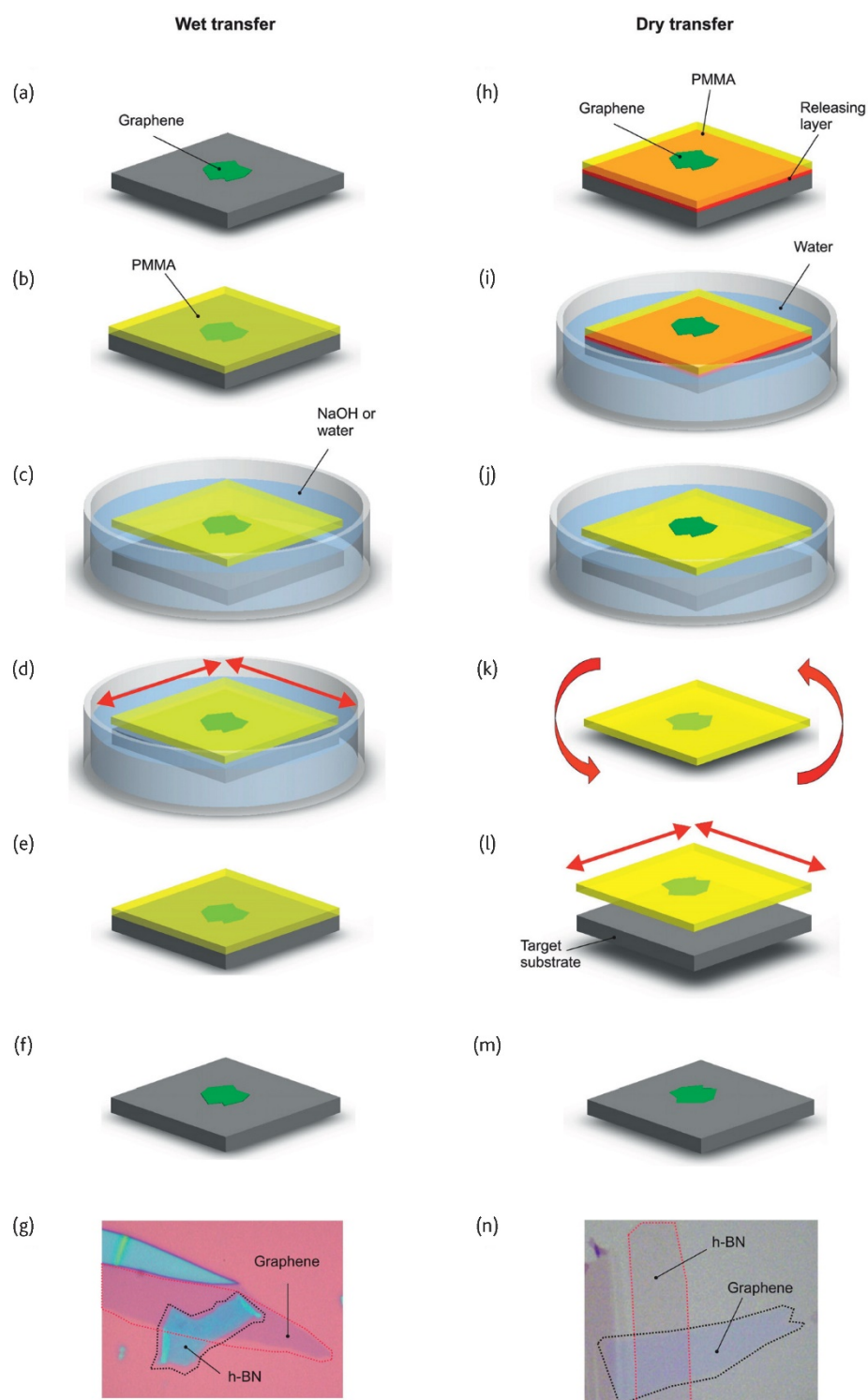


Figure 29 Outline of wet and dry graphene flake transfer techniques onto hexagonal boron nitride substrates. Panels (a) to (g) shows a wet transfer process from a silicon dioxide wafer using a PMMA carrier film. Panels (h) to (n) shows a dry transfer process, where the flake has been exfoliated directly on top of a carrier film on top of a release layer – this can consist of polymers or the thin oxide layer on a silicon wafer. The flake is transferred to the hBN with the interface side having never been in contact with liquid or polymer. Reprinted from reference¹⁹¹, with permission from Elsevier.

4.1.3.3 Aligned crystalline axis transfer

With growing interest in the exotic physical phenomena predicted to exist in twisted graphene^{138,217} and aligned graphene/hBN heterostructures^{218,219}, sophisticated transfer methods allowing rotation control were developed. Initial results on aligned graphene on hBN were observed in a few randomly oriented samples²²⁰, but aligned transfer methods^{211,221,222} allowed much more efficient production of devices. Similarly, studies on tBLG used either misaligned graphene sheets on HOPG during cleaving^{31,129}, twisted islands grown during CVD processes^{135,223}, randomly stacking sheets containing grains with various rotations^{142,224}, or sheets generated by the mechanical folding of monolayer sheets^{139,143,144,147}.

During the exfoliation of graphene, there is a preference for tears in crystallographic directions²²⁵, with a preference for long zigzag and armchair terminated edges²²⁶ with high substrate adhesion, low ‘tearing angle’ and for thicker flakes²²⁷. A mechanically exfoliated flake with crystallographic edges is shown in figure 30. It shows the straight edges at 30° increments which are characteristic of flakes of this type, and can be used to align the crystalline lattices during flake transfer at specified angles.

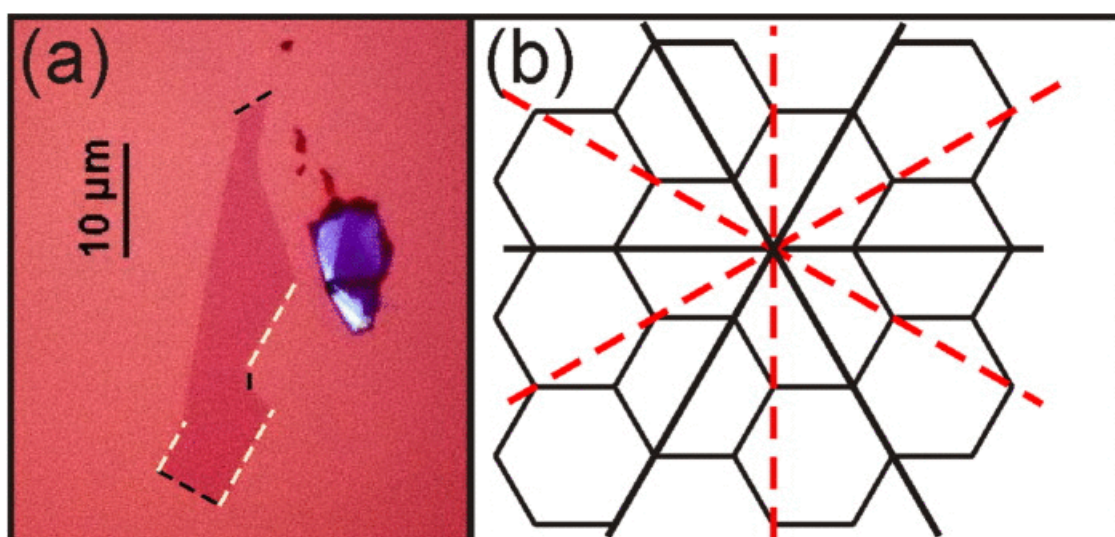


Figure 30 Crystallographic edges in exfoliated graphene flakes. (a) Optical image of an exfoliated graphene flake. The black dashed lines indicate edges oriented at -30° , 30° and 90° to the set of parallel edges indicated by white dashed lines. (b) indicates the preferred tearing edges of the graphene lattice at 30° increments, with the black solid lines indicating armchair edges and the red dashed lines indicating zigzag edges. Reprinted from reference²²⁸, with the permission of AIP Publishing.

Straight edges can be specified as being either zigzag or armchair by scanning probe microscopy²²⁸ or Raman spectroscopy²²⁹. Without this, there is only a 50% chance of obtaining the desired twist angle during transfer due to the possible mismatching of the straight edges.

4.1.3.4 Removing polymer after transfer

As every graphene atom is on the surface, the properties can be drastically affected by polymer contaminants left after exfoliation, transfer, and patterning processes. Most commonly they are removed by annealing in a reducing atmosphere^{230,231} (H_2 in with *Ar* carrier), although good results have also been obtained by annealing in ultrahigh vacuum^{232,233} (UHV). Current annealing²³⁴ and mechanical cleaning with an AFM tip²³⁵ have both been shown to increase the electronic quality of graphene devices. Cleaning routines involving washing in chloroform²³⁶, glacial acetic acid²³⁷, and baking with activated carbon²³⁸ have also been demonstrated, with good results. Annealing graphene in close contact with Pt has been shown to remove all contamination from large areas due to catalytic activity²³⁹, but this is not always practical and has only been demonstrated on suspended graphene.

4.2 Microfabrication techniques

Microfabrication techniques used to pattern materials on the microscale are introduced in this section, with a focus on micromachining silicon and related materials. The patterning of *resist* polymer layers using maskless optical lithography and electron beam lithography is introduced and discussed. Then, methods of transferring the resist pattern to materials, using either subsequent material deposition followed by partial removal (known as *liftoff*), or chemical etching (both *wet* and *dry* etching) to remove previously deposited material are described.

4.2.1 Lithography for nanostructures

Lithography is the name given to the process of transferring a pattern to a surface. In nanoscience this generally done by the selective exposure of a sensitive chemical ‘resist’ layer by radiation, in the form of light or electrons. The pattern is either written on to the resist by a directed beam or via flood exposure through a mask. Maskless techniques are more versatile as they allow for the creation of many different patterns without requiring a costly and time consuming mask production step.

4.2.1.1 Maskless/ scanning optical lithography

Optical lithography is the process of transferring a pattern into photosensitive polymer layer (‘photoresist’) via selective exposure to light with a wavelength below a corresponding threshold energy. Maskless optical lithography^{240,241} uses a focused laser beam which is selectively rastered across a surface to expose a predefined pattern. It can be used to open resist windows that can act as masks during an etch process, for example when patterning silicon microstructures (using a reactive ion etch) or patterning a graphene flake (using a weak oxidative plasma etch). It can also be used to selectively deposit metal to act as contacts, as explained in the section immediately below. The substrate is coated with resist which is then cured. In certain circumstances more than one layer of resist may be used. On the laboratory scale, the resists are generally *spin coated*, and cured using a hot plate. The thickness of the layers can be controlled via the maximum spin rate, and the bake temperature and time can affect the light sensitivity and development behaviour of the resist layer. When exposed by a rastered laser beam in a laserwriter system, a chemical change will

take place in the resist. Depending on whether the resist is 'positive tone' or 'negative tone', when the sample is washed in a developer solution either the exposed or unexposed resist is removed, leaving a patterned area. The choice of resist layer will depend on the desired subsequent processing steps. The smallest feature size attainable using maskless optical lithography is limited by diffraction. It is typically suitable for generating features with sizes larger than 1 μ m, although feature sizes down to 500nm are achievable in special circumstances.

4.2.1.2 Electron beam lithography

Electron beam lithography is similar to maskless optical lithography, but uses a scanning electron beam to selectively expose a predefined area. It is able to produce features on scales of tens of nanometers. Separate electron sensitive resists are required. Typical resists used include *poly (methyl methacrylate)*, known as PMMA (a positive tone resist) and *hydrogen silsesquioxane*, known as HSQ (a negative tone resist). In the laboratory, electron beam lithography is typically carried out in a modified SEM system (with a beam blanker) controlled by a pattern generator. Dedicated systems, operating at accelerating voltages of 100 – 200 KeV are able to produce smaller features. The resolution is practically limited by electron scattering within the resist and from the substrate. Optimisation of the writing and development process has resulted in written feature sizes as low as 5 nm.

4.2.2 Evaporation and lift off

Metallic contacts are typically made to nanoscale devices using the lift-off deposition process. Here, lithography is used to unmask areas in a resist film on a sample where metal is to be deposited, and a thin metallic film is then deposited over the whole area. This can be via sputtering or evaporation (via heat or electron beam) of metal sources. The resist layer is then removed using solvents, removing the metal deposited on top of it and leaving it only on the areas which were initially exposed.

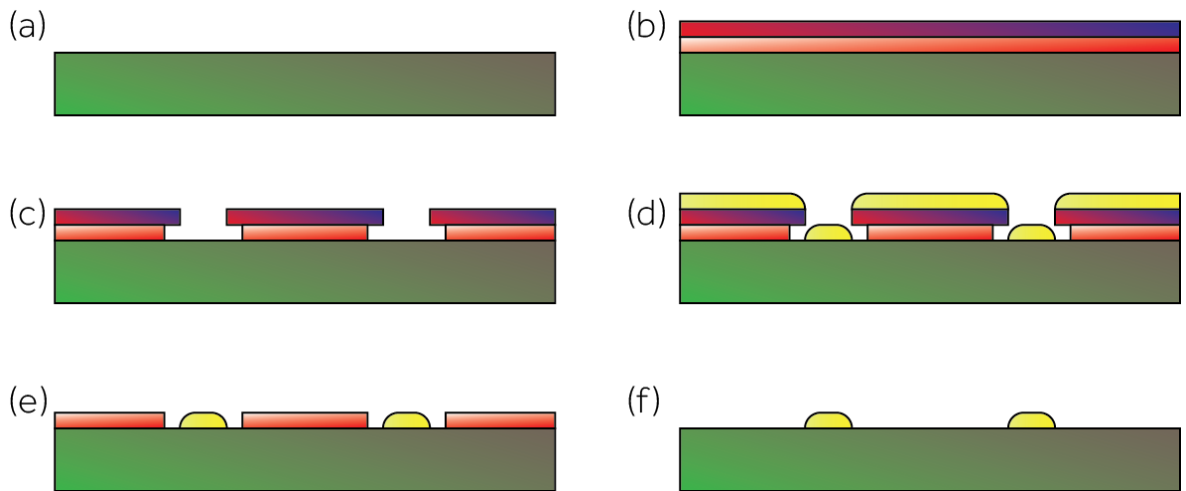


Figure 31 Schematic illustrating the steps in the lift off process using a bilayer resist. The substrate is cleaned (a) and coated with bilayer resist (b). The resist is then patterned via selective exposure and development (c), and a thin metallic film is deposited (d). The resist is then removed in a two-step process, firstly the top layer is dissolved removing the gold film, and then the protective bottom layer is removed leaving the patterned metal structures.

When performing lift-off, a dual layer photoresist is often used. The resists are chosen with the lower one having a higher rate of development, so that with correct exposure and development parameters an undercut is generated. This improves the profile of the deposited metal after resist removal. A step by step diagram illustrating this process is shown in figure 31. If the two layers are soluble in different solvents, the metal layer can be entirely removed whilst the sample is still protected. The underlayer can then be gently removed without the risk of any metal redeposition.

4.2.3 Etching

Etching is used to physically shape material into a pattern defined by a lithographic etch mask which protects part of the sample. In wet chemical etching, the sample is immersed in liquid etchant. In dry etching techniques, material is removed by a reactive plasma, or physically sputtered by ion bombardment. Etch rates for a variety of materials commonly used in microfabrication subject to a large range of etching processes, including wet and dry ones, are tabulated in references^{242,243}. To transfer a pattern using etching, part of the sample must be coated by an etch mask. The rate of etching of the target material, over that of the masking material, is referred to as the selectivity. This defines the thickness of the mask that is required to remove the required amount of material. The etch depth is either controlled by the etching

time, or by the prior insertion of an *etch stop* layer which is highly resistant to the etching process.

4.2.3.1 Wet etching

In wet etching processes, the material which is to be removed is immersed in an etchant solution. One or more chemical reactions then removes atoms from the surface. The reaction products are then dispersed through the etching solution via diffusion. When the chemical reactions take place faster than the diffusive dispersion, the process is said to be *diffusion limited*. In this case, the etch rate may be increased by agitating the solution. Generally, diffusion takes place faster than the surface reaction, and the process is *reaction limited*. In this case, the etching rate can be increased by increasing the reaction temperature and etchant concentration. Common wet etchants used in silicon micromachining include *hydrofluoric acid* (HF) for the selective etching of silicon oxide and nitride over silicon, and *potassium hydroxide* (KOH) and *tetra-methyl ammonium hydroxide* (TMAH) for the selective etching of silicon over oxide and nitride. These processes will be discussed in detail, however there are a wide variety of other etchants in use including *potassium iodide* for gold etching and *ceric ammonium nitrate* for etching chromium.

HF is capable of etching silicon dioxide at rates of the order 1 nm/s , while not appreciably etching silicon. It is an *anisotropic etchant*, meaning that its etch rate is independent of the crystalline direction. It does not attack photoresist, meaning that the deposition of a separate mask is unnecessary for short etching times (photoresist films often become detached during long etches). It also does not attack carbon structures, so can be used to fabricate suspended graphene and carbon nanotube devices by etching away the oxide layer underneath them²⁴⁴.

Alkaline etching of silicon by KOH^{245,246} and TMAH²⁴⁷ is a common microfabrication technique. They both etch silicon at rates of the order $1 \text{ }\mu\text{m/min}$, and oxide at rates of the order 1 nm/min , while not appreciably attacking silicon nitride. Both attack the majority of photoresists, meaning the use of a *hard mask* is necessary. For shallower etches silicon oxide is typically used, although for very deep etches (over around $100 \text{ }\mu\text{m}$) either a very thick layer or a silicon nitride mask is required. They also etch silicon *anisotropically*, with a strong preference for etching [100] silicon planes over [111] planes. TMAH offers higher selectivity

over oxide masking layers²⁴⁸, whilst KOH has a stronger preference for [100] etching over [111] planes.

4.2.3.2 Dry etching

In dry etching, material is removed by a gas or plasma, by either chemical reactions, physical bombardment, or typically both. The gas is typically ionized by the application of an RF field. Oxygen plasma etching is commonly used in microfabrication processes for the removal of photoresist and organic processing residue. It is often used with photoresist masks for the purpose of shaping carbon nanomaterials. It is generally an evaporative etching process, where the reactive species chemically react with surface contaminants to produce gaseous products, such as CO_2 .

In reactive ion etching (RIE) systems, the ions in the plasma are directed normal to the surface, increasing the etch rate and allowing the fabrication of high aspect ratio structures. In this case the plasma may be powered by inductive coupling (ICP) rather than RF power, although many systems use both simultaneously. In this case, the ICP is used to create a high density ion source, and an RF field is applied to the substrate to create local directional fields. Gases containing chlorine and fluorine are normally used. RIE is both an evaporative reactive process and a physical sputtering process. The relative rates can be controlled by the gas flow and power ratio between the RF and ICP electrodes. Very high aspect ratio structures in silicon can be fabricated²⁴⁹ in so-called deep reactive ion etching (DRIE) processes, by etching at cryogenic temperatures or, more commonly, using multistep processes such as the Bosch process. This uses alternate etching and deposition steps to create structures with nearly vertical sidewalls. The process steps are illustrated in figure 32.

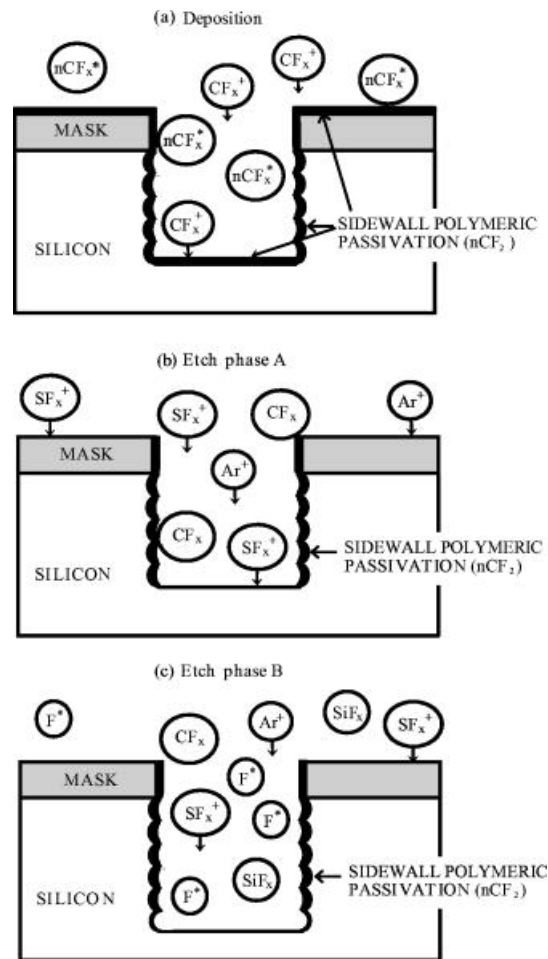


Figure 32 Deep reactive ion etching (DRIE) of silicon during the Bosch process. (a) shows the deposition stage, where fluorinated polymer is deposited anisotropically on the trench floor and sidewalls. (b) during the etching step, the inherent anisotropy in the plasma etching will remove the passivation layer from the floor before the sidewalls. (c) The silicon is etched from the trench bottom, but the sidewalls remain protected by the passivation layer. Image adapted from reference²⁴⁹. Reprinted with permission from reference²⁴⁹. Copyright 2005, American Vacuum Society.

Sulfur hexafluoride (SF_6) is commonly used as the etching gas. Source gases used during the deposition step include fluorofrom (CHF_3) and octafluorocyclobutane (C_4F_8). Similar chlorinated gases are alternatively used. This technique relies on the fact that during the deposition step the etching process is relatively anisotropic, etching the trench bottom faster than the sidewalls. If the deposition of the passivation layer is relatively isotropic, this generates a mismatch on the relative etching minus deposition rate between the walls and floor. If the rate of deposition of the polymer is set to be roughly equal to the etching rate of the sidewalls over a large number of alternate steps, the sidewalls will be preserved, while the higher etch rate on the trench floor causes the overall rate of deposition minus etching to be positive.

4.3 Nanomechanical characterisation with AFM

Atomic force microscopy has been long used to extract mechanical information^{250,251} as well as topography from a sample. Generally this involves ramping a cantilever with a known force constant into a surface²⁵², and capturing the force distance behaviour (or *force curve*) of the tip. Together with a model of the geometry of the tip, this force distance profile allows a variety of nanomechanical parameters to be calculated. This section describes methods of nanoindentation, the material parameters which can be extracted from the *force curve*, calibration techniques used to determine the stiffness of the indentation cantilever, and the use of AFM to spatially map local mechanical properties.

4.3.1 Nano indentation

Probe based indentation is a widely used technique for studying local mechanical material properties²⁵². This technique uses an atomic force microscope cantilever to apply known forces to a sample (which can be deduced by the degree of bend of the cantilever assuming a known spring constant) and measuring the degree by which the surface is displaced. A typical force-displacement plot (hereafter force curve) is shown in figure 33. The diagrams in the lower part of the figure illustrate the position and bend of the cantilever at various points during the process, and are labelled with their corresponding positions on the force curve. At point A the tip is approaching or retracting far from the range of the van der Waals interactions between the tip and the surface, and no bend is seen. As it approaches the surface, the attractive forces pull the tip down onto the surface, bending the cantilever and causing the dip shown at point B. The cantilever continues to move down, pushing the tip into the surface and bending the cantilever until a set deflection value is reached at point C, when the cantilever begins to retract. However, it goes past the zero deflection point and is bent towards the surface as the attractive forces keep the tip held firm. Finally, the upward force on the tip due to the bending becomes larger than the attractive contact forces, and the tip snaps up away from the surface at point D.

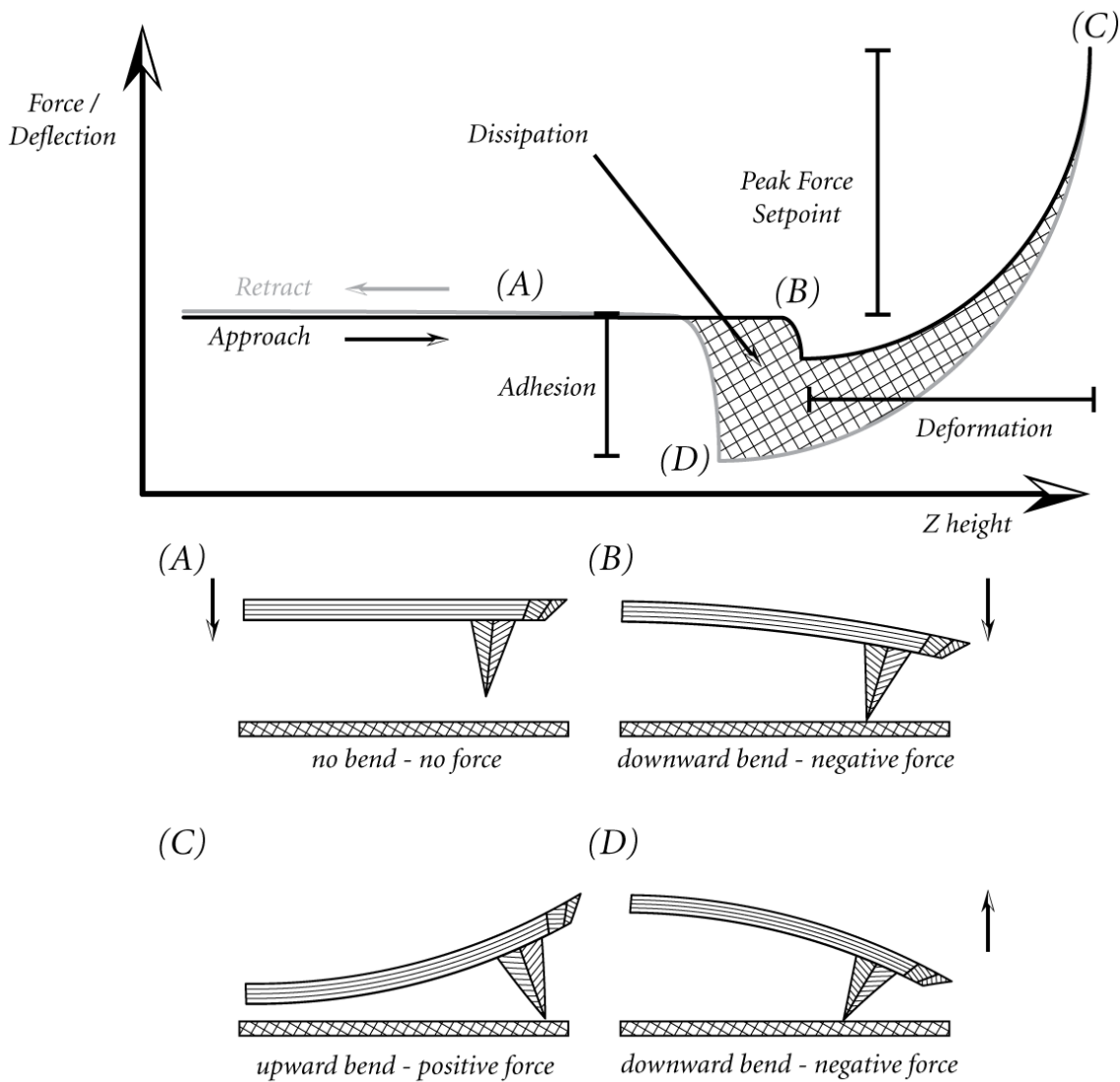


Figure 33 Schematic illustrating the process of taking a force displacement curve in an AFM. The vertical axis corresponds to the degree of bend of the AFM cantilever, and the horizontal axis corresponds to the position of the cantilever relative to the surface.

Various nanomechanical parameters can then be extracted from the force curve information^{250,253-256}. The deformation behaviour, coupled with knowledge of the tip geometry can be used to measure the modulus of the test material. The area of the hysteric loop can be related to the amount of energy dissipated by the sample, and the maximum cantilever bend during 'pull off' can indicate the strength of the adhesive forces between the tip and the sample (along with some knowledge of the relative z-position and tip structure). These derived parameters are shown in the plot in figure 33.

4.3.2 Force calibration

The AFM directly measures the deflection of a laser beam reflected from the tip via a split photodetector. To convert this voltage signal to the bend of the cantilever, we divide by a so-called *deflection sensitivity* (in V/nm). This is dependent on both the properties of the tip, how it is seated, and the position of the beam on the tip. It can be measured relatively simply by capturing the deflection data as the tip is pressed against a much harder surface, such as sapphire or diamond. As the tip remains on the surface, all signal is due to the deflection of the cantilever.

To convert the tip bend distance into a force, we need the force constant of the individual tip. Although an approximate range is specified by the manufacturer, there is considerable variation in thicknesses both within and between batches from the microfabrication process. There are various ways to measure this. The tip can be indented into a softer polymer with a known Young's modulus. From the tip geometry and the indentation depth which can be obtained by scanning the indentation site, the maximum force applied on the polymer during the indentation can be estimated. Tips can also be calibrated by ramping them against reference cantilevers^{251,257} with known force constants. Less direct but more convenient measurements include Sader's method²⁵⁸⁻²⁶¹ and the thermal tune method^{262,263}.

Sader's method approximates the spring constant of a rectangular cantilever in a viscous incompressible fluid (this includes air at the relevant time and length scale) as

$$k = 0.1906 \rho_f w^2 L Q_f \Gamma_i \omega_f^2 \quad (24)$$

where w and L are the width and length of the cantilever respectively, Q_f and ω_f are the cantilevers quality factor and resonant frequency, ρ_f is the fluid density, and $\Gamma_i(\omega_f, Re)$ is the imaginary part of the hydrodynamic function²⁶⁰ which is dependent only on the frequency ω_f and Reynolds number Re . This relates the spring constant to the dimensions of the cantilever, and the resonant frequency and quality factor which can be extracted from an experimentally measured thermal noise spectrum. For stiffer cantilevers thermal oscillations are too small to be observed over the noise threshold, and the cantilever can be

driven through a range of frequencies instead, at low drive amplitudes (higher amplitudes introduce nonlinearities which complicate this picture). The thermal tune method²⁶³ also uses the thermal noise spectrum. Here, the noise spectra is fit to an equipartition²⁶⁴ thermal noise model which is related only to the spring constant and the laser deflection sensitivity. As the thermal noise spectra needs to have a reasonably high signal to noise ratio, this method is not useful for stiffer cantilevers with smaller thermal oscillations.

4.3.2 Mapping / spatial variation

The most accurate way of mapping material properties at the nanoscale has been force-volume imaging²⁵⁴ in an atomic force microscope (AFM). In this mode, the tip is ramped using the z -axis stepper motor to perform a nano indentation at every point in an image, producing a two-dimensional array of force curves, from which a variety of nanomechanical properties can be extracted. However force-volume mapping and standard tapping mode imaging do not deal well with large sudden changes in the surface mechanical properties, and the extensive time required to complete a force volume plot limits its usefulness.

The recently introduced PeakForce QNM (quantitative nanomechanical mapping) AFM mode²⁶⁵⁻²⁶⁷ allows the spatial mapping of the nanomechanical properties of a surface at high speed by effectively ramping with the cantilever rather than the z -piezo; the time taken for a full nanomechanical map is comparable to the time taken for a standard AFM tapping mode topography-only image. PeakForce QNM imaging, like force volume imaging, generates a force curve per image pixel, from which a variety of useful mechanical properties can be extracted. However the extremely low speed of force-volume imaging (~ 1 pixel per second) limits its usefulness and makes it susceptible to drift. In PeakForce imaging, the tip is oscillated at a non-resonance frequency (1-8 kHz) rather than ramped vertically with the z -piezo (few Hz), dramatically increasing the capture speed (approx. 1–4 lines per second).

4.4 Ultraresolution patterning in graphene

This section provides a brief review of lithographic techniques which can be used to produce sub 10nm features in graphene and 2D material systems. Firstly, the limits of resist based patterning, and a few techniques which may be able to extend them, are discussed. Then, the use of highly focused particle beams to directly pattern 2D materials is introduced and reviewed. Scanning probe based lithography on graphene has also been demonstrated on graphene^{268,269} but is slow and unwieldy.

4.4.1 Resist based patterning

Graphene is typically patterned using electron beam lithography (EBL) and subsequent plasma etching, as described in section 4.2, into structures such as Hall bars²⁷⁰, nanoribbons²⁷¹ and quantum dots²⁷², and nanogap electrodes^{273,274}. This is typically able to create structures on scales of 10-20nm depending on the accelerating voltage, but is typically unable to pattern smaller features due to secondary electrons spreading through the resist effectively widening the beam width²⁷⁵. Several strategies have been used to reduce this feature size further, including using SiN_x membranes as substrates to reduce resist development from secondary electrons²⁷⁶, and optimising the development and etching procedures through underexposure and ultrasonication^{277,278} or development at reduced temperatures^{279,280} or with modified chemistries²⁸¹ to prevent areas of resist not exposed by the main beam from being removed. Also, the inherent feature broadening during the etching step can be utilised by designing a structure after development that will result in a small feature as a result of this over etching, such as dash line lithography²⁸². This has enabled the reduction of feature sizes down to 5 nm^{273,274} in graphene/CNT devices, but requires significant experimental optimisation and specialised equipment, and only a few graphene structures with features on sub 10nm scales patterned using this technique have been reported.

4.4.2 Direct write patterning

An alternative to selectively exposing resist to act as an etch mask for patterning materials is the direct writing technique, where a focused beam is selectively scanned across a sample to remove material. This has the advantage of being a clean maskless technique, with the feature

size dependent mainly on the beam width. Focused ion beam (FIB) systems have successfully patterned graphene using both Ga ions²⁸³ and He ions^{284,285}, but can cause damage to the graphene sample²⁸⁶. Use of helium ion microscopes has enabled the fabrication of 5nm pitch structures in substrate supported graphene²⁸⁷, and 2-3nm scale structures in suspended graphene²⁸⁸.

Alternatively, patterning of suspended graphene structures using the highly confined electron beam used in scanning transmission electron microscopes (STEM) to generate structures in graphene such as nanopores^{289,290} and nanoribbons^{291,292} has been reported. This beam patterning technique had previously been used to shape carbon nanotubes^{293,294} but is perhaps more suited to graphene because of its planar nature. It has been demonstrated that this technique is able to produce structures with controlled edge geometries²⁹⁵. Recently, patterning at elevated temperature (600 °C) has been found to induce self-repair of the graphene lattice, which enables repeatable patterning while imaging, which is otherwise necessarily restricted to avoid damage to the rest of the graphene area. However the need for suspended samples means that this technique is only suitable for self-supporting structures such as nanopores and (under certain circumstances) nanoribbons; otherwise the intrinsic tension in any suspended graphene layer will distort the features once cut. This means it is unsuitable for producing structures such as nanogap electrodes²⁹⁶, as any electrically separated electrodes would therefore be mechanically unseparated, and would not maintain the few nm gap required.

5 Experimental procedures

This chapter describes the experimental techniques which were developed and used as part of this thesis to answer the research questions posed in the peer-reviewed articles which are included as results chapters. Firstly, the microfabrication procedures used to fabricate patterned silicon nitride membranes, including optical lithography and wet and dry etching are reviewed. Then, procedures for exfoliation and transfer of graphene and hBN flakes are discussed. The next section describes the procedure used to cleanly pattern graphene layers using optical lithography. These techniques were employed throughout the experimental work undertaken as part of this thesis. Subsequently, 2 methods of segmenting the silicon nitride membrane samples into TEM compatible 3 mm discs are reviewed and compared. Then, there is a brief section describing the procedures used for fitting model EELS spectra to captured experimental data in the published work contained in section 9 of this thesis. Finally, the last 4 sections review the experimental procedures specific to the 4 results chapters, and describe the fabrication process for the eventual samples.

5.1 Microfabrication of silicon structures

In this work, patterned silicon nitride membranes were fabricated from nitride coated silicon wafers, by selectively etching away material in patterns defined using maskless optical lithography. Silicon nitride was removed using deep reactive ion etching with a photoresist mask, and silicon was removed in an anisotropic KOH etch with a silicon nitride mask. The nitride layer on one side is first patterned using DRIE into an etch mask for the wet silicon etch. The silicon nitride layer on the other side of the wafer acts as an etch stop layer, leaving a nitride membrane with a size defined by the etch mask on the other side. This membrane was then patterned using a second DRIE step. This is illustrated in figure 34. This generates *through* holes, meaning that transferring 2D materials over the patterned membranes generates samples suitable for characterisation in a transmission geometry.

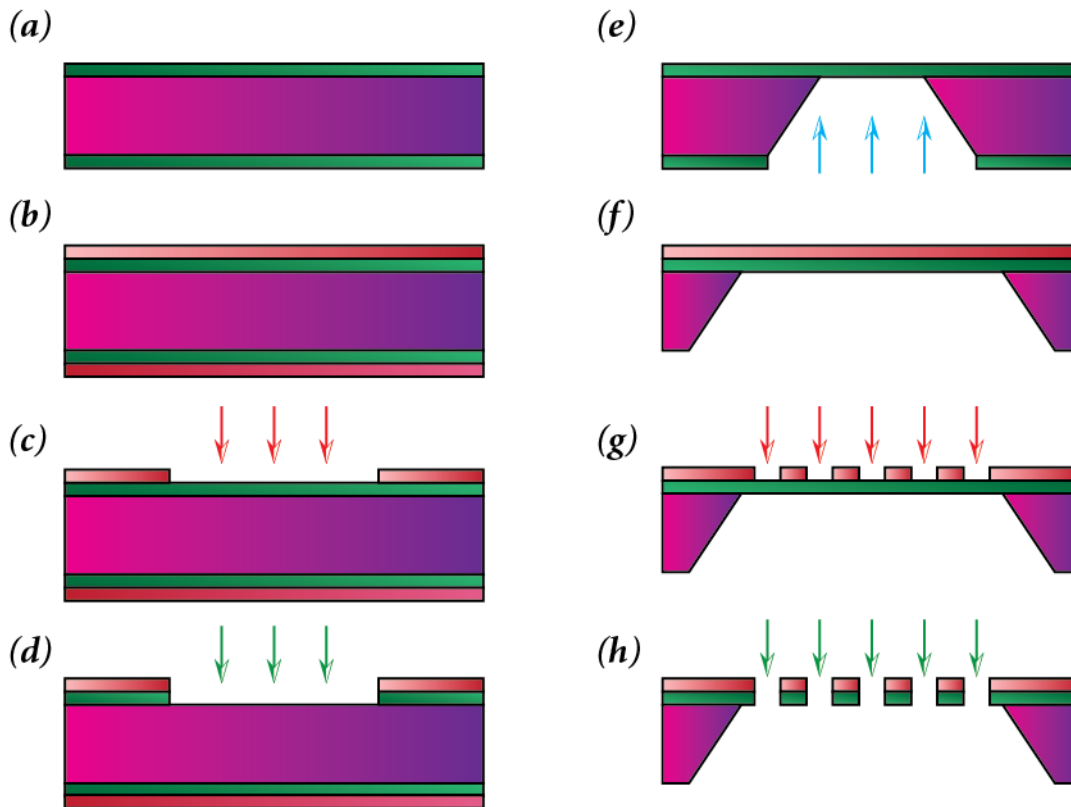


Figure 34 **Fabrication steps involved in the manufacture of patterned silicon nitride membranes.** The silicon wafer is purple, and the nitride coating is green. Photoresist is coloured red. Red arrows indicate photoresist exposure and development, green arrows represent Bosch etching of silicon nitride, and blue arrows indicate KOH etching of silicon. The sample is flipped over between steps (d) and (e).

In the following subsections, the fabrication process steps are discussed in detail.

5.1.1 Wafers and preparation

Initially, the wafers used were $500\ \mu\text{m}$ thick (100) oriented silicon wafers coated with $500\ \text{nm}$ thick silicon nitride membranes. The wafers were supplied by Noel Technologies, with a $\langle 100 \rangle$ orientation and N-doped with a specified resistivity of $1 - 10\ \Omega \cdot \text{cm}$. To enable a simpler and more efficient patterning process to divide wafers into TEM compatible samples, and achieve higher adhesion to 2D materials due to the reduced roughness of the nitride film, a thinner flatter wafer variety from a different supplier was used instead. These were $200\ \mu\text{m}$ thick (100) oriented silicon wafers coated in a $100\ \text{nm}$ film of low stress silicon nitride grown in a low pressure chemical vapour deposition (CVD) process. They were supplied by Structure Probe Inc. (www.2spi.com). They are referred to as *thick* and *thin* wafers respectively throughout this chapter.

Both wafers had 100 mm diameters. They were patterned into 21.8 × 24.8 mm segments by scribing and cracking along the Si crystal planes, using a wafer scribe (manufactured by South Bay Technologies). The scribes were aligned to the ‘flat’ segments of the wafers, which indicate the crystal direction. Normally this resulted in smooth edges, but sometimes jagged edges were caused by slight misalignment between the wafer flat and the actual crystal direction. The samples were opened in a Class 100 cleanroom environment and coated in a protective photoresist layer before being removed for scribing to protect the surface and prevent the deposition of silicon dust. After scribing, the chips were rinsed in acetone, and subsequently sonicated for 5 minutes each in acetone, *deionised* (DI) water, and *isopropyl alcohol* (IPA) to remove any photoresist or silicon dust. They were then stored submerged in IPA until required.

5.1.2 Resist coating and patterning

The etch masks were defined using maskless optical lithography, by a Microtech LW405 LaserWriter system with a 405 nm GaN laser. Resist layers were deposited by spin-coating, with the sample held in place by a vacuum chuck. The chips were removed from IPA, sonicated in solvents, dried using a stream of nitrogen, and then baked on a cleanroom wipe (to protect the nitride layer) on a hotplate at 180 °C for 10 minutes to dehydrate the surface. Adhesion promoter was not used, as there was no delamination observed during etching processes following this wafer cleaning procedure.

Both sides of the sample needed to be coated to protect the nitride layer during the patterning. Even small holes in the nitride film caused by improper resist coverage or scratching can lead to large cavities after the KOH etching process. The ‘back-side’ during the first lithography process is the side that will end up as the area of interest, where the 2D flakes are to be transferred. To achieve good coating on both sides, the sample was suspended on 4 tape pillars attached to a PET base. The base was held by the vacuum chuck, and the resist pipetted both onto the upper sample surface, and into the space between the sample and the plastic support. On spinning, both sides are coated. It is difficult to estimate the thickness of the resist film on the bottom side, but it is sufficient to completely protect the nitride layer during subsequent processing. This arrangement is illustrated in figure 35. For the second lithography step after KOH etching, protecting the backside of the membrane was

no longer necessary. Instead, the samples were patterned with a large area in the centre free of membranes, which could be placed over the vacuum chuck, and the topside could be coated as usual.

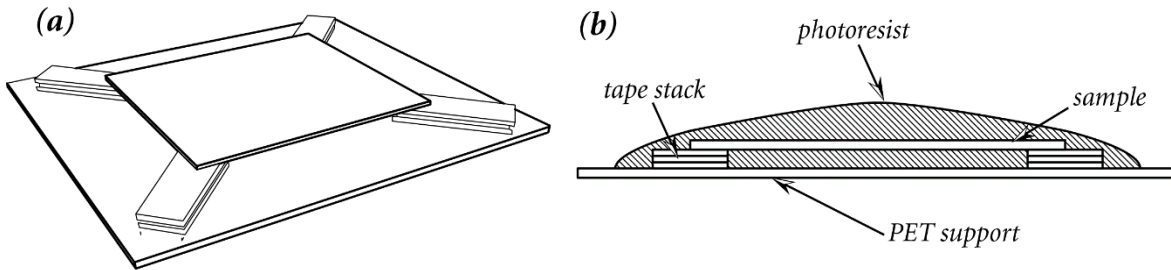


Figure 35 Illustration of the simultaneous double sided spin coating process. The sample is supported at 4 corners by tape stacks, consisting of two layers of high tack low strain tape on either side of double sided tape. This leaves a gap of approximately 1.5 mm under the sample. Resist is pipetted on to the surface and into the gap. The surface tension holds the resist in the gap rather than spreading across the plastic.

For the thick wafers with thicker nitride layers, MicroPosit Shipley S1813 (Rohm-Haas) positive tone photoresist was used. It was spun at 4000 *rpm*, with an acceleration of 500 *rpm s*⁻¹. This leads to a resist thickness of approximately 1300 *nm* on the upper side. It was then cured on a hotplate at 115 °C for 90 seconds. Switching to wafers with thinner nitride layers allowed shorter etching times, and allowed a thinner resist layer to be used. MicroPosit Shipley S1805 (Rohm-Haas) was spun at 7000 *rpm*, with an acceleration of 1000 *rpm s*⁻¹, giving a film thickness of approximately 400*nm*. It was baked on a hot plate at 115 °C, first for 30 seconds on top of a cleanroom wipe and then for 60 seconds directly on the hotplate. Patterning for the backside etch mask was performed using a lens with a numerical aperture of 0.10, which can write feature sizes down to around 8 μm . Fine patterning used a lens with a numerical aperture of 0.65, able to write features of sizes down to around 1 μm . The radiation doses were optimised to fully remove photoresist from exposed areas after 30s immersion in developer solution. After being immersed and gently wafted in TMAH developer solution (MicroPosit MF319 Developer solution from Rohm-Haas) for 25 seconds, the wafers were visually inspected in an optical microscope using a red narrow pass filter so as not to expose the resist further. If required, the sample was immersed in developer for a further 5 seconds and reinspected until adequate development was reached. At this point, the sample would be hard baked on a hot plate at 150 °C for 5 minutes.

5.1.3 KOH etching of silicon

As discussed in section 4.2.3.1, etching of silicon by KOH is an anisotropic process. KOH preferentially etches silicon's (100) plane over its (111) plane. If we can expose a rectangle in a suitable etch mask which is aligned to the crystalline axis, this will lead to an etched volume in the shape which is the inverse of a 4-sided pyramid, with its volume defined by the shape of the rectangle, and (111) planes of the crystalline silicon making up the angled edges, as shown on the left side of figure 36. If there is an etch stop layer on the other side, and the mask size on the back side is large enough, this etch can leave an etch stop layer membrane with a shape corresponding to that of the mask, but minus a constant offset due to the (111) slope, leading to an etched volume corresponding to a 4-sided frustum. This is illustrated on the right hand side in figure 36.

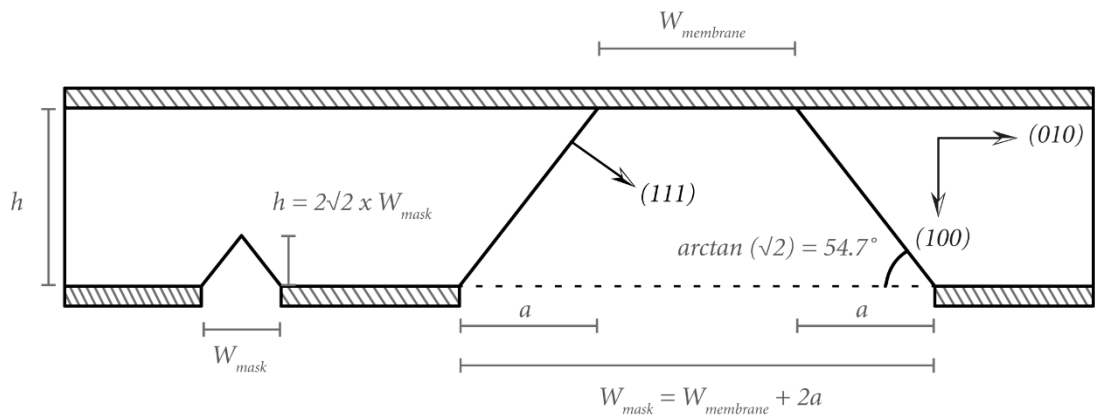


Figure 36 A schematic view of a KOH Si etch with an etch stop layer from the (001) plane. This is equivalent to the view from the (010) direction.

Using trigonometry we can write the size of the membrane as a function of the size of the back etch as

$$W_{mask} = W_{membrane} + 2 \frac{h}{\sqrt{2}} = W_{membrane} + h\sqrt{2} \quad (25)$$

where W_{mask} and $W_{membrane}$ are the widths of the mask and membrane respectively and h is the thickness of the silicon. These parameters are indicated in figure 36. Generally the size and shape of the fabricated membranes was square with a sidelength around $100 \mu m$

squares. For the $500\ \mu\text{m}$ thick wafers, this corresponds to an etch-mask square with a sidelength of around $800\ \mu\text{m}$. For the $100\ \mu\text{m}$ wafers, this corresponds to an etch mask size of around $250\ \mu\text{m}$.

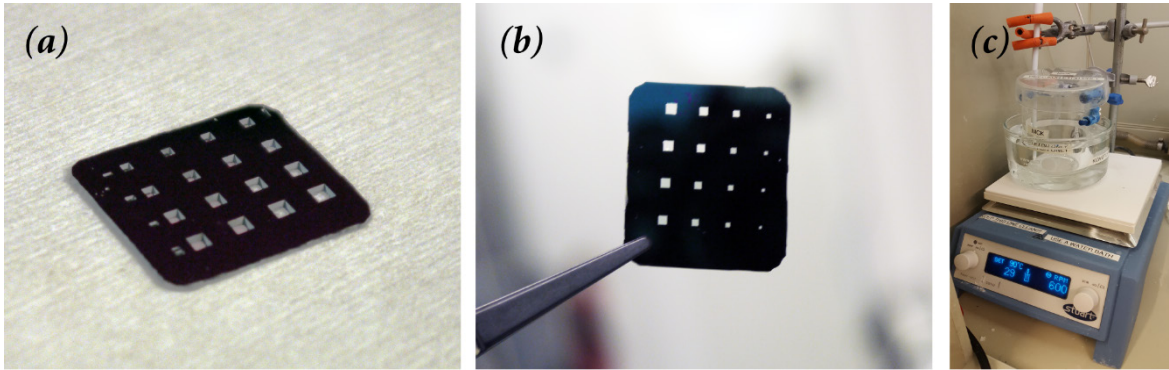


Figure 37 KOH etching of silicon. (a) and (b) show large silicon nitride membranes formed by KOH etching. The whole chip dimensions are $24 \times 21\ \text{mm}$ and the membranes are squares with sidelengths ranging from $200 - 2000\ \mu\text{m}$. Both images have been contrast enhanced to aid visualisation of the trench features. (c) shows the water bath setup to keep the KOH temperature constant.

Once the squares have been defined using lithography and transferred into the nitride layer using DRIE (as discussed in the following section), the sample is immersed in heated KOH solution, after rinsing in acetone, DI water and IPA to remove as much of the remaining photoresist as possible. Any remaining residue is removed during the etching process. The KOH solution was 30% by weight, with the addition of a small amount of IPA. Initially, etches were performed in a beaker on a hot plate set at $90\ ^\circ\text{C}$. The sample was placed at an angle against the side of the beaker. If placed with the etching side up, the membranes can be damaged by sliding and scratching along the bottom. If placed with the etching side down, the hydrogen bubbles produced during the reaction cause the sample to jolt around, potentially fracturing the membranes. The etching process took 8-16 hours for $500\ \mu\text{m}$ thick wafers, indicating an etch rate of $30 - 60\ \mu\text{m}/\text{hour}$. From experimentally measured etch rates^{245,246,248}, this indicates a KOH temperature of around $60 - 70\ ^\circ\text{C}$. A new etching setup was subsequently developed, with a hotplate with an external temperature probe, as pictured in panel (c) of figure 37. This was used to maintain a water bath at a constant $85\ ^\circ\text{C}$. The etchant was then kept in a lidded beaker submerged in the water bath. The etching process repeatedly took around 2 hours for a $200\ \mu\text{m}$ thick wafer, suggesting a KOH etchant temperature around $80\ ^\circ\text{C}$. Once the approximate etching time has been reached, the etch progress can be optically monitored by briefly holding the sample up to a light, as shown in

panel (b) of Figure 37. The silicon nitride windows are transparent, and can be easily seen with the eye. Once the transparent membranes are visible, they are placed back into the etching solution for a further 10 minutes to ensure the complete removal of silicon from the backside of the wafer. They are then rinsed in DI water, and carefully dried using nitrogen, and are ready for subsequent processing. Optical images showing the sample at various stages of this process are collated in figure 38.

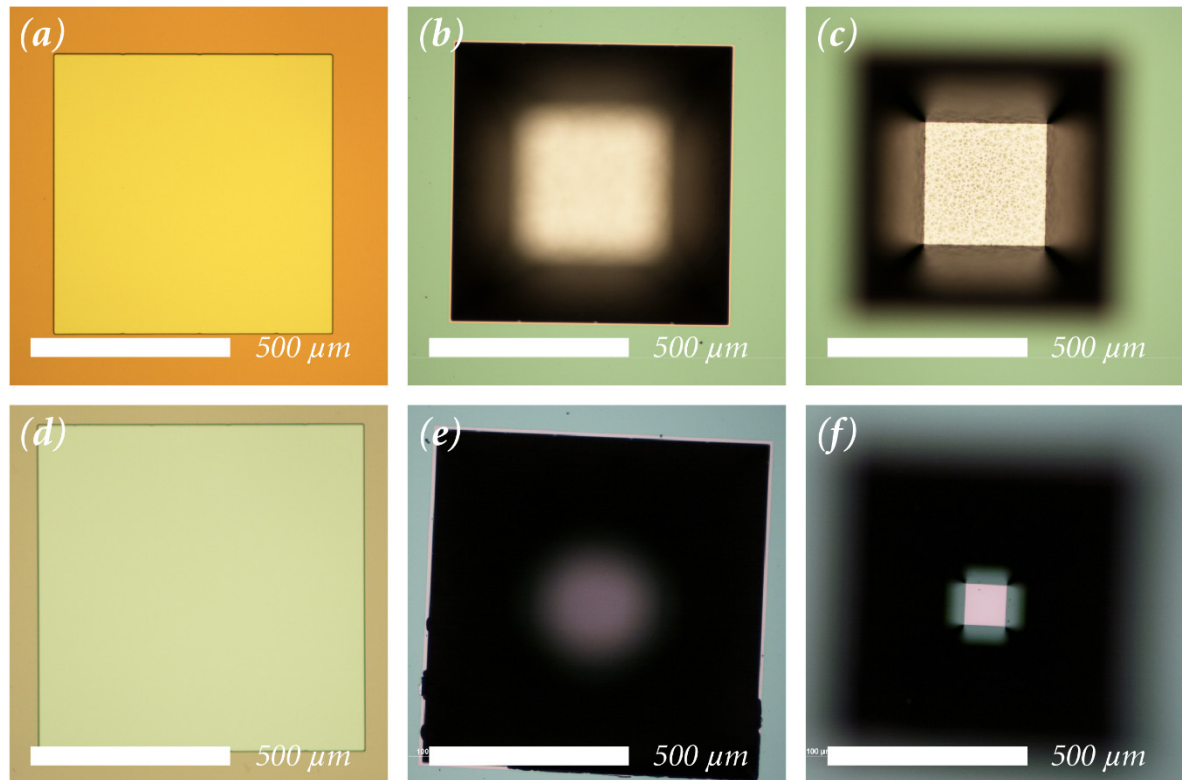


Figure 38 Optical images showing the progression of the wet etching of 500 μm thick silicon wafers using KOH. (a) and (d) show squares patterned into silicon nitride, with sidelengths of 680 μm and 810 μm respectively. (b) and (e) show the same areas after 6 hours and 10 hours of KOH etching respectively. The focal plane is at the upper surface. (c) and (f) show the corresponding areas, but focussed on the bottom of the etched pit. After 6 hours of etching, the KOH has not finished etching all available (100) and (110) planes, and the roughened (100) plane is visible. After 10 hours, the etch process has proceeded all the way through to the nitride etch stop layer on the other side of the wafer. The thin rim around the edge of the pit in (b) and (e) is a nitride membrane formed by the slight underetching of the etch mask caused by the slow attack of KOH in Si (111) planes.

5.1.4 Bosch etching of silicon nitride

Silicon nitride was patterned, when required, using a Bosch etch, as described in section 4.2.3.2. Photoresist etch masks were defined using maskless optical lithography. The resist compositions for both wafer thicknesses, and the patterning and development parameters

are given in section 5.1.2. The etching system used was an Oxford Instruments PlasmaLab 100 system, capable of generating plasmas using simultaneous RF power and inductive coupling. It was equipped with fluorine containing gaseous etchants. First, features on the scale of hundreds of μm are patterned onto one side of a wafer to act as an etch mask for a wet KOH etch. Subsequently, the membrane on the other side is patterned with an array of holes with sizes of a few μm , over which 2D materials could be transferred to create suspended membranes over through holes.

The Bosch etch was used to pattern the silicon nitride membranes, although it failed to produce anything like vertical sidewalls. The source gases were SF_6 and CHF_3 for the etching and deposition steps repeatedly. Photoresist was used as the etch mask, but was actually etched faster than silicon nitride, with a selectivity around 1:2. This meant that films far thicker than the nitride layers were required. Originally, when patterning 500 μm thick nitride membranes, very thick photoresist films were required. The long etch times often led to a highly crosslinked polymer layer on the surface of the remaining layer that was hard to remove using solvents and subsequent plasma etching. In particular, this was a problem during the second etch when writing micron sized features, as the polymer films are often trapped by the holes. Sonication could not be used at any point during the cleaning process due to the risk of damaging the nitride membranes. Increasing the resist thickness, and the use of an acetone insoluble underlayer (PMGI) as in the liftoff process (see section 4.2.2), were partially successful in alleviating this problem, although not entirely. In addition, circular features of the same sizes of the patterned holes were often observed on the membrane after tape removal. Atomic force microscopy (AFM) on the topside of the membrane revealed no features, and the backside of the membranes were inaccessible due to the depth of the KOH pit. The origin and nature of these features is unknown. They are shown in panel (c) in figure 39.

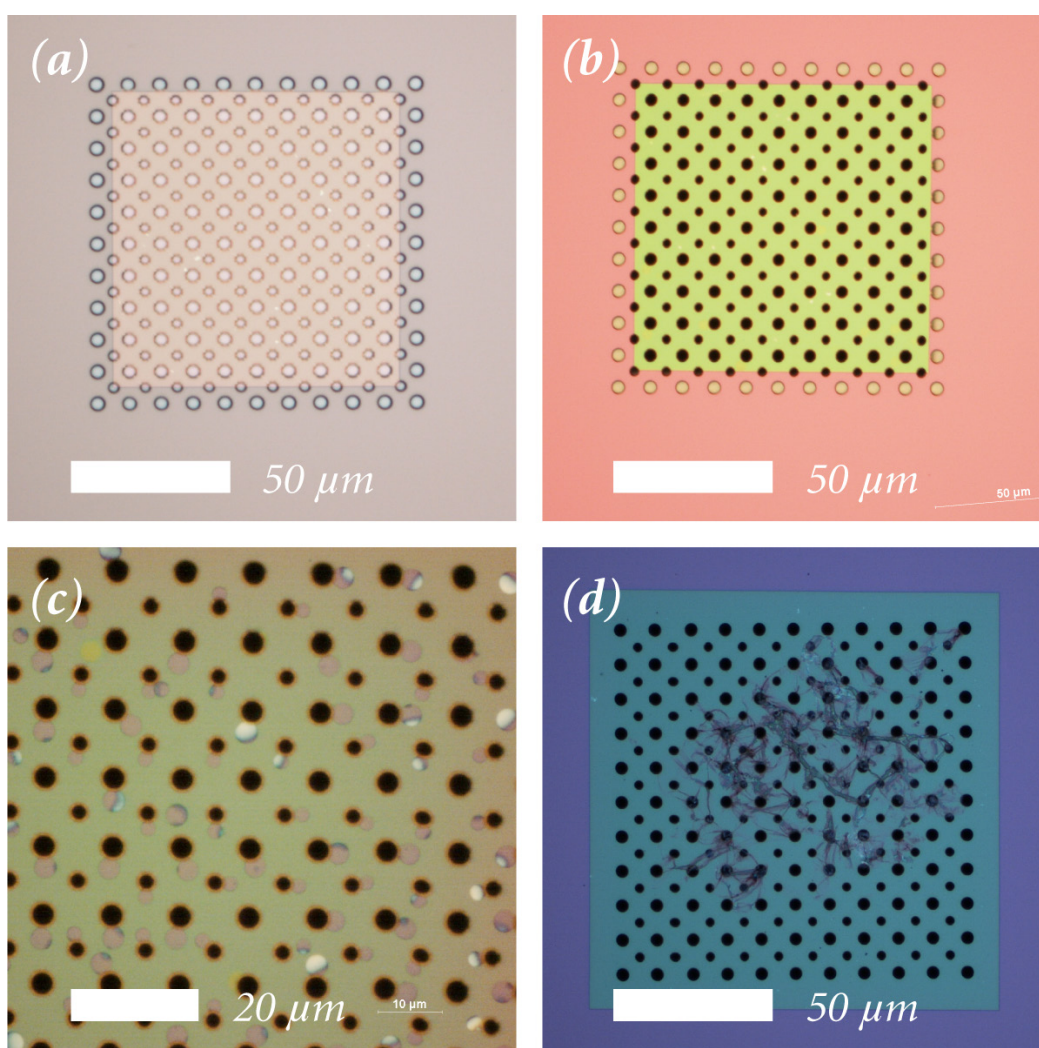


Figure 39 Micron scale holes patterned into silicon nitride membranes using maskless optical lithography and a DRIE process. (a) shows the holes in the resist layer after exposure and development. The square feature is the silicon nitride membrane. Around this the nitride is supported by the surrounding silicon. (b) shows the same membrane after the Bosch etching process and the removal of the resist layer. (c) shows an example of the circular features that appeared on some membranes after the etching process. (d) shows a membrane contaminated with crosslinked photoresist sheets.

The switch to thinner nitride membranes enabled the development of an optimised process. Rather than a relatively thick resist layer, an extremely thin one was chosen. The details of the resist film are given in section 5.1.2. During the Bosch etching process, the resist layer is nearly entirely etched away. It is then immediately removed in a high power oxygen etch process, leaving the nitride membranes clean and ready for immediate transfer. This new processing technique, in addition to the improved flatness of the low-stress nitride membranes made transfers of 2D materials onto them particularly successful due to the high adhesion between the membrane and the PMMA transfer film.

5.2 2D material exfoliation, identification, and transfer

This section reviews the experimental procedures used for the exfoliation, identification and transfer of graphene and hBN during the undertaking of this work. Firstly, two micromechanical exfoliation techniques of graphene directly onto silicon oxide are described. Each technique is designed to maximise the yield of flakes with different but desirable characteristics, and typical flakes produced by both methods are compared. Then, the procedures used for exfoliating hBN on plasma thinned oxide substrates are discussed. The next section reveals the wet transfer processes used to transfer flakes from silicon oxide to arbitrary substrates. Then, an alternative technique used to cleanly transfer graphene onto hBN substrates by exfoliating the graphene flakes directly on the transfer polymer is discussed. Finally, transfer procedures for CVD graphene from its growth substrate are introduced.

5.2.1 Micromechanical exfoliation procedure for graphene

Graphene single crystal flakes for this project were exfoliated as required using the micromechanical cleavage technique, where graphite layers are pulled off a bulk graphite crystal using adhesive tape, and subsequently deposited on silicon wafers coated with a thermally grown oxide layer. Two related methods were used and are described here. One promotes the exfoliation of smaller, isolated flakes (with sizes of 10 – 20 μm), with ‘clean’ edges, where it is easier to identify the crystalline orientation optically. The other produces large (with sizes of 100 – 500 μm) flakes, although they are typically irregular, and surrounded by other flakes of varying thicknesses.

100mm silicon wafers coated with oxide films with thicknesses of 90nm and 290nm, were divided into segments using the scribing and cracking process described in section 5.1.1. Generally 90 nm thick oxide was used due to the slightly higher contrast between monolayer, bilayer, and trilayer flakes under white light illumination. The segments were chosen to maximise the size of the segments and eliminate wafer offcuts whilst comfortably fitting in a standard 50ml beaker. This meant that a lower proportion of flakes exfoliated would be unviable for subsequent transfer due to their proximity to the sample edge. Exfoliation of monolayer flakes when the lowest layer of a thin graphite sheet deposited onto a substrate occurs when the adhesion between the layer and the substrate is higher than with

the other layers above it. When the tape is removed the other layers are peeled off, leaving the lowest monolayer. Thorough cleaning of the substrate is required to maximise the adhesion of the substrate. When required, silicon chips were removed from IPA, rinsed in DI water and IPA, and dried in a stream of nitrogen. They were then cleaned in a low power oxygen plasma etch, in a Moorfield etching system (power 10W), for 10 minutes. This not only removes organic contaminants by chemical reactions with the oxygen ions, but also dramatically increases the hydrophilicity of the substrate²⁹⁷. This helps to maximise the adhesion²⁹⁸ with the graphite layers, generating better coverage on the substrate and a higher chance of thin flakes. The chamber is vented using bottled nitrogen to prevent contact with air until the chamber is opened. In order to prevent hydrocarbon adsorption, the chamber is not opened until the last possible moment before graphite deposition.

While the substrates are being cleaned using oxygen etching, the graphite films are prepared. Natural graphite flakes supplied by NaturGraphit GmbH were used. Upon receipt, the crystals are cleaved using a scalpel, and the cleaved side is cleaned by repeatedly peeling off layers with adhesive tape. The tape used is BT-150E-KL (Denko Nitto), which is designed as a support tape for wafer dicing in the semiconductor industry. Large graphene flakes are obtained when there are large areas without terracing on the graphite. This can be monitored using an optical microscope. When the graphite shows large shiny areas on one side, it is repeatedly stamped onto a sheet of tape to cover a large area. A second sheet of tape is then pressed onto the graphite film and firmly pressed, before being peeled off at a low angle to cleave the film. Both films are covered with a fresh piece of tape, and set aside.

When the plasma etching of the samples is complete and the chamber has vented, these graphite films are then cleaved apart. The films now have, on average, a quarter of the thickness of the original films, but are still mostly opaque. Immediately after this final cleave, the plasma etching chamber is opened, and samples are removed one by one, and the tape covered with graphite is placed onto them, and pressed down with considerable force using the thumb using downward pressure and trying to avoid any shear force. The chamber is closed while this occurs to minimise the atmospheric contact of the remaining samples. The next step is dependent on the kind of flakes which are desired. For smaller, 'sharper' flakes, the tape is immediately peeled away from the substrate, with as small an angle between the tape and substrate as possible. Typical flakes produced using this method are shown in panel

(b) of figure 40. Samples show far less coverage of graphitic material, with isolated, small, thin graphene flakes.

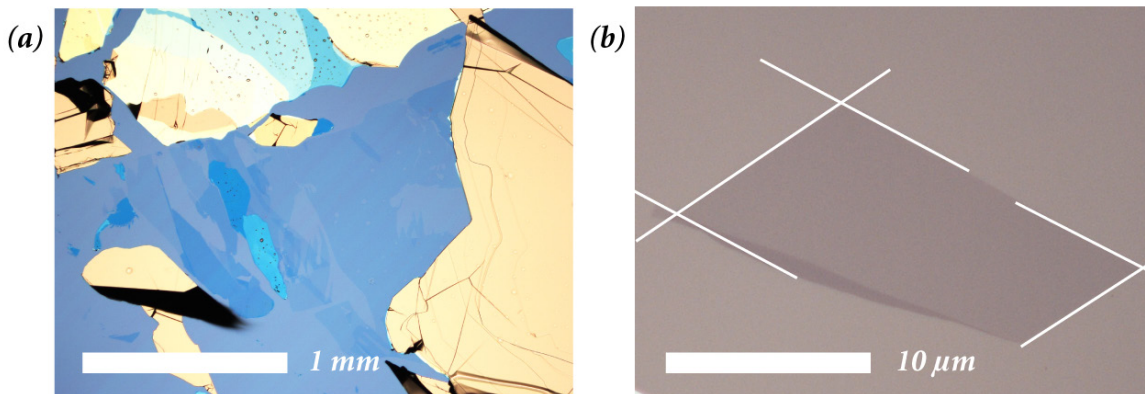


Figure 40 Optical images of thin graphene flakes on oxide coated silicon wafers produced using two micromechanical exfoliation techniques. In (a), the oxide layer is 290nm thick and in (b) it is 90nm thick. The area in (a) is characteristic of flakes produced using the tape dissolution method. Most of the thin area is monolayer graphene, with thinner purple flakes of a few nm thickness. The central thick light and dark blue flakes are of thickness of around ten nm. The white areas are bulk graphite flakes of thicknesses of tens of nm and upwards. The flake in (b) is characteristic of those produced using the direct exfoliation approach. It is isolated, and exhibits sharp edges at crystallographic directions, as indicated by the white lines. The long edge consists of three straight sections, with the central one out of alignment to the crystal axis.

For larger flakes, the sample is set aside for a minimum of two hours, to allow the tape to relax. The tape and adhesive residue are removed using *methyl isobutyl ketone* (MIBK). Several beakers of MIBK are placed on a hot plate at 85°C. A tape covered sample is immersed in one beaker. After a few minutes, the adhesive is dissolved and the tape curls up away from the substrate. Most of the graphite should remain attached to the substrate. The sample is immediately removed and left in a fresh heated beaker for 5 minutes, and then transferred to another fresh beaker for a further 5 minutes. During the transfer between beakers, the sample is not allowed to dry at any time, as any contamination which is ‘dried on’ is far harder to subsequently remove. It is then transferred to a beaker of hot IPA, which is removed from the hot plate and left to cool for 5 minutes. The sample is dried using a stream of nitrogen perpendicular to the surface. Using IPA rather than MIBK or another relatively volatile solvent, such as acetone, for the drying step means any contamination is blown off the surface, rather than left behind as the solvent evaporates. The sample is then baked on a hot plate for 10 minutes at 130 °C. This drives out any moisture and increases the adhesion of the lower graphite layers with the substrate. Excess graphite is then removed in a second

peel; high tack low strain tape is placed onto the surface, firmly pressed down, and peeled away at a low angle. After this second peel, a mixture of thin flakes and thicker, shiny graphitic material remains on the surface. Large area monolayer flakes of sizes around $500\ \mu\text{m}$ are typically seen on the substrate, though often connected to thicker areas, or surrounded by other flakes. Although straight edges are sometimes seen, it is generally far harder to optically assign them a crystalline orientation. Optical images of graphene flakes produced using this method are shown in panel (a) in figure 40. All flakes were stored in a desiccator cabinet within a class 1000 cleanroom environment until required.

5.2.2 Micromechanical exfoliation of hexagonal boron nitride

Hexagonal boron nitride flakes were exfoliated in nearly exactly the same way as the small graphene flake method outlined above. They were exfoliated from single crystal hBN flakes purchased from *HQ graphene* (www.hqgraphene.com). Silicon oxide (90nm) coated wafers were prepared as in 5.2.2, but were then etched in a RIE process (CHF_3/O_2) to thin the oxide layer down to 70nm, which provided the highest optical contrast. The surface was then cleaned in a high power oxygen etch. The 2 step etch process was carried out in an Oxford Instruments PlasmaLab 100 DRIE system.

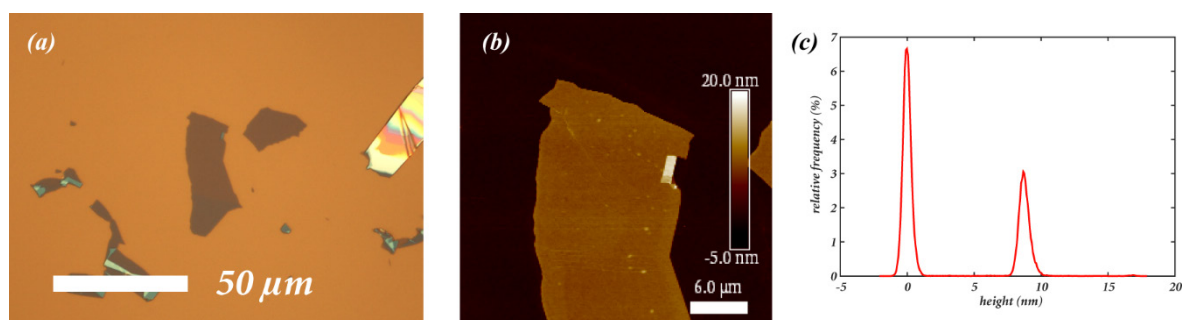


Figure 41 Optical and AFM images of a representative mechanically exfoliated hBN flake. (a) shows an optical image of the flake. The contrast is enhanced as the silicon oxide substrate has been thinned to 70nm. (b) AFM image of the upper area of the flake shown in (a). (c) height histogram of the height image shown in (b). The main peak at 0 nm is the silicon substrate, and the higher peak at 8.7 nm is the hBN flake (the third small peak is the folded area). The peak widths are similar, indicating a similar roughness for the flake and substrate in this case.

While the substrates are being prepared, a single impression of a BN crystal is taken on a piece of tape (area of approx. 1 x 1 mm) and repeatedly cleaved and spread around until a large area (approx. 2 x 2 cm) is covered. This is then covered, and pressed onto the 70nm

oxide film as soon as it has been removed from the plasma system. The tape is then pushed down with considerable force, before being peeled off very slowly, and a low angle from the substrate. This leaves a large amount of flakes of different thicknesses. Monolayers and bilayers can be clearly distinguished using an optical microscope, but are rarer and far smaller than those seen in graphene. For use as a support layer for graphene during TEM patterning (as described in section 5.9), flakes of 3-8 nm thickness are required. Flakes with thicknesses between 3 and 20 nm can be identified by their light purple colouring (comparable to 3-4 layer graphene) in optical microscopy, but must be scanned in an AFM to determine the thickness. Figure 41 shows a flake which looks suitable under optical observation but is actually slightly too thick. Flakes of thicknesses below around 20 nm share the substrate morphology (as shown in panel (c) in figure 41), and often have bubbles trapped underneath, while flakes thicker than around 30 nm typically exhibit atomically flat sections.

5.2.3 Wet transfer processes

Graphene flakes were transferred to other substrates as required using the carrier film method, as discussed in section 4.1.3.2. Flakes to be transferred were first photographed at a range of magnifications, including images of the surrounding graphitic debris. This helps when subsequently locating them on the carrier film. This method was also used to transfer graphene/ hBN stacks fabricated on silicon oxide using a dry transfer process (described in section 5.2.4) to silicon nitride membranes.

The carrier film consisted of PMMA deposited via spin coating. PMMA with a molecular weight of 950 kD dissolved in *anisole* ($CH_3OC_4H_9$) in concentrations of 3% and 8%. The film thickness was chosen depending on the location of any graphitic debris around the flake. Sometimes, this could be carefully removed using tweezers and small sections of tape, but this was not always possible. When there were large graphite chunks near the flake and a risk of the membrane being damaged, the 8% concentration was used, generating robust films of over a micron in thickness. Otherwise, thinner films were used, as they were found to adhere to the transfer substrate better, presumably due to their higher flexibility. The thin films had thicknesses of around 150 nm. Double layers were used for larger transfer membranes. Before the film deposition, the samples were baked for 5 minutes at 130 °C to dehydrate the surface. Whilst still slightly warm, the PMMA was deposited on the surface, and left for 10 seconds.

It was then spun at 3000 rpm, using an acceleration of 1000 rpm/s. It was subsequently cured on a hotplate at 130 °C for 5 minutes.

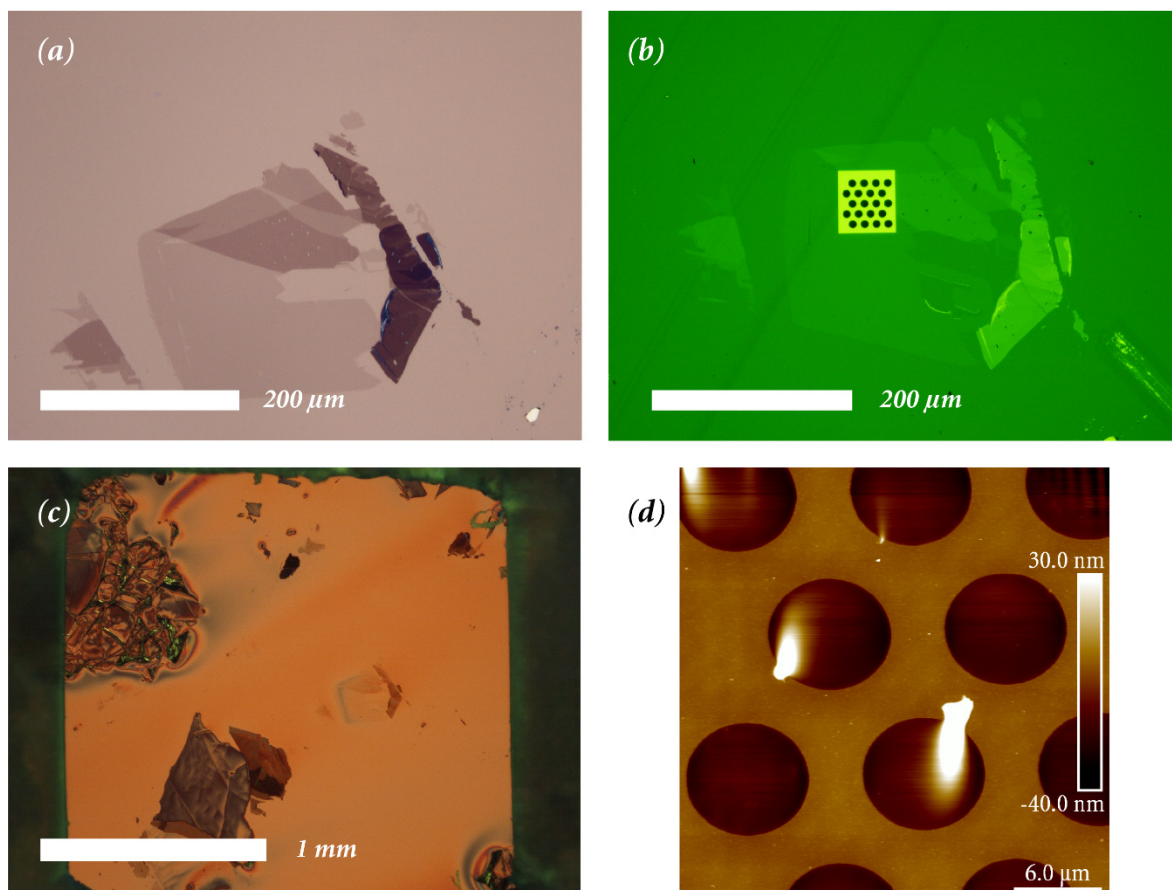


Figure 42 Optical and AFM images showing various steps in a wet transfer process. (a) shows a mechanically exfoliated graphene flake with large 1, 2 and 3 layer areas on a 90nm silicon oxide substrate. (b) shows the same flake after transfer to a silicon nitride membrane patterned with 8.8 μm diameter circular holes. (c) shows the flake after the deposition of the PMMA carrier film and attachment of the tape window, but before the removal of the oxide substrate. The flake is the area to the right of the centre. It is barely visible when the membrane is freestanding, but its position can be identified by the thicker areas of graphene surrounding it. (d) shows an AFM height image of the suspended graphene membranes shown in (b). Most membranes lie flat, but a few are distorted by particles attached around the edge of the hole.

To enable transfer of particular flakes to specified areas, tape windows consisting of a roughly 8mm square containing a few mm hole were placed over the flakes. The optical images taken earlier were used as a guide, as the thin flakes are very hard to see under the PMMA layer. The film is divided by mechanically scratching away the areas around the tape windows, so that the individual areas will float freely after the silicon oxide layer is removed. A very weak KOH solution (roughly 5 % by weight at room temperature which varied around 20 °C) is

used to etch away the oxide layer and release the film. The process takes around 6-8 hours. The substrate is immersed in the etchant solution, and once the films are detached they float freely to the surface. The tape windows are then used to pick up the areas of the PMMA membrane attached to flakes of interest. They are dipped in DI water, and then left floating flake side down in fresh DI water to remove any etch residue.

Two systems were used to mechanically position the flake on the required substrate. Originally, a SUSS MJB4 mask aligner was used to align the flake with the intended area of the substrate, and then bring the substrate and membrane into contact. For the later part of this work, a specialist graphene flake transfer system designed and built by Graphene Industries was used, incorporating both a substrate heater and rotation stage. In both cases, the membranes were removed from DI water, and dried very carefully using cleanroom wipes. They were then attached using tape stacks similar to those in figure 35 to a metal arm/plate that could be mechanically manipulated by the transfer system/mask aligner. Using the mask aligner, the position of the flake had to be inferred by the positions of thicker, more visible graphite debris. The transfer system allowed the use of narrow pass filters, as well as real time image averaging and post processing software that enabled visualisation of the flake on any substrate, or even when freestanding (as shown in panel (f) of Figure 52). It also included a heated stage, to improve the transfer adhesion. Transfers were carried out at temperatures of 65 °C when possible. Once the membrane and substrate are brought into contact, if the surface has high adhesion the membrane adheres to the substrate. Tweezers were then used to scratch around the perimeter of the membrane, separating it from the tape window. The tape window was removed, and the sample was baked at 130 °C for 10 minutes to increase the flakes adhesion to the substrate. The sample was then placed into acetone heated on a hotplate at 70 °C while still warm to remove the PMMA layer. It is then removed and dried using nitrogen. If the transfer is over holes to generate suspended graphene structures, drying in this manner causes tears of the graphene by surface tension. Instead, for small suspended structures, with diameters less than around 3 μm , they were immersed into hexane, which was then allowed to evaporate. Larger suspended structures were dried *supercritically* from acetone in a critical point dryer (CPD) system.

5.2.4 Dry transfer process

An alternative transfer method was used in order to transfer the graphene flake without exposing the underside to liquid, by exfoliating it directly onto the transfer polymer film. The motivation was to improve the cleanliness of the underside of the graphene on hexagonal boron nitride substrates^{22,225}, as discussed in section 4.1.3.2.

Here, a polymer stack consisting of an alkaline soluble polymer covered by an organic soluble transfer polymer is produced using spin coating. The lower layer is PMGI SF6 (Microchem), an alkaline soluble polymer typically used as an underlayer in a bilayer resist for liftoff processing, as described in section 4.2.2. It was deposited on bare silicon wafers (company info, resistivity) segmented following the process in 5.1.1. The substrates were removed from IPA and rinsed in DI water and IPA, before being dried using a stream of nitrogen and baked on a hotplate at 180 °C for at least 5 minutes. After it has cooled, it is spin coated in PMGI SF6 with a spin speed of 4000 rpm, with an acceleration of 1000 rpm/s. This layer is cured at 170 °C for 5 minutes. It is subsequently coated with PMMA (950 kD, 8% in anisole). This is pipetted onto the sample, and after 10 seconds spun at 6000 rpm, with an acceleration of 1000 rpm/s. It is then cured on a hotplate at 130 °C for 5 minutes. This leads to a PMGI thickness of approximately 280 nm, and a PMMA thickness of approximately 900nm.

Flakes are then exfoliated directly onto the PMMA surface. Graphite films are deposited on tape from natural graphite crystals using the method described in section 5.2.1. The tape is then pressed graphite side down onto the PMMA surface, and firmly pressed. The tape is then peeled away at a low angle from the substrate, leaving a variety of flakes of different thicknesses. The yield of monolayer flakes is much lower than on silicon oxide. Finding and identifying thin flakes is far more challenging than on silicon oxide, but possible through the use of narrow pass optical filters. Images of a flake exfoliated on the PMMA surface are shown in figure 44. The filter that gives the highest contrast varies over the sample as the film thickness changes slightly, meaning that scanning the sample whilst changing filters is necessary. It is much harder to unambiguously identify monolayer flakes.

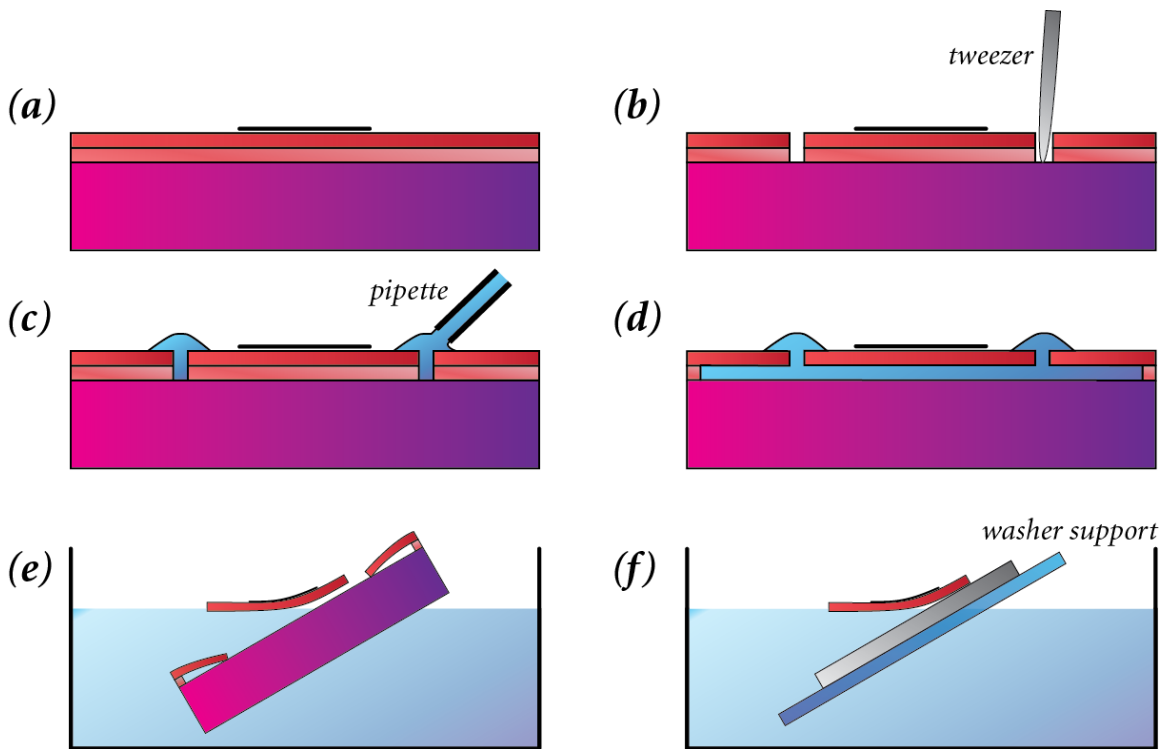


Figure 43 Schematic illustrating the dry transfer process. (a) shows a graphene flake on a dual layer polymer film, on a silicon wafer. In (b) a scratch has been made around the flake using tweezers to allow the alkaline developer solution to reach the underlayer. (c) The TMAH solution is pipetted around the scratch. (d) The TMAH dissolves the alkaline soluble PMGI layer, leaving a free floating PMMA membrane. (e) The sample is lowered into a container of DI water, leaving the PMMA membrane floating on the surface. (f) The PMMA membrane is carefully picked up using a PMMA coated washer supported by a tape window.

The whole membrane preparation process for dry transferred flakes is shown in figure 43. Once a desired flake has been identified, a circular scratch is made around the flake using tweezers, using the field of view of an optical microscope with a 5x objective as a guide. This leads to a circle with a diameter of around 3.5 mm, with the flake of interest at the centre. Alkaline TMAH solution (MicroPosit MF319 Developer, Rohm-Haas) is then pipetted around the scratch, whilst taking care to keep it away from the flake at all times. The TMAH dissolves the PMGI layer, gradually detaching the PMMA membrane from the subject. This process is monitored using optical microscopy, and more TMAH solution is added as required. Once the membrane is detached completely from the substrate, the silicon is lowered gently into a dish of DI water. It sinks to the bottom, leaving the small PMMA membrane floating on top, with the flake on top of it. To be able to manually handle it, the membrane needs to be attached to a support structure. Small metal washers with internal diameters of around 2mm are coated in PMMA (950 kD, 3% in anisole) by immersion and subsequent baking on a cleanroom wipe on a hot plate at 150°C for a few minutes to increase

their adhesion with the PMMA membrane. One side is affixed to a tape window, which makes it easier to handle and attach to the transfer systems using tape. This washer is then brought up from under the water surface to pick up the membrane. Excess water is removed very carefully using the corner of a cleanroom wipe. The membrane is then transferred onto the required substrate, typically thin hBN on silicon oxide, in the same manner as the tape window in the wet transfer process as described in the previous section.

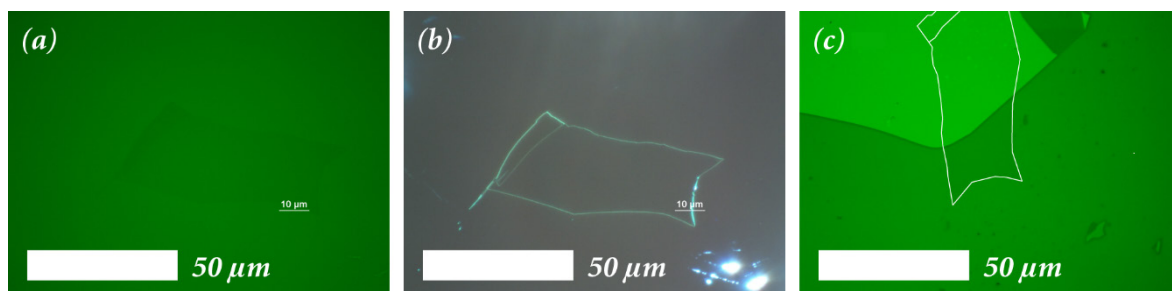


Figure 44 Optical images showing the dry transfer process. (a) shows a large monolayer graphene flake exfoliated on the bilayer polymer film, using a green narrow band filter to aid visualisation of the flake. (b) shows a dark field image of the same area. (c) shows the flake transferred onto a thick, atomically flat hBN flake on silicon oxide. A green narrow pass filter has again been used to help visualise the flake on top of the hBN. The outline has been traced to guide the eye. Bubbles are clearly visible between the two flakes even though they are both freshly exfoliated and have never been in contact with any material.

5.2.5 CVD transfer process

CVD graphene grown on copper foils (provided by Bluestone Global Technologies) was used in this work. CVD growth was not a part of this work, and is not discussed here, but the optimised transfer process used in this work is described. As the graphene is grown on both sides of the copper foil, it first needs to be removed from one side before the copper can be etched away. The foil is carefully cut to the required size using sharp scissors, and then one side is coated with PMMA to act as both a protection layer during the back side graphene removal and subsequently as a carrier film for transfer. To prevent the foil bending, a thin PET film is punctured a few times, and then placed over the vacuum chuck on the spin coater. The copper foil is then placed over the plastic film, and the vacuum is switched on. The film prevents the area around the vacuum hole from being deformed too much, which makes it harder to spin a good film, and can damage the graphene.

PMMA (950 kD, 8% in anisole) was pipetted onto the copper, left to settle for 10 seconds, and spun at 2000 rpm with a ramp of 1000 rpm/s. This results in a film thickness of approximately $1.3 \mu\text{m}$. The copper is then pressed flat between two thin PET sheets, and baked at $130 \text{ }^\circ\text{C}$ to cure the PMMA. The sample was then placed, PMMA coated side down in a Moorfield plasma etching system, using a 2:1 Ar:O₂ ratio at around 10^{-2} mbar and providing 10 W of RF power. The graphene layer on the back side was removed during a 60 second plasma etch. The sample is then removed, and floated on the surface of the copper etchant, with the graphene and PMMA film remaining dry on the upper surface. The etching solution is 35 mg/ml APS in water, and the process was left to proceed overnight.

After the etching process, the PMMA supported graphene film is repeatedly transferred to fresh containers of DI water and left to soak to wash away as much APS as possible. This is achieved by fishing it out by bringing up a silicon wafer underneath it, but not allowing it to dry. The graphene/PMMA film can be made easier to see by shining a desk lamp onto the surface of the water. Then, the film is transferred to the (freshly plasma cleaned) substrate of interest by submerging it and slowly bringing it up under the film, going diagonally from corner to corner. Excess moisture is then very carefully wicked away using the corner of a cleanroom wipe. The sample is then left to dry for around an hour, at a slight angle to the horizontal. The remaining moisture is removed by baking the sample on a hot plate at $130 \text{ }^\circ\text{C}$ for 10 minutes. Before removing the PMMA, a second layer is spun on and cured in the same manner as the first. This relaxes the PMMA membrane, and reduces wrinkles and tears in the CVD film after resist removal, as discussed in section 4.1.3.1. The sample is dropped into cool acetone while still warm, and subsequently transferred to a lidded acetone beaker on a hotplate at $60 \text{ }^\circ\text{C}$. The sample is stirred for a few seconds every 5 minutes using a stirrer bar, before being removed after 30 minutes, rinsed in fresh, hot acetone, and left in a heated IPA beaker that is allowed to cool for 5 minutes. The sample is then dried using a nitrogen stream parallel to the surface, and dehydrated by baking on a hot plate at $130 \text{ }^\circ\text{C}$ for 5 minutes. It would then be stored in a desiccator cabinet in a class 1000 clean room environment for storage prior to further processing.

5.2.6 Graphene annealing procedure

After graphene transfer and patterning, most resist was removed using organic solvents, as described in section 5.2.3. For samples where cleanliness was particularly important, the solvent cleaning process was extended, with long soaks in successive beakers of heated acetone with occasional agitation. Following drying, the samples are then annealed in a reducing atmosphere to further reduce the amount of surface contamination. The annealing procedures are outlined in table 3. The maximum temperature used was the highest found to not degrade the electronic quality of graphene devices annealed for prolonged temperatures using the specific furnace. A tube furnace was used, with alumina ceramic furnace tubes surrounded by a heating coil. Separate tubes were used for samples with different levels of contamination: there was one tube for polymer removal from graphene/hBN flakes, one for CVD sheets with may show exhibit metal contamination from the growth substrate, one for other 2D materials and one for liquid phase exfoliated graphene.

Table 3 Annealing procedures for removing polymer (typically PMMA) residue from graphene sheets after transfer and patterning procedures. The atmosphere is 10% hydrogen with argon as a carrier gas. The final step provides no power to the heater and simply allows the furnace to cool at its natural rate. The maximum temperature of 280°C is the maximum found not to degrade the electronic behaviour of graphene devices after prolonged exposure.

Step	Rate/Time
Ramp to 100°C	5°C/min
Hold at 100°C	1 hour
Ramp to 200°C	5°C/min
Hold at 200°C	2 hours
Ramp to 280°C	2.5°C/min
Hold at 280°C	3+ hours
Cool to 30°C	*System limited – Takes approx. 3 hours

5.3 Selective patterning of graphene

Large scale graphene patterning was achieved using a 3-layer resist process which achieves a far higher level of cleanliness than typical photolithography procedures. A PMMA underlayer is used to prevent the graphene from coming into contact with photoresist at any time, as it is far harder to remove than PMMA. The bilayer photoresist on top acts as an etch mask in a low power oxygen etching process, where the uncovered PMMA layer and the graphene underneath are simultaneously removed. The thickness of the protective layer needs to be as low as possible to enable it to be etched through in as short a time as possible, minimizing any photoresist crosslinking on the top. The layers are then removed sequentially to prevent the photoresist from ever coming to contact with the graphene, even in solution.

The sample was spin coated first with a very thin layer of PMMA to act as a protective layer for the graphene. The solution was 1.5% in anisole, the PMMA molecular weight was 950kD, and it was spun at 7000rpm with a spin-up speed of 1000rpm/s. This results in a film thickness of approximately 40nm. The PMMA was cured on a hotplate at 130 °C for 5 minutes. The next layer was the alkaline soluble MicroChem PMGI SF6 (Rohm Haas) resist spun at 6000rpm with a spin-up speed of 1000rpm/s, and subsequently cured at 160 °C for 5 minutes. The top layer was MicroChem Shipley S1805 (Rohm-Haas) photoresist, again spun at 6000rpm with a spin-up speed of 1000rpm/s, and cured at 110 °C for 1 minute. The resist is then selectively exposed in a maskless optical lithography process, with the radiation dose optimized to give good feature reproduction after 30s development. After being immersed and gently wafted in TMAH developer solution (MicroPosit MF319 Developer solution from Rohm-Haas) for 25 seconds, the wafers were visually inspected in an optical microscope using a red narrow pass filter so as not to expose the resist further. If required, the sample was immersed in developer for a further 5 seconds and reinspected until adequate development was reached. At this point, the sample would be hard baked on a hot plate at 150 °C for 5 minutes.

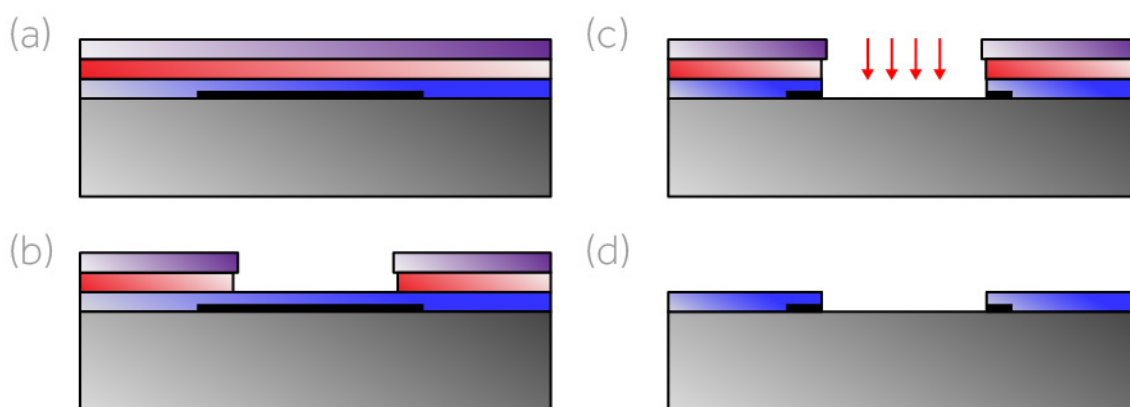


Figure 45 Schematic illustrating the 3-layer resist technique for clean patterning of graphene flakes. (a) The substrate is sequentially spin coated with PMMA, PMGI, and then S1805 (b) after selective exposure and development, the exposed areas of S1805 are washed away as well as the PMGI that was formerly protected (c) Oxygen plasma etching is used to burn through the PMMA and the graphene in unprotected areas (d) The layers are removed sequentially allowing the clean removal of the protective PMMA layer.

After the top photoresist layers have been patterned, the uncovered PMMA areas and the graphene underneath are etched using low power oxygen plasma etching in a Moorfield etching system. 2 minutes is sufficient to remove the thin PMMA film and a graphene layer underneath. An extra 30s is added to the etch time for subsequent layers. With care, the remaining resist layers can be removed one by one; holding the substrate under a stream of acetone for ~10s removes the majority of the top S1805 layer, before the sample is immersed in DI water to prevent the PMMA under-layer from being attacked by the acetone. Leaving the sample in alkaline developer (TMAH, MicroPosit MF319) for a minute removes the PMGI layer, lifting off any remaining S1805 photoresist. Then only the thin protective layer remains, which can then be cleanly removed in a solvent bath (containing a minimum of photoresist residue) as described in the previous section. After annealing as described in section 5.2.6, atomic force microscopy of graphene on silicon dioxide patterned in this way shows residual contamination around the edges, but no measurable amount of residue in the central areas.

5.4 Optimised TEM sample fabrication procedure

TEM sample holders are designed to hold 3mm circular samples. Originally, these were cut from silicon nitride wafers using an abrasive slurry disc cutter, from South Bay Technology (model 360). It is impossible to perform lithography on the sample after it has been reduced to the 3mm disc, as it is impossible to obtain a resist coating for lithography, the nitride layer on one side is destroyed by the slurry, and it becomes very difficult to keep the sample flat when exposing. It was therefore necessary to cut the sample after the silicon nitride membrane had been both fabricated and patterned.

The samples, after fabrication as described in section 5.1, were coated in very thick photoresist films on both sides, by repeatedly spin coating and baking. Films varied in composition but were at least $2\mu\text{m}$ thick. The sample was then affixed to the drill stage using the mildly tacky adhesive strip from a post-it note which was affixed to the stage with double sided tape. The sample is placed with the membrane side facing up. The cutting tool is aligned with the nitride membrane by eye. A circular guide was etched into the nitride layer during the membrane patterning step to help identify the correct location. The tool is a 30mm diameter tube with a flat end, and a notch cut out to help 'pick up' the cutting particles. It is pictured, along with the rotary cutter, in figure 46. The slurry was abrasive SiC powder with an average particle size of $30\mu\text{m}$, mixed with glycerine. A small amount was pipetted over the membrane and the cutting tool was lowered. It rotated at a speed of 60 rpm, with an adjustable downward force. The force was adjusted manually by listening to the grinding noise and adjusting to make it as loud as possible. Too high a force and the cutting fluid is forced out from between the tool and the cutting surface, reducing the abrasiveness. The process was stopped when an electrical connection was measured between the cutting tool and substrate using a multimeter. The process took 2-8 hours. The discs were rinsed in water, and then acetone, and then soaked in NMP heated to 60°C in a hotplate for one hour while being stirred. They were then rinsed again in acetone, DI water, and IPA, and dried using a nitrogen gun. Prior to flake transfer, they were cleaned using a low power oxygen etch for 10 minutes (using the etching system described in section 5.2.1) to remove any remaining organic contamination, and increase the surface adhesion when transferring 2D materials on top.

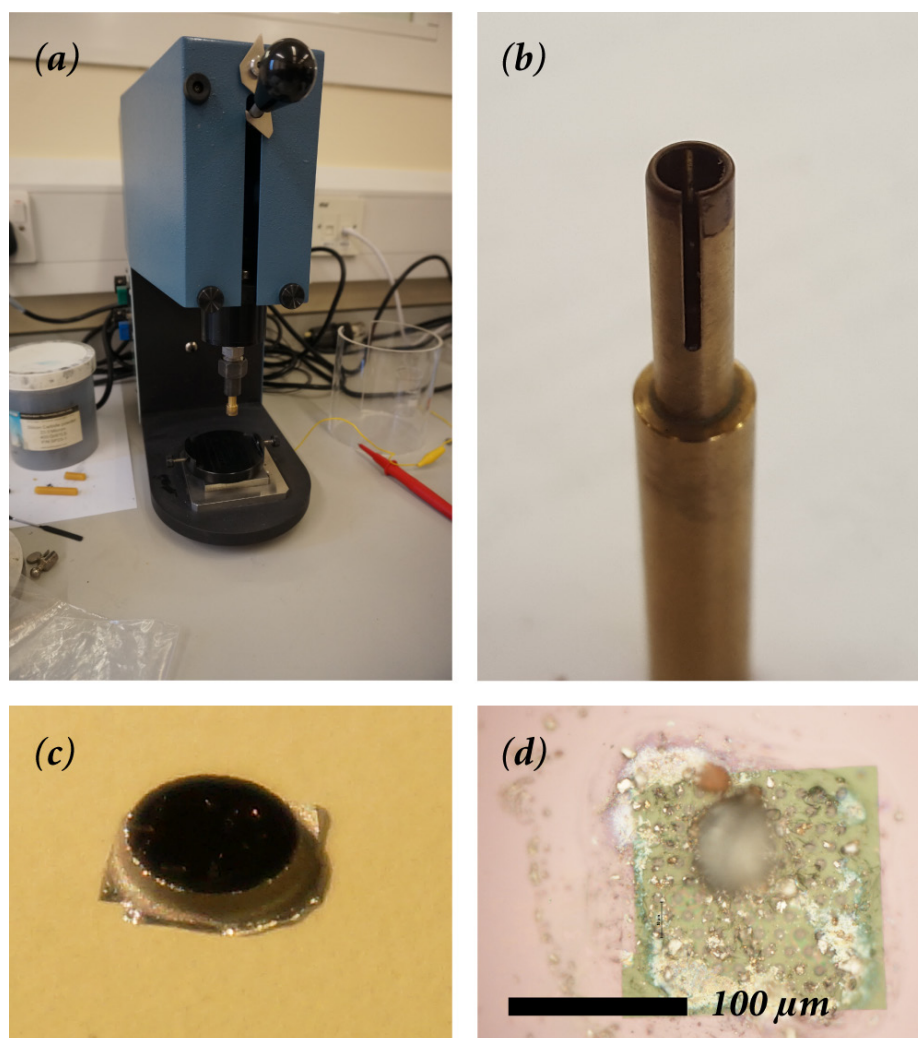


Figure 46 Old method of segmenting wafers into TEM compatible samples. (a) the rotary cutter used to grind out the 3 mm discs. (b) The cutting tool. The notch promotes the pickup of cutting fluid. (c) A grid manufactured using the grinding process. The flaggy edges on the bottom side are typically seen and often make it difficult to fit in TEM holders, at least in the preferential orientation. (d) A perforated membrane contaminated by an agglomeration of cutting slurry after photoresist removal.

In practice, many samples were destroyed or irreparably contaminated during the cutting process. SiC particles often got stuck to the patterned membrane areas, and many membranes were broken. Also, many discs were unable to fit properly in TEM sample holders due to irregular jagged edges on one side. Images of a contaminated grid, the cutting tool, and the jagged edges are pictured in figure 46. In addition, the relatively rough surface of the nitride film (typical RMS roughness is around 1 nm) caused problems when trying to transfer flakes. Often the PMMA membrane would not stick to the nitride layer even when it was heated and in contact. Perpendicular air flow and/ or tweezers could be used to ‘push’ the PMMA down onto the substrate but often caused large lateral shifts, drastically reducing the transfer positioning accuracy.

A new method of patterning the silicon nitride membrane structures was developed using bulk KOH etching to define weak points in the sample during the membrane fabrication step. The wafer can then be cleanly snapped into individual 3mm samples after further processing steps and 2D material transfer. The procedure is outlined in figure 48. Patterning the etch mask in this grid pattern generates a series of 12 sided discs²⁹⁹, connected to 4 adjacent discs by a thin silicon section. The KOH etch mask dimensions are given in figure 47, along with the approximate dimensions of individual grids after the etching process. The main source of variation in the grid size is misalignment between the crystal axis and that of the etch mask, often caused by wafer flat misalignments as described in figure 47.

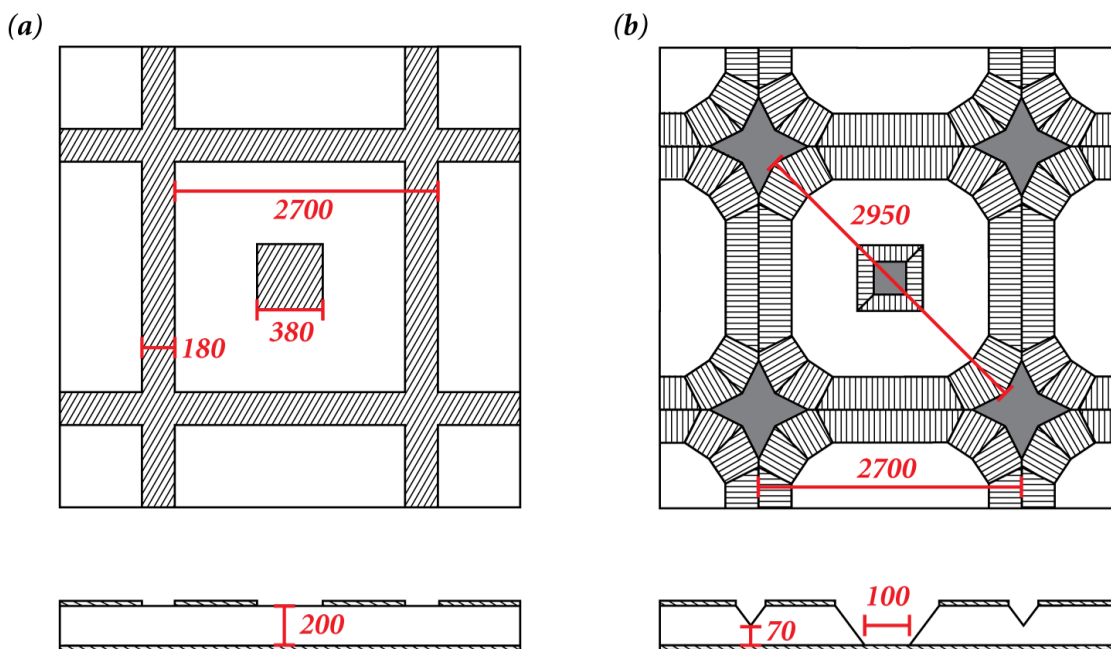


Figure 47 Etch mask and produced structure dimensions in the improved TEM sample fabrication process. (a) shows the etch mask dimensions as exposed by the Laserwriter. The actual etch mask dimensions will vary slightly with development procedures. (b) shows the typical dimensions of the generated structure. These can vary (especially the corner to corner distance) due to crystalline imperfections in the silicon and misrotation between the silicon crystalline axis and the vertical and horizontal directions of the etch mask. Top down and side on views are included.

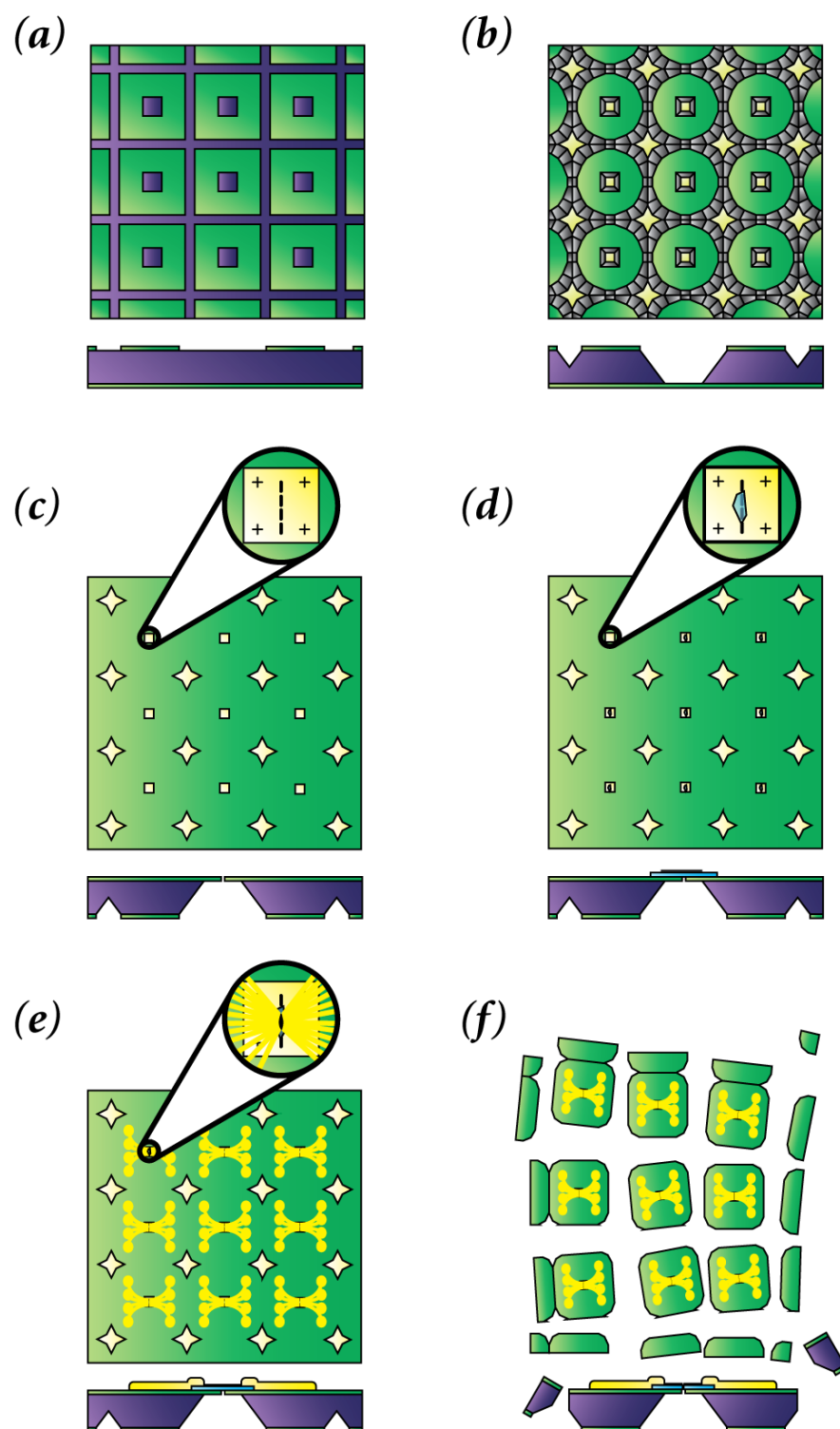


Figure 48 Series of diagrams showing the steps in the improved TEM sample fabrication process using a top down view of the sample array, and a side view of an individual sample in the array. (a) The nitride layer on one side of the wafer is patterned into a etch mask for the KOH silicon etch using photolithography and DRIE etching. (b) After the KOH etch, the wafer has trenches spanning its length, although the silicon is thick enough that it is mechanically stable. (c) The nitride membranes are patterned using subsequent photolithography and DRIE etching from the other side. This method enables processing steps such as (d) flake transfer and (e) photolithography, evaporation and liftoff to define metal contacts. This was impossible using the previous fabrication technique. (f) The samples can then be cleanly snapped into 3mm TEM compatible segments.

This production method motivated the switch to thinner wafers to enable more efficient patterning of wafers into TEM compatible samples. These were 200 μm thick (100) oriented silicon wafers coated in a 100 nm film of low stress silicon nitride grown in a low pressure CVD process. They were purchased from Structure Probe Inc. (www.2spi.com). They were segmented, patterned, and etched according to the process described in section 5.1. The KOH etch mask is shown in figure 47. Generally, arrays were patterned with a space in the central area (as shown in figure 49) where there are no membrane structures so that the sample can be spin coated safely (for the membrane patterning step) using a vacuum chuck. This process enables the spinning of resist layers, and thus subsequent patterning steps on the sample array after transfer of 2D materials, whilst maintaining TEM compatibility. This could be used, for example, to make electrical contacts to 2D materials, or pattern them into desired shapes. After the final processing step, they could be cleanly snapped out along the pre-etched trenches to use in a TEM.

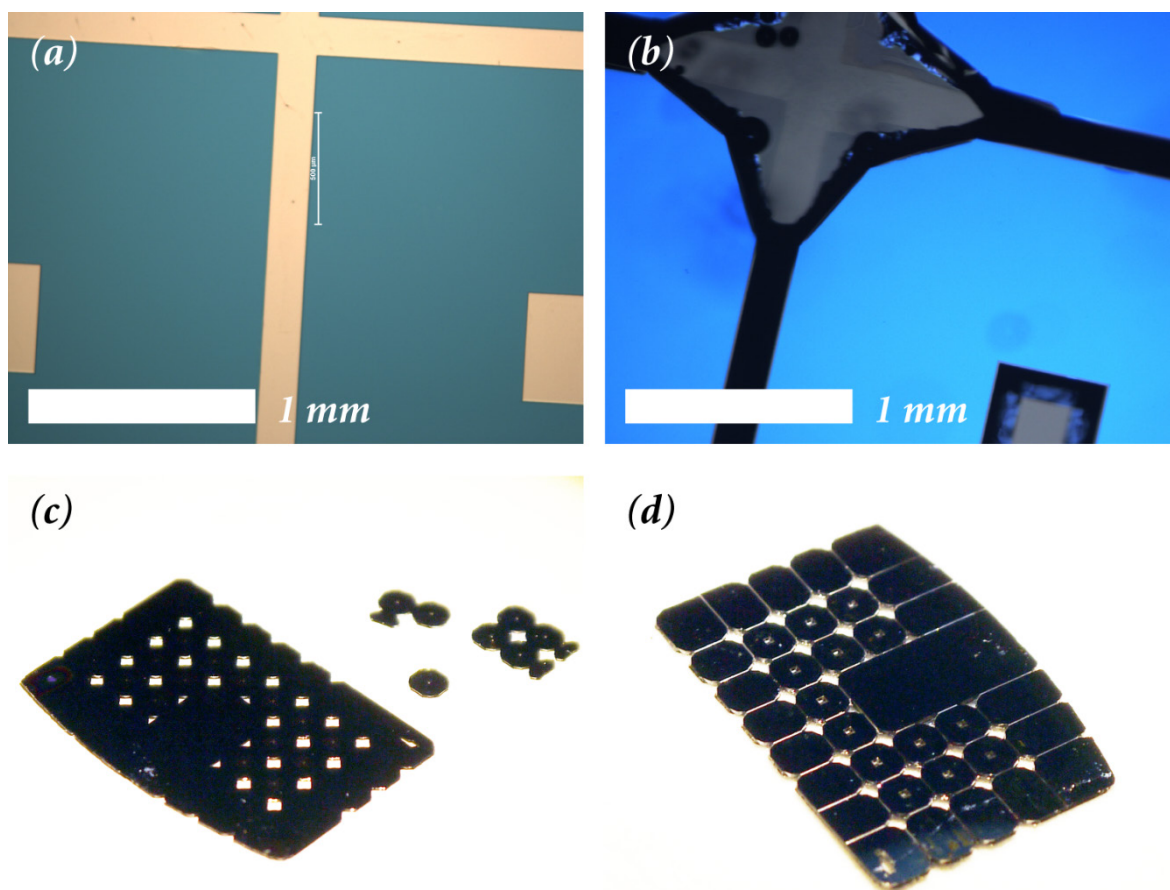


Figure 49 New method of fabricating TEM samples. (a) shows the silicon nitride (in blue) etch mask before the KOH etch. (b) shows the same sample during etching (hence the visible bubbles). The silvery silicon has been almost completely removed. The corners of the original square nitride membrane are still just visible – they are broken during the drying process. (c) and (d) show an example of a wafer of grids fabricated using this method from the front and back side respectively.

The low stress silicon nitride membranes on the new wafers were far flatter than previously. They exhibit typical RMS roughness values of 0.3 nm or lower. This means that they are remarkably easy to transfer 2D materials to, with the PMMA membrane being ‘pulled down’ onto the surface as soon as the central point (ideally where the flake is) makes contact. This improves the positional accuracy of the transfer process from $\sim 20 \mu\text{m}$ of uncertainty to $\sim 5 \mu\text{m}$.

5.5 EELS spectra; fitting and quantification

EELS spectra were processed using a combination of Gatan Digital Micrograph, and the open source Hyperspy python package³⁰⁰. In most cases, measured spectra were fit to a model EELS spectra^{186,187} using Hyperspy, which is dependent on the microscope as well as the sample. This requires spectra with a high signal to noise ratio. Often, these were integrated spectra, where all point like spectra along a line map are summed. If analysis of individual spectra was required, principal component analysis³⁰¹ (PCA) was used to reconstruct a signal, which could then be fit. However this method tends to fail in regions where there is a very small peak relative to the noise level³⁰², and tended to generate spurious peaks from the noise if no expected components were found in a particular region of a spectral image, so was not used when, for example, mapping areas where the background spectra differed remarkably. Before fitting using a least squares technique, the energy axis of each spectra is calibrated using a subpixel fit to the zero loss peak in the low-loss spectra. Where required, plural scattering effects were minimised by operating a Fourier-ratio deconvolution³⁰³ with the low loss spectra, after power law background removal³⁰⁴.

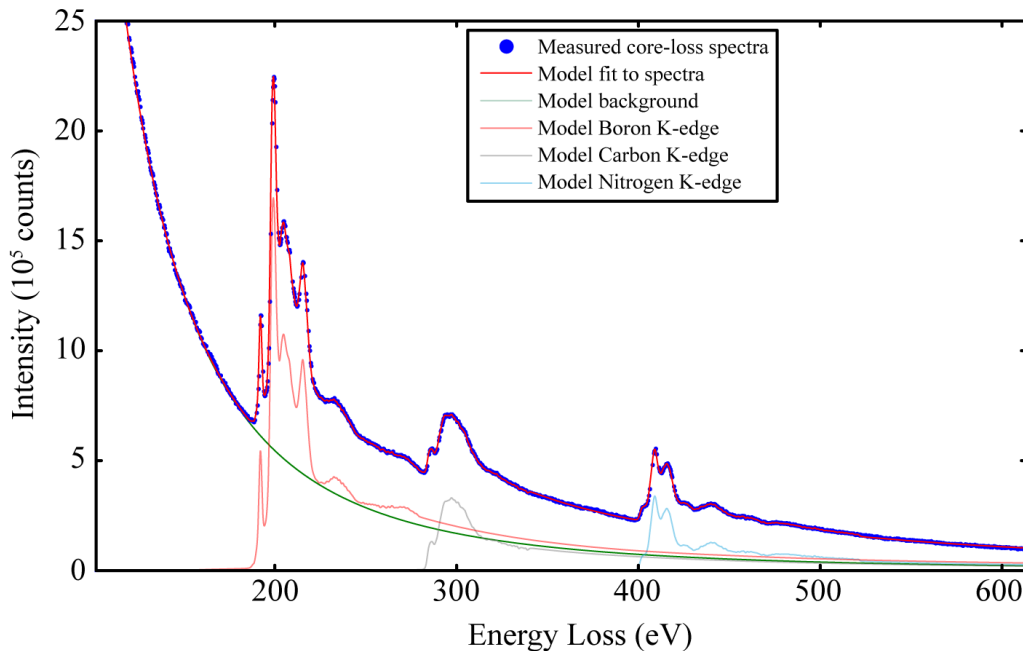


Figure 50 Least squares fitting of EELS spectra using Hyperspy. The blue dots show an integrated core-loss EELS spectrum of a monolayer graphene flake on thin (6.5 nm) hexagonal boron nitride. The core-loss edges for Boron (188 eV), Carbon (284 eV) and Nitrogen (401 eV) are clearly visible. The fit model used for elemental quantification is also shown, along with its individual components.

Core loss spectra were fit to a model combining a power law background¹⁸², and a group of individual edge models corresponding to user defined elemental species, each with their own power law background representing plural scattering effects. A model fit to an experimentally obtained EELS spectra is shown in figure 50, showing its individual components. Elemental quantification was carried out by normalising the extracted edge intensities by the (acceleration energy and spectrometer angle dependent) Hartree-Slater cross sections contained within Digital Micrograph's database.

5.6 Mechanical measurements on graphene membranes – 1st paper

Graphene membranes were manufactured for mechanical measurements by transferring thin graphene flakes onto patterned silicon nitride membranes. The membranes were fabricated according to the process outlined in section 5.1 for the ‘thick’ wafers. This generated 500 nm thick silicon nitride membranes which were rigid at the forces applied to the graphene membranes. This was verified by comparing force curves taken on the membrane to those on the silicon supported area. Graphene flakes were exfoliated on silicon oxide (see section 5.2.1) and then transferred over the membranes using a wet transfer process (see section 5.2.3), before being dried in a CPD system. The transfer process steps and resulting membrane are pictured in figure 42. Membrane sizes between 2 – 10 μm were fabricated, but the majority of measurements were performed on 3 μm diameter membranes.

Measurements were carried out on a Bruker Dimension Icon AFM, using PeakForce Quantitative Nanomechanical Mapping (QNM) mode, with PeakForce Capture enabling the saving of a representative force curve for every pixel in the image. These were compared to conventional nanoindentation and force volume measurements. Then, using the technique described in section 3.4.2.2, the central force deformation behaviour was fit to equation (15) to enable the extraction of the elastic properties of thin graphene sheets.

All AFM tips used were sold by Bruker (www.BrukerAFMProbes.com). For low force mapping, at forces up to 100 nN, ScanAsyst-Air tips were used. These use a triangular silicon nitride cantilever, and have a rated force constant of 0.4 N/m. At higher forces, TESPA tips were used. These use a silicon rectangular cantilever and have a rated force constant of 42 N/m. They have a reflective aluminium coating on the back of the cantilever to increase the reflectivity. To try and probe the failure properties of the membranes, TESPd tips were used. These are similar to TESPA but lack the reflective coating and are coated in a 10nm thick diamond like carbon (DLC) film. Before use, they were coated in a 30nm Cr layer on the back of the cantilever to increase the cantilever reflectivity. At intermediate forces, TAP150A tips were sometimes used. These consist of a rectangular silicon cantilever, have a rated stiffness of 5N/m, and also have a reflective aluminium coating. To calibrate the deflection

sensitivity (see section 4.3.2), after the tips were loaded they were ramped on a sapphire crystal to a setpoint corresponding to 10nm of cantilever bend. The gradient of the obtained force curve (in V) was then assumed to be entirely due to the cantilever bend, specifying the deflection sensitivity. Force constants were obtained using the thermal noise method for the ScanAsyst-Air tips, and using Sader's method (and a thermal noise spectrum) for the other rectangular silicon cantilevers.

Custom scripts were developed to import force displacement data into Matlab, calling functions from the NSMatlabUtilities utility provided by Bruker to access the proprietary file format. This allowed simultaneous processing of all force curves in an image, rather than being exported pixel by pixel. The membrane force displacement data was then extracted from the force curves, and fit to equation (15). The dominant source of error in the measurements was the determination of the zero displacement point (ZDP). Various algorithmic methods were trialed, including those described in references^{75,305} and leaving it as a free parameter with the full retract curve, including the adhesive part. Due to the level of noise at low forces, it was not possible to come up with a single fitting algorithm which could be used to specify the ZDP in all cases. In this case fits with differing possible ZDPs were visually inspected to choose the most appropriate. This led to a large estimated experimental error on the measured 2D modulus, and a larger one on any pretension, as the linear coefficient is more sensitive to the ZDP moving than the cubic one. Experimental errors on the measured pretension values exceeded that of the measured pretensions. Previously reported pretension values for membranes fabricated in this way^{70,306} have been low but should have been measurable in this case. This difference may be down to the larger relative size of the membranes (and therefore less effect from sidewall adhesion as described in), or fabrication or flake transfer differences. In particular, in the mentioned cases the flakes have been exfoliated directly over drums whereas here they have been transferred, which induces extra compressive strain in the flake³⁰⁷.

5.8 Selectively graphene coating SOI ring resonator waveguides – 2nd paper

The silicon on insulator (SOI) ring resonators used in chapter 7 were coated in CVD graphene following the process outlined in section 5.2.5, which was subsequently patterned using the process outlined in section 5.3. A relatively thin strip of CVD graphene ($\sim 5\text{ mm}$) was used to avoid depositing it over the surface gratings used to couple light into the waveguide. Optical images of the waveguides before and after graphene coating and patterning are shown in figure 51. It was not possible to cover the entire ring cavities, as it was imperative to leave the input-pass waveguide free of graphene, and the coupling gap was only 300nm wide. Over a centimetre scale wafer with few sharp marks on the surface to align to, this level of alignment accuracy is impossible in optical systems. After optical measurements, AFM was used to confirm the graphene layer is continuous and flat to the waveguide surface around the ring.

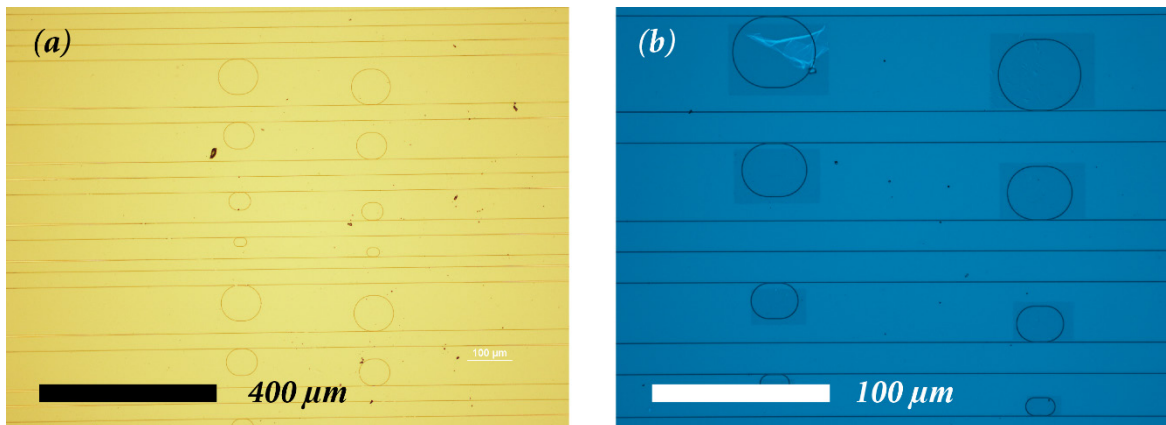


Figure 51 Optical images of SOI ring resonators before and after selective patterning with CVD graphene. (a) shows a white light image of the ring resonators before graphene transfer. (b) shows squares of CVD graphene over the ring optical cavities. The image has been enhanced using postprocessing and averaging to enhance the visibility of the graphene areas. The upper left square is contaminated with a sheet of crosslinked resist. Tears are also clearly visible in the upper right area.

5.7 Fabrication of large area suspended tBLG – 3rd paper

Aligned transfer of graphene^{220,225} typically uses small flakes of sizes up to around 10 μm . This is not only because small flakes are produced in much greater numbers than larger flakes during micromechanical exfoliation, but that they are more likely to exhibit straight edges at crystallographic angles, and it is therefore more likely that the crystal orientation can be ascertained by optical inspection.

To maximise the signal to noise ratio in the Raman measurement, a suspended tBLG sample was necessary to enable measurement of Raman spectra using a transmission geometry. To reduce background information, the membranes had to be as large as possible compared to the laser spot size. Flakes transferred over holes often tend to scroll or crack when drying if there is not a large area of membrane supported graphene around the holes. Although the transfer alignment described in section 5.2.3 is accurate to $\sim 0.5^\circ$, there is a lateral positioning error of a few μm . As two transfers are required, and the hole needs to be relatively large (at least 8 μm diameter), this makes small flakes unsuitable for this process.

It was therefore necessary to identify the crystal axis of large flakes, with ‘flaggy’ edges. Monolayer flakes of this size very rarely show sharp edges. However, large flakes containing many areas with different layer numbers would occasionally be identifiable as having many parallel edges or particularly long straight terraces, where the ‘upper’ flake shows edges with crystallographic orientation. Two such flakes are shown in panels (a), (b) and (c) in figure 52, with the crystalline edges marked. AFM imaging was also often able to determine the directions of flakes which seem to have flaggy edges at the large scale, but have straight edges at 30° orientations at smaller scales, as shown in figure 53.

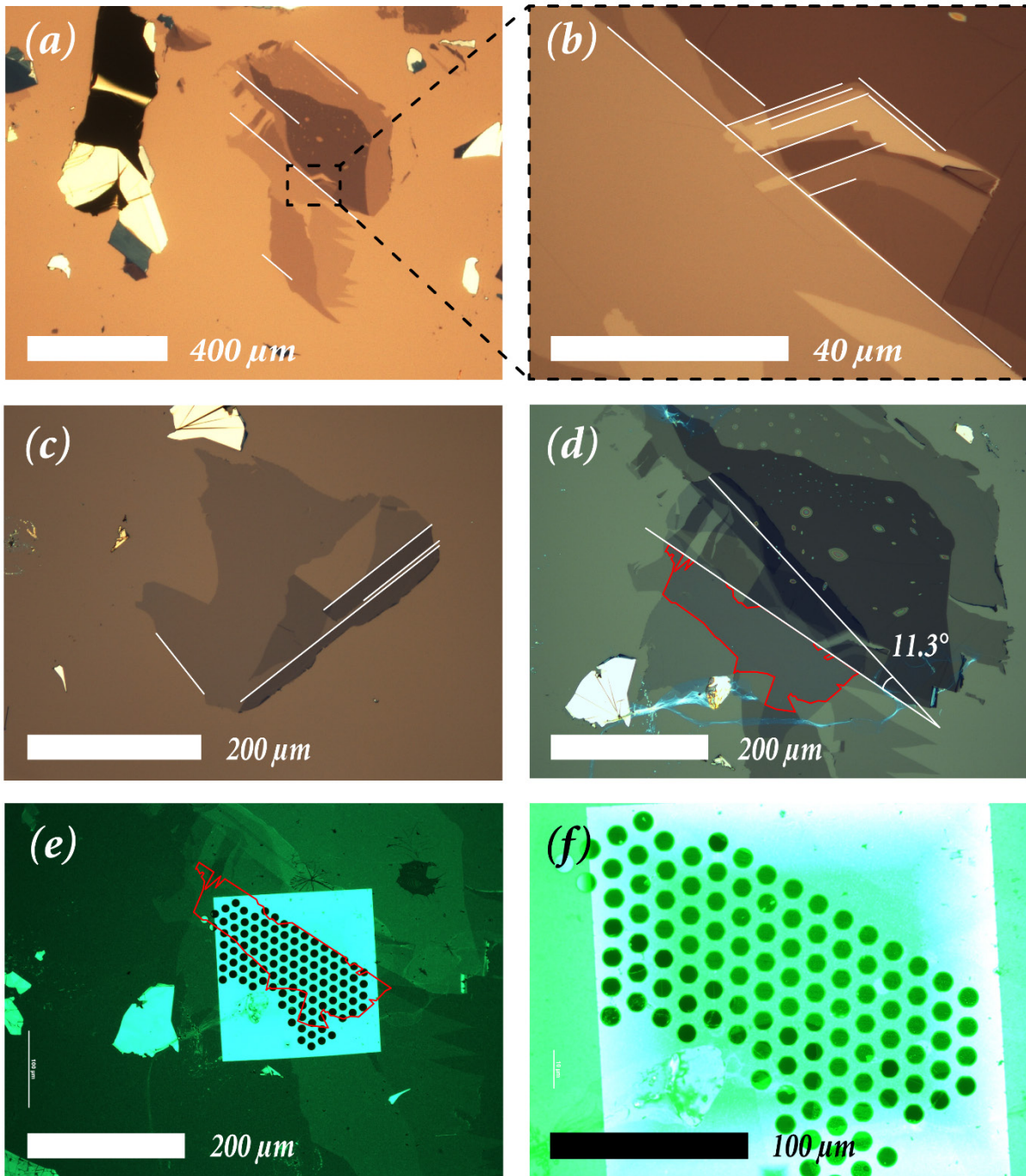


Figure 52 Sequence of optical images showing stages in the tBLG suspended membrane fabrication process. (a) shows a large flake, with an abundance of parallel straight edges in the indicated direction. (b) shows a zoomed in region of the flake in (a), showing a series of parallel edges at a 30° angle to the original set. (c) shows a second graphene flake, with presumed crystallographic edges marked. (d) shows the flake from panel (c) stacked on top of the flake from panel (a), with an 11.3° misalignment between the assigned crystal directions. The area bounded in red is the tBLG area, surrounded by monolayer graphene and thicker material. (e) shows the flake after transfer to the specially designed membrane. A green low pass filter is used to aid visibility. The tBLG area from panel (d) is again shown. (f) shows the suspended graphene under high illumination with green light. The lighter tBLG area is visible compared to the darker monolayer areas.

Once identified as likely candidates for crystal axis orientation, tBLG samples were fabricated by transferring one on top of the other in a wet transfer process (as described in section 5.2.3), with a $\theta \approx 11.5^\circ$ misalignment between the two identified axes. As we were not able to identify the nature of the edges (zigzag or armchair), this resulted in tBLG structures with twist angles of $\theta \approx 11.5^\circ$ or $\theta \approx 30^\circ + 11.5^\circ = 41.5^\circ$ (which is equivalent to $\theta \approx 60^\circ - 41.5^\circ = 18.5^\circ$). There is a 50% chance of generating either twist angle, assuming there is an equal chance of generating either kind of edge (which is not necessarily true³⁰⁸). Panel (d) in figure 52 shows the flake from panel (a) after the flake from panel (c) has been transferred on top. The estimated misrotation angle is shown. The resulting tBLG area is highlighted in red.

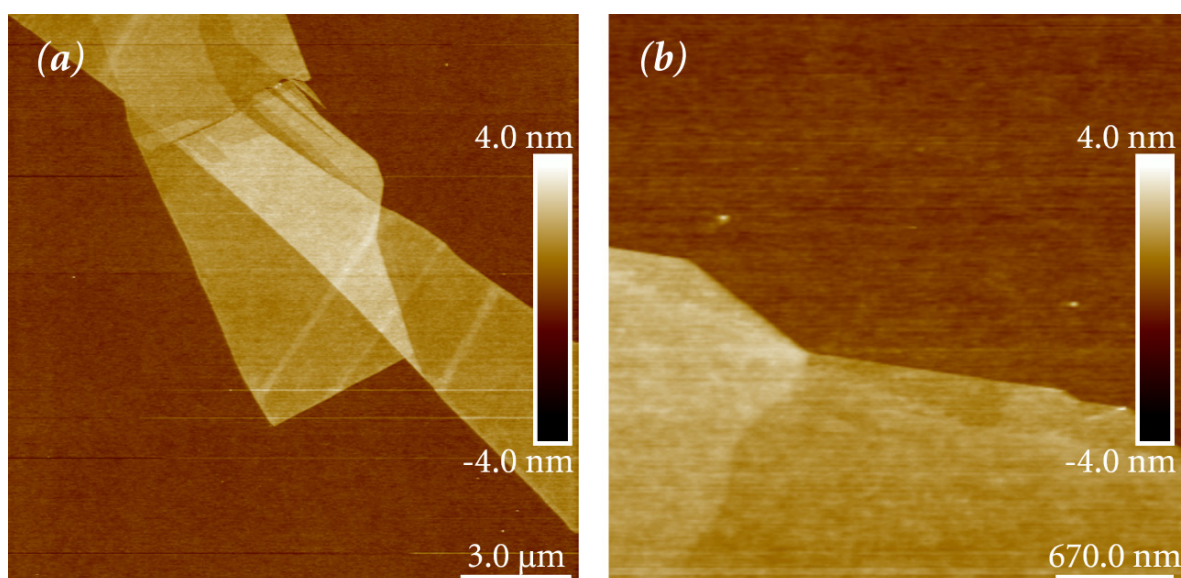


Figure 53 AFM images of graphene flakes with straight, crystalline edges on the smaller scale, but a messy appearance at scales observable using optical microscopy. (a) and (b) show large and small scale images respectively of a thin flake. In panel (b), the characteristic straight edges at 30° angles are observed.

Silicon nitride membranes were produced following the techniques described in section 5.1 for ‘thick’ wafers. The lithography design for the membrane patterning stage consisted of $10\ \mu\text{m}$ diameter holes in a triangular lattice with a $20\ \mu\text{m}$ pitch. The array shape was defined by the tBLG areas for the individual samples. This was to maximise the yield of large tBLG membranes, whilst ensuring a seal around the bilayer area to reduce the risk of the membranes breaking or the flakes scrolling during the drying process after polymer removal. After patterning and etching, the holes had an average diameter of $11\ \mu\text{m}$. The tBLG stacks were transferred on top using a second wet transfer process, and the resist was removed using acetone before the sample was dried using CPD as described in section 5.2.3.

As this was a wet transfer process, the characteristic triangular bubbles connected by wrinkles appear between the tBLG layers. However we are confident that between these bubbles the interfaces are atomically clean. AFM images of the membranes are shown in figure 54.

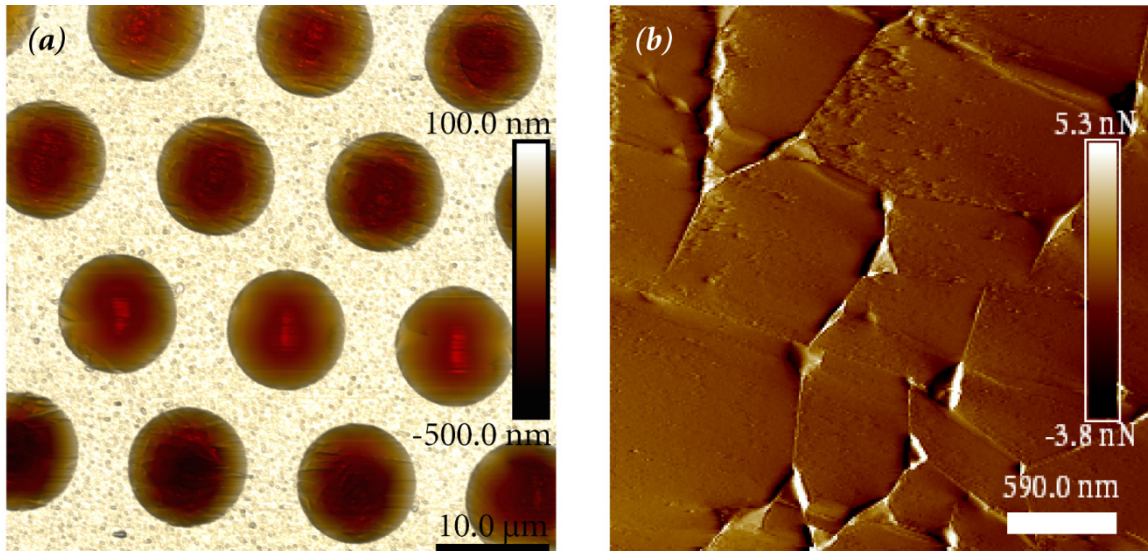


Figure 54 AFM images of large (11 μm diameter) suspended tBLG membranes. (a) shows a height image of the membrane array. The third row of holes down is only covered with one layer of graphene, showing smooth membranes. The others are tBLG membranes, showing the bubbles and wrinkling due to transfer contamination. (b) shows an error signal image of a wrinkled tBLG region, showing the typical triangular bubbles joined by wrinkles. Between the wrinkles the membranes are smooth. The ‘smudgy’ features in the upper part are imaging artefacts.

Following the AFM imaging, and immediately prior to posting the samples to the group of collaborators, they were annealed in H/Ar as described in section 5.2.6.

5.9 Fabrication and TEM patterning of suspended 2D materials - 4th paper

The silicon nitride support structures for the suspended membrane samples in this work were fabricated using the optimised process described in section 5.4. The hBN flakes were mechanically exfoliated onto thinned silicon oxide films on silicon substrates as described in section 5.2.2. Thin flakes were identified optically, and imaged with AFM to estimate their thickness. To minimise contamination between the graphene and hBN, the graphene flakes were exfoliated on a PMMA film and dry transferred directly onto the selected hBN flake, following the process outlined in section 5.2.4. Thin flakes were again identified optically, and AFM was used after transfer to unambiguously identify the number of graphene layers (layer step height on hBN is observed at 330\AA intervals). The graphene/hBN stack was then transferred over the selected hole on the SiN_x membrane following the procedure outlined in section 5.2.3. The samples were then cleaned and annealed following the process in 5.2.6. The sample used in the majority of the paper is pictured in figure 55.

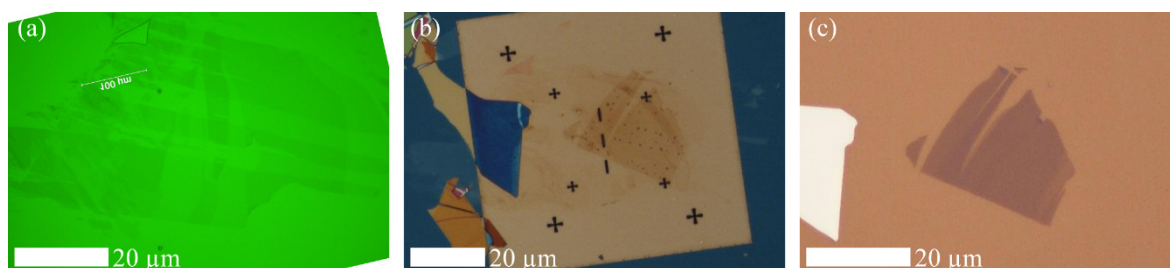


Figure 55 2 layer membrane patterned in 4th paper. (a) shows an optical image taken using a green narrow pass filter of the exfoliated graphene flake on the bilayer polymer dry transfer membrane. Areas of monolayer, bilayer and trilayer graphene are clearly visible. (b) shows a white light optical image of the hBN flake. Steps are faintly visible across the main part of the flake. The heights of the different areas were measured using AFM. (c) The dual layer membrane after transfer to the patterned nitride grid.

All data contained in the 4th paper with the exception of the first figure was taken from one sample, in two sessions. For the first session (cutting with EELS monitoring), the sample was annealed overnight and loaded into the microscope in the morning. For the second session, the sample was annealed again the day before imaging, and loaded into the microscope the night before imaging, producing slightly lower levels of mobile contamination and better patterning conditions. However, metallic nanoparticles containing principally Cu and Ag were observed on the particle after the second anneal, due to contamination in the ceramic

furnace tube. They are discussed in a section of the supplementary information included with the research paper.

Patterning and imaging were performed in a FEI Titan G2 80-200 kV with an X-FEG electron source operated at 200 kV, equipped with a Gatan image filter (HAADF/EELS) and a Super-X four silicon drift EDXS detector system. Images and spectral data were processed and analysed using Gatan Digital Micrograph software and the open source python package Hyperspy. EELS spectra were used to quantify the elemental composition of the sample using the process outlined in section 5.5.

6 1st paper

“Ultrafast quantitative nanomechanical mapping of suspended graphene”

Nick Clark, Antonios Oikonomou and Aravind Vijayaraghavan

Physica status solidi (b)

250(12): pg2672–2677

(2013)

6.1 Introduction to 1st paper

Suspended graphene membranes are a useful experimental testbed and have been proposed for use in next generation sensors and actuators, but are challenging to characterise. Central point nanoindentation on circular suspended membranes is the leading technique for investigating the static mechanical properties of graphene. Tapping mode AFM has been previously used to image small graphene membranes, but the high interaction forces between the AFM probe and graphene make this challenging and can induce significant imaging artefacts. The newly introduced PeakForce AFM mode allows the spatial mapping of the nanomechanical properties of a surface at high speed by capturing a force curve per pixel. This paper investigates the utility of this imaging technique for extracting both local sample and intrinsic graphene nanomechanical behaviour.

6.2 Summary of 1st paper

Graphene membranes were fabricated by transferring mechanically exfoliated graphene flakes onto a SiN_x membrane lithographically patterned with circular through holes. We show that it was possible to use peak-force imaging to capture topographic and nanomechanical data on large soft graphene membranes, of 3 – 10 μm scale and with a high dynamic vertical range at known deformations, in contrast with standard tapping mode. We present maps of mechanical properties derived from the captured force distance behaviour. We compare the force distance behaviour of the central area of the membrane captured from a peak-force map, and obtained using conventional nanoindentation, and find them to be in good agreement. By fitting this force distance behaviour to a semi-empirical model of a clamped circular elastic membrane, a ‘derived’ Young’s modulus for graphene of 1 TPa was measured on the large scale graphene membranes fabricated, which agrees with theoretical predictions and experimentally measured literature values.

6.3 Author contribution to 1st paper

The sample was fabricated and characterised by the thesis author. The data was analysed and interpreted by the author. The paper was written by the author with advice from AV and AO, and revised and edited by the author and AV. The experiment was conceived and planned by the author and AV.

Ultrafast quantitative nanomechanical mapping of suspended graphene

Nick Clark¹, Antonios Oikonomou², and Aravind Vijayaraghavan^{*1}

¹ School of Materials and Centre for Mesoscience and Nanotechnology, The University of Manchester, Manchester M13 9PL, UK

² School of Computer Science and Centre for Mesoscience and Nanotechnology, The University of Manchester, Manchester M13 9PL, UK

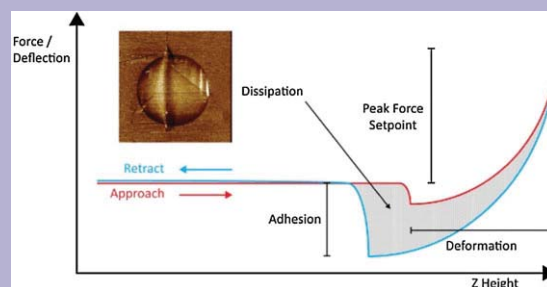
Received 18 May 2013, revised 17 October 2013, accepted 23 October 2013

Published online 25 November 2013

Keywords graphene, nanomechanical mapping, peak-force, scanning-probe microscopy

* Corresponding author: e-mail aravind@manchester.ac.uk, Phone: +44 161 275 0136, Fax: +44 161 275 4527

Understanding the mechanical properties of suspended graphene membranes is crucial to the development of graphene nano-electromechanical devices. PeakForce QNM (quantitative nanomechanical mapping) atomic force microscopy imaging was used to rapidly map the nanomechanical properties of a range of suspended graphene membranes. The force–displacement behavior of monolayer graphene extracted from the peak-force imaging map was found to be comparable to that taken using standard nanoindentation. By fitting to a simple elastic model, the two-dimensional elastic modulus was measured at around 350 N m^{-1} , corresponding to a Young's modulus of around 1 TPa.



Nanomechanical parameters which can be directly extracted from force curve data in real time. Inset shows a dissipation map of a suspended graphene membrane.

© 2013 WILEY-VCH Verlag GmbH & Co. KGaA, Weinheim

1 Introduction Probe based indentation is a widely used technique for studying local mechanical material properties [1]. The most accurate way of mapping material properties at the nanoscale has been force-volume imaging in an atomic force microscope (AFM) [2]. In this mode, the tip is ramped using the z -axis stepper motor to perform a nanoindentation at every point in an image, producing a two-dimensional array of force curves, from which a variety of nanomechanical properties can be extracted. However force-volume mapping and standard tapping mode imaging do not deal well with large sudden changes in the surface mechanical properties, and the extensive time required to complete a force volume plot limits its usefulness.

The recently introduced PeakForce QNM (quantitative nanomechanical mapping) AFM mode [3, 4] allows the spatial mapping of the nanomechanical properties of a surface at high speed by effectively ramping with the cantilever rather than the z -piezo; the time taken for a full nanomechanical map is comparable to the time

taken for a standard AFM tapping mode topography-only image.

Graphene, a two dimensional (2D) carbon lattice, has attracted broad interest due to its unique electrical, thermal, and mechanical properties [5–7], and could play an important role in the next generation of micro/nano-electromechanical systems (M/NEMS). Its measured intrinsic strength exceeds that of any other material [8]. Suspended graphene membranes [9] are a useful experimental testbed in a wide range of areas [10–12], but are challenging to characterize due to their extreme optical and electronic transparency.

AFM nanoindentation and force volume experiments on suspended graphene are the primary way through which the mechanical properties of graphene and other two-dimensional materials can be measured [13–16]. Previous attempts to image graphene membranes using tapping mode AFM have been problematic due to the unusual combination of their high strength and high elasticity. The high interaction forces between the AFM probe and graphene induce large

high frequency oscillations of the graphene membrane, producing a triangular wave like artifact as the oscillation is repeatedly induced and subsequently decays. Although it was possible to image the topography of smaller membranes in tapping mode, by carefully controlling the scan parameters to reduce the tip-sample interaction force, the height data was misleading due to the lack of knowledge about the force applied to the membrane (the topography of which changes with the applied tip force). These issues can be overcome in peak-force tapping mode which allows for a pre-defined force to be applied during each “tap,” and this force can be minimized to very small values. Since this process involves capturing a full force curve at every “tap” during imaging, it also provides a full nanomechanical characterization at every data-point on the AFM image. Here we present nanomechanical maps of suspended graphene taken using the PeakForce QNM imaging mode and compare extracted force curves to those measured using conventional nanoindentation/force volume mode. The force–displacement data was in agreement, and by fitting this to a simple model of a circular 2D elastic film under central point loading the Young’s modulus of graphene was measured at around 1 TPa [8, 16], in agreement with literature values. We also demonstrate that peak-force imaging allows the capture of topographic data from large soft membranes with a high dynamic vertical range using non-contact AFM, as opposed to tapping mode imaging where the tip–membrane adhesion induces oscillations in the membrane which result in triangular artifacts.

2 Materials and methods The suspended graphene membranes used in this study were supported by patterned silicon nitride membranes. The nitride membranes were patterned with 8 μm diameter holes using photolithography and reactive ion etching (RIE). Graphene flakes were mechanically exfoliated [17] from graphite onto silicon dioxide coated substrates. A 90 nm thick SiO_2 coating was used to maximize the optical contrast and allow the number of layers to be easily visualized [18]. A flake containing regions of both monolayer and trilayer graphene was selected and transferred onto the patterned nitride membranes using a standard flake transfer procedure [19]. Pictures of the flake before and after transfer and a schematic cross section of the resultant membrane are shown in Fig. 1.

PeakForce Tapping and conventional TappingMode AFM images were taken using a Dimension Icon (Bruker Nano) AFM with a Nanoscope V controller. PeakForce images up to a force setpoint of 100 nN were taken using ScanAsyst Air probes, and up to 10 μN , along with the tapping mode images, with ATESP probes (both from Bruker). Probe spring constants were calculated using the thermal tune method [20] for the ScanAsyst Air tips and Sader’s method [21] for the stiffer ATESP probes.

Figure 2 shows a comparison of PeakForce and TappingMode images of identical suspended graphene membranes. Both images contain 512×512 pixels and were captured using a scan rate of 1 line per second for a total of

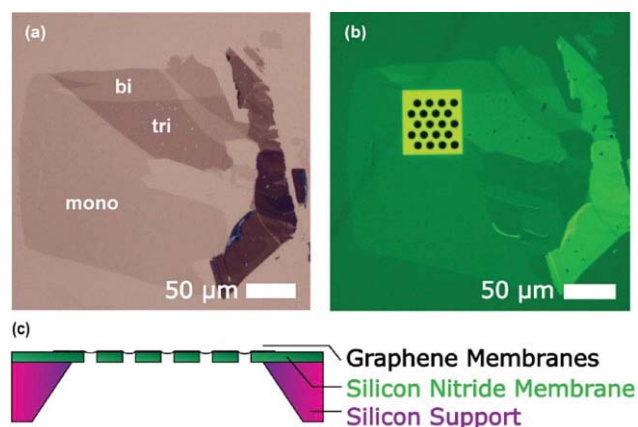


Figure 1 (a) Mechanically exfoliated graphene flake on 90 nm SiO_2 substrate, to highlight the monolayer, bilayer, and trilayer regions. (b) Graphene flake after transfer to patterned silicon nitride membrane. The lighter green square is the unsupported nitride membrane; it is backed by silicon everywhere else. (c) Schematic cross-section of suspended graphene membrane, covering a suspended patterned silicon nitride grid.

8½ min. The peak-force mode image (Fig. 2b) was taken using a ScanAsyst Air probe with a peak-force setpoint of 5 nN to minimize the resulting membrane deflection. The sawtooth like artifact in the tapping mode image is characteristic of the kind of artifact that is observed when imaging membranes of this type. While it is possible to obtain clean images on smaller suspended membranes with careful control of the scanning parameters it is extremely challenging to do the same on membranes of diameters of more than around 5 μm . Larger membranes are desirable as the quality

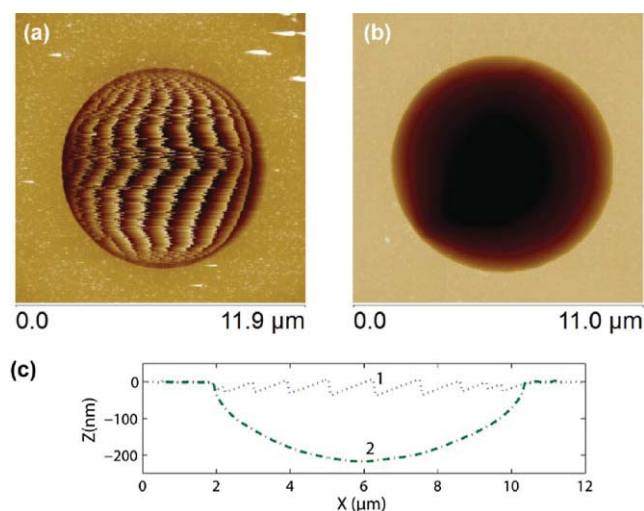


Figure 2 Comparison of TappingMode and PeakForce images of suspended membranes. (a) TappingMode image of 8 μm diameter monolayer graphene membrane captured using an ATESP probe. (b) PeakForce image of same membrane captured using a ScanAsyst Air Probe with a 5 nN force setpoint. (c) Comparison of height traces across the center of the membrane. Trace 1 is from the tapping mode image and trace 2 is from the peak force image.

factor of circular graphene mechanical resonators increases in proportion to their size [22]. They are also interesting experimentally for their use as novel electron microscopy samples and sample supports [23], as well as investigations into proton transport through thin films [24, 25], as well as potential applications as molecular sieves and pressure/strain sensors. In PeakForce mode, the voltage signal from the photodetector is linked to the force on the membrane, and the tip is repeatedly ramped using the piezo until the voltage signal corresponding to the force setpoint is reached, when the tip is retracted. This enables fine control over the force which is applied by the tip, which can be minimized to reduce the induced oscillations of the membrane.

PeakForce QNM imaging, like force volume imaging, generates a force curve per image pixel, from which a variety of useful mechanical properties can be extracted. However the extremely low speed of force-volume imaging (~ 1 pixel per second) limits its usefulness and makes it susceptible to drift. In PeakForce imaging, the tip is oscillated at a non-resonance frequency rather than ramped vertically with the z -piezo, dramatically increasing the capture speed (approx. 1–4 lines per second). A schematic of how the extracted parameters are obtained from the force curve is shown in Fig. 3a. The deformation channel is the vertical

distance between the position at which the tip first contacts the sample and the maximum extension and represents the vertical distance through which the sample is deformed by applying a known force (the peak force setpoint) via the tip. The dissipation of energy by the sample is obtained by the area between the measured extend and retract force curves. During the retract phase, short range attractive van der Waals forces keep the tip anchored to the surface until sufficient force is applied to pull the tip away from the surface. The force at which this occurs is saved as the adhesion quantity. The high adhesion values which are observed when scanning suspended graphene help suggest an explanation for the cause of the observed artifacts in tapping mode; the membrane is pulled up by the tip and violently released, inducing the membrane oscillations. As the frequency of these oscillations is much higher than that of the tip (the fundamental frequency is expected to be around 10 MHz [22]) the upper point of the graphene oscillation envelope is imaged. The membrane oscillation gradually decays due to damping, and when it gets low enough such that the restoring force at the top of the oscillation is lower than that of the tip–graphene attractive force, the membrane is again picked up, deformed, and released. In PeakForce mode, the tip sticks to the graphene during every indentation, and measures the static membrane behavior rather than the dynamic. Despite the use of tips with different degrees of stiffness, up to 200 N m^{-1} , and trying a wide variety of scanning parameters, we have been unable to produce a convincing image using tapping mode of a suspended monolayer membrane larger than $3 \mu\text{m}$.

Figure 3 contains nanomechanical property maps of an interesting membrane structure. Most of the hole is covered by monolayer graphene, but the area in the top right is covered by trilayer graphene. The number of layers was confirmed by the well-calibrated optical contrast of graphene on Si/SiO₂ substrate [18] before the transfer. The hole is surrounded by a “hard” silicon nitride membrane which does not deform at the forces used in these experiments. The PeakForce maps allow us to quickly say that the trilayer region is harder to deform (from Fig. 3c), dissipates relatively the same amount of energy per strike (from Fig. 3e), and exhibits a stronger AFM tip–graphene adhesive interaction (from Fig. 3d). All the data from Fig. 3b–e was taken in one 512×512 pixel (data point) scan taking around 8 min to complete, orders of magnitude faster than a traditional force volume mode scan would have taken (72 h using a typical ramp rate of 1 pixel per second). A recorded force curve from the slack region in the center of the graphene from this scan is shown in Fig. 4.

PeakForce maps were taken on a range of membranes at increasing force, up to that required to fracture the graphene membranes (between 2 and $3 \mu\text{N}$). Nanoindentations in the centers of suspended membranes at similar forces were also taken to verify the mechanical response of the membranes. A comparison of force response curves from nanoindentations and extracted from PeakForce maps in the center of the same membrane is shown in Fig. 5. The force displacement

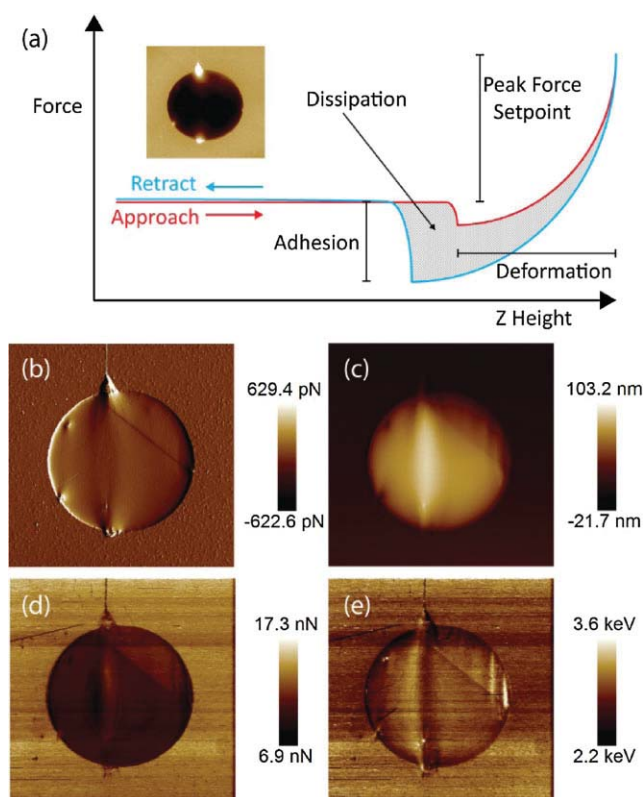


Figure 3 (a) Schematic force curve illustrating how the nanomechanical parameters are extracted. Inset shows the height data from a semi supported graphene membrane. (b)–(e) PeakForce images of same membrane showing variety of PeakForce channels: (b) error, (c) deformation, (d) adhesion, and (e) dissipation.

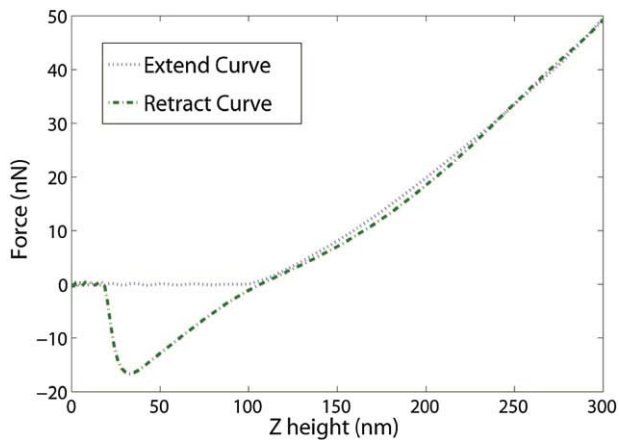


Figure 4 Force curve from slack region of graphene membrane illustrated in Fig. 3. The peak force setpoint was set at 50 nN, and the maximum adhesive force was 16.6 nN.

behavior of circular graphene monolayer membranes can be described to a high degree of accuracy [8] by the model of a clamped circular linearly elastic membrane under a point load at its center [26, 27]. The force–displacement behavior is approximated by:

$$F = (\pi T)\delta + (E^{2D}q^3a^2)\delta^3,$$

where F is the upward force applied on the tip by the membrane and δ is the deflection of the membrane, and a is the radius of the circular membranes. T is the pretension in the membrane and $q = 1/(1.05 - 0.15\nu - 0.16\nu^2) = 1.02$ is a dimensionless constant where ν is the Poisson's ratio of graphene, taken to be equal to 0.165 [28]. E^{2D} is the two-dimensional Young's modulus, with units of force divided by length. Fitting this model to the force curves should therefore yield both the pretension and the elastic modulus of the membranes. An offset was often observed between the

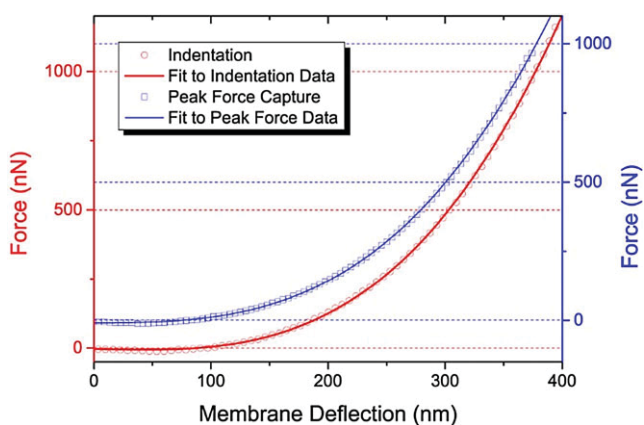


Figure 5 Comparison of force–deflection data of the center of a membrane. The blue data was extracted from a peak force image, whilst the red data was taken using a point indentation (a single force volume image “pixel”). Fits of both sets of data to the elastic model are also shown.

nominal zero deflection point and the force minima, so a free parameter was added to the fit to account for this discrepancy. The true zero deflection point was taken to be the force minimum, which was output during the fit. In practice, there was a good agreement between the moduli obtained using peak force and nanoindentation methods, with both yielding measurements of the modulus of monolayer graphene as around $350 \pm 50 \text{ N m}^{-1}$. This can be compared to the 3D modulus by dividing by the nominal thickness of a graphene layer (0.335 nm [29]) to yield values of the Young modulus of graphene around 1 TPa, in good agreement with that measured by other groups [8, 16, 30, 31]. Pretension in the membranes was not observed in most cases. Previous reports [8] suggest that the observed pretension is entirely due to the extension of the membrane due to the adhesion of the graphene to the edges of the hole for the first few nm, and that mechanically exfoliated graphene is nominally compressed when not suspended. As our membranes are significantly larger than those used in that study (1–1.5 μm) without a significantly larger adhered

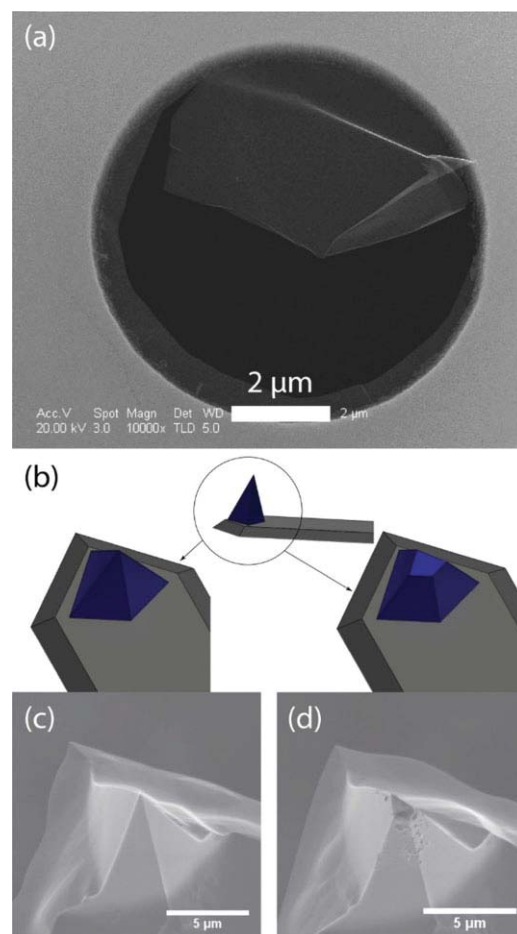


Figure 6 (a) SEM image of a broken graphene membrane after failure test. (b) Schematic highlighting the location of the tip (the tip is colored in blue and the cantilever in gray) in the SEM images shown in (c) and (d) of an ATESP probe before and after performing a failure test.

region around the edges, the predicted tension due to extension is far lower, and consequently cannot be observed in our measurements.

At very high forces no slipping of the graphene or permanent deformation was observed until the failure of the membrane. The high forces (above around $1 \mu\text{N}$) were enough to significantly damage the silicon tips used here. An SEM image of a broken membrane is shown in Fig. 6, along with images of the tip used to puncture it both before and after the scan. Extensive tip damage was observed on all the silicon ATESP tips after high force imaging and graphene fracture. The force–displacement behavior is independent of the tip radius as long as it is far smaller than the size of the membrane. However the breaking force of the membrane is highly dependent on the tip radius, as it is the area of extremely high stress directly under the tip which is significant. Therefore extracting the ultimate tensile strength of the membranes was not possible.

3 Discussion PeakForce AFM imaging looks to be an ideal technique for imaging suspended graphene, and therefore more complicated structures based on graphene membranes as well as those based on other 2D materials. The speed with which nanomechanical data can be obtained is a dramatic improvement over the equivalent force–volume technique, and is comparable to tapping mode imaging speeds. It opens up lots of possibilities of new experiments involving graphene membranes. Deformation and dissipation are important quantities when investigating damping in graphene resonator systems [13, 15, 32], and adhesion mapping enables a variety of tip and graphene functionalization experiments [33].

The force–displacement behavior of the membranes, and the dissipation and deformation channels was highly repeatable and independent of the tip, depending only on the size of the membrane and the number of layers. By fitting a model to the extracted force data, the measured two-dimensional elastic modulus was found to agree with data taken in a standard nanoindentation experiment, as well as literature values obtained using diamond tip nanoindenters [8, 14]. The large error on the measured modulus was largely due to uncertainties about the z height that corresponded to zero membrane deflection, to which the model, especially the linear term was highly sensitive.

Derived quantities which depend on knowledge of the tip condition were less repeatable. The tip–graphene adhesion, for example, is dependent on the contact area. The breaking force is also determined by the extreme stress concentrations directly underneath the tip, and is highly sensitive to tip radius. This made extracting parameters such as the intrinsic strength and nonlinear elastic behavior challenging due to the extreme degradation of the silicon tips at these high forces.

4 Summary PeakForce QNM AFM imaging was used to rapidly map the nanomechanical properties of a range of suspended graphene membranes, something which was not

previously possible using other AFM modes. Structures and ripples on the membrane are clearly visible when compared to images taken in other modes. The force–displacement behavior of monolayer graphene extracted using peak-force imaging mode was found to be comparable to that taken using standard nanoindentation. By fitting to a simple elastic model, the two-dimensional elastic modulus was measured at around 350 N m^{-1} , corresponding to a Young's modulus of around 1 TPa, which is in good agreement with the literature values.

Acknowledgements The authors thank S. Lesko (Bruker Nano Surfaces Europe) and S. Hu for useful discussions, and acknowledge the Engineering and Physical Science Research Council (EPSRC) U.K. (Grant EP/G035954/1).

References

- [1] M. R. Van Landingham, *J. Res. Natl. Inst. Stand.* **108**, 249 (2003).
- [2] D. Tranchida, S. Piccarolo, and M. Soliman, *Macromolecules* **39**, 4547 (2006).
- [3] M. E. Dokukin and I. Sokolov, *Langmuir* **28**, 16060 (2012).
- [4] T. J. Young, M. A. Monclus, T. L. Burnett, W. R. Broughton, S. L. Ogin, and P. A. Smith, *Meas. Sci. Technol.* **22**, 125703 (2011).
- [5] A. H. Castro Neto, F. Guinea, N. M. R. Peres, K. S. Novoselov, and A. K. Geim, *Rev. Mod. Phys.* **81**, 109 (2009).
- [6] K. S. Novoselov, S. V. Morozov, T. M. G. Mohinddin, L. A. Ponomarenko, D. C. Elias, R. Yang, I. I. Barbolina, P. Blake, T. J. Booth, D. Jiang, J. Giesbers, E. W. Hill, and A. K. Geim, *Phys Status Solidi B* **244**, 4106 (2007).
- [7] K. S. Novoselov, V. I. Fal'ko, L. Colombo, P. R. Gellert, M. G. Schwab, and K. Kim, *Nature* **490**, 192 (2012).
- [8] C. Lee, X. D. Wei, J. W. Kysar, and J. Hone, *Science* **321**, 385 (2008).
- [9] T. J. Booth, P. Blake, R. R. Nair, D. Jiang, E. W. Hill, U. Bangert, A. Bleloch, M. Gass, K. S. Novoselov, M. I. Katsnelson, and A. K. Geim, *Nano Lett.* **8**, 2442 (2008).
- [10] R. R. Nair, P. Blake, J. R. Blake, R. Zan, S. Anissimova, U. Bangert, A. P. Golovanov, S. V. Morozov, A. K. Geim, K. S. Novoselov, and T. Latychevskaia, *Appl. Phys. Lett.* **97**, 153102 (2010).
- [11] R. R. Nair, H. A. Wu, P. N. Jayaram, I. V. Grigorieva, and A. K. Geim, *Science* **335**, 442 (2012).
- [12] J. C. Meyer, A. K. Geim, M. I. Katsnelson, K. S. Novoselov, T. J. Booth, and S. Roth, *Nature* **446**, 60 (2007).
- [13] M. Poot and H. S. J. van der Zant, *Appl. Phys. Lett.* **92**, 3 (2008).
- [14] C. Lee, X. D. Wei, Q. Y. Li, R. Carpick, J. W. Kysar, and J. Hone, *Phys. Status Solidi B* **246**, 2562 (2009).
- [15] M. Huang, T. A. Pascal, H. Kim, W. A. Goddard, and J. R. Greer, *Nano Lett.* **11**, 1241 (2011).
- [16] M. Annamalai, S. Mathew, M. Jamali, D. Zhan, and M. Palaniapan, *J. Micromech. Microeng.* **22**, 11 (2012).
- [17] K. S. Novoselov, A. K. Geim, S. V. Morozov, D. Jiang, Y. Zhang, S. V. Dubonos, I. V. Grigorieva, and A. A. Firsov, *Science* **306**, 666 (2004).
- [18] P. Blake, E. W. Hill, A. H. Castro Neto, K. S. Novoselov, D. Jiang, R. Yang, T. J. Booth, and A. K. Geim, *Appl. Phys. Lett.* **91**, 063124 (2007).

- [19] A. Reina, H. Son, L. Jiao, B. Fan, M. S. Dresselhaus, Z. Liu, and J. Kong, *J. Phys. Chem. C* **112**, 17741 (2008).
- [20] R. Levy and M. Maaloum, *Nanotechnology* **13**, 33 (2002).
- [21] J. W. M. Chon, P. Mulvaney, and J. E. Sader, *J. Appl. Phys.* **87**, 3978 (2000).
- [22] R. A. Barton, B. Ilic, A. M. van der Zande, W. S. Whitney, P. L. McEuen, J. M. Parpia, and H. G. Craighead, *Nano Lett.* **11**, 1232 (2011).
- [23] S. Buckhout-White, J. T. Robinson, N. D. Bassim, E. R. Goldman, I. L. Medintz, and M. G. Ancona, *Soft Matter* **9**, 1414 (2013).
- [24] S. Garaj, W. Hubbard, A. Reina, J. Kong, D. Branton, and J. A. Golovchenko, *Nature* **467**, 190 (2010).
- [25] J. S. Bunch, S. S. Verbridge, J. S. Alden, A. M. van der Zande, J. M. Parpia, H. G. Craighead, and P. L. McEuen, *Nano Lett.* **8**, 2458 (2008).
- [26] U. Komaragiri and M. R. Begley, *J. Appl. Mech. T – ASME* **72**, 203 (2005).
- [27] K.-T. Wan, S. Guo, and D. A. Dillard, *Thin Solid Films* **425**, 150 (2003).
- [28] O. L. Blakslee, D. G. Proctor, E. J. Seldin, G. B. Spence, and T. Weng, *J. Appl. Phys.* **41**, 3373 (1970).
- [29] R. Al-Jishi and G. Dresselhaus, *Phys. Rev. B* **26**, 4514 (1982).
- [30] C. L. Wong, M. Annamalai, Z. Q. Wang, and M. Palaniapan, *J. Micromech. Microeng.* **20**, 115029 (2010).
- [31] I. W. Frank, D. M. Tanenbaum, A. M. Van der Zande, and P. L. McEuen, *J. Vac. Sci. Technol. B* **25**, 2558 (2007).
- [32] H. L. Lee, Y. C. Yang, and W. J. Chang, *Jpn. J. Appl. Phys.* **52**, 025101 (2013).
- [33] P. Lazar, S. Zhang, K. Šafářová et al., *ACS Nano* **7**, 1646 (2013).

7 2nd paper

“Determination of the quasi-TE mode (in-plane) graphene linear absorption coefficient via integration with silicon-on-insulator racetrack cavity resonators”

Iain F Crowe, Nick Clark, Siham Hussein, Brian Towlson, Eric Whittaker, Milan Milosevic, Frederic Gardes, Goran Mashanovich, Matthew Halsall, and Aravind Vijayaraghavan

Optics Express

22(15): pg18625–18632

(2014)

7.1 Introduction to 2nd paper

Along with graphene's unique mechanical properties, its ability to absorb light over an extremely wide wavelength range and its high carrier mobility make a variety of graphene based photonic devices possible. The large surface area of graphene, as well as its chemical purity, reactivity and simplicity of functionalisation, make it an ideal sensing platform, potentially leading to ultra-sensitive devices that can detect specific biological species. Understanding the nature of light's interaction with graphene is critical for the development of graphene integrated silicon photonic sensors taking advantage of these properties. The linear attenuation coefficient of graphene had previously been measured using a cutback method, but there was a discrepancy between published results. We aimed to unambiguously determine this attenuation factor, and guide future designs for both optoelectronic devices and sensing devices working using this concept.

7.2 Summary of 2nd paper

CVD graphene was transferred onto an array of silicon racetrack cavity resonators and selectively patterned to remove it from the input-pass waveguides. The waveguide spectra were collected both before and after graphene modification. Analysis of the spectra showed that the graphene induced a strong quenching of the resonance signal as the light-graphene interaction length (racetrack length) is increased. The linear attenuation due to graphene (as a function of its length) was measured using both a cutback method (as had been performed previously) and by fitting it as a parameter in the ring resonator transmission spectrum. From this work a model of cavity resonance attenuation with respect to graphene length and height over said cavity was developed, which should provide future design rules for developing graphene integrated silicon photonic devices for chemical sensing and optoelectronic applications.

7.3 Author contribution to 2nd paper

The previously fabricated silicon racetrack resonators were selectively patterned with CVD graphene by the thesis author. The topography of the CVD membranes over the resonators was confirmed by the author using AFM. The author also contributed to the design of the experiment, the interpretation of the experimental data, and the editing of the paper.

Determination of the quasi-TE mode (*in-plane*) graphene linear absorption coefficient *via* integration with silicon-on-insulator racetrack cavity resonators

Iain F Crowe,^{1,*} Nick Clark,² Siham Hussein,¹ Brian Towlson,¹ Eric Whittaker,¹ Milan M Milosevic,^{3,§} Frederic Y Gardes,³ Goran Z Mashanovich,³ Matthew P Halsall¹ and Aravind Vijayaraghavan²

¹Photon Science Institute and School of Electrical and Electronic Engineering, University of Manchester, Oxford Road, Manchester M13 9PL, UK

²School of Materials, University of Manchester, Oxford Road, Manchester M13 9PL, UK

³Optoelectronics Research Centre, University of Southampton, SO17 1BJ, UK

[§]now at Etaphase, Inc., Bellevue, WA, USA

iain.crowe@manchester.ac.uk

Abstract: We examine the near-IR light-matter interaction for graphene integrated cavity ring resonators based on silicon-on-insulator (SOI) racetrack waveguides. Fitting of the cavity resonances from quasi-TE mode transmission spectra reveal the real part of the effective refractive index for graphene, $n_{\text{eff}} = 2.23 \pm 0.02$ and linear absorption coefficient, $\alpha_{\text{gTE}} = 0.11 \pm 0.01 \text{ dB}\mu\text{m}^{-1}$. The evanescent nature of the guided mode coupling to graphene at resonance depends strongly on the height of the graphene above the cavity, which places limits on the cavity length for optical sensing applications.

©2014 Optical Society of America

OCIS codes: (240.0240) Optics at surfaces; (240.0310) Thin films; (240.6490) Spectroscopy, surface.

References and links

1. K. S. Novoselov, V. I. Fal'ko, L. Colombo, P. R. Gellert, M. G. Schwab, and K. Kim, "A roadmap for graphene," *Nature* **490**(7419), 192–200 (2012).
2. M. Liu, X. Yin, E. Ulin-Avila, B. Geng, T. Zentgraf, L. Ju, F. Wang, and X. Zhang, "A graphene-based broadband optical modulator," *Nature* **474**(7349), 64–67 (2011).
3. K. Kim, J. Y. Choi, T. Kim, S. H. Cho, and H. J. Chung, "A role for graphene in silicon-based semiconductor devices," *Nature* **479**(7373), 338–344 (2011).
4. D. J. Thomson, F. Y. Gardes, J.-M. Fedeli, S. Zlatanovic, Y. Hu, B. P. P. Kuo, E. Myslivets, N. Alic, S. Radic, G. Z. Mashanovich, and G. T. Reed, "50-Gb/s silicon optical modulator," *IEEE Photon. Technol. Lett.* **24**(4), 234–236 (2012).
5. G. Li, X. Zheng, J. Yao, H. Thacker, I. Shubin, Y. Luo, K. Raj, J. E. Cunningham, and A. V. Krishnamoorthy, "25Gb/s 1V-driving CMOS ring modulator with integrated thermal tuning," *Opt. Express* **19**(21), 20435–20443 (2011).
6. W. Bogaerts, P. De Heyn, T. Van Vaerenbergh, K. De Vos, S. K. Selvaraja, T. Claes, P. Dumon, P. Bienstman, D. Van Thourhout, and R. Baets, "Silicon microring resonators," *Laser and Photonics Reviews* **6**(1), 47–73 (2012).
7. M. K. Park, J. S. Kee, J. Y. Quah, V. Netto, J. Song, Q. Fang, E. M. La Fosse, and G.-Q. Lo, "Label-free aptamer sensor based on silicon microring resonators," *Sens. Actuators B Chem.* **176**, 552–559 (2013).
8. M. Iqbal, M. A. Gleeson, B. Spaugh, F. Tybor, W. G. Gunn, M. Hochberg, T. Baehr-Jones, R. C. Bailey, and L. C. Gunn, "Label-free biosensor arrays based on silicon ring resonators and high-speed optical scanning instrumentation," *IEEE J. Sel. Top. Quantum Electron.* **16**(3), 654–661 (2010).
9. C. Ciminelli, F. Dell'Olio, D. Conteduca, C. M. Campanella, and M. N. Armenise, "High performance SOI microring resonator for biochemical sensing," *Opt. Laser Technol.* **59**, 60–67 (2014).
10. J. E. Moses and A. D. Moorhouse, "The growing applications of click chemistry," *Opt. Express* **19**(21), 20435–20443 (2011).
11. H.-Y. Chen, M. Hirtz, X. Deng, T. Laue, H. Fuchs, and J. Lahann, "Substrate-independent dip-pen nanolithography based on reactive coatings," *J. Am. Chem. Soc.* **132**(51), 18023–18025 (2010).

12. X. Li, W. Cai, J. An, S. Kim, J. Nah, D. Yang, R. Piner, A. Velamakanni, I. Jung, E. Tutuc, S. K. Banerjee, L. Colombo, and R. S. Ruoff, "Large-area synthesis of high-quality and uniform graphene films on copper foils," *Science* **324**(5932), 1312–1314 (2009).
13. H. Wang, Y. Wang, X. Cao, M. Feng, and G. Lan, "Vibrational properties of graphene and graphene layers," *J. Raman Spectrosc.* **40**(12), 1791–1796 (2009).
14. K. Kim, S. Coh, L. Z. Tan, W. Regan, J. M. Yuk, E. Chatterjee, M. F. Crommie, M. L. Cohen, S. G. Louie, and A. Zettl, "Raman spectroscopy study of rotated double-layer graphene: misorientation-angle dependence of electronic structure," *Phys. Rev. Lett.* **108**(24), 246103 (2012).
15. V. M. Menon, W. Tong, and S. R. Forrest, "Control of quality factor and critical coupling in microring resonators through integration of a semiconductor optical amplifier," *IEEE Photon. Technol. Lett.* **16**(5), 1343–1345 (2004).
16. J. Niehusmann, A. Vörckel, P. H. Bolivar, T. Wahlbrink, W. Henschel, and H. Kurz, "Ultrahigh-quality-factor silicon-on-insulator microring resonator," *Opt. Lett.* **29**(24), 2861–2863 (2004).
17. L. Pechtel, L. Song, D. Schuh, P. Ajayan, W. Wegscheider, and A. W. Holleitner, "Time-resolved ultrafast photocurrents and terahertz generation in freely suspended graphene," *Nat Commun* **3**, 646 (2012).
18. I. Jung, M. Pelton, R. Piner, D. A. Dikin, S. Stankovich, S. Watcharotone, M. Hausner, and R. S. Ruoff, "Simple approach for high-contrast optical imaging and characterization of graphene-based sheets," *Nano Lett.* **7**(12), 3569–3575 (2007).
19. Z. H. Ni, H. M. Wang, J. Kasim, H. M. Fan, T. Yu, Y. H. Wu, Y. P. Feng, and Z. X. Shen, "Graphene thickness determination using reflection and contrast spectroscopy," *Nano Lett.* **7**(9), 2758–2763 (2007).
20. P. Blake, E. W. Hill, A. H. Castro Neto, K. S. Novoselov, D. Jiang, R. Yang, T. J. Booth, and A. K. Geim, "Making graphene visible," *Appl. Phys. Lett.* **91**(6), 063124 (2007).
21. Z. Lu and W. Zhao, "Nanoscale electro-optic modulation based on graphene-slot waveguides," *J. Opt. Soc. Am. B* **29**(6), 1490–1496 (2012).
22. R. Kou, S. Tanabe, T. Tsuchizawa, K. Warabi, S. Suzuki, H. Hibino, H. Nakajima, and K. Yamada, "Characterization of optical absorption and polarization dependence of single-layer graphene integrated on a silicon wire waveguide," *Jpn. J. Appl. Phys.* **52**(6R), 060203 (2013).
23. H. Li, Y. Anugrah, S. J. Koester, and M. Li, "Optical absorption in graphene integrated on silicon waveguides," *Appl. Phys. Lett.* **101**(11), 111110 (2012).
24. R. Kou, S. Tanabe, T. Tsuchizawa, T. Yamamoto, H. Hibino, H. Nakajima, and K. Yamada, "Influence of graphene on quality factor variation in a silicon ring resonator," *Appl. Phys. Lett.* **104**(9), 091122 (2014).
25. Q. Bao, H. Zhang, B. Wang, Z. Ni, C. H. Y. X. Lim, Y. Wang, D. Y. Tang, and K. P. Loh, "Broadband graphene polarizer," *Nat. Photonics* **5**(7), 411–415 (2011).

1. Introduction

The disruptive technological potential of graphene is extremely wide ranging [1], with the emergence of the first commercial devices anticipated as early as 2015. In particular, graphene's ability to absorb light over an extremely wide (UV to IR) wavelength range, coupled with its high carrier mobility offer the potential for a plethora of photonic devices including ultrafast, high band-width photo-detectors and optical modulators [2]. On the other hand, as a true 2D material, it has an extremely large surface area, which combined with its chemical purity, reactivity and simplicity of functionalization make for an ideal sensing platform that could lead to ultra-sensitive devices for the detection of biological and/or gas molecules in fields as diverse as healthcare, environment and homeland security.

However, there are certain fundamental limitations associated with graphene when compared with conventional semiconductors. For instance, intrinsic graphene is a semi-metal (zero band-gap semiconductor) which means that it exhibits a poor 'on/off' current ratio when integrated into electronic devices [3]. This, coupled with the huge financial and intellectual investment in the silicon CMOS micro-electronics industry and, more recently, the emerging field of silicon photonics, means that graphene is unlikely to completely supersede silicon in the foreseeable future. Rather, there are distinct and obvious advantages to be gained by combining these two power-house material systems. For instance, despite its large operating bandwidth, the relatively small fraction of photons absorbed at normal incidence (2.3%) and the small effective detection area of defect-free graphene limits its responsivity to levels well below that required for a commercial photo-detector [1]. However, by integrating graphene with a silicon waveguide, the light-matter (graphene) interaction length and therefore optical absorption can be increased considerably [3]. And the relationship is bi-lateral; for instance, integrating graphene with current commercial silicon optical modulators, such as the Mach-Zehnder Interferometer (MZI) [4] and the cavity ring resonator [5], which are used to encode transmission data for optical interconnects, offers the potential to improve device

performance precisely because of graphene's ultra-fast response over an extremely broad spectral range.

Whatever the application, understanding the nature of the light-matter interaction in graphene integrated silicon photonic devices is critical if the combined potential 'greater than the sum of its parts' is to be realized.

Our immediate focus is trying to understand the limitations on the practical sensitivity of silicon photonic cavities, in which graphene acts as a sensitization layer or pre-concentrator with improved reactivity over the silicon surface, for sensing applications. The ring resonator is one such cavity, in which the wavelength specific mode confinement of light arises from the high refractive index contrast at the silicon/air interface. Such cavity resonators are routinely fabricated, *via* deep UV or e-beam lithography with sub- μm precision, from the commercial silicon-on-insulator (SOI) platform with a wire-ring, positioned adjacent to a straight section wire-waveguide, providing a low loss resonant cavity into which light is evanescently coupled when the wavelength matches an integer number of round-trips of the ring [6]. The efficiency with which this coupling is achieved, and the very narrow (sub-nm) cavity resonances, provides a tightly confined (both physically and spectrally) intense evanescent field for near-surface molecular interaction, and therefore sensing [7–9]. The transmission spectrum (of a tuneable laser or broadband source) at the wire-guide output reveals these cavity resonances, the spectral position of which is also a strong function of the local (near surface) refractive index, which depends on the concentration of the bound target molecule. By monitoring this transmitted light intensity it is therefore possible to detect extremely small changes in the refractive index of the near surface region as molecules attach themselves to the primed silicon cavity surface. The functionalization of such silicon micro-cavities for bio-sensing applications has now been reasonably well explored, for instance for the detection of single-stranded DNA by peptide nucleic acid functionalization [7], streptavidin detection by biotin functionalization [8] and glucose detection by glucose oxidase functionalization [9]. However, the chemical functionalisation of silicon is limited in its scope due to its relatively poor reactivity, so that even the versatile 'click-chemistry' route to bio-functionalization [10] is not possible directly on silicon. Whilst methods to improve the reactivity of silicon surfaces, such as coating with poly-p-xylylenes have been described [11], these still leave a relatively thick (μm -scale) coating on the surface. For waveguide based photonic sensors such as these, the evanescent field decays exponentially away from the surface, and therefore it is essential that the reactive groups (be they biological or gaseous molecular compounds) be located as close to the silicon surface as possible and thus relatively thick coatings are undesirable. Rather, our approach is to coat our cavity surfaces with monolayer graphene with the expectation that the highly versatile reactivity of graphene will open up a wide variety of sensing applications that would otherwise be inaccessible to purely silicon photonic platforms. As a first step in this process, in this contribution we report measurement of the optical response of graphene coated cavities and in so doing determine both the real part of the effective refractive index and the quasi-TE (*in-plane*) linear absorption coefficient for single layer graphene.

2. Experimental details

Strip waveguides and racetrack resonators with height of 220nm and width of $w = 350\text{nm}$ were fabricated, from commercial SOI with a $2\mu\text{m}$ thick buried oxide layer, via deep UV (193nm) lithography using standard complementary metal-oxide semiconductor fabrication processes. Three racetrack resonators, with equivalent racetrack-to-wire coupling length, $L_c = 13\mu\text{m}$ and coupling gap, $g = 0.3\mu\text{m}$ but different radii of curvature, $r = 10, 20$ and $40\mu\text{m}$ are reported here, with only the smaller devices integrated with graphene.

The graphene was grown by chemical vapour deposition (CVD) on copper foils (Gratome-R-Cu, Bluestone Global Tech) and transferred on to the SOI wafer containing the devices using a polymer-mediated wet transfer procedure described elsewhere [12]. The graphene was patterned, to ensure selective coverage of the racetrack resonators, using raster-scan photolithography and oxygen plasma etching. The sample was subsequently cleaned

with acetone and annealed at 270°C in a reducing atmosphere to remove residual photo-resist contamination. In order to confirm we have deposited single layer graphene, we have used Raman scattering spectroscopy. The samples were excited with a 514nm (Cobolt Fandango solid state diode) laser via a 50x microscope objective lens and the Raman spectra (not shown here) collected in a back-scattering geometry, dispersed in a Renishaw 1000 micro-Raman system and detected using a charge coupled device (CCD) camera. Three key factors from the scattering spectra may be used to determine whether graphene is single ($n = 1$) or multi- ($n = 2, 3, 4 \dots$) layer; the G-peak position, $\omega_G(n) = 1581.6 + 11/(1 + n^{1.6})$ [13], the width (w_{2D}) and symmetry of the 2D-peak and the ratio of the 2D and G integrated intensities, I_{2D}/I_G [14]. From Lorentzian fits to our measured G and 2D scattering peaks, we obtain $\omega_G(n = 1) = 1587.2 \pm 0.1 \text{ cm}^{-1}$, a symmetric 2D peak with width, $w_{2D} = 28 \text{ cm}^{-1}$ and $I_{2D}/I_G \sim 6$, all of which confirm we have single layer graphene.

In order to facilitate optical device characterization in a sensing environment, we have developed a novel system, Fig. 1 for achieving free-space delivery and collection of the optical signal from an external cavity laser (Thorlabs TLK-L1550R), which has a narrow (100kHz) linewidth and tuning range from 1480 to 1600nm.

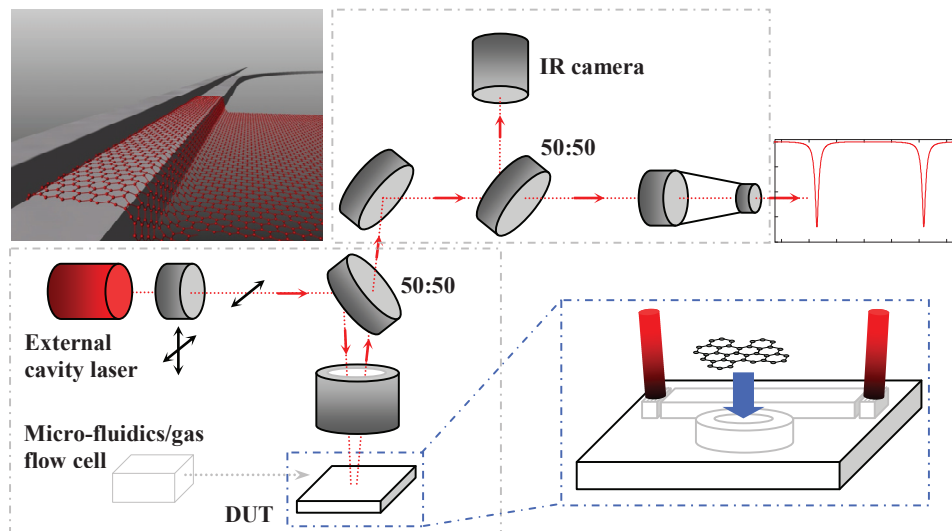


Fig. 1. (a) Schematic of the graphene integrated race-track resonator; The image illustrates the selective (partial) coverage of the race-track at the coupling section with the un-coated wire-guide (b) free-space optical set-up for measuring the resonator device transmission characteristics

The laser output is delivered, *via* a single mode fiber and polarizer, to a 50:50 beam-splitter, where it is reflected at near ($\sim 11^\circ$) normal incidence onto a wide field of view, long working distance 5x microscope objective lens (Thorlabs LMS03-BB). Unlike the fiber based techniques for characterization of such devices, this arrangement provides a ‘stand-off’ optical system (of $\sim 3\text{cm}$) above our device under test for future integration of micro-fluidic channels and/or gas flow cell. The laser spot is focused onto a surface grating (optimized for TE mode coupling) at one end of the strip waveguide, which tapers over $\sim 1\text{mm}$ to achieve single-guided mode operation. The total length of the strip waveguide is $\sim 3\text{mm}$ at the end of which the light emerges, *via* another tapering section and equivalent surface grating, at a similar angle off the normal. The light is then collected using the same objective lens and passes through the other side of the beam-splitter, whereupon it is reflected from a mirror onto a second beam-splitter, dividing the collected light between the aperture of an IR camera, which is used to image the waveguide input and output for alignment, and a fiber-coupler, which focuses the light onto the end of a fiber where it is delivered to a bench-top,

Bayspec SuperGamut© spectrometer with thermo-electrically cooled InGaAs array detector from which we determine the transmitted light intensity as a function of wavelength. The transmission spectra are all corrected for spectral variations in the laser output power and waveguide insertion loss.

3. Results and discussion

A typical transmission spectrum for the race-track ring resonator device ($r = 40\mu\text{m}$) without graphene is shown in Fig. 2.

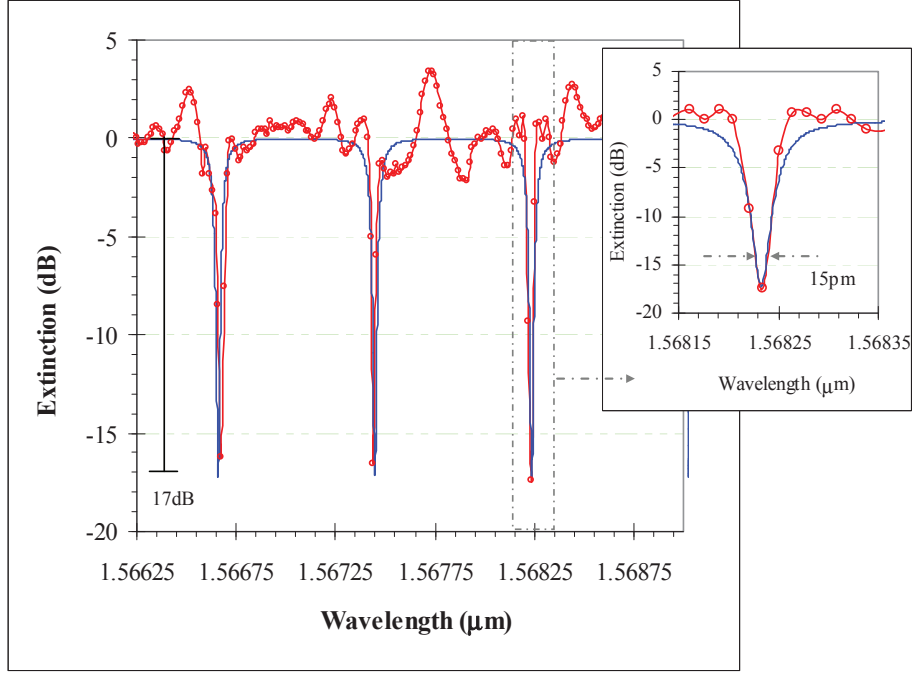


Fig. 2. Measured (red) transmission spectrum for a silicon racetrack cavity resonator (physical dimensions, $r = 40\mu\text{m}$ and $L_c = 13\mu\text{m}$) without graphene. The model (blue) curve is derived from a fit using Eq. (1) with $r = 42.5\mu\text{m}$, $L_c = 14\mu\text{m}$, $\alpha = 1.737\text{dBcm}^{-1}$ and $n_{\text{eff}} = 3.249$. Inset: close-up of the resonance peak around 1.56825nm

The device exhibits a relatively high extinction ($\sim 17\text{dB}$) on resonance with a quality factor ($Q = \lambda_0/\Delta\lambda$) of the order of 10^5 . The measured transmission spectrum is well described by the following expression, modified after [15]:

$$T(\lambda, L, n_{\text{eff}}, \alpha) = (1 - \gamma) \left[\frac{(\sqrt{1-k}) - (\sqrt{1-\gamma}) e^{-\alpha \frac{(Ln_{\text{eff}})}{2} - i(2\pi n_{\text{eff}}^2 \frac{L}{\lambda})}}{1 - (\sqrt{1-\gamma})(\sqrt{1-k}) e^{-\alpha \frac{(Ln_{\text{eff}})}{2} - i(2\pi n_{\text{eff}}^2 \frac{L}{\lambda})}} \right]^2 \quad (1)$$

Where k and γ are respectively power coupling and intensity loss factors, which depend on the coupling efficiency of the ring resonator structure, L ($= 2\pi r + 2L_c$) is the total physical round-trip length of the racetrack waveguide with radius of curvature, r and coupling length, L_c . n_{eff} is the effective refractive index and α is the loss coefficient, which includes contributions from both scattering and absorption. The model values obtained from the fit for r and L_c agree well with the design (and known physical) dimensions of the racetrack and the

values for n_{eff} and α are in excellent agreement with literature values [16] for this type of device.

Figure 3 shows typical transmission spectra for the two graphene integrated racetracks with different radius of curvature ($r = 10$ and $20\mu\text{m}$) but otherwise identical physical parameters (L_c , g and w) to the device without graphene.

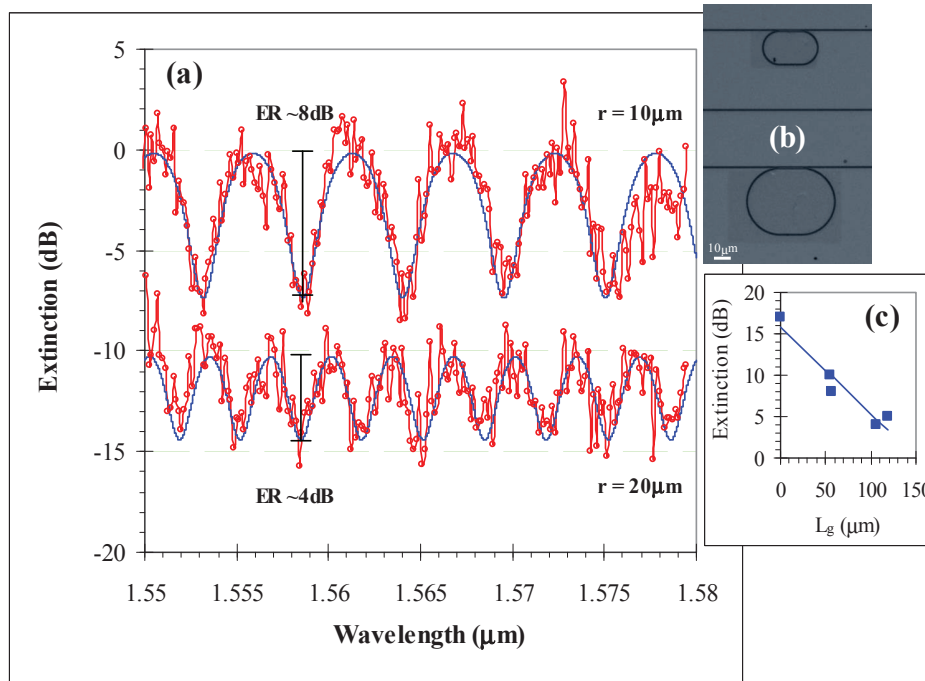


Fig. 3. (a) Measured (red) and modelled (Eq. (1), blue) transmission spectra (offset for clarity). Fits to both data sets yield residual minima with physical dimensions $r = 10, 20\mu\text{m}$ and $L_c = 13\mu\text{m}$, $n_{\text{eff}} = 2.23 \pm 0.02$ and $\alpha = 0.11\text{dB}\mu\text{m}^{-1}$ (b) Optical images of the two corresponding, selectively coated graphene integrated silicon racetrack cavity resonators with (top) $r = 10\mu\text{m}$ and (bottom) $r = 20\mu\text{m}$. (c) Measured peak extinction as a function of the light-matter (graphene) interaction length, L_g with linear regression fit of the form $\text{ER}(L_g)_{\text{dB}} = \text{ER}(0)_{\text{dB}} - \alpha L_g$ with slope $\alpha = 0.104\text{dB}\mu\text{m}^{-1}$

Figure 3 reveals a good fit to the transmission spectra using Eq. (1) for both cavity lengths with an effective refractive index, $n_{\text{eff}} = 2.23 \pm 0.02$. It is important to stress here that n_{eff} is representative of the waveguide core and cladding material and it is not trivial to extract a precise value for the refractive index of graphene, n_g from this. Published values for n_g [17–19] tend to be somewhat higher than that of graphene oxide and lower than that of bulk graphite [20].

The large variation we obtain in n_{eff} , going from un-coated to graphene coated cavities indicates dramatically altered modal propagation in our system and suggests that the optical properties, including the index of refraction are dominated by the graphene. Whilst n_{eff} can be expected to vary to a lesser degree according to the exact cavity dimensions, which determine the mode profile, we note that the value we have obtained here is in good agreement with previously reported values for modelled graphene-slot waveguides integrated into silicon platforms [21].

In general, although ring resonator scattering losses tend to increase with smaller ring radii, this should be balanced by lower propagation losses due to the smaller overall round-trip length. In the case of the graphene integrated devices we have measured, variation in the scattering losses due to tighter bend radii are negligible and the losses leading to the significant reduction of the extinction ratio and broadening of the resonances observed in Fig.

3 are almost entirely the result of increased propagation loss (absorption) in the graphene layer situated at the cavity surfaces. These losses are a strong function of the light-matter (graphene) interaction length, L_g and so as the racetrack size increases the observed extinction diminishes. Thus by examining the change in the peak extinction ratio for different overall graphene integrated racetrack lengths, one can independently determine the absorption coefficient for graphene and cross-correlate this with the value obtained by fitting the resonance spectra with Eq. (1). A total of four graphene integrated devices (two with $r = 10\mu\text{m}$ and two with $r = 20\mu\text{m}$) were measured and their extinction ratio is plotted as a function of L_g , along with the data point for the no graphene device, in **Fig. 3(c)**. Analysis of the optical images in Fig. 3(b) revealed that the rings were not completely coated by the graphene and so L_g has been corrected for this fractional coverage, $n (= L_g/L; 0 < n < 1)$. A linear regression fit to the data in Fig. 3(c), of the form $ER(L_g)_{dB} = ER(0)_{dB} - \alpha L_g$, yields a value for the graphene linear absorption coefficient, $\alpha = 0.104\text{dB}\mu\text{m}^{-1}$, which is equivalent (within experimental error) to the value derived from the fitting of Eq. (1) to the transmission spectra in Fig. 3(a). We note that similar analyses were recently reported for graphene integrated silicon wire waveguides without cavities [22], graphene integrated MZI devices [23] and from analysis of the Q-factor variation for a single ring resonator, partially coated with graphene [24], all of which yield similar values of α to that we have obtained. In [23] the authors increased the graphene-waveguide separation using a spin-on glass (HSQ) spacer layer, which revealed a dependence of the absorption coefficient on height, h , due to the interaction strength of the evanescent field, according to:

$$\alpha(h) = \alpha_0 e^{-2\gamma h} \quad (2)$$

We assign $\alpha_0 (= 0.11\text{dB}\mu\text{m}^{-1})$ as the experimental value we have obtained for the TE-mode linear absorption coefficient for $h = 0$ and $\gamma (= 8.5\mu\text{m}^{-1})$ is the waveguide evanescent field decay constant determined from a fit to the data of Fig. 4(d) in [23]. Expanding our analysis of the change in peak extinction with L_g , to include Eq. (2), we can write a general expression for the resonant signal attenuation in our cavities, $A_g(L_g, h)$ induced by the graphene as:

$$A_g(L_g, h)_{dB} = [ER(0) - ER(L_g)]_{dB} = \alpha_0 e^{-2\gamma h} L_g \quad (3)$$

A contour plot of A_g as a function of both L_g and h is shown in Fig. 4.

Figure 4 reveals that, for $L_g \leq 25\mu\text{m}$, the cavity signal attenuation induced by a graphene layer is negligible at large h (max 3dB at $h = 0$) but this becomes increasingly significant for longer lengths of graphene, particularly if it is deposited at the waveguide surface. For instance, for $L_g = 150\mu\text{m}$, the cavity signal is reduced to half its original value for a graphene height, $h \sim 120\text{nm}$ and for this length of graphene deposited at the surface ($h = 0$), a cavity resonance with $ER(0) \sim 17\text{dB}$ (similar to that described in Fig. 2) would be all but quenched. This agrees well with our observations for fully coated racetrack resonators with $r > 20\mu\text{m}$ and $L_c = 13\mu\text{m}$ ($L_g = 2\pi r + 2L_c > 152\mu\text{m}$), for which the transmission spectra yields no resonances. In order to confirm that the graphene we have deposited sits at the cavity surface, we have carried out a careful analysis, using scanning probe microscopy (not shown here) of a step from the plasma etched substrate to the graphene, which indicates a height, $1 < h \leq 1.5\text{nm}$. This is typical for graphene on a (native) silicon dioxide surface, particularly under ambient conditions and indicates that the graphene layer resides at the cavity surface.

The predictive power of our model has important implications for the design of graphene/silicon photonic devices, depending on the target application. For instance, in refractive index sensing applications, where one relies upon being able to measure small shifts in the cavity resonant wavelength, these design rules dictate that small L_g and/or large h should be employed to improve the reactivity of the silicon surface without sacrificing the cavity resonance signal. Practically, L_g can be controlled using selective etching to partially coat the race-track cavities with graphene whilst the inclusion of a (low-loss) dielectric spacer layer (such as HSQ) can be used to increase the height, h of the graphene above the cavity

surface. Indeed, control over such spacer layer thickness (at the 10's nm range) has already been demonstrated on silicon Mach-Zehnder type devices [23]. On the other hand, for e.g. photo-detector applications, one requires maximum absorption in the graphene layer and therefore designs should aim for large L_g and/or small h . It is worth pointing out that, for TM-mode operation, a different set of curves can be expected due to graphene's polarization sensitive absorption coefficient [22, 25].

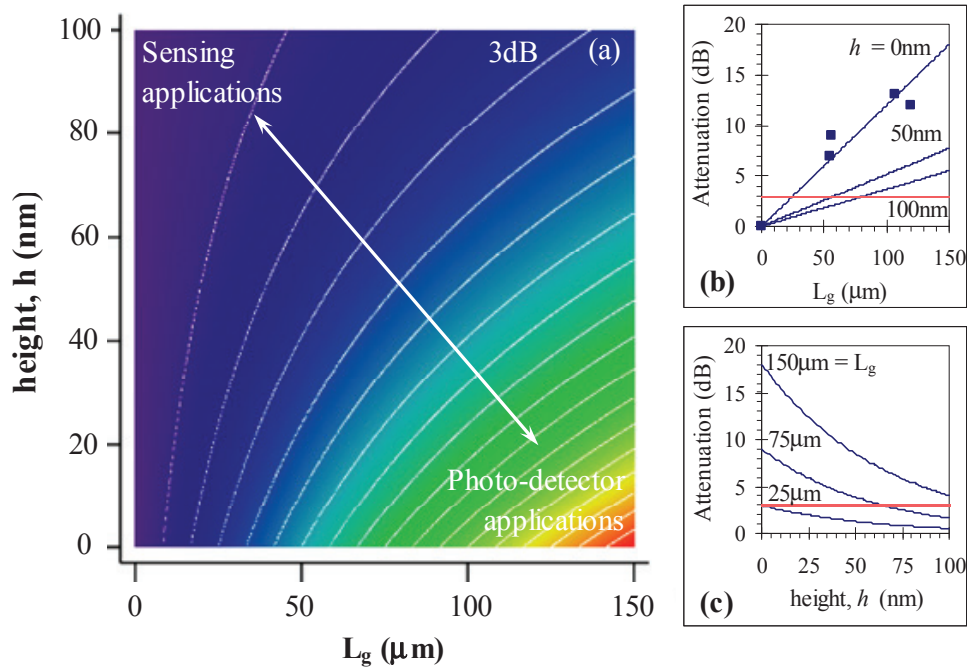


Fig. 4. (a) contour plot of the calculated signal attenuation, A_g (blue – low, red – high, contour lines – 1dB increment) as a function of length, L_g and height, h of graphene over the silicon cavity ring resonator (b) calculated A_g as a function of L_g for specific heights ($h = 0, 50, 100$ nm) along with our measured data (blue squares) and (c) calculated A_g as a function of height for specific lengths ($L_g = 25, 75, 150$ μm). The red dashed lines in (b) and (c) indicate the graphene (L_g, h) co-ordinates where the cavity resonance signal is attenuated by 3dB

4. Conclusions

We have deposited CVD graphene on racetrack type silicon cavity resonators as a route to improving the surface reactivity for bio-molecular and/or gas sensing applications. Measurements and analysis of the transmission spectra for a cavity with no graphene and for graphene integrated cavities reveal a strong quenching of the resonance signal with increasing light-graphene interaction length, which is due to the quasi-TE mode (*in-plane*) absorption in graphene. From these analyses we obtain a value for the graphene linear absorption coefficient, $\alpha_{gTE} = 0.11 \pm 0.01 \text{ dB}\mu\text{m}^{-1}$, which is in excellent agreement with literature values if we assume the graphene intersects the evanescent field of the guided mode at the cavity surface. A model of the cavity resonance signal attenuation for different graphene length and height co-ordinates over such cavities provides design rules for different graphene integrated silicon photonic devices according to the required application.

Acknowledgments

This work was supported by the Engineering and Physical Sciences Research Council grant EP/K016946/1. NC and AV also acknowledge P. Gorgojo for her assistance.

8 3rd paper***“Optical-phonon resonances with saddle-point excitons in twisted-bilayer graphene”***

Ado Jorio, Mark Kasperczyk, Nick Clark, Elke Neu, Patrick Maletinsky, Aravind Vijayaraghavan, and Lukas Novotny

Nano Letters

14(10): pg5687–5692

(2014)

8.1 Introduction to 3rd paper

Twisted bilayer graphene has a peak in its optical conductivity associated with its van Hove singularities, in the visible region of the spectra and with an energy dependent on the twisting angle. This peak generates resonances in the respective Stokes and anti-Stokes Raman processes at energies which can be controlled by the twist angle. We aimed to produce a large, suspended tBLG sample mode engineered to work in Stokes and anti-Stokes resonance under illumination from standard laboratory 532 nm and 633 nm lasers, and demonstrate the production of correlated Stokes anti-Stokes photons at the anti-Stokes resonance condition.

8.2 Summary of 3rd paper

A method to control the twist angle between layers of graphene had not previously been successfully developed prior to this work, and all studies were performed on ‘randomly’ oriented twisted samples. Large, suspended tBLG membranes were fabricated with a chosen twist angle. Changing the laser energy, we observed significant enhancement of the anti-Stokes Raman signal under illumination with a 532 nm laser. The laser power dependence of the spectra indicated the generation of correlated Stokes and anti-Stokes photon pairs under this condition.

8.3 Further work related to 3rd paper

Some results from this paper were included in a further, wider paper³⁰⁹ on Stokes and anti-Stokes correlation in diamond and graphene systems, where the laser power dependence of the signals in diamond and a variety of graphene systems is reported. This is then used to explain the signal ratio in terms of both laser induced heating and the production of correlated Stokes/ anti-Stokes photons for each system.

8.4 Author contribution to 3rd paper

The author designed the exfoliation, fabrication, transfer and cleaning procedures necessary to generate the required tBLG sample, and performed the entire fabrication process, as well as characterising the membranes using AFM. The author also assisted with the preparation of the manuscript.

Optical-Phonon Resonances with Saddle-Point Excitons in Twisted-Bilayer Graphene

Ado Jorio,^{*,†,‡} Mark Kasperczyk,[†] Nick Clark,[¶] Elke Neu,[§] Patrick Maletinsky,[§] Aravind Vijayaraghavan,[¶] and Lukas Novotny[†]

[†]Photonics Laboratory, ETH Zürich, 8093 Zürich, Switzerland

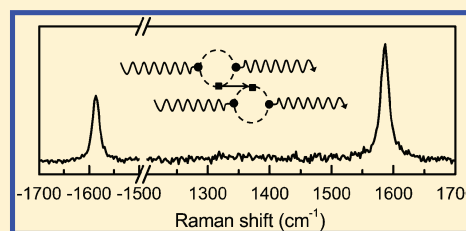
[‡]Departamento de Física, Universidade Federal de Minas Gerais, Belo Horizonte, MG 31270-901, Brazil

[¶]School of Materials and National Graphene Institute, The University of Manchester, Manchester M13 9PL United Kingdom

[§]Department of Physics, University of Basel, Klingelbergstrasse 82, CH-4056 Basel, Switzerland

ABSTRACT: Twisted-bilayer graphene (tBLG) exhibits van Hove singularities in the density of states that can be tuned by changing the twisting angle θ . A θ -defined tBLG has been produced and characterized with optical reflectivity and resonance Raman scattering. The θ -engineered optical response is shown to be consistent with persistent saddle-point excitons. Separate resonances with Stokes and anti-Stokes Raman scattering components can be achieved due to the sharpness of the two-dimensional saddle-point excitons, similar to what has been previously observed for one-dimensional carbon nanotubes. The excitation power dependence for the Stokes and anti-Stokes emissions indicate that the two processes are correlated and that they share the same phonon.

KEYWORDS: Graphene, Raman scattering, optical reflectivity, coherence



Saddle points in the electron dispersion of two-dimensional systems generate logarithmically diverging van-Hove singularities (vHs) in the density of states (DOS).¹ In single-layer graphene (Figure 1a), the vHs occur at the M point for both the valence (π) and conduction (π^*) bands (Figure 1b) and consequently in the joint density of states (JDOS) for optical properties. The JDOS vHs falls into the ultraviolet frequency region in graphene,² as well as the related peak in the optical conductivity (E_{opt}), which should be redshifted from the JDOS vHs due to excitonic effects.³

Twisted-bilayer graphene (tBLG) is formed by adding a twist angle θ between two graphene layers on top of each other.^{4–7} The expansion of the real lattice parameter when building a superstructured tBLG (see arrow in Figure 1c) generates a shrinking of the reciprocal space (Figure 1d), thus bringing the Dirac (K and K') points close together and moving them closer to the M saddle point. Consequently, the vHs will shift in energy, thereby redshifting the JDOS vHs to visible frequencies and even into the far-infrared, depending on the twisting angle θ . This effect has been measured in tBLG using scanning tunneling spectroscopy⁶ and it has been explored using Raman spectroscopy.^{7–16}

Until now, the studied tBLGs have been produced randomly, that is, without controlling the twist angle θ . Furthermore, the generated 2D vHs have been directly measured only by scanning tunneling spectroscopy,⁶ which is limited to energies near the Fermi level and is usually more invasive and less accurate than optical measurements. Here we report the production and optical characterization of a tBLG with a previously selected θ angle, chosen specifically to explore

Stokes and anti-Stokes resonance Raman scattering effects. By mode-engineering the system to work in resonance with the anti-Stokes line, we observe a quadratic power dependence of the anti-Stokes process. This power dependence is indicative of Stokes-induced anti-Stokes scattering in which the phonon generated by the Stokes scattering is consumed by the anti-Stokes process.

Resonance Raman studies show that the peak in the optical conductivity is given by $E_{\text{opt}} = E_0 \sin(3\theta)$ with $E_0 = 3.9$ eV obtained experimentally.¹⁶ By choosing $\theta = 11.3^\circ$, we expect $E_{\text{opt}} = 2.175$ eV. Our tBLG sample was prepared as follows: two mechanically exfoliated single-layer graphene flakes with well-defined edges were found on top of a solid SiO₂ surface. The samples are shown in the optical images in Figure 2a,b, where the well-defined edge directions are indicated by the larger and smaller white lines, respectively, as sufficient indication of either zigzag or armchair crystallographic orientations. In sequence, one of the graphene flakes was transferred and placed on top of the second flake with the well-defined edge rotated with respect to the second by an angle $\theta = 11 \pm 1^\circ$, as indicated by translation of the larger white line from Figure 2a into Figure 2b. Then the $\theta = 11 \pm 1^\circ$ tBLG was transferred onto a 500 nm thick SiN_x membrane perforated with holes of 10 μm diameter (see optical image in Figure 2c and schematics in Figure 2d). Because the samples have areas with bi-, tri-, and many-layer graphene, it is only where the monolayers of each flake overlap

Received: June 27, 2014

Revised: August 18, 2014

Published: September 8, 2014

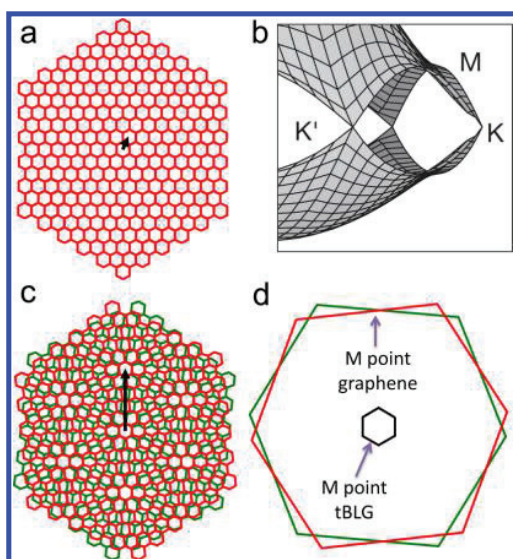


Figure 1. (a) Illustration of a single-layer graphene in real space, and (b) the dispersion of the π and π^* electrons at the edge of the Brillouin zone, close to the Dirac (K and K') and saddle (M) points.² (c) Illustration of a tBLG showing the superstructure Moiré pattern that defines the increased lattice periodicity (arrow). (d) The first Brillouin zones of the two single-layer graphenes (green and red) and of the tBLG (black). The location of the M points are indicated.



Figure 2. (a,b) The optical images of two exfoliated graphene samples with well-defined edges (see white traces). The two graphene samples were superimposed with an angle $\theta = (11 \pm 1)^\circ$ between the well-defined edges. The twisted bilayer graphene (tBLG) is then deposited on top of a Si substrate with a 500 nm thick layer of SiN_x , perforated with 10 μm diameter holes (optical image in (c) and schematics in (d)). The red dot in (c) indicates the hole where the specific tBLG experiments reported here were performed.

that the tBLG is present. In the image in Figure 2c, a dark contour outlines where the tBLG occurs. Notice that while well-defined edges are a sufficient indication of crystallographic orientation, armchair or zigzag cannot be differentiated optically, and the procedure here has 50% chance of generating a $(30^\circ + \theta)$ angle, rather than the wanted θ . A reference sample with $\theta = 0^\circ$ was also fabricated by directly depositing a mechanically exfoliated AB-stacked bilayer graphene (AB-BLG) onto a similar 500 nm thick SiN_x membrane perforated with holes of 10 μm diameter (not shown). All experiments were performed in the freely suspended regions of the graphene tBLG and AB-BLG, that is, in the holes of the SiN_x membranes. This excludes any substrate-related background scattering and artifacts.

Figure 3 shows the reflectivity of the tBLG shown in Figure 2c, measured with a supercontinuum laser and normalized to

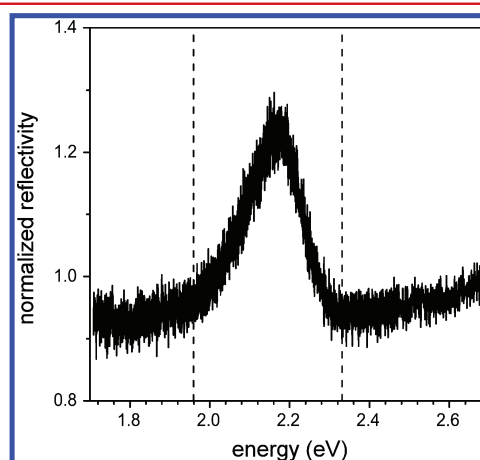


Figure 3. Reflectivity of the tBLG normalized by the reflectivity of AB-BLG. The vertical dashed lines show the energies of the excitation lasers $E_{\text{laser}} = 1.96$ eV and $E_{\text{laser}} = 2.33$ eV.

the response of the AB-BLG. The tBLG reflectivity peak is observed at $E_{\text{opt}} = 2.18$ eV, in excellent agreement with the prediction for $\theta = 11.3^\circ$.¹⁶ The asymmetric reflectivity line shape observed in the ultraviolet for graphene has been identified as a result of the convolution between a well-defined (excitonic) transition with a continuum density of electronic states, which results in a Fano resonance feature.³ The asymmetric line shape shown in Figure 3 is fully consistent with this picture, showing that many-body effects leading to the formation of two-dimensional saddle-point excitons are persistent, remaining in the modified structure of tBLG, as discussed by Havener et al.¹⁷

Having properly characterized the energy of the saddle-point exciton ($E_{\text{opt}} = 2.18$ eV), we can now explore different phenomena in the resonance Raman scattering. Figure 4 shows the anti-Stokes and Stokes G band Raman spectra for AB-BLG (a,b) and tBLG (c,d). In Figure 4a,c, the samples were excited with a frequency doubled YAG laser at $E_{\text{laser}} = 2.33$ eV ($\lambda_{\text{laser}} = 532.0$ nm), while in Figure 4b,d the samples were excited with a HeNe laser at $E_{\text{laser}} = 1.96$ eV ($\lambda_{\text{laser}} = 632.8$ nm). These two laser energies are marked in Figure 3 by the vertical dashed lines. Notice that the two lasers are off resonance with respect to the saddle-point exciton, E_{laser} being blue- or red-shifted from E_{opt} by approximately the G band phonon energy ($E_G = 0.2$ eV).

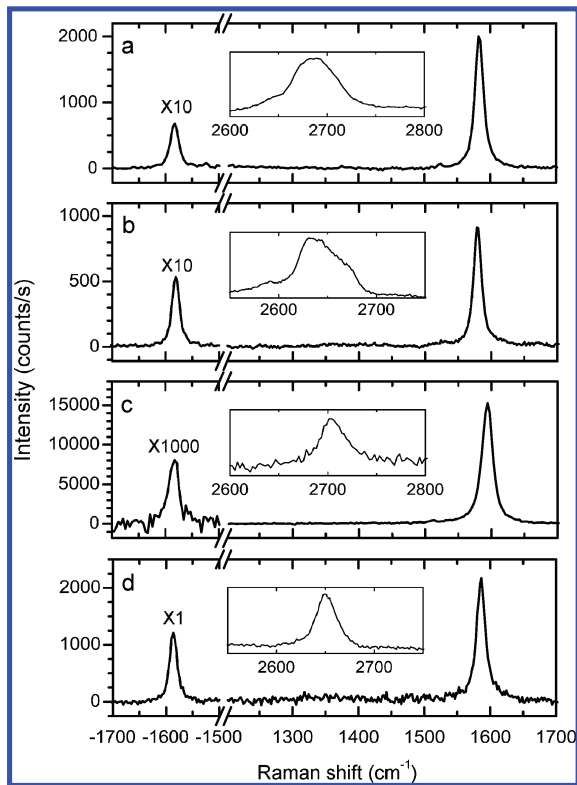


Figure 4. Stokes and anti-Stokes Raman spectra of AB-BLG (a,b) and tBLG (c,d). Panels a and c have been obtained with excitation at $E_{\text{laser}} = 2.33$ eV, while panels b and d have been obtained with excitation at $E_{\text{laser}} = 1.96$ eV. All spectra have been acquired with $P_{\text{laser}} \sim 5$ mW reaching the sample through an air objective (NA = 0.8). The signal is collected in transmission by another air objective with larger NA (= 0.9). The Stokes spectra are displayed down to 1200 cm^{-1} to highlight the absence of the disorder-induced (D) band. The insets show the respective second-order G' (or 2D) bands, characteristic for AB-stacked (a,b) and misoriented (c,d) bilayer graphene. The anti-Stokes signals are magnified for clarity (magnification indicated on top of the respective peaks). All spectra have been corrected to account for detector (charged-coupled device from Excelon - Pixis 100B) and spectrometer (Acton SP2300 from Princeton Instruments, equipped with a 600 grooves/mm grating blazed at 750 nm) nominal efficiencies.

In the AB-BLG case (Figure 4a,b), the Stokes and anti-Stokes signals do not change significantly when changing the excitation laser energy. The spectra obtained with $E_{\text{laser}} = 2.33$ eV is only two times more intense than the spectra obtained with $E_{\text{laser}} = 1.96$ eV (see Figure 4a,b, respectively), due to the E_{laser}^4 dependence of the G-band scattering cross section.^{2,18} The intensity ratio between the Stokes and the anti-Stokes peaks ($I_{\text{aS}}/I_{\text{S}}$) is basically unchanged. However, in the case of tBLG, the spectra change significantly when changing the excitation laser energy. Figure 4c ($E_{\text{laser}} = 2.33$ eV) shows a Stokes signal ~ 10 times stronger than the signal obtained from the AB-BLG, while the anti-Stokes signal is ~ 10 times weaker. On the other hand, Figure 4d ($E_{\text{laser}} = 1.96$ eV) shows a Stokes signal with comparable intensity but an anti-Stokes signal ~ 10 times stronger than in the AB-BLG. The $I_{\text{aS}}/I_{\text{S}}$ ratio thus changes by 3 orders of magnitude when comparing the measurements with $E_{\text{laser}} = 2.33$ eV and $E_{\text{laser}} = 1.96$ eV. This result happens because, while the $E_{\text{laser}} = 1.96$ eV laser leads to a resonance with the anti-Stokes photon emission, the $E_{\text{laser}} = 2.33$ eV laser

gives rise to a resonance with the Stokes photon emission. Qualitatively, similar Stokes versus anti-Stokes resonances were observed in one-dimensional (1D) carbon nanotubes,¹⁹ where sharp resonances are characteristics of the 1D band structure.²⁰ Interestingly, similar effects can be observed in a two-dimensional graphene system due to the saddle-point exciton resonance.

Notice that in Figure 4d, the anti-Stokes G band signal intensity is close to the Stokes intensity. Although similar anti-Stokes scattering resonance has been observed in carbon nanotubes before,^{19,20} an important question remains: where do these high energy G band phonons, which are being annihilated in the highly efficient resonant anti-Stokes emission, come from? To answer this question, we refer to the Feynman diagrams shown in Figure 5. The S diagram shows the Stokes

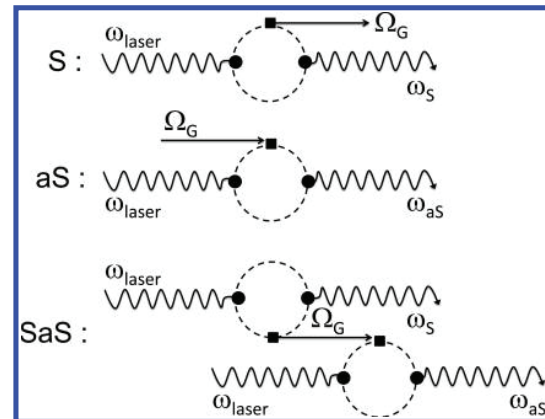


Figure 5. Feynman diagrams for three different Raman scattering processes. Wavy and straight arrows stand for photons and phonons, respectively, while the dashed circles represent electron–hole pairs. Black dots and black squares represent electron–photon and electron–phonon interactions. S stands for Stokes Raman process, aS for anti-Stokes Raman process, and the last diagram, named here SaS, represents the generation of a Stokes and anti-Stokes photon pair via creation and annihilation of the same phonon.

Raman scattering event where a phonon and a Stokes-shifted Raman photon are generated. The aS diagram shows the anti-Stokes Raman scattering process, where one existing phonon is annihilated, generating the anti-Stokes shifted Raman photon. The aS process depends on the previous existence of the phonon in the lattice. In the case of graphene, $E_{\text{G}} = 0.2$ eV is much higher than the thermal (room temperature) energy. The last diagram in Figure 5, which we call here the Stokes–anti-Stokes (SaS) event, describes a nonlinear process where a phonon created by the Stokes process is subsequently annihilated in the anti-Stokes process. The Stokes and anti-Stokes photons emerging from the SaS event can be correlated and, as discussed by Klyshko,²¹ the character of this correlation can be continuously varied from purely quantum to purely classical. In order to observe the SaS scattering, we need to efficiently consume photogenerated phonons in the anti-Stokes process. Otherwise, the phonons will decohere via scattering. We also need high energy optical phonons that are unlikely to be populated at room temperature. These constraints are achieved in our θ -defined tBLG system.

To differentiate the anti-Stokes signal originated from the SaS event from that produced by the usual aS process, we analyze the excitation laser power (P_{laser}) dependence of the

anti-Stokes Raman intensity (I_{aS}). Considering both the aS and SaS events in Figure 5 separately, I_{aS} assumes the form

$$I_{aS} = P_{\text{laser}} \{ C_{aS} \eta + C_{\text{SaS}} P_{\text{laser}} \} \quad (1)$$

where C_{aS} and C_{SaS} are constants and $\eta = 1/[e^{(\hbar\omega_{\text{phonon}}/k_B T)} - 1]$ is the temperature dependent Bose–Einstein phonon distribution function. Here we considered $\eta + 1 \approx \eta$. The sources for I_{aS} are the laser and the phonon, and the two components on the right side of eq 1 are direct consequences of the aS and SaS Feynman diagrams shown in Figure 5, respectively. The first component (aS) in eq 1 is well-known,² while the second term has been proposed here. In the thermal regime, the dependence of I_{aS} on P_{laser} reflects the material temperature through η . In the regime where the SaS event dominates, I_{aS} is proportional to P_{laser}^2 .

Figure 6 shows the power dependence of the Stokes (a) and anti-Stokes (b) signals from the tBLG (blue) and from the AB-

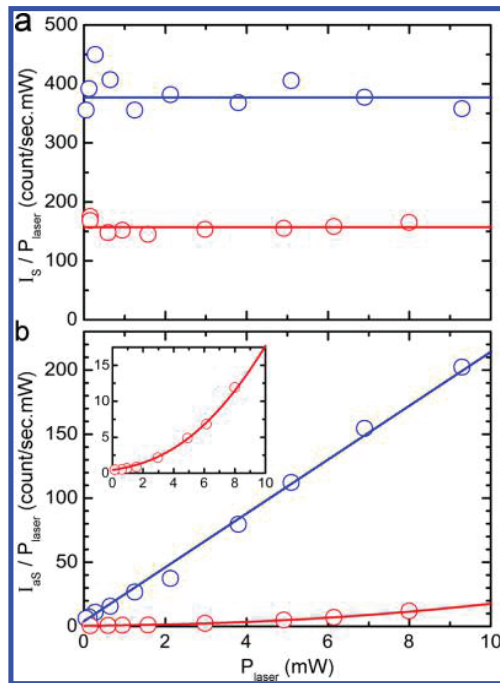


Figure 6. Power dependence of (a) Stokes (I_S) and (b) anti-Stokes (I_{aS}) Raman intensities for the tBLG (blue) and AB-BLG (red) obtained with $E_{\text{laser}} = 1.96$ eV. The G band peaks were fit with a Lorentzian function. The Raman intensities were obtained from the peak integrated areas and then normalized by the laser power (I_S/P_{laser} and I_{aS}/P_{laser}) to clearly demonstrate the difference in behavior. Circles are experimental data and lines are fitting functions according to eq 1 (see text for fitting values). The inset in (b) is a magnified version of the AB-BLG data.

BLG (red), when excited with $E_{\text{laser}} = 1.96$ eV. The intensities are normalized by the excitation laser power. Figure 6a shows that the Stokes signal scales linearly with excitation power for both samples, which is indicative for the spontaneous scattering regime. However, the anti-Stokes Raman signals of the two samples show markedly different behaviors (Figure 6b).

The anti-Stokes intensity of the tBLG excited at $E_{\text{laser}} = 1.96$ eV shows a quadratic power dependence within the measured range (0–10 mW, blue data in Figure 6b). The data can be accurately fitted by eq 1 considering η constant at $T = 295$ K with $C_{aS} = 9.1 \text{ W}^{-1} \text{ s}^{-1}$ and $C_{\text{SaS}} = 2.3 \times 10^{-9} \text{ W}^{-2} \text{ s}^{-1}$. For

comparison, the power-normalized anti-Stokes intensity (I_{aS}/P_{laser}) from the AB-BLG reference shows a much less pronounced enhancement within the measured range (see red data in Figure 6b) with a clear nonlinear power dependence behavior (see inset). The AB-BLG I_{aS}/P_{laser} data can be fit by eq 1 with $C_{aS} = 1.0 \text{ W}^{-1} \text{ s}^{-1}$, assuming that the temperature depends linearly on the excitation laser power as $T = 295 + C_T P_{\text{laser}}$ with $C_T = 27 \text{ mW}^{-1} \text{ K}$ and $C_{\text{SaS}} = 0$. According with this latest equation, for $P_{\text{laser}} > 10$ mW the AB-BLG temperature crosses 600 °C. The AB-BLG sample burns for laser powers above 12 mW, while the tBLG withstands higher powers, evidencing the cooling process induced by the efficient anti-Stokes resonant emission in tBLG. Consistent with this picture, Figure 7 shows that the G band frequency (ω_G) from tBLG

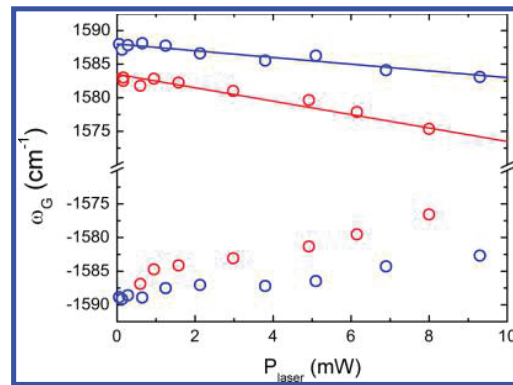


Figure 7. Power dependence of the G band frequencies ω_G for tBLG (blue) and AB-BLG (red). Positive and negative values stand for Stokes and anti-Stokes peaks, respectively. The lines are fit to the Stokes data, given by $\omega_G^{\text{tBLG}} = 1588.0 - 0.5 P_{\text{laser}}$ (blue) and $\omega_G^{\text{AB-BLG}} = 1583.5 - 1.0 P_{\text{laser}}$ (red).

(blue data) exhibits a smaller power dependence (frequency downshift with increasing power) when compared to ω_G from AB-BLG (red data). It is important to comment, however, that the presence of some heating in the tBLG or the SaS event in the AB-BLG reference sample cannot be ruled out from the results shown here, since a relatively small nonzero temperature increase for tBLG or C_{SaS} term for AB-BLG can be added to the fitting curves without significantly compromising the fitting qualities.

The SaS process has been measured in diamond.²² The experiments were carried out in the femtosecond pump regime, where the extremely high number of photons per pulse significantly enhances the SaS probability. It is surprising that our results indicate the observation of the SaS event in graphene with a significantly low power from a CW laser. Lee et al.²² demonstrated the quantum nature of the SaS correlation in bulk diamond at room temperature by measuring a nonclassical SaS second-order time correlation function $g^{(2)}$. This type of measurement has to be developed in tBLG, so that the correlation nature of the SaS event, as proposed by Klyshko²¹ and observed for bulk diamond,²² could be explored. This effect places tBLG as a candidate for a source of entangled photons and for a host for quantum memory.^{21,22}

It is important to make clear the reason why we built a tBLG and performed the experiment in the condition of anti-Stokes Raman resonance. When the system is in resonance with the anti-Stokes photon emission, the probability that the exciton and the phonon decay into a photon is high. Out of resonance,

the exciton and the phonon may rather decay through different processes. We actually performed similar power dependence measurements in tBLG with the 2.33 eV laser, that is, in resonance with the Stokes photon emission. The possibility that the SaS process is ruling the aS photon intensity in the Stokes resonance case cannot be ruled out. However, the signal intensities are not strong enough for the data to support this assumption (or to reject it). Therefore, the SaS process introduced may apply to graphene systems more broadly.

We expect the SaS event also to play a role in the anti-Stokes Raman scattering intensity from other low dimensional materials, like carbon nanotubes. Steiner et al.²³ observed laser-induced phonon cooling in single-wall carbon nanotubes by introducing them into an external optical cavity. They discussed how this scheme can be used to remove high energy hot phonons, which play an important role in the thermal and electrical properties of low-dimensional structures.^{24,25} Here, we designed a system that can perform like a cooling system, but the nanostructure itself is the cavity. Because of the M-point engineering scheme used to build the tBLG, the resonance can be tuned to work at any selected wavelength from the far-infrared up to the ultraviolet, in the vibration amplifying or cooling mode, just by changing the tBLG angle θ . Also, multiple twisted bilayer graphenes can be stacked to enhance the efficiency further (separated for example by hexagonal-BN to avoid tBLG–tBLG electronic interaction).

Finally, because Raman spectroscopy is established as an important tool to study and characterize nanostructures, our findings indicate that the SaS event has to be considered when using this technique to extract structural and transport properties of low-dimensional structures. For example, the SaS phenomena will have to be considered for quantitative analysis of temperature, thermal conductivity, and carrier dynamics, when extracted from the G band, because the peak properties (intensity, frequency, and line width) are significantly dependent on the Kohn anomaly²⁶ statistics. In future work, it will be interesting to study changes of the phonon (G band) line width and frequency as a function of detuning ($E_{\text{opt}} - E_{\text{laser}}$), which may change the influence of the Kohn anomaly effects in the G band properties. Furthermore, because defects change the phonon lifetimes, there could be a competition between defect scattering and the coherent anti-Stokes generation, thus opening another route for further studies.

■ AUTHOR INFORMATION

Corresponding Author

*E-mail: adojoorio@fisica.ufmg.br. Phone: +55 (31)34096610. Fax: +55 (31)34095600.

Notes

The authors declare no competing financial interest.

■ ACKNOWLEDGMENTS

The authors strongly acknowledge valuable discussions with Dr. P. Bharadwaj and L. G. Cançado. A.J. acknowledges Inmetro for the background developed in tBLG, CAPES and ETH for financing his visit to ETH Zurich. L.N. thanks financial support by the Swiss National Science Foundation (SNF) through Grant 200021-14 6358. A.V. thanks the Engineering and Physical Sciences Research Council (EPSRC) for financial support through Grants EP/G035954/1 and EP/K009451/1.

■ REFERENCES

- (1) Hove, L. V. The occurrence of singularities in the elastic frequency distribution of a crystal. *Phys. Rev. B* **1953**, *89* (6), 1189.
- (2) Jorio, A.; Dresselhaus, M. S.; Saito, R. *Raman Spectroscopy in Graphene Related Systems*; Wiley-VCH: New York, 2011.
- (3) Mak, K. F.; Shan, J.; Heinz, T. F. Seeing many-body effects in single- and few-layer graphene: observation of two-dimensional saddle-point excitons. *Phys. Rev. Lett.* **2011**, *106*, 046401.
- (4) Mele, E. J. Commensuration and interlayer coherence in twisted bilayer graphene. *Phys. Rev. B* **2010**, *81*, R161405.
- (5) Suárez Morell, E.; Correa, J. D.; Vargas, P.; Pacheco, M.; Barticevic, Z. Flat bands in slightly twisted bilayer graphene: Tight-binding calculations. *Phys. Rev. B* **2010**, *82*, R121407.
- (6) Li, G.; Luican, A.; Lopes dos Santos, J. M. B.; Castro Neto, A. H.; Reina, A.; Kong, J.; Andrei, E. Y. Observation of Von Hove singularities in twisted graphene layers. *Nat. Phys.* **2010**, *6*, 109.
- (7) Jorio, A.; Cançado, L. G. Raman spectroscopy of twisted bilayer graphene. *Solid State Commun.* **2013**, *175–176*, 3.
- (8) Ni, Z.; et al. G-band Raman double resonance in twisted bilayer graphene: Evidence of band splitting and folding. *Phys. Rev. B* **2009**, *80*, 125404.
- (9) Gupta, A. K.; Tang, Y.; Crespi, V. H.; Eklund, P. C. Nondispersive Raman D band activated by well-ordered interlayer interactions in rotationally stacked bilayer graphene. *Phys. Rev. B* **2010**, *82*, 241406.
- (10) Carozo, V.; et al. Raman Signature of Graphene Superlattices. *Nano Lett.* **2011**, *11*, 4527.
- (11) Righi, A.; et al. Graphene Moiré patterns observed by umklapp double-resonance Raman scattering. *Phys. Rev. B* **2011**, *84*, 241409.
- (12) Havener, R. W.; Zhuang, H.; Brown, L.; Hennig, R. G.; Park, J. Angle-Resolved Raman Imaging of Interlayer Rotations and Interactions in Twisted Bilayer Graphene. *Nano Lett.* **2012**, *12*, 3162.
- (13) Kim, K.; et al. Raman spectroscopy study of rotated double-layer graphene: misorientation-angle dependence of electronic structure. *Phys. Rev. Lett.* **2012**, *108*, 246103.
- (14) Sato, K.; Saito, R.; Cong, C.; Yu, T.; Dresselhaus, M. S. Zone folding effect in Raman G-band intensity of twisted bilayer graphene. *Phys. Rev. B* **2012**, *86*, 125414.
- (15) Campos-Delgado, J.; Cançado, L. G.; Achete, C. A.; Jorio, A.; Raskin, J.-P. Raman scattering study of the phonon dispersion in twisted bilayer graphene. *Nano Res.* **2013**, *6*, 269.
- (16) Carozo, V.; et al. Resonance effects on the Raman spectra of graphene superlattices. *Phys. Rev. B* **2013**, *88*, 085401.
- (17) Havener, R. W.; Liang, Y.; Brown, L.; Yang, L.; Park, J. Van Hove Singularities and Excitonic Effects in the Optical Conductivity of Twisted Bilayer Graphene. *Nano Lett.* **2014**, *14*, 3353.
- (18) Cançado, L. G.; Jorio, A.; Pimenta, M. A. Measuring the absolute Raman cross section of nanographites as a function of laser energy and crystallite size. *Phys. Rev. B* **2007**, *76*, 064304.
- (19) Souza Filho, A. G.; Jorio, A.; Hafner, J. H.; Lieber, C. M.; Saito, R.; Pimenta, M. A.; Dresselhaus, G.; Dresselhaus, M. S. Electronic transition energy E_{ii} for an isolated (n, m) single-wall carbon nanotube obtained by anti-Stokes/Stokes resonant Raman intensity ratio. *Phys. Rev. B* **2001**, *63*, 241404(R).
- (20) Jorio, A.; Souza Filho, A. G.; Dresselhaus, G.; Dresselhaus, M. S.; Saito, R.; Hafner, J. H.; Lieber, C. M.; Matinaga, F. M.; Dantas, M. S. S.; Pimenta, M. A. Joint density of electronic states for one isolated single-wall carbon nanotube studied by resonant Raman scattering. *Phys. Rev. B* **2001**, *63*, 245416.
- (21) Klyshko, D. N. *Photons and Nonlinear Optics*; Gordon and Breach Science Publishers: New York, 1988.
- (22) Lee, K. C.; et al. Macroscopic non-classical states and terahertz quantum processing in room-temperature diamond. *Nat. Photonics* **2012**, *6*, 41.
- (23) Steiner, M.; Qian, H.; Hartschuh, A.; Meixner, A. J. Controlling Nonequilibrium Phonon Populations in Single-Walled Carbon Nanotubes. *Nano Lett.* **2007**, *7* (8), 2239.

(24) Steiner, M.; et al. Phonon populations and electrical power dissipation in carbon nanotube transistors. *Nat. Nanotechnol.* **2009**, *4*, 320.

(25) Barreiro, A.; Lazzeri, M.; Moser, J.; Mauri, F.; Bachtold, A. Transport properties of graphene in the high-current limit. *Phys. Rev. Lett.* **2009**, *103*, 076601.

(26) Piscanec, S.; Lazzeri, M.; Mauri, F.; Ferrari, A. C.; Robertson, J. Kohn Anomalies and Electron-Phonon Interactions in Graphite. *Phys. Rev. Lett.* **2004**, *93*, 185503.

9 4th paper

***“Nanometre electron beam sculpting of suspended
graphene and hexagonal boron nitride
heterostructures”***

Nick Clark, Edward Lewis, Sarah Haigh, Aravind Vijayaraghavan

Manuscript in Submission

(2016)

9.1 Introduction to 4th paper

Patterning of graphene at few-nm resolution is desired to enable the creation of graphene based electrodes for molecular electronics. Patterning suspended graphene using a STEM beam has been demonstrated, but is unsuitable for the creation of nanogaps as the edges sag away once mechanically separated due to tension in all suspended sheets. We aimed to pattern graphene on top of a thin hBN support, meaning that we could electrically separate graphene areas without mechanically separating them. We aimed to monitor the progress of the cuts using EELS and EDXS to guide us in optimising the cutting process, and work out a repeatable and reliable patterning procedure.

9.2 Summary of 4th paper

We successfully demonstrated cuts on graphene/ hBN structures down to sub 2nm widths along lengths of hundreds of nm. The cutting process was monitored using EELS and EDXS spectrometry, and the effects of various writing parameters were investigated. We were able to find a repeatable, reliable set of cutting parameters, but the cutting behaviour was strongly dependent on the local environmental conditions, i.e. the level of contamination.

9.3 Author Contribution

The thesis author designed the experiment, with advice from AV and SH. The fabrication process was designed, optimised and carried out by the author. The TEM characterisation was performed by EL and SH. The data was analysed and interpreted by the author. The manuscript was prepared and written by the thesis author with assistance from AV, EH and SH.

Nanometre electron beam sculpting of suspended graphene and hexagonal boron nitride heterostructures

N. Clark,^{1,2} E. Lewis,¹ S. Haigh,¹ A. Vijayaraghavan^{1,2*}

¹School of Materials, University of Manchester, Sackville Street, Manchester, M13 9PL, UK

²National Graphene Institute, University of Manchester, Sackville Street, Manchester, M13 9PL, UK

*e-mail: aravind@manchester.ac.uk

Nano-patterned and suspended graphene membranes find applications in electronic devices, filtration and nano-pore DNA sequencing. However, the fabrication of suspended graphene structures with nanoscale features is challenging. We report the direct patterning of suspended membranes consisting of a graphene layer on top of a thin layer of hexagonal boron nitride which acts as a mechanical support, using a highly focused electron beam to fabricate structures with extremely high resolution within the scanning transmission electron microscope. The boron nitride support enables the fabrication of stable graphene geometries which would otherwise be unachievable, by preventing intrinsic strain in graphene membranes from distorting the patterned features after areas are mechanically separated. Line cuts with widths below 2 nm are reported. We also demonstrate that the cutting can be monitored *in situ* utilising electron energy loss spectroscopy (EELS).

Graphene is an atomically thin¹ carbon allotrope with exceptional mechanical strength² and electron conductivity³. Patterning graphene at extremely small length scales can be used to create interesting physical systems, such as nanogap electrodes for molecular electronics⁴, molecular separation membranes⁵, nanopores for DNA sequencing⁶, and nanoribbons⁷ for studying electron transport phenomena.

Molecular electronics^{8,9} represent the ultimate in device miniaturisation, where individual molecules are used as circuit components. The overall performance of such systems is largely determined by the electrode/molecule interface (anchor) and ensuring the stability of such contacts is a major challenge. Gold based systems are limited by the instability of thiol-gold bonding due to the mobility of gold atoms at ambient temperatures, and variability in electrode geometry between repeat devices¹⁰. Systems based on sp² bonded carbon electrodes formed from graphene¹¹ or carbon nanotubes (CNTs)¹² have been suggested as an alternative, with a number of theoretically predicted advantages¹³ as long as the gap can be made narrow enough to bridge molecules with lengths up to a few nm. Carbon electrodes also have the advantage of being atomically stable at room temperature¹⁴. Molecules terminated with polyaromatic hydrocarbon endgroups can bridge to carbon electrodes in a secure and conductive way via mechanical attachment of the aromatic moieties either side of the gap¹⁵⁻¹⁷.

Solid state nanopores are of interest for filtration and biomolecular analysis, particularly DNA sensing⁶. Typically, a DNA molecule is threaded through a hole in a thin membrane using an applied voltage, and the ionic current across the membrane is monitored. It has been suggested that different bases along the DNA molecule block the ionic current through the pore by differing amounts, in principle allowing determination of the

base order. Nanopores in large graphene sheets have demonstrated DNA detection¹⁸⁻²⁰, although in all cases the translocation has occurred too quickly to resolve signals from individual bases. An alternative strategy is measuring the conductance of a graphene nanoribbon patterned with a nanopore in the centre. Theoretical simulations have suggested that electron transport through the ribbon is strongly affected by interactions with nucleotides in the pore²¹, with different bases having differing signals due to the differences in coupling strength. Detection using this mechanism has been reported²², although sequencing remains elusive due to the high speed of the translocation and low signal to noise ratios seen in realised devices most likely as a result of the fabrication challenges.

Graphene nanoribbons themselves are of particular scientific and technological interest. As the ribbon width is reduced, there are significant structure dependent (primarily edge orientation) changes to the electronic, magnetic and optical properties²³⁻²⁶, including the opening of a band gap^{7,27}, due to the quasi 1D spatial confinement at few nm scale widths²⁸. They are therefore promising candidates for building electrical interconnects, transistors, and sensors²⁹⁻³². Fabrication limitations mean that the properties of graphene nanoribbons with widths below around 10 nm have not been fully experimentally explored³³.

Graphene is typically patterned using electron beam lithography (EBL) and subsequent plasma etching into structures such as Hall bars³⁴, nanoribbons²³, quantum dots³⁵ and nanogap electrodes^{12,36}. However, fundamental limitations³⁷ mean that this technique cannot be used to pattern features at length scales of less than ~10 nm. Scanning probe based lithography on graphene has also been demonstrated^{38,39}, but is slow and unwieldy. Carbon nanogap electrodes are typically fabricated using feedback controlled electroburning^{14,40} to open a narrow physical gap in a graphene ribbon. Direct write patterning of suspended graphene promises a far higher patterning resolution and control of the edge geometry. Patterning in focused ion beam (FIB) systems using Ga ions⁴¹ or He ions^{42,43} has been reported, but can cause damage to the neighbouring graphene reducing the potential of this approach for electronic applications⁴⁴.

Recently, the highly focussed electron beam of the scanning transmission electron microscope (STEM) has been used to generate nanopores^{45,46} and nanoribbons^{47,48} in suspended graphene sheets. The use of this technique in patterning carbon nanotubes has previously been reported^{49,50}, but the geometry means that it can be more usefully applied to planar structures. Nanopatterning in the STEM can be combined with simultaneous electron diffraction or atomic resolution imaging, enabling the fabrication of nanostructures with controlled edge geometries⁵¹. *In situ* holders also allow patterning to be performed at a range of temperatures and patterning at 600 °C has been found to induce

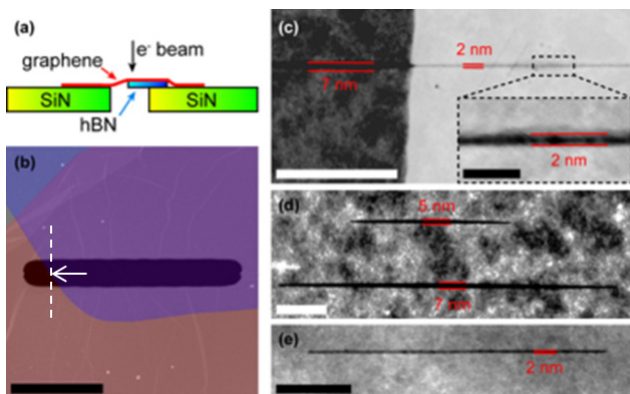


Figure 1 Patterning monolayer graphene and hBN supported monolayer graphene using a 1.4 nA STEM beam. (a) schematic (not to scale) showing the membrane structure when viewed in cross section at the position indicated by the dotted line superimposed on the image in (b). (b)-(e) HAADF STEM images illustrating the patterning of this structure. (b) shows a low magnification image of the sample. The dark pill shape in the centre is the hole in the silicon nitride membrane. A 9 nm thick hBN flake covers the majority of the membrane and is false coloured blue. A monolayer graphene flake covers the entire membrane, and is false coloured red. The scale bar is 5 μm . (c) shows a STEM cut in the suspended region of the sample across the edge of the hBN flake. The cut has a width of $\sim 7\text{ nm}$ on the unsupported graphene, and a width of just $\sim 2\text{ nm}$ on the hBN supported area. The equivalent line dose for this cut was 625 mC/m. The scale bar is 100 nm. The inset shows a higher magnification image of the indicated area. Small bridges over the cut are visible. The scale bar is 20 nm. (d) shows 2 cuts in unsupported monolayer graphene with lengths of 161 and 332 nm, using equivalent line doses of 311 and 151 mC/m for the short and long cuts respectively. The cut features are broadened by tension within the membrane, with the widest areas in the centre of the cut. The scale bar is 50 nm. (e) shows a long cut on an hBN supported region of monolayer graphene, with a line dose of 1.8 mC/m. In contrast to (d) no bowing or deformation of the membrane after patterning is visible. The scale bar is 50 nm.

self-repair of the graphene lattice⁵². However, the fact that the graphene structure needs to be self-supporting limits the type of structures that can be produced. For example, use of this technique to produce nanogap electrodes is extremely challenging, as the electrodes need to be electrically isolated from each other, meaning they must be mechanically unseparated. Once cut, they would be unlikely to maintain the required sub-5nm gap due to intrinsic tension and mechanical instability at the electrode ‘tip’.

In order to overcome these limitations, we demonstrate the direct write electron beam nanopatterning of two layer heterostructures consisting of monolayer or bilayer graphene on top of a thin (6-9 nm) hexagonal boron nitride (hBN) layer. hBN is commonly used as a substrate for graphene due to its insulating nature and atomic flatness⁵³ (for thick flakes). Here we propose its use as an insulating mechanical support in suspended devices, to prevent distortion of the membrane after partial patterning. We report successful patterning of these heterostructures, reproducibly generating line cuts in graphene with lengths of hundreds of nanometers and widths less than 2 nm. Figure 1 compares the patterning of thin lines in unsupported and hBN supported monolayer graphene. Figure 1(c) and (d) show that cuts in the unsupported graphene ‘bow’ outwards such that the width of the central part of the cut depends on the cut length, rather than any patterning conditions. In contrast, we observe that cuts in the hBN supported graphene show a much narrower cut profile, as the hBN prevents distortion of the membrane (Figure 1(e)). Minimum cut widths in the heterostructure were less than 2 nm, whereas in unsupported graphene widths were limited to greater than 5 nm.

A two-step approach whereby conventional EBL and oxygen plasma etching are used to pattern the graphene-hBN heterostructure into nanoribbons and then followed by STEM nanosculpting is a viable route to the fabrication of extremely narrow nanogap electrodes. When applied creatively, this approach could be applied to create a wide array of geometries which are not achievable when the graphene is required to be self-supporting.

A significant challenge in generating ultra-narrow patterns is the verification of the effectiveness of the patterning – whether the

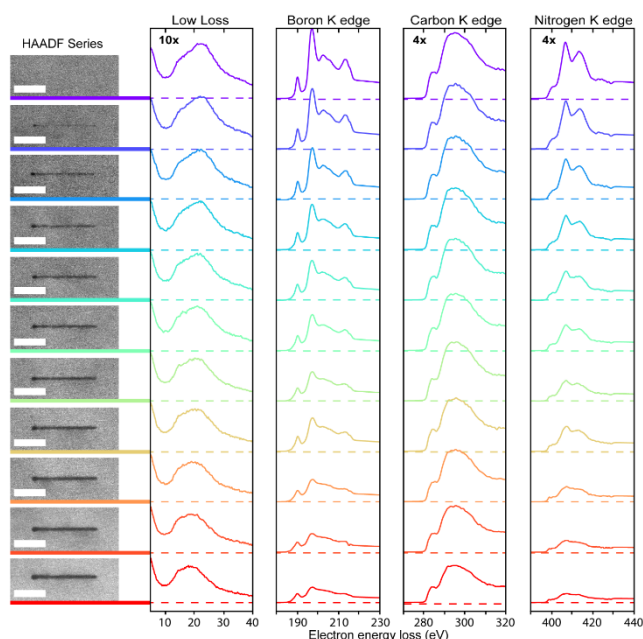


Figure 2 Successive EEL spectra obtained whilst patterning. The evolution of the EELS spectra captured whilst patterning monolayer graphene on 6.5 nm thick hBN. All 11 scans/cuts were made with the same writing parameters, with an effective line dose of 100 mC/m per scan. 4 features of the energy loss spectra are shown; the low loss region (5-40eV) and the extracted elemental edges (after background subtraction) for boron, carbon and nitrogen. The intensity of the low loss region of the spectra has been enhanced by a factor of 10, and the C and B edges by a factor of 4 to aid visibility. Low dose HAADF images of the cutting region before scanning are shown to the left of the corresponding spectra. The scale bars are 20 nm.

cut has proceeded to entirely separate the graphene on both side, and if so what the true width of the cut is. This has been typically done by imaging the graphene at atomic resolution after the cutting, which necessitates a high electron dose and may cause further damage or edge reconstruction to the graphene, and can induce broadening or closure of the cut⁵². In order to overcome this, we demonstrate here that it is possible to monitor the cutting progression in real time as well as the width of the cut using electron energy loss spectroscopy (EELS), removing the need for subsequent additional atomic resolution imaging.

RESULTS

Imaging whilst cutting was performed in STEM mode, which allowed accurate control over the electron dose in order to avoid unwanted beam induced damage¹⁸. The probability of knock-on damage from the beam is dependent on the incident electron energy, the beam current, and the electron dose. The threshold for knock-on damage for graphene has been theoretically predicted to be $\sim 113\text{ keV}$ ⁵⁴, but experimental measurements observe some electron sputtering at high magnification for lower voltages between 80-100 keV, possibly as a result of catalytic impurities^{55,56}. For hBN monolayers the knock-on threshold energies are 80 keV and 120 keV for B and N sites respectively^{57,58}. Experimentally, it is challenging to frequently modify the accelerating voltage. Therefore a constant accelerating voltage of 200 keV provides a suitable compromise between the energy needed to reliably perform patterning with that required to preserve the structure while imaging. We find that no damage is detectable after repeated imaging by employing low magnifications and short dwell times ($\sim 2\mu\text{s}$). However, longer dwell times did result in visible damage to the sample.

Figure 1 shows the series of EEL spectra obtained over repeated scans whilst patterning a line in a graphene monolayer

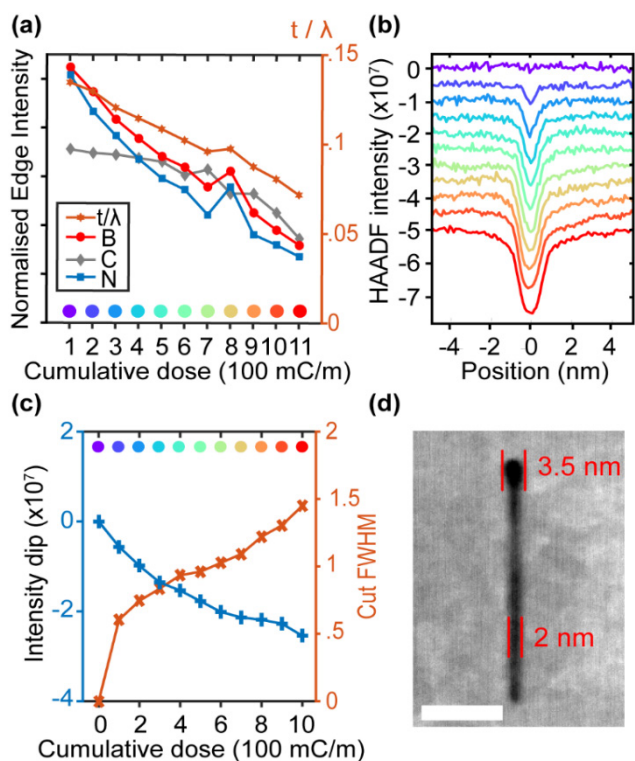


Figure 3 Tracking cutting progression using electron energy loss spectroscopy. Extracted parameters from the spectral series shown in figure 1. The colours in (a)-(c) represent the spectra of corresponding colour. (a) shows the evolution of the normalised core loss edge intensities of B, C and N derived from the energy loss spectra, and the estimated ratio t/λ . (b) shows the HAADF intensity perpendicular to the cut, integrated along the cut for the image series in (a). The progressive traces are offset for clarity. (c) shows the difference in the HAADF intensity measured on the membrane and in the centre of the cut from (b), as well as the width (FWHM) of the cut feature. (d) shows a HAADF STEM image of the area after patterning.

supported by a 6.5 nm thick hBN flake. In total, 11 cuts or scans were used, with each scan corresponding to a line dose of 100mC/m. The individual edges shown were obtained from the captured core loss EELS spectra integrated along the length of the cut to reduce noise. The edge shapes do not change significantly during the cutting process, but the position of the inelastic scattering peak in the low loss spectrum reduces from ~ 23 eV to ~ 18 eV. The progression of the peak intensities with subsequent cuts, normalised by the expected ionization cross-section, is plotted in figure 4(a), and allows us to track the relative quantities of boron, nitrogen, and carbon atoms within the interaction volume of the probe. As can be seen from the plot (and the original spectra in figure 1), the ionization edges are still present even when a continuous cut has been formed.

The low loss spectral region is widely used to monitor specimen thickness by estimating a value for t/λ from the relative intensities of the parts of the spectrum corresponding to elastic and inelastic scattering and using the log ratio technique⁵⁹, where t is the sample thickness and λ is the mean free path for inelastic scattering. Hence we can use the t/λ value obtained during successive scans to monitor cutting progression. Figure 4(a) shows the t/λ value plotted alongside the normalised ionization edge strengths for the 3 main atomic species present. While a significant drop in the t/λ value is observed during cutting, it does not drop to near zero after patterning is finished, and sees a smaller relative decline than the core loss signals in the high loss region of the EEL spectra.

The cut progression can also be monitored by looking at the change in the HAADF intensity of the cut feature. The line profiles from the successive survey images in figure 2(a) perpendicular to the cut are integrated along the cut direction and collated in figure

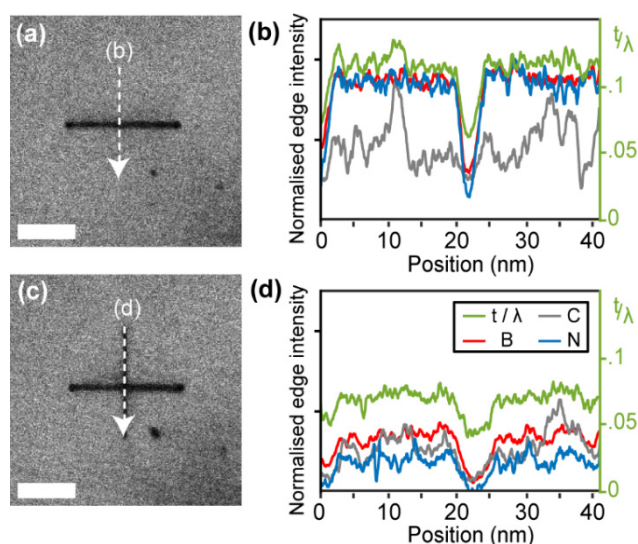


Figure 4 Elemental core loss EEL intensity profiles obtained during vertical line cutting across an existing horizontal cut. (a) and (c) show HAADF STEM images of the same area at different patterning stages. The horizontal line was first patterned using 4 successive cuts with a line dose of 247 mC/m. The same conditions were then used to pattern the vertical line. (a) shows the area prior to starting the vertical line, and (c) shows the area after 3 vertical cuts. The scale bars are 20 nm. (b) and (d) show the elemental core loss intensities at each point along the first vertical cut and along the final (fourth) vertical cut at the positions indicated by the arrows in (a) and (c) respectively. Even in the region where the vertical cut crosses the horizontal cut, the measured edge intensities do not reach zero, although the nitrogen peak becomes weaker than the noise level in the final spectra. The right axes and the green trace show the value of t/λ extracted from the respective low loss spectra. More details on the cutting of this cross feature can be found in figures S3 and S4 of the SI.

2(c). The relative intensity changes and FWHM of the successive cuts are plotted in figure 2(d).

The final resultant cut is pictured in figure 4(d) (rotated 90° clockwise from the low dose images in figure 1). The width of the feature is around 2 nm for most of its length, but broadens to 3.5 nm at one end, which was the beam rest position during scanning and received a slightly higher dose during fly back correction. It can be seen that the cut feature is not completely continuous, with bridges crossing the gap, especially in the centre of the line. The nature of these bridge regions is investigated further in figure 5.

The data shown in figure 2 are integrated sum spectra for the whole cut region, although the same features are observed in all individual point spectra within these scans even at the widest part of the cut. However, we can also interrogate the individual pixel EEL spectra to gain information on the local structure and composition across the scan. Figure 4 shows the elemental profiles obtained while patterning vertically across an existing horizontal line cut. The EELS spectra at each point were fit to obtain peak intensities corresponding to B, C and N ionization edges and the t/λ values obtained from the low loss EEL point spectra are also plotted. It is noted that the elemental edge signals do not drop to zero in the centre of the cut region, even after 3 subsequent line scans, although the nitrogen edge in (d) became significantly smaller than the noise. However, as was observed in figure 1, the relative intensity change for the core loss ionization peaks is greater than that for the low loss t/λ region.

Figure 5 depicts the results of prolonged scanning of the same specimen area after line cutting, in which a large hole has appeared around the original cut (supplementary video 1 shows the formation of this feature during imaging). After prolonged scanning of this region the (horizontal) cut feature width is increased to ~ 7 nm wide, and is bordered on the upper side by a dark grey area of > 5 nm width. The frame border from the video is visible as a vertical feature on the left, which has etched completely through close to the original cut. EEL spectrum image of this region allows mapping of the composition for areas with different HAADF intensity. Summed EEL spectra from various

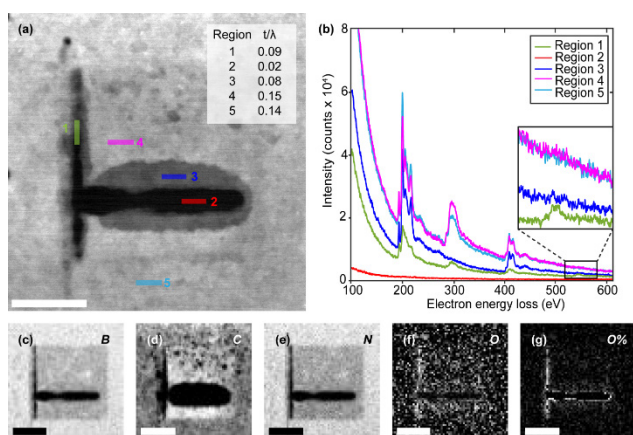


Figure 5 EELS mapping of large cut features in monolayer graphene on 6.5 nm thick hBN. The horizontal feature is the cut corresponding to that shown in figure 1 after progressive imaging as shown in supplementary video 1. The vertical feature corresponds to the left edge of the frame during the video acquisition. (a) shows a HAADF STEM image of the area. (b) shows the EELS spectra integrated over the areas highlighted by the corresponding colours in (a). The inset is a zoomed in region showing the location of the O edge. (c) - (f) show maps of the core loss peak intensities for B, C, N and O edges respectively. (g) shows the elemental O percentage. All scale bars represent 20 nm.

locations indicated in Figure 5(a) on the higher resolution HAADF STEM image) are plotted in Figure 5(b). In region 1 (on the video frame boundary), indicated by the green colour, B, C and N core loss edges are clearly visible, as well as a faint oxygen edge (visible in the inset in panel (b)) at an energy loss of 532 eV. Region 2 is completely within the hole region, and is indicated by the red spectra. Here no edges are visible, although there is a small inelastic scattering background visible in the spectra. Region 3 is in the dark grey area on the image, and is indicated by the dark blue spectra. Here, only edges due to B and N are present. This grey area is similar to that seen in other images after repeated imaging (for example the bridges shown in figure 1(c), the strip in figure 7(a), the etched corners in figure 8(b), with further examples being found in the supplementary information); we reason that in all cases this dark grey area corresponds to the region where the graphene has been etched away from its edges due to prolonged irradiation when cutting or imaging but the hBN substrate still survives. Regions 4 (light blue) and 5 (pink) in figure 6(a) represent similar areas, however region 4 was part of the scanning area during the prolonged imaging, whilst region 5 has only previously been exposed to a minimal amount of radiation. Compared to region 5, the irradiated region shows a slight drop in the counts for B and N, but a significant rise in the amount of carbon, due to the beam attracting local mobile contamination. The lower panels in the figure show elemental maps extracted from the spectral image. All are normalised so that a black pixel represents no signal, and a white pixel represents the highest signal level in the image. The ‘square’ feature corresponding to the image border during the video capture is visible as a darker area in the B and N maps and a lighter area in the C map, as indicated by the spectra from regions 4 and 5. The areas where the graphene has been etched away, including holes separate from the main cut feature, are clearly visible in the C map. The O map is unclear due to the relatively low signal to noise level, but the relative oxygen percentage map in panel (g) shows that the O signal is only significant around the edges of the main cut feature. This distribution of oxygen signal is also seen in elemental maps of cut features acquired using energy dispersive x-ray spectroscopy (as illustrated in figure S14 in the supplementary material). This is consistent with previous atomic resolution EELS studies of hBN monolayers which show oxygen atoms can substitute into nitrogen sites⁶⁰.

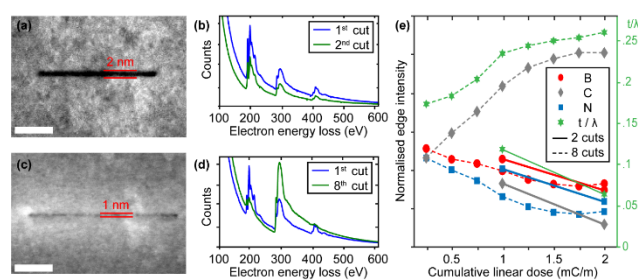


Figure 6 Comparing the effect of dose rate for cutting of bilayer graphene. (a) and (c) show HAADF STEM images of lines patterned in bilayer graphene supported on hBN (7 nm thick), using the same total line dose (2 mC/m), but using 2 and 8 beam scans respectively. The scale bars are 20 nm. (b) and (d) show the initial and final integrated core loss EEL spectra captured while patterning the lines in (a) and (c). Ionization edges for B, C and N are clearly visible at energies of 188, 284 and 401 eV respectively. The blue and green profiles represent the initial and final cuts respectively. (e) shows the evolution of the normalised core loss intensities of B, C and N derived from the integrated energy loss spectra captured while patterning the two areas (left axes). The dose plotted on the horizontal axis corresponds to the total cumulative dose received by the sample after the scan. The right axis and the green traces show the values of t/λ , extracted from the respective low loss EEL spectra.

The feature shown in figure 5 is sufficiently large that the EELS core-loss signals for B, C, and N all drop to zero in the centre (as shown by the red EELS profile). This only occurs when the probe is >2 nm from the cut edge, giving us an estimate of our effective EELS interaction radius. In contrast the low loss spectra contains inelastic scattering events even in the centre of the cut feature; 3.5 nm from any edge (calculated t/λ values are superimposed in a table in figure 5(a)). This data is consistent with the behaviour observed for the thinner cut features shown in figure 2 and 3 and indicates that the effective area under test when using the log ratio⁵⁹ method to specify the sample thickness has a radius of over 3.5 nm under our patterning conditions. The localization distance^{61,62} for inelastic scattering processes is inversely proportional to the energy loss involved, therefore higher energy loss processes (such as the core loss ionization peaks) are more spatially constrained than lower energy processes, such as the inelastic scattering events in the low loss spectrum. Thus it is to be expected that the low loss features will persist further from the sample edge than the core-loss.

We also used in situ energy dispersive X-ray spectroscopy (EDXS) to characterise patterned features, as discussed in the supplementary information. When capturing EDXS line scans perpendicular to previously patterned line features, we note that the EDXS elemental signals for B, C and N did drop to zero even when the original cuts were less than 2 nm in diameter (as shown in figure S8 in the supplementary information). EDXS maps of cut features also show an absence of elemental counts within the cut features. However, the signal to noise ratio of EDXS spectroscopy is poorer than EELS for these light elements, therefore EELS was the preferred technique for monitoring cutting progression.

Although the effective EELS interaction area can be affected by the accelerating voltage, the interaction energy loss, and beam broadening (in thicker samples), it is dominated by the effective electron probe size⁶². The presence of significant core loss peak intensities 2 nm from the sample edge suggests the electron probe has tails which extend to this radius, although the main probe peak is estimated to be <1 nm. This larger than would normally be used in an aberration corrected STEM but is unsurprising given the exceptionally high probe current (1 nA) used here in order to ensure effective patterning in a timely manner.

To test the wider use of this patterning approach we have also investigated patterning of bilayer graphene supported on a hBN flake (7 nm thick). Figure 6 illustrates the importance of electron dose rate in addition to overall electron dose. Both cuts received a total line dose of 2 C/m, but in figure 4(a) and 4(b) two separate scans were used, with a line dose of 1 C/m per scan, while in figure 4(c) and 4(d) 8 separate scans were used each at a lower dose of 0.25 C/m per scan. The line was successfully patterned using 2

scans at 1 C/m per scan, and has a final measured width of ~2 nm but when using 8 scans at 0.25 C/m per scan the cutting failed. Figure 4(d) shows the initial and final integrated EELS spectra collected during patterning, and a large growth in the carbon K-edge is clearly visible. This suggests that the beam is drawing in local carbon containing contamination whilst removing the underlying hBN. More information can be found in figure S5 and S6 of the supplementary information. The normalised peak intensities as a function of total dose received for both cuts are shown in figure 4(e). It is clear that while the reduction in the B and N signals are similar for both cases, the carbon content and t/λ values are highly affected by number of scans used. For the 8-scan case the C signal actually increased during cutting and this together with the overall increase in the value of t/λ measured for subsequent scans indicates that the rate of beam driven carbon increase was larger than the combined sputtering rate for B, C and N.

While electron sputtering is the key process governing the B and N content, the C content is also affected by the beam driven ingress of mobile carbon contaminants present on the surface. Inhomogeneous hydrocarbon contamination is a ubiquitous problem in electron microscopy⁶³, especially with organic samples where plasma cleaning is challenging. The brighter areas in our HAADF images of the membranes correspond to hydrocarbon contamination on the graphene surface, as shown by the EELS peak intensity profiles in figure S5 in the supplementary information. The initial flake thicknesses were the same in both cases and attempts were made to ensure the radiation received by the sample *before* the scan was taken were similar. However, we note that the initial carbon signal was slightly greater in the area of the 8 scan cut, suggesting an increased level of local carbon contamination in this region. Nevertheless, the results in figure 4 are consistent with our other tests which support the need for high dose rates to ensure sputtering is greater than beam induced carbon build-up.

We reason that for individual beam scans with a linear dose below a certain threshold, which may be dependent on the level of local mobile contamination in the immediate area, the rate of ingress of carbon-containing contaminants is greater than that of carbon removal due to beam sputtering. In the flakes shown in figure 4, this corresponds to a dose between 0.25 and 1 C/m for bilayer graphene on 7 nm thick hBN. This critical sputtering threshold was not observed for monolayer graphene on 6.5 nm thick hBN, indicating a threshold below our minimal individual scan dose of 0.1 C/m.

Figure 7 illustrates further the effect of electron dose on the quality of the cut for monolayer graphene supported on hBN (6.5 nm thick). Here, the total linear dose was varied systematically for a series of horizontal cuts all with a length of 196 nm but which were written using different cutting times with a line dose of 610 mC/m per minute. From bottom to top, the lines were written with total cutting times of 8, 6, 4, 2, 1 and 0.5 minutes with the corresponding electron doses (in mC/m) given next to each cut. Only total cutting times of >2 minutes (>1.22 C/m) have produced a cut through in the sample, although the lines are not continuous until the cut time >6 minutes (>3.66 C/m). The FWHM of the lines at the ends and in the centre as a function of the received total dose is shown in figure 6(b). For the 6 minute (3.66 C/m) line, two values are given for the central width; the dark data-point indicates the width of the central cut feature, and the light data-point includes the width of the dark grey area above the line. Subsequent EDXS mapping reveals that this dark grey region responds to the local peeling of the graphene away from the cut, as was previously observed in figure 5. The small differences in the cutting behaviour along the length of the cut are most likely due to local variations in the level of contamination and could be reduced by careful specimen cleaning^{64,65}. In addition although there is a clear increase in the width of the cut for longer cutting times there

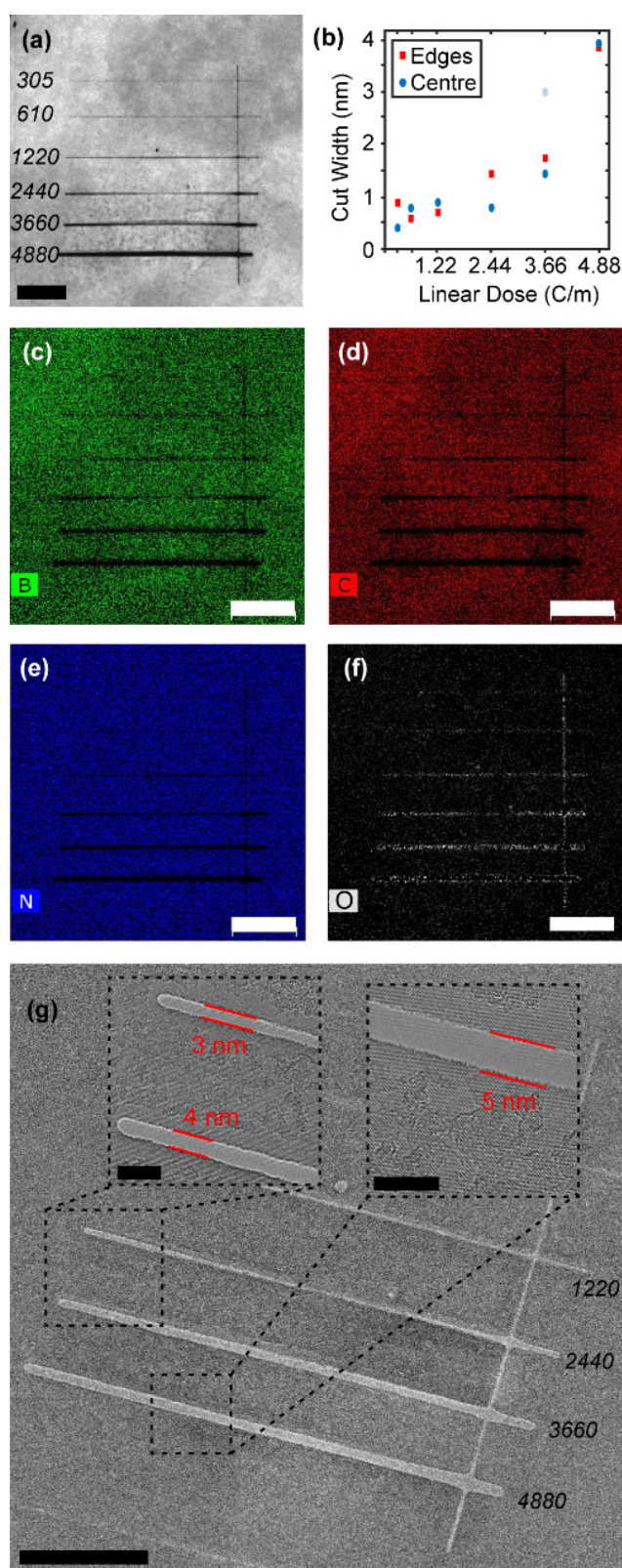


Figure 7 Effect of dose on the resultant cut width. (a) shows a HAADF STEM image showing a series of line cuts with varying total times 0.5, 1, 2, 4, 6, and 8 minutes with the number to the left of each cut indicating the total dose in mC/m. The scale bar represents 50 nm. (b) shows the widths of the cuts in (a) as a function of their dose, for the end and central portions of the cut features. The translucent data point on the 6 minute cut includes the width of the dark grey area seen above the cut in panel (a). (c) - (e) show EDXS elemental maps of the area for B, C, and N respectively. The scale bars represent 60 nm. (f) shows the elemental percentage of O counts from the EDXS map. The scale bar represents 60 nm. (g) shows a high magnification TEM image of the produced pattern. The scale bar represents 50 nm. The left inset shows the 4 minute and 6 minute cuts, with the scale bar representing 10nm, and the right inset shows just the 8 minute cut, with a scale bar representing 8 nm.

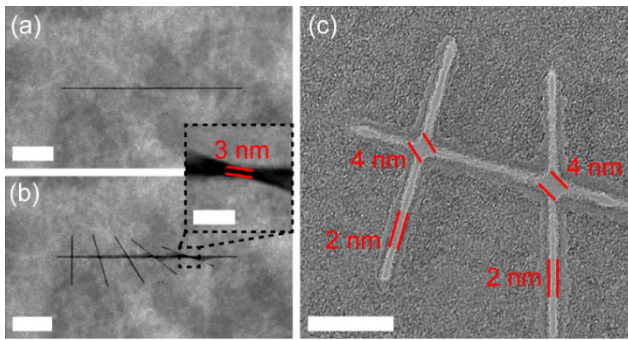


Figure 8 Patterning angled crosses in a graphene monolayer supported by 6.5 nm thick hBN. (a) shows a HAADF image of initial line cut with a length of 220nm, with an equivalent line dose of 1.64 mC/m. The scale bar represents 50 nm. (b) shows a HAADF image of the location after a series of cuts of length 60-70 nm (line dose 1.7 – 2 mC/m) crossing the initial cut, at angles of 90°, 75°, 58°, 36° and 20° to the initial cut. The scale bar represents 50 nm. The inset shows a higher magnification image of the most acute cross, showing a less than 3 nm gap between the opposite areas. (c) shows a high magnification HRTEM image of the produced pattern. The scale bar represents 20 nm.

appears to be an optimal dose (and dose rate) where effective cutting is achieved with a cut width of <2 nm. The cutting behaviour also varies depending on the proximity to previously patterned features as discussed further in the supplementary information.

We also investigated the potential for patterning acute angles by cutting angled crosses. This is of particular interest for creating nanogap electrodes for molecular electronic applications; if nanoribbons were simply cut using a linear pattern, this would result in ‘long’ cuts (minimum nanoribbon width is limited by conventional EBL resolution) that could be bridged at any point along their length. However, by cutting a cross feature into the ribbon, it would be possible to define a set of nanogap contacts that are both narrow and ‘short’, so that they can only be bridged in the central area. Figure 8 shows an example of the patterning of angled crosses in a graphene monolayer supported by hBN (6.5 nm thick). An equivalent line dose of 1.64 C/m was used for the 220 nm long horizontal line, and doses in the range of 1.7-2 C/m were used for the crossing lines. The lines were cut sequentially from left to right without intermediate imaging. The resulting lines were continuous, and had widths below 2 nm. The ‘acute wedge peninsulas’ surrounding the crosses were found to be self-supporting during cutting but to be more sensitive to damage during subsequent imaging, with additional etching of these regions observed during acquisition of the subsequent EDXS maps (see figure S10 in the supplementary information). The ‘obtuse wedge peninsulas’ were more stable and are separated by just 3 nm at the apex of the cross as shown in the inset of figure 6(b) (although after EDXS mapping and TEM imaging, the distance across the crosses increased to around 4 nm due to the additional radiation dose received). These distances compare favourably with gap widths reported previously for carbon electrodes for molecular electronics^{12,36}.

DISCUSSION

We conclude that a critical line dose of 1.5 C/m was consistently able to cut through clean areas of suspended membranes consisting of monolayer graphene on 6.5 nm thick hBN in the STEM. We find that the patterning is relatively robust for monolayer and bilayer graphene with widths of 2 nm achievable for a range of doses up to twice the threshold dose. We observe a weak dependence on dose rate of the cut quality, with higher dose rates providing more effective cutting as a result of the balance between sputtering from the electron beam and the beam driven ingress of mobile carbon contaminants. Inhomogeneous contamination is a ubiquitous problem for graphene research and

here significant contamination has been observed to negatively affect cut quality and can even lead to cuts being repaired⁶⁶.

We demonstrate that it is possible to reproducibly pattern cut lengths of >100 nm whilst maintaining cut widths below 2 nm. Thinner line widths of ~ 1.5 nm were possible but these lines were not consistently continuous, and were highly dependent on the level of local contamination. We hypothesise that even thinner cut widths could be achievable for cleaner samples.

Analysis of the EELS spectra obtained during cutting allowed us to plot the evolution of the relative quantities of different elements in the probe area and hence monitor the sputtering or deposition of B, C and N during cutting. We found that it was possible to use EELS to successfully track the cutting process, although the inelastic scattering signals did not fall to zero within the cut until the beam was several nm from the edge. However, using calibrated baseline values for the EELS core loss peak intensity allows the spectra acquired during cutting to be used to infer the completion of the cutting progress without directly imaging the sample in a ‘blind’ patterning procedure.

These proof of principle results offer the promise of a 2 stage patterning process for the manufacture of parallel graphene nanodevices with few nanometre resolution. Firstly, the stack is transferred onto a SiN_x membrane. Conventional EBL and oxygen plasma etching can then be used to pattern the graphene into isolated structures on top of the hBN. As the etch rate of hBN is relatively slow and easy to control, this could also be done with a protective hBN sheet on top of the graphene layer as well, although it would need to be relatively thin. EBL, metallization and lift-off can also be used at this point to connect the graphene devices to metallic electrodes. This would lead to a linear array of graphene nanoribbons which could then be individually patterned (narrowed or cut) using a STEM beam in a second patterning step, while the whole membrane remains mechanically stable. Ideally, this would be performed at elevated temperature⁵² to enable lattice self-repair, or using a pattern generator such as those commonly seen on EBL SEM systems to control the exact position of the beam and avoid exposure of the active elements. Etched or deposited features created near the membrane during the EBL step could be used to work out the affine transform between the sample and beam coordinate systems and produce the desired pattern without exposing any of the remaining graphene. This would enable current annealing of the nanoribbons (ideally *in situ* in the TEM)¹⁸ to reduce the level of surface contamination. Other strategies to reduce contamination after transfer could include high temperature vacuum annealing before⁶⁵, or even during patterning⁵², or annealing in the presence of platinum to help catalytically break down the PMMA residue at high temperature⁶⁴.

The nanosculpting results we demonstrate here could be extended to other 2-dimensional (2-d) materials heterostructures. One obvious application is the patterning of materials encapsulated in hBN using the hot stamping transfer technique⁶⁷, where the residual contamination layers around the central material are much lower. It could also allow sculpting of air and beam sensitive 2-d materials such as black phosphorus, which is of technological interest due to its layer number dependent band gap.

In summary, we have demonstrated that it is possible to pattern thin suspended graphene and graphene/hBN heterostructures using a high current 200 keV aberration corrected STEM probe. The addition of the thin hBN substrate allows thinner cuts to be achieved by preventing ‘bowing’ of the monolayer due to tension by acting as a mechanical support. We have demonstrated the nanosculpting of cuts with widths of less than 2 nm. We identified a set of optimal cutting parameters which enable ‘blind’ patterning for device fabrication and show that the EELS signal acquired during patterning can be used to track progress. This approach allows the cut nanostructures to remain unimaged until they have been electrically characterised, thus preserving the electronic

properties and very narrow linewidth structures. Performing this technique on pre-patterned graphene (using conventional EBL and plasma etching) on hBN is suggested as a convenient route for the fabrication of near-atomic precision graphene device structures, such as nanoribbon and nanogap electrode arrays.

METHODS

Sample fabrication: The sample fabrication process is illustrated in figure S1, and discussed in detail in the supplementary information. Briefly, the flakes were deposited on patterned membranes of SiN_x supported by 2.8 mm diameter Si chips. The Si chips were 200 μm thick and coated with 100 nm thick low stress SiN_x. The membrane was produced by removing the silicon from the central area using a masked KOH etch, and then patterning the membrane using masked reactive ion etching. hBN flakes were exfoliated from a bulk crystal on oxide coated silicon wafers. Monolayer graphene flakes were exfoliated onto a PMMA film, which was then used as a carrier film to transfer the graphene onto the hBN flake using a dry transfer⁵³ process. Flake thicknesses were measured using AFM for the hBN, and optically identified for the graphene⁶⁸. The hBN/graphene stack was then transferred from the oxide coated silicon wafer to the patterned SiN_x membrane using a conventional wet transfer process⁶⁹. After polymer removal, it was annealed at 280°C in a H/Ar atmosphere to remove as much polymer contamination as possible. Immediately prior to insertion into the TEM, samples were baked on a hotplate at 300°C. The produced membranes were monolayer and bilayer graphene on hBN substrates 6 - 9 nm thick.

Imaging and spectroscopy: High resolution TEM and STEM imaging with simultaneous energy dispersive X-ray spectroscopy (EDXS) and electron energy loss spectroscopy (EELS) was performed using a probe side aberration-corrected FEI Titan G2 80-200 kV with an X-FEG electron source operated at 200kV. High angle annular dark field (HAADF) STEM imaging was performed using a probe current of 0.5-2 pA, a convergence angle of 21 mrad and a HAADF inner collection angle of 54 mrad. Electron energy loss spectroscopy (EELS) was carried out using a Gatan Quantum ER spectrometer with an energy dispersion of 0.25 eV and a collection angle of 60 mrad. The data was acquired in Dual EELS mode where the low loss region and high loss region were collected separately with different acquisition times (typical acquisition times were 1E-5s for the low loss region and 0.01s for the high loss) and an energy offset of ~150eV. Energy dispersive x-ray (EDX) spectrum imaging was performed using the Titan's Super-X four silicon drift EDX detector system with a total collection solid angle of 0.7 srad.

Beam patterning: Cutting was performed by acquiring intense line scans using Gatan's Digital Micrograph software (for EELS) or Bruker's Esprit v1.9 (for EDXS). This approach enabled simultaneous cutting and chemical analysis of the heterostructures using EELS and EDXS to monitor the progress of the cutting. The linear dose (mC/m) experienced by the sample can be adjusted by altering the pixel step size (and number of pixels), the beam current, the pixel dwell time, and/or the number of repeat scans in the same location. In this work we investigated the effect of the dwell time, beam current, and number of repeat scans but kept the step size below 0.5 Å in all cases. Beam currents between 0.5 and 2 nA were used. Full patterning parameters are listed in the supplementary information.

Analysis of EELS spectra: EELS core loss edge intensities were obtained from the captured spectra by using a model based fitting routine contained in the open source python package Hyperspy⁷⁰ to split the spectra into its various components. The total intensity of each peak (and its resultant tail) were extracted and

normalised using the tabulated Hartree-Slater cross sections from Gatan Digital Micrograph. Full details are provided in the supplementary material.

REFERENCES

- 1 Novoselov, K. S. *et al.* Electric Field Effect in Atomically Thin Carbon Films. *Science* **306**, 666-669, (2004).
- 2 Lee, C., Wei, X. D., Kysar, J. W. & Hone, J. Measurement of the elastic properties and intrinsic strength of monolayer graphene. *Science* **321**, 385-388, (2008).
- 3 Bolotin, K. I. *et al.* Ultrahigh electron mobility in suspended graphene. *Solid State Commun* **146**, 351-355, (2008).
- 4 Prins, F. *et al.* Room-Temperature Gating of Molecular Junctions Using Few-Layer Graphene Nanogap Electrodes. *Nano Lett.* **11**, 4607-4611, (2011).
- 5 Joshi, R. K. *et al.* Precise and Ultrafast Molecular Sieving Through Graphene Oxide Membranes. *Science* **343**, 752-754, (2014).
- 6 Heerema, S. J. & Dekker, C. Graphene nanodevices for DNA sequencing. *Nat Nano* **11**, 127-136, (2016).
- 7 Han, M. Y., Özyilmaz, B., Zhang, Y. & Kim, P. Energy Band-Gap Engineering of Graphene Nanoribbons. *Phys Rev Lett* **98**, 206805, (2007).
- 8 Aviram, A. & Ratner, M. A. Molecular Rectifiers. *Chem Phys Lett* **29**, 277-283, (1974).
- 9 Xiang, D., Wang, X., Jia, C., Lee, T. & Guo, X. Molecular-Scale Electronics: From Concept to Function. *Chemical Reviews*, (2016).
- 10 Strachan, D. R. *et al.* Clean Electromigrated Nanogaps Imaged by Transmission Electron Microscopy. *Nano Lett.* **6**, 441-444, (2006).
- 11 Cao, Y. *et al.* Building High-Throughput Molecular Junctions Using Indented Graphene Point Contacts. *Angew Chem Int Edit* **51**, 12228-12232, (2012).
- 12 Marquardt, C. W. *et al.* Electroluminescence from a single nanotube-molecule-nanotube junction. *Nat Nanotechnol* **5**, 863-867, (2010).
- 13 Cho, Y., Kim, W. Y. & Kim, K. S. Effect of Electrodes on Electronic Transport of Molecular Electronic Devices†. *The Journal of Physical Chemistry A* **113**, 4100-4104, (2009).
- 14 Burzur^a, E., Prins, F. & Zant, H. S. J. v. d. Characterization of Nanometer-Spaced Few-Layer Graphene Electrodes. *Graphene* **2**, 4, (2012).
- 15 Peterfalvi, C. G. & Lambert, C. J. Suppression of single-molecule conductance fluctuations using extended anchor groups on graphene and carbon-nanotube electrodes. *Phys Rev B* **86**, (2012).
- 16 Perez-Jimenez, A. J. & Sancho-Garcia, J. C. Conductance Enhancement in Nanographene-Gold Junctions by Molecular pi-Stacking. *J Am Chem Soc* **131**, 14857-14867, (2009).
- 17 He, J., Chen, K. Q. & Sun, C. Q. The weak pi-pi interaction originated resonant tunneling and fast switching in the carbon based electronic devices. *Aip Adv* **2**, (2012).
- 18 Puster, M., Rodriguez-Manzo, J. A., Balan, A. & Drndić, M. Toward Sensitive Graphene Nanoribbon-Nanopore Devices by Preventing Electron Beam-Induced Damage. *Acs Nano* **7**, 11283-11289, (2013).
- 19 Schneider, G. F. *et al.* DNA Translocation through Graphene Nanopores. *Nano Lett.* **10**, 3163-3167, (2010).
- 20 Merchant, C. A. *et al.* DNA Translocation through Graphene Nanopores. *Nano Lett.* **10**, 2915-2921, (2010).
- 21 Nelson, T., Zhang, B. & Prezhdo, O. V. Detection of Nucleic Acids with Graphene Nanopores: Ab Initio Characterization of a Novel Sequencing Device. *Nano Lett.* **10**, 3237-3242, (2010).
- 22 Traversi F *et al.* Detecting the translocation of DNA through a nanopore using graphene nanoribbons. *Nat Nano* **8**, 939-945, (2013).
- 23 Han, M. Y., Brant, J. C. & Kim, P. Electron Transport in Disordered Graphene Nanoribbons. *Phys Rev Lett* **104**, 056801, (2010).
- 24 Son, Y. W., Cohen, M. L. & Louie, S. G. Half-metallic graphene nanoribbons. *Nature* **444**, 347-349, (2006).
- 25 Ribeiro, R. *et al.* Unveiling the Magnetic Structure of Graphene Nanoribbons. *Phys Rev Lett* **107**, (2011).

- 26 Soavi, G. *et al.* Exciton-exciton annihilation and biexciton
stimulated emission in graphene nanoribbons. *Nat Commun* **7**,
(2016).
- 27 Son, Y. W., Cohen, M. L. & Louie, S. G. Energy gaps in
graphene nanoribbons. *Phys Rev Lett* **97**, 216803, (2006).
- 28 Nakada, K., Fujita, M., Dresselhaus, G. & Dresselhaus, M. S.
Edge state in graphene ribbons: Nanometer size effect and edge
shape dependence. *Phys Rev B* **54**, 17954-17961, (1996).
- 29 Schwierz, F. Graphene transistors. *Nat Nano* **5**, 487-496,
(2010).
- 30 Chen, Z., Lin, Y., Rooks, M. & Avouris, P. Graphene nano-
ribbon electronics. *Physica E* **40**, (2007).
- 31 Behnam, A. *et al.* Transport in Nanoribbon Interconnects
Obtained from Graphene Grown by Chemical Vapor
Deposition. *Nano Lett.* **12**, 4424-4430, (2012).
- 32 Hwang, W. S. *et al.* Transport properties of graphene
nanoribbon transistors on chemical-vapor-deposition grown
wafer-scale graphene. *Appl Phys Lett* **100**, 203107, (2012).
- 33 Ferrari, A. C. *et al.* Science and technology roadmap for
graphene, related two-dimensional crystals, and hybrid
systems. *Nanoscale* **7**, 4598-4810, (2015).
- 34 Novoselov, K. S. *et al.* Room-Temperature Quantum Hall
Effect in Graphene. *Science* **315**, 1379-1379, (2007).
- 35 Ponomarenko, L. A. *et al.* Chaotic Dirac Billiard in Graphene
Quantum Dots. *Science* **320**, 356-358, (2008).
- 36 Cao, Y., Dong, S., Liu, S., Liu, Z. & Guo, X. Toward functional
molecular devices based on graphene-molecule junctions.
Angewandte Chemie International Edition English **52**, 3906-
3910, (2013).
- 37 Cord, B. *et al.* Limiting factors in sub-10 nm scanning-electron-
beam lithography. *J Vac Sci Technol B* **27**, 2616-2621, (2009).
- 38 Tapaszto, L., Dobrik, G., Lambin, P. & Biro, L. P. Tailoring
the atomic structure of graphene nanoribbons by scanning
tunnelling microscope lithography. *Nat Nanotechnol* **3**, 397-
401, (2008).
- 39 Byun, I. S. *et al.* Nanoscale Lithography on Monolayer
Graphene Using Hydrogenation and Oxidation. *Acs Nano* **5**,
6417-6424, (2011).
- 40 Mol, J. A. *et al.* Graphene-porphyrin single-molecule
transistors. *Nanoscale* **7**, 13181-13185, (2015).
- 41 Archanjo, B. S. *et al.* The use of a Ga⁺ focused ion beam to
modify graphene for device applications. *Nanotechnology* **23**,
255305, (2012).
- 42 Lemme, M. C. *et al.* Etching of Graphene Devices with a
Helium Ion Beam. *Acs Nano* **3**, 2674-2676, (2009).
- 43 Archanjo, B. S. *et al.* Graphene nanoribbon superlattices
fabricated via He ion lithography. *Appl Phys Lett* **104**, 193114,
(2014).
- 44 Lehtinen, O. *et al.* Effects of ion bombardment on a two-
dimensional target: Atomistic simulations of graphene
irradiation. *Phys Rev B* **81**, 153401, (2010).
- 45 Song, B. *et al.* Atomic-Scale Electron-Beam Sculpting of Near-
Defect-Free Graphene Nanostructures. *Nano Lett.* **11**, 2247-
2250, (2011).
- 46 Garaj, S. *et al.* Graphene as a subnanometre trans-electrode
membrane. *Nature* **467**, 190-193, (2010).
- 47 Lu, Y., Merchant, C. A., Drndic, M. & Johnson, A. T. C. In Situ
Electronic Characterization of Graphene Nanoconstrictions
Fabricated in a Transmission Electron Microscope. *Nano Lett.*
11, 5184-5188, (2011).
- 48 Sommer, B. *et al.* Electron-beam induced nano-etching of
suspended graphene. *Scientific Reports* **5**, 7781, (2015).
- 49 Zobelli, A., Gloter, A., Ewels, C. P. & Colliex, C. Shaping
single walled nanotubes with an electron beam. *Phys Rev B* **77**,
045410, (2008).
- 50 Jin, C., Lan, H., Peng, L., Suenaga, K. & Iijima, S. Deriving
Carbon Atomic Chains from Graphene. *Phys Rev Lett* **102**,
205501, (2009).
- 51 Qi, Z. J. *et al.* Correlating Atomic Structure and Transport in
Suspended Graphene Nanoribbons. *Nano Lett.* **14**, 4238-4244,
(2014).
- 52 Xu, Q. *et al.* Controllable Atomic Scale Patterning of
Freestanding Monolayer Graphene at Elevated Temperature.
Acs Nano **7**, 1566-1572, (2013).
- 53 Dean, C. R. *et al.* Boron nitride substrates for high-quality
graphene electronics. *Nat Nanotechnol* **5**, 722-726, (2010).
- 54 Zobelli, A., Gloter, A., Ewels, C. P., Seifert, G. & Colliex, C.
Electron knock-on cross section of carbon and boron nitride
nanotubes. *Phys Rev B* **75**, 245402, (2007).
- 55 Smith, B. W. & Luzzi, D. E. Electron irradiation effects in
single wall carbon nanotubes. *J. Appl. Phys.* **90**, 3509-3515,
(2001).
- 56 Meyer, J. C. *et al.* Accurate Measurement of Electron Beam
Induced Displacement Cross Sections for Single-Layer
Graphene. *Phys Rev Lett* **108**, 196102, (2012).
- 57 Kim, J. S., Borisenko, K. B., Nicolosi, V. & Kirkland, A. I.
Controlled Radiation Damage and Edge Structures in Boron
Nitride Membranes. *Acs Nano* **5**, 3977-3986, (2011).
- 58 Kotakoski, J., Jin, C. H., Lehtinen, O., Suenaga, K. &
Krasheninnikov, A. V. Electron knock-on damage in hexagonal
boron nitride monolayers. *Phys Rev B* **82**, 113404, (2010).
- 59 Malis, T., Cheng, S. C. & Egerton, R. F. EELS log-ratio
technique for specimen-thickness measurement in the TEM.
Journal of Electron Microscopy Technique **8**, 193-200, (1988).
- 60 Krivanek, O. L. *et al.* Atom-by-atom structural and chemical
analysis by annular dark-field electron microscopy. *Nature*
464, 571-574, (2010).
- 61 Muller, D. A. & Silcox, J. Delocalization in inelastic scattering.
Ultramicroscopy **59**, 195-213, (1995).
- 62 Egerton, R. F. Limits to the spatial, energy and momentum
resolution of electron energy-loss spectroscopy.
Ultramicroscopy **107**, 575-586, (2007).
- 63 Mitchell, D. R. G. Contamination mitigation strategies for
scanning transmission electron microscopy. *Micron* **73**, 36-46,
(2015).
- 64 Longchamp, J. N., Escher, C. & Fink, H. W. Ultraclean
freestanding graphene by platinum-metal catalysis. *J Vac Sci
Technol B* **31**, 020605, (2013).
- 65 Zan, R. *et al.* Scanning tunnelling microscopy of suspended
graphene. *Nanoscale* **4**, 3065-3068, (2012).
- 66 Zan, R., Ramasse, Q. M., Bangert, U. & Novoselov, K. S.
Graphene Reknits Its Holes. *Nano Lett.* **12**, 3936-3940, (2012).
- 67 Pizzocchero, F. *et al.* The hot pick-up technique for batch
assembly of van der Waals heterostructures. *Nat Commun* **7**,
(2016).
- 68 Blake, P. *et al.* Making graphene visible. *Appl Phys Lett* **91**,
063124, (2007).
- 69 Reina, A. *et al.* Transferring and Identification of Single- and
Few-Layer Graphene on Arbitrary Substrates. *The Journal of
Physical Chemistry C* **112**, 17741-17744, (2008).
- 70 HyperSpy: multi-dimensional data analysis toolbox v0.81
(2015).

Nanometre electron beam sculpting of suspended graphene and hexagonal boron nitride heterostructures

N. Clark,^{1,2} E. Lewis,¹ S. Haigh,¹ A. Vijayaraghavan^{1,2*}

¹School of Materials, University of Manchester, Sackville Street, Manchester, M13 9PL, UK

²National Graphene Institute, University of Manchester, Sackville Street, Manchester, M13 9PL, UK

*e-mail:aravind@manchester.ac.uk

SUPPLEMENTARY INFORMATION

This document contains the supplementary information referred to in the main text, along with the descriptions of the two supplementary videos. The detailed experimental procedures used to fabricate the samples are given in section 1. Section 2 discusses the details of the line patterning parameters used, and records the exact parameters used when patterning the areas shown in the figures in the main text. Section 3 details the procedures used to analyse the collected EEL spectra. Section 4 contains additional experimental data and images not shown in the main text.

1 SAMPLE FABRICATION PROCEDURES

The sample fabrication process is illustrated in figure S1. The flakes were deposited on patterned membranes of SiN_x supported by 2.8 mm diameter Si chips, as shown in panel (a). They were produced from Si wafers which were 200 μm thick and coated with a 100 nm thick film low stress SiN_x purchased from SPI Supplies. Firstly, the SiN_x film on one side was patterned to act as a hard mask for a subsequent KOH etch, using photolithography and reactive ion etching (RIE). KOH etching was then used to remove the areas of silicon that were not masked by SiN_x with the nitride layer on the other side acting as an etch stop layer. This left a thin nitride membrane, which was subsequently patterned using a second stage of photolithography and RIE to produce μm scale holes.

hBN flakes were exfoliated from a bulk crystal (purchased from HQGraphene) on oxide coated silicon wafers. An oxide thickness of ~70 nm was used to maximise the optical contrast.¹ Relatively thin flakes were identified optically, and their thickness was measured using atomic force microscopy (AFM). Graphene flakes were exfoliated from natural graphite samples onto a PMMA film supported on a silicon substrate. This layer was detached from the substrate and used as a carrier film to transfer the graphene onto the hBN flake in a dry transfer² process, as shown in figure S1(c). Monolayer and bilayer flakes were identified optically³, and their thickness was confirmed using AFM after the transfer onto the hBN flake. The hBN/graphene stack was then transferred from the oxide coated silicon wafer to the patterned SiN_x membrane using a conventional wet transfer process⁴. After polymer removal, it was annealed at 280°C in a H/Ar atmosphere to remove as much polymer contamination as possible. Immediately prior to insertion into the TEM, samples were baked on a hotplate at 300°C. Our samples contained membrane regions with monolayer and bilayer graphene areas supported on hBN flakes with thicknesses of 6 – 9 nm.

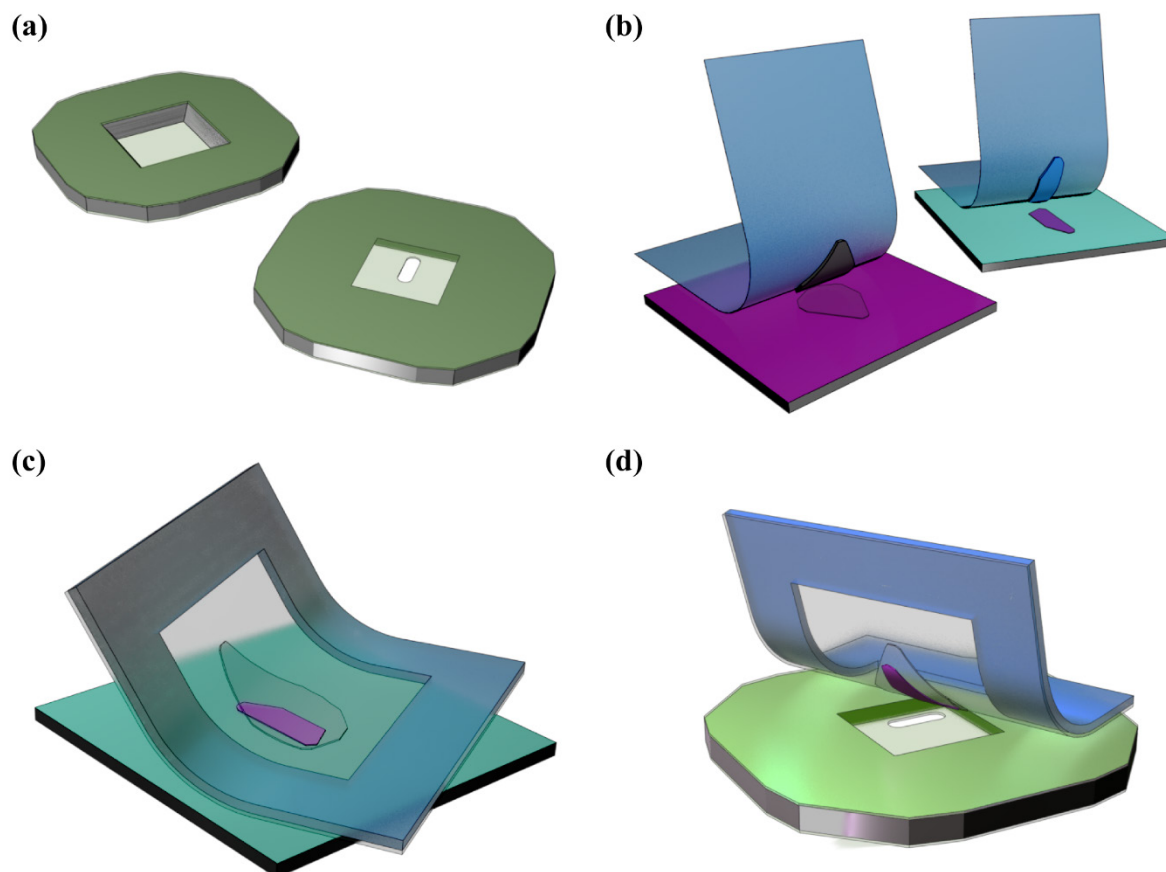


Figure S1 Schematic showing fabrication steps for hBN supported graphene TEM compatible membranes. (a) Fabrication of patterned SiN membranes. Firstly the nitride coating on the reverse side of the wafer is patterned to form a mask for a KOH etch which removes a defined volume of silicon, leaving a thin nitride membrane, as shown in the left panel. The membrane is then patterned using optical lithography and SF₆ plasma etching, as shown in the right image. (b) Graphene and boron nitride are mechanically exfoliated. hBN is exfoliated onto a silicon oxide coated substrate, and graphene is exfoliated onto a polymer film. (c) After characterising the flakes, the chosen graphene flake is transferred onto the chosen hBN flake using the polymer film as a support membrane in a dry transfer process. This means that the interface between the 2 flakes is as clean as possible. (d) The heterostructure is transferred (hBN side down) onto the patterned TEM grid using a second polymer film in a wet transfer process.

2 DETAILED PATTERNING PARAMETERS

When performing patterning while collecting simultaneous EEL spectral data, each individual line scan was specified by the length, number of pixels and dwell time per pixel. In between line scans, the area was imaged using a low electron dose (example low dose images are shown in figure S2) to ascertain the progress of the cutting process. Subsequent line scans were then made in the same location as the first to continue the cutting process. When performing patterning while collecting simultaneous EDXS data, as in figures S7-S12, the pixel number and dwell time as well as a total cutting time were specified, and the resulting scans occurred consecutively, with no pause for imaging the area.

PATTERNING PARAMETERS FOR MAIN TEXT FIGURES

FIGURE 2

Shows data obtained whilst patterning of a line in a graphene monolayer supported by a thin (6.5 nm thick) hBN flake. The patterning parameters used (for an individual scan/cut) were a probe current of 1 nA scanned over 400 points along 40 nm with a pixel dwell time of 10 ms, corresponding to a line dose of 100 mC/m per cut. The line was patterned using 11 cuts, corresponding to an effective total dose of 1.1 C/m, and has a final measured linewidth of between 2 and 3.5 nm.

FIGURE 3

Shows data obtained whilst patterning a cross in a graphene monolayer supported by a thin (6.5 nm thick) hBN flake. The spectra correspond to the 5th and 8th cuts in figure S3. The patterning parameters used were a probe current of 1 nA scanned over 1000 points along 40.5 nm with a pixel dwell time of 10 ms, corresponding to a line dose of 247 mC/m per cut. The cross is made up of 2 perpendicular lines consisting of 4 cuts each.

FIGURE 4

2 examples of patterning lines in a graphene bilayer supported by a thin (7 nm thick) hexagonal boron nitride flake. The patterning parameters used for figure 4(a) were a probe current of 1nA scanned over 4000 points along 40 nm with a pixel dwell time of 10 ms, corresponding to a line dose of 1 C/m per cut. The line was successfully patterned using two cuts, and has a final measured linewidth of ~2 nm. For figure 4(b) the patterning parameters used were a probe current of 1 nA scanned over 1000 points along 40 nm with a pixel dwell time of 10 ms, corresponding to a lower line dose of 250 mC/m per cut. The beam was not able to open a clear gap in this case after 8 cuts.

FIGURE 5

Figure 5 depicts a patterned line feature (main text figure 4) which has enlarged after prolonged imaging, (supplementary video 2). The (horizontal) cut is now ~7 nm wide, bordered by a dark grey area of > 5 nm width. The frame border from the video acquisition is visible as a vertical feature, which has etched completely through the membrane close to the original cut.

FIGURE 6

Figure 6 shows an example of the patterning of lines in a graphene monolayer supported by a thin (6.5 nm thick) hexagonal boron nitride flake. The patterning parameters used were a probe current of 2 nA scanned over 4000 points with a pixel dwell time of 2 ms for a variety of total cutting times. The horizontal cuts have lengths of 196nm, giving a line dose of 610 mC/m per minute of cutting time. From bottom to top, the lines were written with total cutting times of 8, 6, 4, 2, 1 and half a minute. Only total cutting times of 2 minutes (1.22 C/m) and above seem to have opened a cut in the sample.

FIGURE 7

Figure 7 shows data obtained while patterning of lines in a graphene monolayer supported by a thin (6.5 nm thick) hBN flake. The patterning parameters used were a probe current of 2 nA scanned over 4000 points with a pixel dwell time of 2 ms. The horizontal cut was patterned for 3 minutes and is 220 nm long, giving a line dose of 1.64 C/m. The shorter lines took 1 minute and are 60-70 nm long, corresponding to doses in the range 1.7-2 C/m. They were cut sequentially from left to right without intermediate imaging. The area is the same as that shown in Figure S10 in the supplementary information.

3 ANALYSIS OF EELS SPECTRA

EELS spectra were analysed using the open source python package Hyperspy⁵. Firstly, the individual spectra corresponding to single pixels along the cut lines were aligned on the energy axis so that the zero loss peak occurs at zero energy. Both the (separate) low loss and core loss spectra were shifted. Generally, the individual spectra were summed to provide an average spectra along the line with a higher signal:noise ratio. Plural scattering events were removed using a fourier-ratio deconvolution⁶ technique. A model containing components corresponding to the core loss background and the 3 principal edges was then fit to the spectra, enabling us to view the individual components (for example, the spectra from figure 4 (d) in the main text are split into their components in figure S6 in the supplementary material. The total peak intensities for the individual elements are then normalised using the (energy dependent) Hartree-Slater-Foch cross sections tabulated within Gatan's Digital Micrograph software, allowing us to identify their relative quantities.

4 ADDITIONAL PATTERNED AREAS

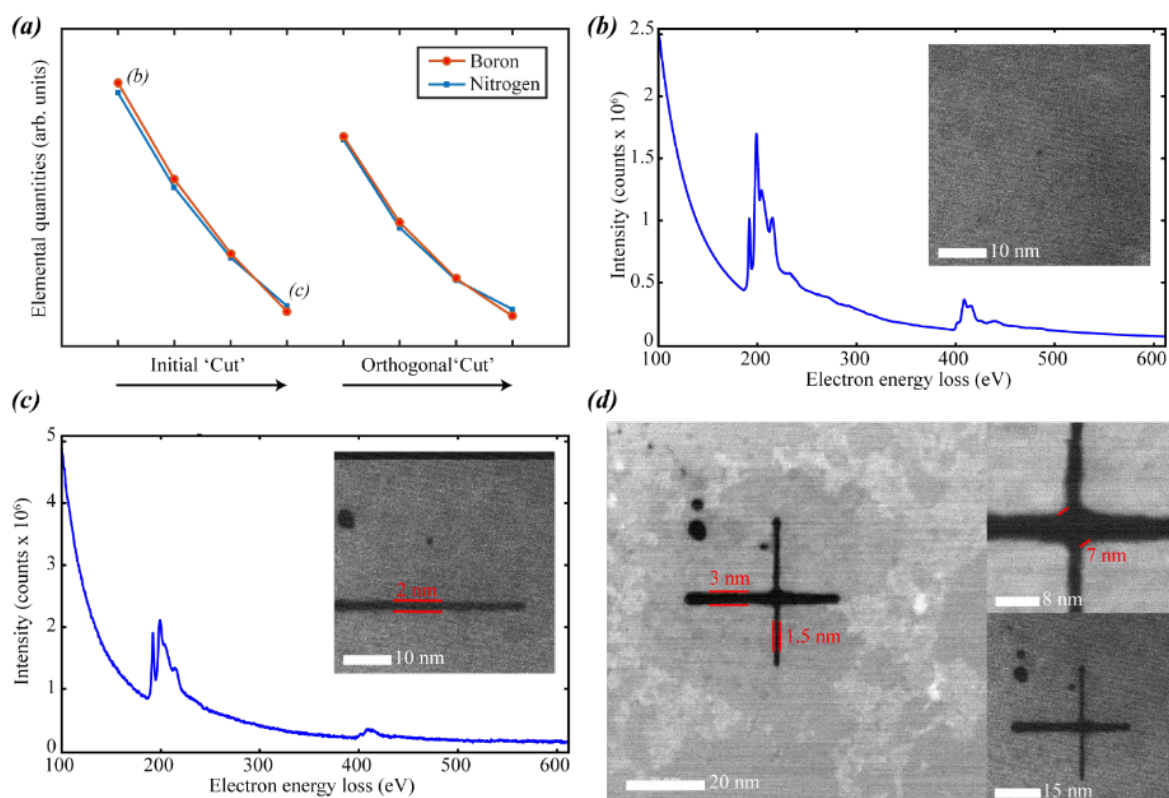


Figure S2 Patterning a cross in 6.5 nm thick hBN. (a) shows the evolution of the elemental quantities of B and N derived from the EEL spectra. The first four cuts correspond to the horizontal cut in the images, and the second four cuts correspond to the vertical cut. All cuts were made with the same writing parameters, corresponding to a line dose of 244 mC/m per cut. (b) shows the integrated EEL spectrum along the line during the initial cut. The inset shows a low dose HAADF STEM image of the area before cutting. (c) shows the integrated EELS spectrum along the horizontal line during the final cut. The inset shows a low dose HAADF STEM image of the area prior to cutting the vertical line. (d) shows HAADF STEM images of the area after patterning. The upper inset shows a higher magnification image of the central area. The lower inset shows a low dose image of the same area as the main image. The holes seen in the top left quadrant of the cross are a result of the beam resting at these locations between line cuts.

Initially we investigated the cutting an uncovered hBN membrane (6.5 nm thick). The resulting cross is shown in figure S2. The patterning parameters used were a probe current of 1 nA scanned over 1000 points along 41 nm with a pixel dwell time of 10 ms, corresponding to a line dose of 244 mC/m per cut. The cross is made up of 2 perpendicular lines consisting of 4 cuts each. The core loss edges corresponding to B (edge onset energy = 188 eV) and N (edge onset energy = 401 eV) are clearly visible in both the initial and final collected EELS spectra. The horizontal cut of the cross appears much wider than the vertical cut, with a width of ~3nm as opposed to ~1.5nm. The horizontal line was patterned first so this may be attributed to additional widening caused by the imaging performed between the cuts.

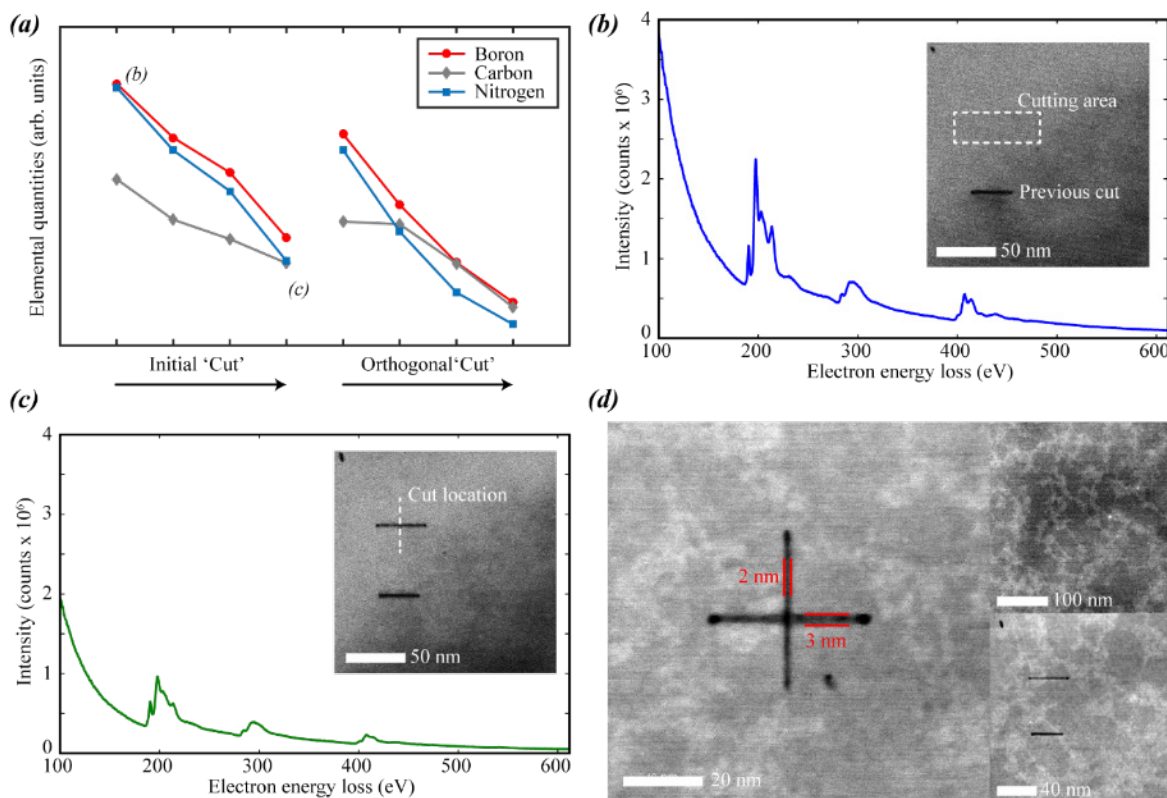


Figure S3 Patterning a cross in a graphene monolayer supported by 6.5 nm thick hBN. (a) shows the evolution of the elemental quantities of B, C and N derived from the energy loss spectra using the procedure described in the text. The first four cuts correspond to the horizontal cut in the images, and the second four cuts correspond to the vertical cut. All cuts were made with the same writing parameters, with a beam of current 1nA scanning 1000 points along 40.5 nm with a dwell time of 10ms (b) shows the integrated EELS spectrum along the line during the initial cut. The inset shows a low dose HAADF STEM image of the area before cutting. The area where the cut is made is highlighted. (c) shows the integrated EELS spectrum along the horizontal line during the final cut. The inset shows a low dose HAADF STEM image of the area prior to cutting. (d) shows a HAADF STEM image of the area after patterning. The upper inset shows the wider area prior to patterning. The lower inset shows the wider area prior to making vertical cuts.

Figure S3 shows a further example of the patterning of a cross in a graphene monolayer supported by a 6.5 nm thick hBN flake. The white areas seen around the cross are polymer remnants on top of the graphene from the transfer process. EELS elemental profiles obtained while cutting across this contaminated area show a much stronger EELS carbon K edge in these regions (shown in figure S5). The patterning parameters used were a probe current of 1nA scanned over 1000 points along 40.5nm with a pixel dwell time of 10ms, corresponding to a line dose of 247 mC/m per cut. The cross is made up of 2 perpendicular lines consisting of 4 cuts each. The core loss edge corresponding to C-K edge (284 eV) is now visible along with those of B-K edge (188eV) and N-K (401eV) in both the initial and final collected spectra. The horizontal cut of the cross appears wider than the vertical cut, with a width of ~3nm as opposed to ~2 nm. The horizontal cut is not completely continuous, with dark grey bridges spanning the gap. The evolution of these bridges under sustained imaging is shown in supplementary video 2. The (continuous) vertical cut and (bridged) horizontal cut both widen under the continued exposure, but the effect is greater for the vertical cut, which was initially narrower. The dark grey bridges crossing the horizontal cut appear to remain intact despite the imaging. As before, the tracked EELS edge intensities were non zero during the final cut.

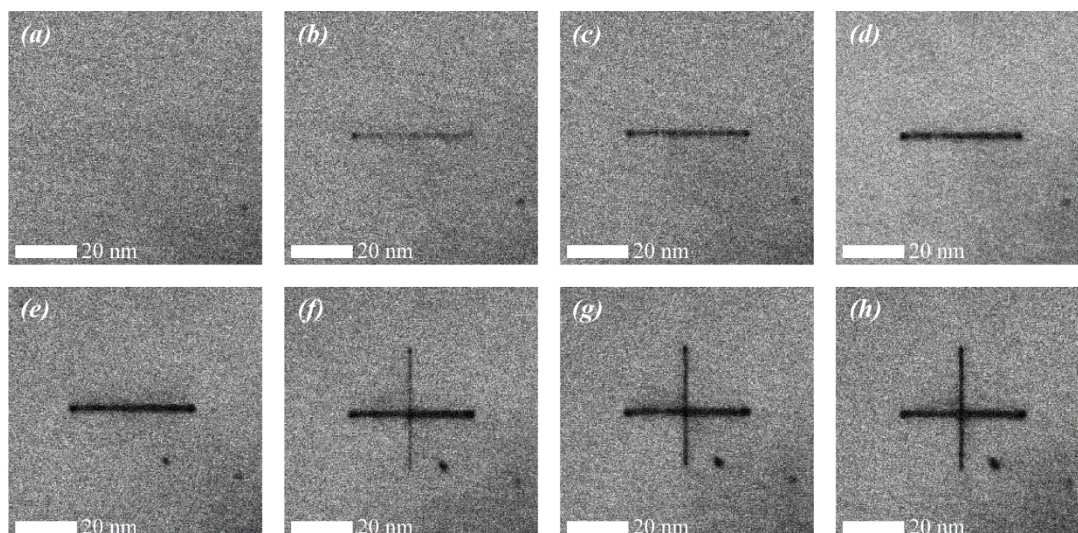


Figure S4 Monitoring cutting process using low dose HAADF STEM imaging. The 8 frames show the evolution of the cross feature pictured in figure 3 in the main text. Each cut was made immediately after the frame (horizontal for (a) – (d) and vertical from (e) – (h), with a line dose of 247 mC/m. Elemental profiles during the cuts after frames (e) and (h) are shown in figure S5 in the supplementary information.

Figure S4 shows an example of the low dose HAADF survey images used to position the individual cuts in when cutting whilst collecting EELS spectra. The images correspond to the feature in figure S3. Cut features are clearly visible, although features visible in high dose (longer dwell time) images such as panel (d) in figure S3, such as the areas of graphene surface contamination, are not.

Figure S5 shows the elemental intensity profiles along the cut during the initial scan. The area of the cut that corresponds to the white area of contamination on the HAADF image corresponds to an area with significantly higher carbon core loss edge intensity, suggesting it is primarily composed of carbon. No peaks due to other atomic species were observed.

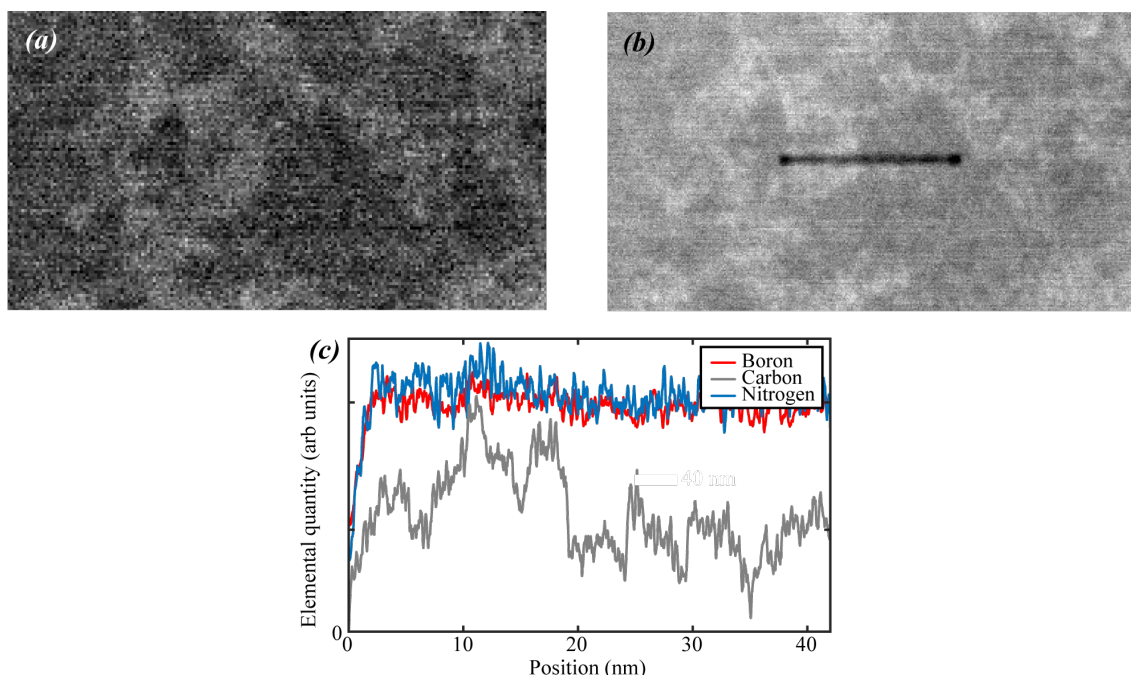


Figure S5 EELS contamination signal. (a) shows a HAADF STEM image region of monolayer graphene supported by 9nm thick hBN. Polymer contamination on the graphene surface is visible as lighter areas. (b) the region shown in (a) after patterning with a line cut. (c) shows the elemental quantities extracted from the EELS spectra collected while cutting, as a function of the position along the cut, from left to right as shown in panel (b). The whiter areas in panel (b) correspond to a larger carbon peak in the EELS spectra. The cut also appears narrower in the region of the contaminated area.

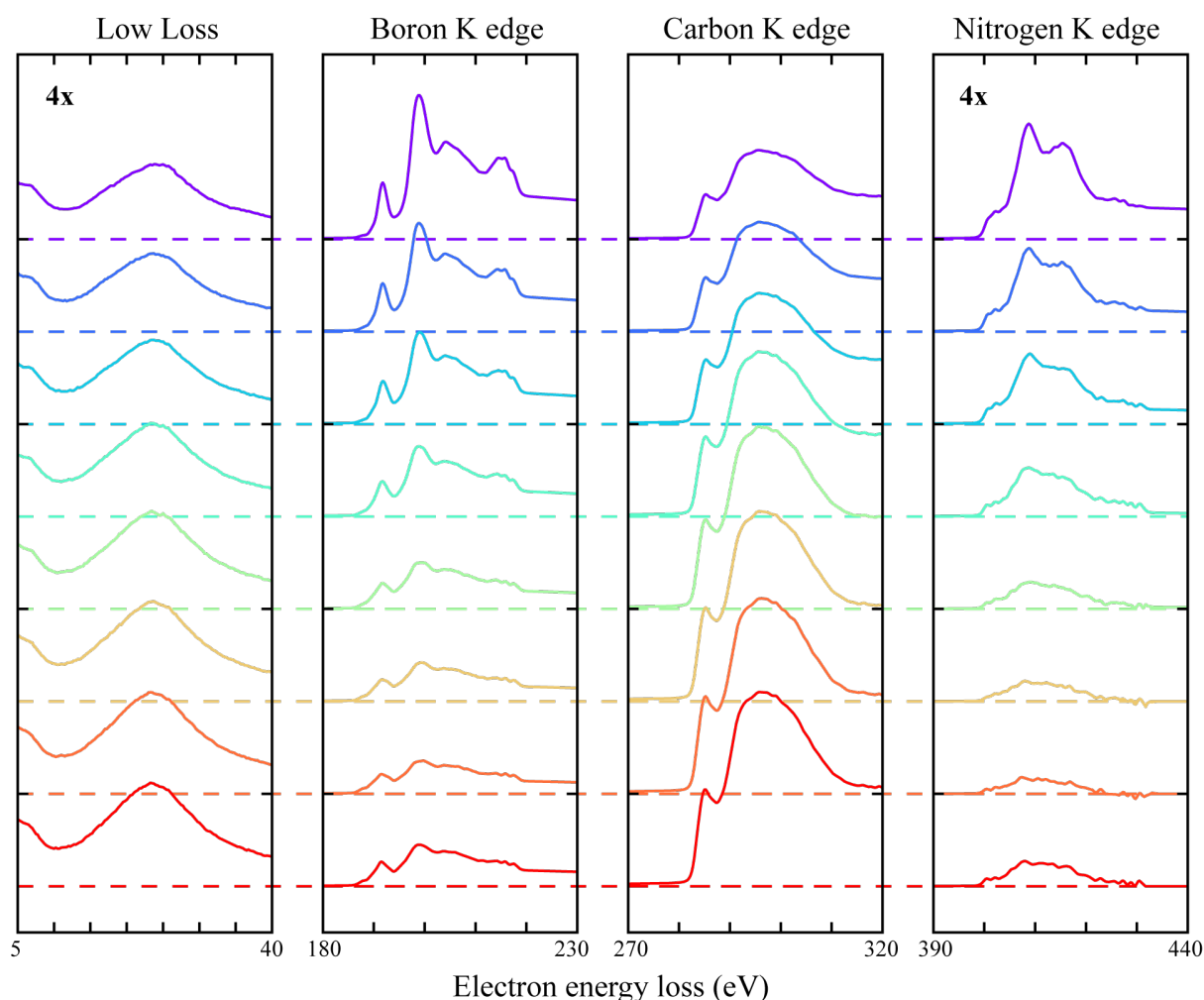


Figure S6 Evolution of EELS spectra over progressive cuts of bilayer graphene on 7 nm thick hBN. This is the EELS data collected during the cuts featured in figure 5 in the main text. All cuts were made with the same writing parameters, with a beam of current 1nA scanning 1000 points along 40nm with a dwell time of 10ms. 4 features of the energy loss spectra are shown; the low loss spectra and the extracted elemental edges (after background subtraction) for boron, carbon and nitrogen. The low loss spectra and the N edge have been enhanced by a factor of 4 to aid visibility. The offset between adjacent spectra corresponds to 1,000,000 counts.

Figure S6 shows the progression of the EELS spectra captured during the failed attempt to pattern bilayer graphene highlighted in figure 4 in the main text. The initial cut is shown at the top, and successive ones below. Separate edge components extracted from the captured spectra integrated along the length of each cut are shown. Whilst the boron and nitrogen edges clearly decline, there is a clear rise in the carbon peak. There is also an increase in the intensity of inelastic scattering peak in the low loss spectrum, implying an increase in the sample thickness. This suggests that the rate of carbon ingress during this procedure was greater than the combined sputtering rates for B, C and N.

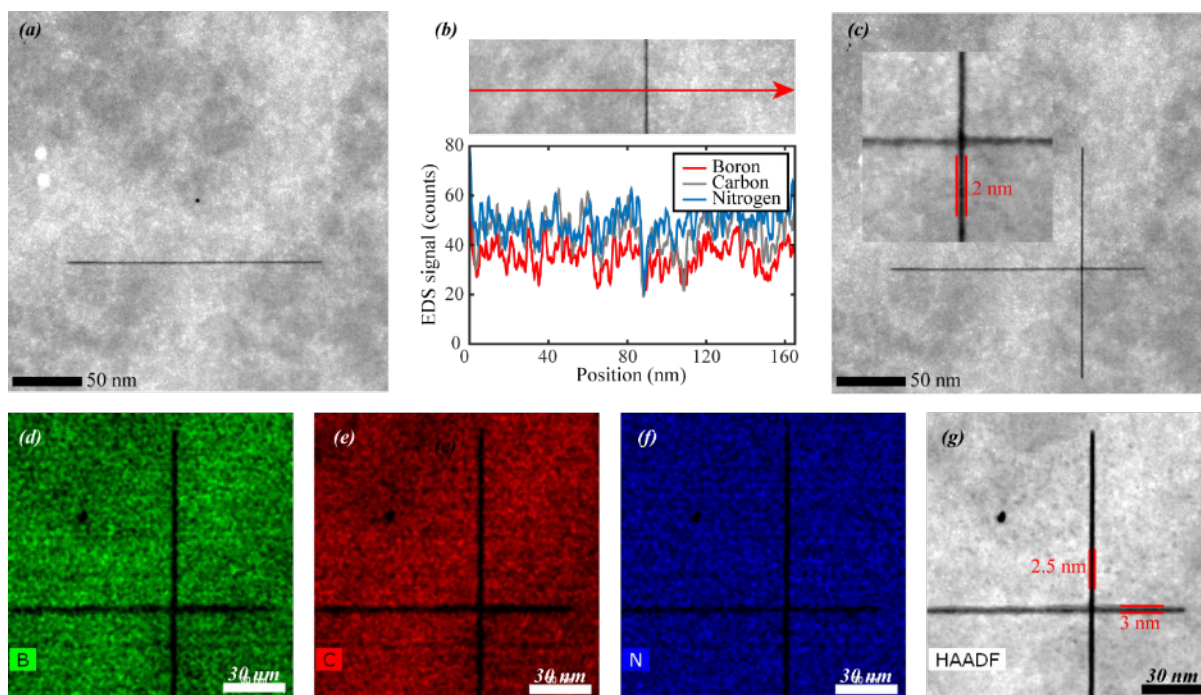


Figure S7 Patterning a cross in a graphene monolayer supported by 6.5 nm thick hBN. Both cuts were made using a probe current of 2nA, and by repeatedly scanning the beam over 4000 points for a total of 2 minutes, with a pixel dwell time of 15ms. (a) HAADF STEM image of the initial line cut, with a length of 187nm. (b) shows the location of the orthogonal cut, with a length of 168nm, along with the elemental counts for B, C and N from the EDS signal collected during cutting. The x-axis corresponds to that shown in the image. (c) HAADF STEM image after orthogonal cut. The inset shows a higher magnification image of the central area. (d) to (f) show EDX elemental maps of the area for B, C, and N respectively, whilst (g) shows the HAADF image captured during the EDX mapping process.

Figure S7 shows an example of the patterning of a cross in a graphene monolayer supported by a 6.5 nm thick hBN flake. The patterning parameters used were a probe current of 2nA scanned over 4000 points with a pixel dwell time of 15ms, for a total cutting time of 2 minutes. This corresponds to rastering the beam along the length only once. The cross is made up of 2 perpendicular cuts of lengths of 168 and 187 nm for the horizontal and vertical cuts respectively, meaning that the total line dose received was 1.43 and 1.28 C/m. The horizontal cut of the cross appears slightly wider than the vertical cut, with a width of ~2.5 nm as opposed to ~2 nm. EDX elemental maps of the area after cutting and imaging are also shown for B, C and N. An EDX map of the oxygen content is shown in figure S14. There is a distinctly wider area without C counts in the immediate area of the cross, corresponding to the dark grey areas above the horizontal cut in the HAADF image. This looks very similar to the area of graphene in the vicinity of a cut which was etched away during imaging shown in figure 5 in the main text.

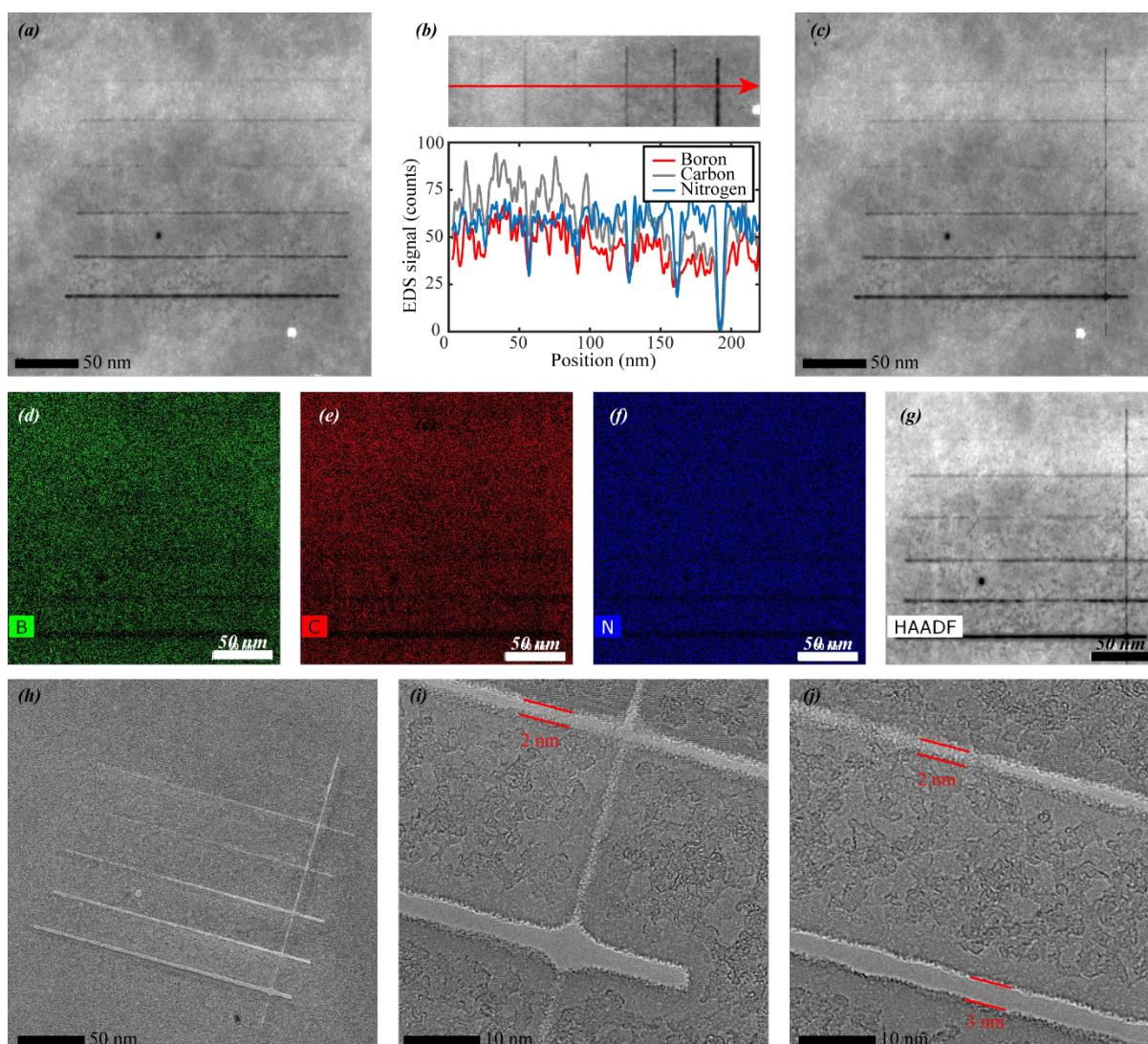


Figure S8 Patterning lines in a graphene monolayer supported by 6.5 nm thick hBN. All horizontal cuts were made using a probe current of 1nA, and by repeatedly scanning the beam over 4000 points over 213 nm with a pixel dwell time of 2ms, with a varying total time. (a) shows HAADF STEM image showing a series of line cuts with varying total times. From the thickest cut upwards, the total cutting times used were 8, 6, 4, 2 and 1 minutes and 30s respectively. (b) shows the location of the orthogonal cut, with the same writing parameters as the horizontal cuts but with a length of 222nm, and a total cutting time of 2 minutes, along with the elemental counts for B, C and N from the EDS signal collected during cutting. The x-axis corresponds to that shown in the upper image. (c) shows a HAADF STEM image of the same area after the orthogonal cut. (d) to (f) show EDX elemental maps of the area for B, C, and N respectively, whilst (g) shows the HAADF image captured during the EDX mapping process. (h) to (j) show high magnification HRTEM images of the produced pattern. (i) shows the lower two cuts and the orthogonal cut. (j) shows just the lower two cuts.

Figure S8 shows an example of the patterning of lines in a graphene monolayer supported by a 6.5 nm thick hBN flake. The patterning parameters used were a probe current of 2nA scanned over 4000 points with a pixel dwell time of 2ms for a variety of total cutting times. The horizontal cuts have lengths of 213nm, giving a line dose of 280 mC/m per minute of cutting time. From bottom to top, the lines were written with total cutting times of 8, 6, 4, 2, 1 and half a minute. Only total cutting times of 4 minutes and above seem to have opened a cut in the sample, and only the 8 minute cut is completely continuous. In this case, only one line is wide enough (above ~3nm) such that the elemental EDX profiles captured during the orthogonal cut drop to zero counts across the previously cut lines.

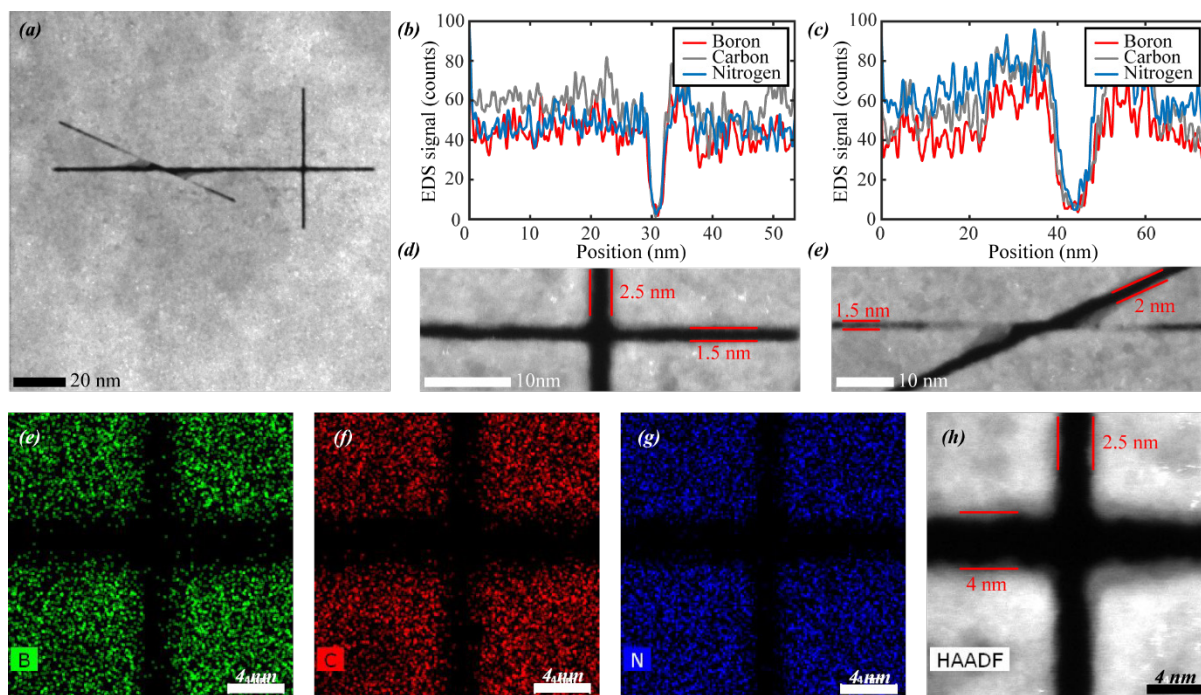


Figure S9 Patterning crosses in a graphene monolayer supported by 6.5 nm thick hBN. All cuts were made using a 2nA probe current, with the beam scanned along 4000pts with a dwell time of 2ms. The horizontal cut has a length of 124nm and was written using a total write time of 2 minutes. The vertical cut has a length of 55nm, and took 1 minute. The angled cut has a length of 75nm, is angled at 25° to the horizontal, and also took 1 minute. (a) shows a HAADF STEM image of the area after patterning. (b) and (c) show elemental counts for B, C and N from the EDS signal collected during cutting for the perpendicular and angled cuts respectively. The x-axis corresponds to that shown in the lower HAADF STEM images (d) and (e). (e) to (g) show EDX elemental maps of the area for B, C, and N respectively, whilst (h) shows the HAADF image captured during the EDX mapping process.

Figure S9 shows an example of the patterning of lines in a graphene monolayer supported by a 6.5 nm thick hBN flake. The patterning parameters used were a probe current of 2nA scanned over 4000 points with a pixel dwell time of 2ms. The horizontal cut has a length of 124nm, giving a line dose of 1.94 C/m. The perpendicular and angled cuts have lengths of 55 and 75nm and line doses of 2.18 and 1.6 C/m respectively. The perpendicular cut is continuous, whilst the angled cut failed to penetrate the sample in the area around the initial cut. EDX elemental maps of the perpendicular cross after cutting and imaging are also shown for B, C and N. The dark grey areas around the centre of the cross after imaging and mapping correspond to the area with reduced C counts, but B and N look unaffected.

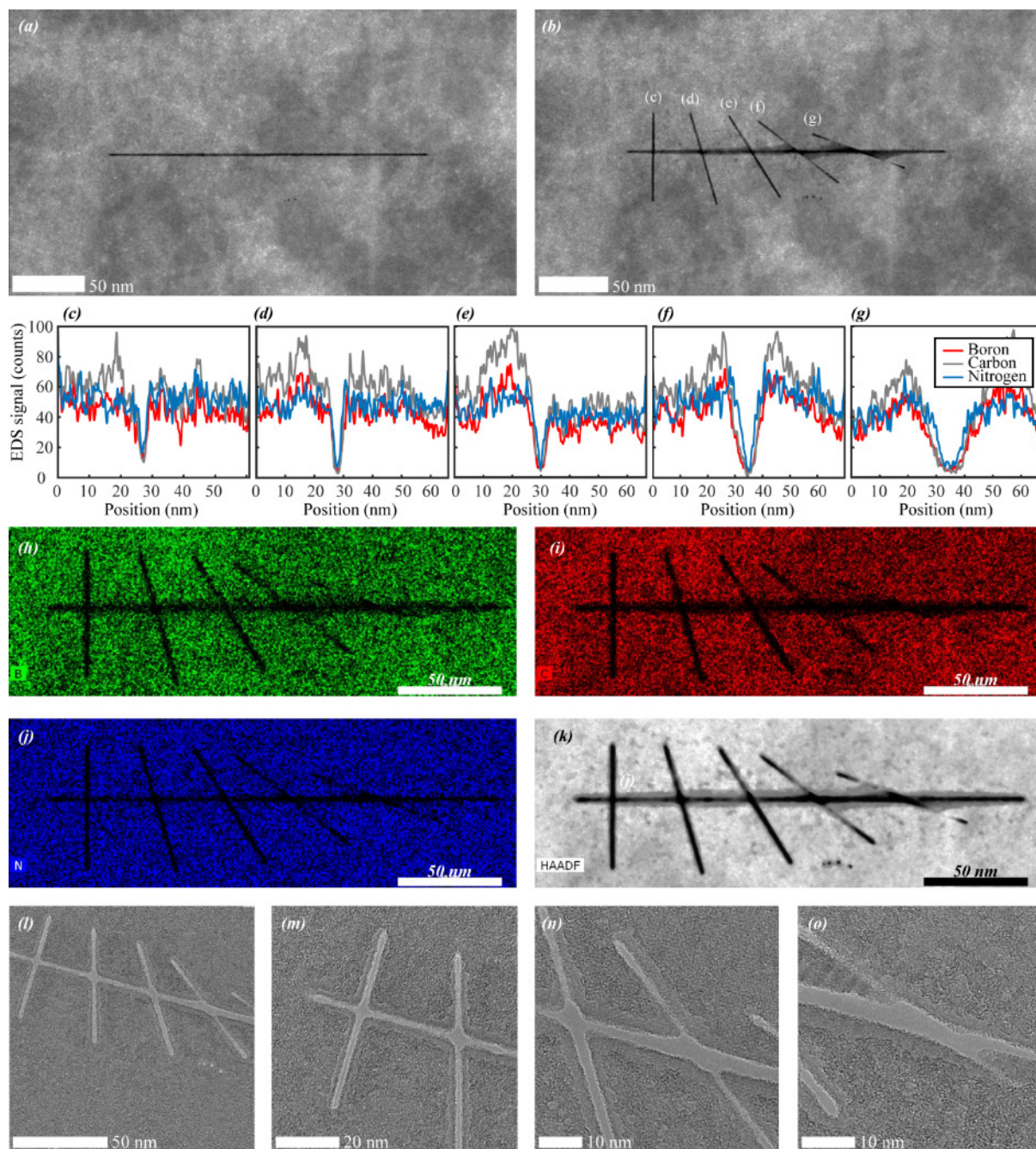


Figure S10 Patterning angled crosses in a graphene monolayer supported by 6.5 nm thick hBN. All cuts were made using a probe current of 2nA, and by repeatedly scanning the beam over 4000 points with a pixel dwell time of 2ms. (a) HAADF STEM image of initial line cut with a length of 220nm, using a total cutting time of 3 minutes. (b) shows a HAADF STEM image of the location after a series of cuts of length 60-70 nm crossing the initial cut, all with a total cutting time of 1 minute, and at angles of 90°, 75°, 58°, 36° and 20° to the initial cut. (c) to (g) shows elemental counts for B, C and N from the EDS signal collected during cutting the lines indicated in (b), from top to bottom. (h) to (j) show EDX elemental maps of the area for B, C, and N respectively, whilst (k) shows the HAADF image captured during the EDX mapping process. (l) to (o) show high magnification HRTEM images of the produced pattern.

Figure S10 shows an example of the patterning of lines in a graphene monolayer supported by a 6.5 nm thick hBN flake. The patterning parameters used were a probe current of 2 nA scanned over 4000 points with a pixel dwell time of 2. The horizontal cut was patterned for 3 minutes and is 220 nm long, giving a line dose of 1.64 C/m. The shorter lines took 1 minute and are 60-70 nm long, corresponding to doses in the range 1.7-2 C/m. They were cut sequentially from left to right without intermediate imaging. After the mapping, the graphene has been removed from a wide area around the horizontal line, especially inside the ‘acute’ angles within cuts

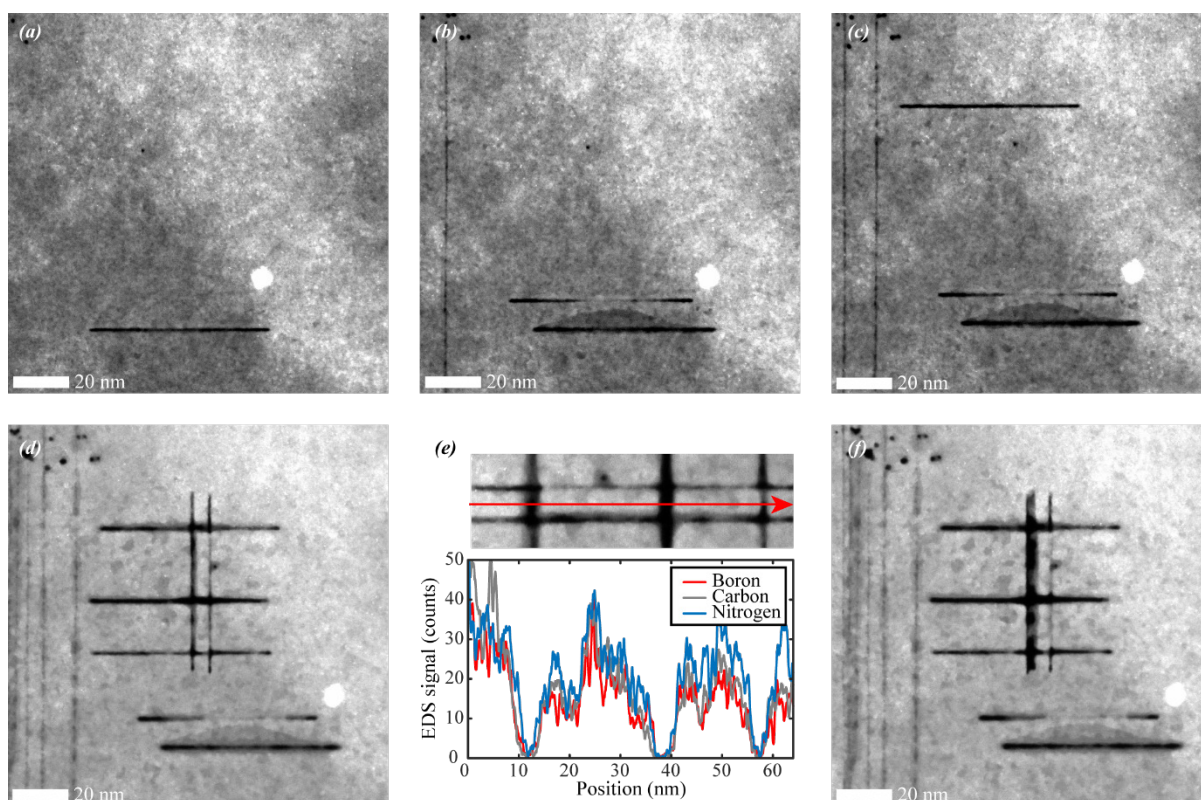


Figure S11 HAADF STEM images showing line cuts in monolayer graphene supported by 6.5 nm thick hBN. All cuts were made using a probe current of 2nA, and by repeatedly scanning the beam over 4000 points over 65nm for a total of 1 minute, with a varying pixel dwell time. (a) Image of cut patterned using a pixel dwell time of 20 μ s. (b) Image of same area with new cut patterned with a dwell time of 200 μ s. (c) Same area with new cut with the same parameters as that shown in (b), but farther from a previously patterned region. (d) same area with 4 new cuts. The new upper and lower horizontal cuts were patterned using dwell times of 2ms and 15ms respectively. Both new vertical cuts were made with dwell times of 15ms. (e) shows the location of a new orthogonal cut, along with the elemental counts for B, C and N from the EDS signal collected during cutting. The x-axis corresponds to that shown in the upper image. (f) shows the area after the cut shown in (e).

Figure S11 shows an example of the patterning of lines in a graphene monolayer supported by a 6.5 nm thick hBN flake. The patterning parameters used were a probe current of 2nA scanned over 4000 points over a length of 65nm for a total time of 1 minute, corresponding to a line dose of 1.85 C/m. The pixel dwell time was varied between 20 μ s and 15ms, corresponding to rastering the beam along the line w times and one respectively. The data does not appear to indicate a strong dependence of the shape/width of the line on the patterning conditions independent of dose. Rather, the cutting behaviour is dependent on the local cut environment. In contrast to the data presented in figure 4 in the main text, the beam was rastered sequentially, rather than with gaps for imaging. The initial successful cut shown in panel (a) was made using a dwell time of 20 μ s. The next two cuts, shown in panels (c) and (d), were patterned with identical parameters, but look very different. Far from the previous cut, these parameters work successfully, giving a clean cut with a width under 2nm. However in panel (b), the cut is unsuccessful, and the area above the previous cut shows a dark area, which we attribute to the removal of the graphene layer, as indicated by figure 5 in the main text. This shows how the level of local contamination and the extent of previous imaging and patterning in the immediate area appeared to control the eventual cut shape far more than the patterning parameters independent of the line dose.

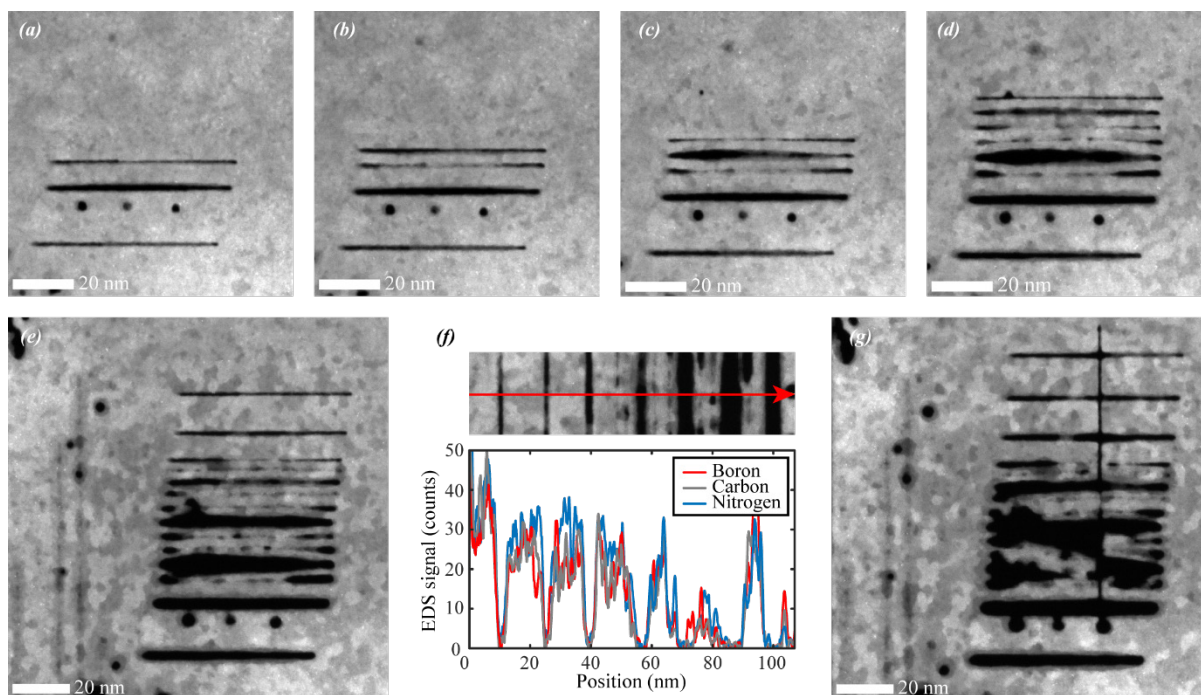


Figure S12 HAADF STEM images of line cuts in monolayer graphene supported by 6.5 nm thick hBN. All horizontal cuts were made using a probe current of 2nA, and by repeatedly scanning the beam over 4000 points over 62nm for a total of 1 minute, with a pixel dwell time of 15ms. (a)-(e) show a progressive series of images captured whilst making a series of parallel cuts. The cuts grow over time as they are repeatedly imaged. Also shown are 3 holes grown by leaving the beam in one place for 20s. (f) shows the location of a new orthogonal cut, with the same writing parameters as the horizontal cuts but with a length of 108nm along with the elemental counts for B, C and N from the EDS signal collected during cutting. The x-axis corresponds to that shown in the upper image. (g) shows the area after the cut shown in (f).

Figure S12 shows an example of the patterning of lines in a graphene monolayer supported by a thin (6.5 nm thick) hexagonal boron nitride flake. The patterning parameters used were a probe current of 2nA scanned over 4000 points over a length of 62nm for a total time of 1 minute, corresponding to a line dose of 1.94 C/m. The dwell time was fixed at 15ms, meaning the lines were cut by scanning the beam along only once. In this series of cuts, the sample was imaged prior to each cut, so the wider sample area received a very high electron dose, and much of the graphene was removed by the end of the sequence. However, panel (a) demonstrates the use of the technique to create a clearly defined ‘nanoribbon’ with less than 10nm width. We believe that this technique is capable of patterning clearly defined nanoribbons down to less than 5nm width, as previously demonstrated in monolayer graphene⁷.

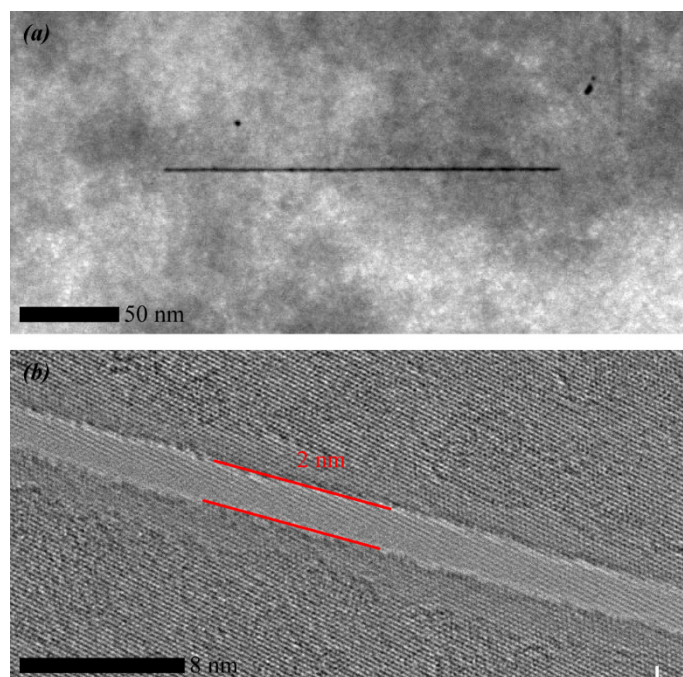


Figure S13 Line cut in monolayer graphene supported by 6.5 nm thick hBN. Patterned using a probe current of 2nA, and by repeatedly scanning the beam over 4000 points over 200nm for a total of 3 minutes, with a pixel dwell time of 2ms. (a) shows a HAADF STEM image. (b) shows a HRTEM image of the central area of the cut.

Figure S13 shows a 200nm long continuous cut with a line dose of 1.8 nm and a width of approximately 2nm, although it narrows slightly where it crosses an area of higher local contamination, shown by the lighter area in panel (a). This is an example of a 'pristine' cut with close to our empirically ideal cutting conditions, and without subsequent nearby patterning and imaging.

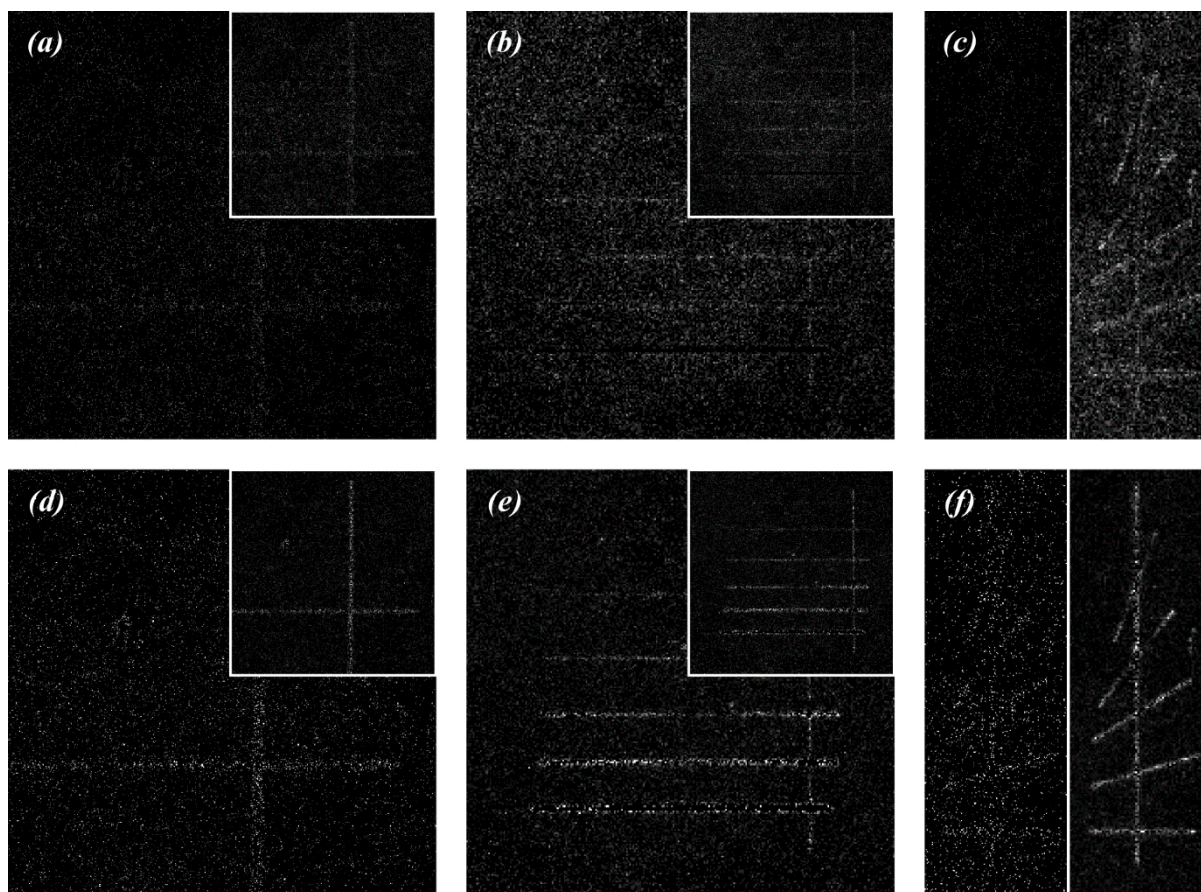


Figure S14 Oxygen content in EDS maps. (a), (b) and (c) show the elemental oxygen counts from the mapped patterned regions in figures 7, 8 and 9 in the main text. (d), (e) and (f) show percentage of elemental oxygen counts from the mapped regions in (a), (b), and (c) respectively. The inset images show the same map rebinned by 2 (for a,b,d,e) or 4 (for c,f) to aid visibility.

Figure S14 shows a selection of oxygen elemental maps of the cut features shown in figures S7 and S10 in the supplementary information and figure 6 in the main text. The oxygen counts are strongly localised around the cut features, and around the edges of the cut features where the cuts are larger than the image pixel size, such as the lower areas in panels (b) and (c). When the relative proportion of oxygen counts is mapped, the relationship is even clearer. This localisation was also seen when mapping using EELS, shown in figure 6 in the main text.

SUPPLEMENTARY VIDEOS

Supplementary video 1 shows a line feature in monolayer graphene on hBN under continuous imaging. It corresponds to the area of the sample shown in figure 2 in the main text. After the video was taken and the feature was widened, the area was studied again in figure 5 in the main text. The vertical feature in figure 5 corresponds with part of the left frame of the video.

Supplementary video 2 shows a cross feature cut in monolayer graphene on hBN under continuous imaging. It corresponds to the area of the sample shown in figures S3, S4 and S5 in the supplementary text, although it was captured after of all of the other data. The (continuous) vertical cut and (bridged) horizontal cut both widen under continued exposure, but the effect is greater for the vertical cut, which was initially narrower.

SUPPLEMENTARY MATERIAL REFERENCES

- 1 Gorbachev, R. V. *et al.* Hunting for monolayer boron nitride: optical and Raman signatures. *Small* **7**, 465-468, (2011).
- 2 Dean, C. R. *et al.* Boron nitride substrates for high-quality graphene electronics. *Nat Nanotechnol* **5**, 722-726, (2010).
- 3 Blake, P. *et al.* Making graphene visible. *Appl Phys Lett* **91**, (2007).
- 4 Reina, A. *et al.* Transferring and Identification of Single- and Few-Layer Graphene on Arbitrary Substrates. *The Journal of Physical Chemistry C* **112**, 17741-17744, (2008).
- 5 Fauske, V. T. *et al.* hyperspy: HyperSpy 0.8.5. (2016).
- 6 Wang, F., Egerton, R. & Malac, M. Fourier-ratio deconvolution techniques for electron energy-loss spectroscopy (EELS). *Ultramicroscopy* **109**, 1245-1249, (2009).
- 7 Xu, Q. *et al.* Controllable Atomic Scale Patterning of Freestanding Monolayer Graphene at Elevated Temperature. *Acs Nano* **7**, 1566-1572, (2013).

10 Conclusions and outlook

This thesis presents a range of cleanroom fabrication techniques developed by the author related to the fabrication of novel graphene samples. Their use to answer scientific questions has been illustrated in the 4 papers presented as part of this thesis. However, using this range of techniques, the author also contributed to a number of other published works, which are listed in a section immediately following this one.

The rest of this chapter reviews the material presented in the 4 preceding chapters. The contents of each are summarised with reference to the aims outlined in chapter 2. There follows a discussion of the results presented, along with a summary of conclusions which can be drawn, and how this relates to other work in the field. Finally, suggestions are made for fruitful further research building on the work presented here, and the conclusions drawn.

1st paper

We demonstrated that the PeakForce tapping off-resonance imaging AFM mode was able to image suspended graphene membranes, avoiding the imaging artefacts seen when using conventional non-contact modes due to membrane oscillations. We showed how the maps of derived mechanical quantities can be used to infer the tension distribution in the sheet, which is important for providing feedback necessary for optimizing the fabrication process, as alternative imaging techniques are unsuitable for such thin membranes. Performing feedback using the force applied to the sample makes it possible to image even very fragile samples at minimal applied forces. We also verified that the pixel force curves captured in the extended QNM capture mode were comparable to those captured during conventional nanoindentation, and that both agreed with a model of the central deformation previously reported in the literature. This also enabled us to make a measurement of the 2D modulus of graphene. This approach means that force curve arrays can be quickly captured and compared to whole membrane models of membrane deflection, for example finite element models for noncircular geometries.

This technique enables a variety of further studies into the various uses of suspended membranes, such as sensors and resonators. The results suggest a range of further possible

investigations into membrane behaviour under a wide variety of external conditions are possible, for instance applying a voltage between the tip and a silicon back gate. This will be of great use in the development of quasi-static electromechanical sensors.

2nd paper

We deposited and patterned CVD graphene on racetrack type silicon cavity resonators to investigate their optical behaviour, with a view to using the graphene to improve the waveguide surface reactivity for highly sensitive bio-molecular and gas sensing applications. Analysis of the transmission spectra for equivalent racetrack cavities with and without monolayer graphene coating show a strong quenching of the cavity resonance signal with increasing light-graphene interaction length, due to the strong in-plane absorption in graphene. From a fit to the transmission spectra, along with using a cutback method, we obtain a value for the (TE-mode) graphene linear absorption coefficient as $\alpha_g = 0.11 \pm 0.01 \text{ dB}\mu\text{m}^{-1}$. Combining this value with an exponential dependence for the strength of the evanescent coupling based on the height of the graphene above the waveguide surface, we suggest a model of the cavity resonance signal attenuation for different graphene lengths and heights above the cavity surface.

The results presented here provide useful design rules for different graphene integrated silicon photonic devices according to the required application. For instance, in refractive index sensing applications, relatively low attenuation is required; small shifts in the cavity wavelength are desirable rather than quenching the resonance signal. Therefore, a modified cavity with a small graphene interaction length and/or large height from the surface are desirable. On the other hand, for photo-detector applications, maximum absorption in the graphene layer is required and therefore designs should aim for a large interaction length and a low height. Practically, the interaction can be controlled by using selective etching of the graphene layer to only partially coat the race-track cavities or embed most of the device in thick silicon dioxide and only expose part of the track. The height can be easily controlled at the range of tens of nm, by coating the waveguides with a (low-loss) dielectric spacer layer (use of HSQ or silicon dioxide is typical) of chosen thickness prior to the CVD graphene transfer.

3rd paper

We created the first reported tBLG system with a previously specified twist angle, chosen to generate an anti-Stokes optical scattering resonance under illumination from a HeNe laser with $\lambda_{laser} = 632.8 \text{ nm}$. This also resulted in a Stokes scattering resonance under illumination from a frequency doubled Nd:YAG (Neodymium doped yttrium aluminium garnet) laser with $\lambda_{laser} = 532.0 \text{ nm}$. Previous optical studies relied on small samples with randomly oriented twist angles, but investigating the Stokes Anti-Stokes (SaS) correlated scattering process required a transmission optical setup, with a very large ($> 10 \mu\text{m}$) tBLG suspended sample to negate any background signal. A new exfoliation technique was developed that successfully generated suitably large flakes (flakes significantly larger than the membranes are required if the membranes are to be mechanically stable). Characterisation techniques to estimate the crystallographic axis were also developed.

The ratio between the scattered Stokes and anti-Stokes G-band intensity when switching between the two lasers varied by 3 orders of magnitude. The laser power dependence of the respective intensities indicates cooling of the tBLG sample under the anti-Stokes resonance condition due to the ejection of ‘hot’ phonons, and allows the tBLG sample to survive illumination under laser powers significantly higher than those which are able to burn away equivalent AB stacked BLG membranes. It also showed evidence of the correlated Stokes anti-Stokes process at far lower laser powers than that needed to observe it in diamond due to the extremely high anti-Stokes emission efficiency. The engineered structure acts as both a ‘self-cooling’ system and a source of entangled photons. The twist engineering technique can be used to generalise this to work using any incoming laser, from ultraviolet to far-infrared, in either ‘heating’ (Stokes G-band Resonance) or ‘cooling’ / ‘SaS’ mode (anti-Stokes G-band resonance).

4th paper

We reported the first example of the nanosculpting of a heterostructure created by stacking 2D materials, by directly ablating material with a STEM beam from a suspended membrane consisting of a mono/bilayer graphene sheet supported by a thin (sub 10 nm) hBN flake. The mechanical stability provided by the hBN sheet allowed us to consistently create long (hundreds of nm) cuts of widths between 2 and 2.5 nm, although they widened significantly

on imaging at 200 keV. We used information from the EELS and EDX spectra captured while patterning, and subsequently mapping cut areas, to monitor the cutting process and the structure of the patterned membrane. We observed elemental oxygen around the edge of cuts using both EELS and EDXS mapping. It was found that for monolayer graphene on 6.5 nm thick hBN, within the range of experimental parameters we used, that the cutting behaviour was mainly dependent on the total linear dose, and independent of other patterning parameters. For bilayer graphene the patterning conditions appeared to strongly affect the patterning behaviour, with two cuts with the same line dose showing very different behaviour when applying this total line dose in 8 scans rather than 2. However, we did not explore the cutting parameters for bilayer graphene in enough detail to understand the relative effect of the local contamination level. For monolayer graphene on 6.5 nm thick hBN, we suggest ideal patterning parameters of a line dose of 1.5 C/m, and a beam current of 2nA. This is much higher than the threshold cutting energy, but leads to cuts of uniform width over areas with differing levels of contamination.

Patterning suspended graphene with a STEM beam has been investigated previously, with a view to creating structures such as nanoribbon and nanopores with sub 10 nm precision. However the fact that individual areas cannot be electrically isolated from each other without being mechanically separated, and compromising the integrity of the suspended structure. The addition of an insulating support, however, makes a wide array of new device designs possible using a 2 step patterning process, and negates many of the restrictions imposed by the need for suspended samples for STEM nanosculpting.

List of publications

- [1] Sebastian Heeg, **Nick Clark**, and Aravind Vijayaraghavan. *High-accuracy placement of carbon nanotubes in hotspots of plasmon-enhanced Raman scattering*. In preparation, (2016).
- [2] Niclas S. Mueller, Sebastian Heeg, Patryk Kusch, Soeren Wasserroth, **Nick Clark**, Fred Schedin, Roman Gorbachev, Aravind Vijayaraghavan and Stephanie Reich. *Strained graphene probes local doping at hotspots of plasmon enhanced Raman scattering*. In submission, (2016).
- [3] Michael Hirtz, Antonios Oikonomou, **Nick Clark**, Yong Jin Kim, Harald Fuchs, and Aravind Vijayaraghavan. *Self-limiting Multiplexed Assembly of Lipid Membranes on Large-area Graphene Sensor Arrays*. *Nanoscale*, **8**(33), pp. 15147-15151, (2016).
- [4] **Nick Clark**, Edward Lewis, Sarah Haigh, and Aravind Vijayaraghavan. *Nanometre electron beam sculpting of suspended graphene and hexagonal boron nitride heterostructures*. In submission, (2016).
- [5] Lan Nguyen, Edward Lewis, Eric Prestat, Yang Cao, **Nick Clark**, Reza Kashtiban, Jeremy Sloan, Demie Kepaptsoglou, Roman Gorbachev, Sarah Haigh. *Nanosculpting graphene-encapsulated black phosphorus*. In submission, (2016).
- [6] Patryk Kusch, Sebastian Heeg, Christian Lehmann, Niclas Müller, Sören Wasserroth, Antonios Oikonomou, **Nick Clark**, Aravind Vijayaraghavan, and Stephanie Reich. *Quantum nature of plasmon-enhanced Raman scattering*. ArXiv:1503.03835 (2015).
- [7] Ado Jorio, Mark Kasperczyk, **Nick Clark**, Elke Neu, Patrick Maletinsky, Aravind Vijayaraghavan, and Lukas Novotny. *Stokes and anti-stokes Raman spectra of the high-energy C-C stretching modes in graphene and diamond*. *Physica status solidi (b)*, **22**(11), pp. 2380-2384, (2015).
- [8] Antonios Oikonomou, **Nick Clark**, Sebastian Heeg, Andrey Kretinin, Sarah Varey, Geliang Yu, and Aravind Vijayaraghavan. *Scalable bottom-up assembly of suspended carbon nanotube and graphene devices by dielectrophoresis*. *Physica status solidi (RRL)-Rapid Research Letters*, **9**(9), pp. 539-543, (2015).

[9] Hollie V. Patten, Matej Velicky, **Nick Clark**, Christopher A. Muryn, Ian A. Kinloch, and Robert A. W. Dryfe. *Electrochemistry of well-defined graphene samples: role of contaminants*. Faraday Discussions, **172**, pp. 261–272, (2014).

[10] Sebastian Heeg, **Nick Clark**, Antonios Oikonomou, Aravind Vijayaraghavan, and Stephanie Reich. *Plasmon-enhanced Raman scattering by suspended carbon nanotubes*. physica status solidi (RRL), **8**(9), pp. 785–789, (2014).

[11] Ado Jorio, Mark Kasperczyk, **Nick Clark**, Elke Neu, Patrick Maletinsky, Aravind Vijayaraghavan, and Lukas Novotny. *Optical-phonon resonances with saddle-point excitons in twisted-bilayer graphene*. Nano Letters, **14**(10), pp. 5687–5692, (2014).

[12] Iain F Crowe, **Nick Clark**, Siham Hussein, Brian Towlson, Eric Whittaker, Milan M Milosevic, Frederic Y Gardes, Goran Z Mashanovich, Matthew P Halsall, and Aravind Vijayaraghavan. *Determination of the quasi-TE mode (in-plane) graphene linear absorption coefficient via integration with silicon-on-insulator racetrack cavity resonators*. Optics Express, **22**(15), pp. 18625–18632, (2014).

[13] **Nick Clark**, Antonios Oikonomou, and Aravind Vijayaraghavan. *Ultrafast quantitative nanomechanical mapping of suspended graphene*. physica status solidi (b), **250**(12), pp. 2672–2677, (2013).

[14] Lauren Newton, Thomas Slater, **Nick Clark**, and Aravind Vijayaraghavan. *Self-assembled monolayers (SAMS) on metallic surfaces (gold and graphene) for electronic applications*. Journal of Materials Chemistry C, **1**(3), pp. 376–393, (2013).

References

- 1 K.S. Novoselov, A.K. Geim, S.V. Morozov, D. Jiang, Y. Zhang, S.V. Dubonos, I.V. Grigorieva & A.A. Firsov. Electric Field Effect in Atomically Thin Carbon Films. *Science* **306** (5696), 666-669 (2004).
- 2 K.S. Novoselov, D. Jiang, F. Schedin, T.J. Booth, V.V. Khotkevich, S.V. Morozov & A.K. Geim. Two-dimensional atomic crystals. *Proceedings of the National Academy of Sciences of the United States of America* **102** (30), 10451-10453 (2005).
- 3 K.S. Novoselov, V.I. Fal'ko, L. Colombo, P.R. Gellert, M.G. Schwab & K. Kim. A roadmap for graphene. *Nature* **490** (7419), 192-200 (2012).
- 4 A.K. Geim & I.V. Grigorieva. Van der Waals heterostructures. *Nature* **499** (7459), 419-425 (2013).
- 5 L. Pauling. *The Nature of the Chemical Bond*. 3rd edn, 145-180 (Cornell University Press, 1960).
- 6 S. Iijima. Helical Microtubules of Graphitic Carbon. *Nature* **354** (6348), 56-58 (1991).
- 7 H.W. Kroto, J.R. Heath, S.C. O'brien, R.F. Curl & R.E. Smalley. C60: Buckminsterfullerene. *Nature* **318** (6042), 162-163 (1985).
- 8 N.D. Mermin. Crystalline Order in Two Dimensions. *Physical Review* **176** (1), 250-254 (1968).
- 9 L.D. Landau & E.M. Lifshitz. *Statistical Physics*. 3rd edn, 455-478 (Elsevier Science, 2013).
- 10 J.W. Evans, P.A. Thiel & M.C. Bartelt. Morphological evolution during epitaxial thin film growth: Formation of 2D islands and 3D mounds. *Surface Science Reports* **61** (1-2), 1-128 (2006).
- 11 J.C. Meyer, A.K. Geim, M.I. Katsnelson, K.S. Novoselov, T.J. Booth & S. Roth. The structure of suspended graphene sheets. *Nature* **446** (7131), 60-63 (2007).
- 12 P.R. Wallace. The Band Theory of Graphite. *Physical Review* **71** (9), 622-634 (1947).
- 13 J.C. Slonczewski & P.R. Weiss. Band Structure of Graphite. *Physical Review* **109** (2), 272-279 (1958).
- 14 S. Reich, J. Maultzsch, C. Thomsen & P. Ordejon. Tight-binding description of graphene. *Physical Review B* **66** (3), 035412 (2002).
- 15 K. Nakada, M. Fujita, G. Dresselhaus & M.S. Dresselhaus. Edge state in graphene ribbons: Nanometer size effect and edge shape dependence. *Physical Review B* **54** (24), 17954-17961 (1996).
- 16 A.K. Geim. Graphene: Status and Prospects. *Science* **324** (5934), 1530-1534 (2009).
- 17 A.H. Castro Neto, F. Guinea, N.M.R. Peres, K.S. Novoselov & A.K. Geim. The electronic properties of graphene. *Reviews of Modern Physics* **81** (1), 109-162 (2009).
- 18 M. Xu, T. Liang, M. Shi & H. Chen. Graphene-Like Two-Dimensional Materials. *Chemical Reviews* **113** (5), 3766-3798 (2013).
- 19 B. Radisavljevic, A. Radenovic, J. Brivio, V. Giacometti & A. Kis. Single-layer MoS2 transistors. *Nature Nanotechnology* **6** (3), 147-150 (2011).

- 20 B. Radisavljevic, M.B. Whitwick & A. Kis. Integrated circuits and logic operations based on single-layer MoS₂. *Acs Nano* **5** (12), 9934-9938 (2011).
- 21 K. Watanabe, T. Taniguchi & H. Kanda. Direct-bandgap properties and evidence for ultraviolet lasing of hexagonal boron nitride single crystal. *Nature Materials* **3** (6), 404-409 (2004).
- 22 C.R. Dean, A.F. Young, I. Meric, C. Lee, L. Wang, S. Sorgenfrei, K. Watanabe, T. Taniguchi, P. Kim, K.L. Shepard & J. Hone. Boron nitride substrates for high-quality graphene electronics. *Nature Nanotechnology* **5** (10), 722-726 (2010).
- 23 A.K. Geim & K.S. Novoselov. The rise of graphene. *Nature Materials* **6** (3), 183-191 (2007).
- 24 A. Grüneis, C. Attaccalite, L. Wirtz, H. Shiozawa, R. Saito, T. Pichler & A. Rubio. Tight-binding description of the quasiparticle dispersion of graphite and few-layer graphene. *Physical Review B* **78** (20), 205425 (2008).
- 25 P.E. Trevisanutto, C. Giorgetti, L. Reining, M. Ladisa & V. Olevano. Ab initio GW Many-Body Effects in Graphene. *Physical Review Letters* **101** (22), 226405 (2008).
- 26 C.H. Park, F. Giustino, C.D. Spataru, M.L. Cohen & S.G. Louie. Angle-Resolved Photoemission Spectra of Graphene from First-Principles Calculations. *Nano Letters* **9** (12), 4234-4239 (2009).
- 27 M.I. Katsnelson. *Graphene: Carbon in Two Dimensions*. 503-504 (Taylor & Francis, 2012).
- 28 M. Smollett. The Frequency Spectrum of a Two-Dimensional Ionic Lattice. *Proceedings of the Physical Society. Section A* **65** (2), 109 (1952).
- 29 M. Morse. *The Calculus of Variations in the Large*. 1st edn, 173-188 (American Mathematical Society, 1934).
- 30 L. Van Hove. The Occurrence of Singularities in the Elastic Frequency Distribution of a Crystal. *Physical Review* **89** (6), 1189-1193 (1953).
- 31 G.H. Li, A. Luican, J.M.B.L. Dos Santos, A.H. Castro Neto, A. Reina, J. Kong & E.Y. Andrei. Observation of Van Hove singularities in twisted graphene layers. *Nature Physics* **6** (2), 109-113 (2010).
- 32 E. Mccann & V.I. Fal'ko. Landau-level degeneracy and quantum Hall effect in a graphite bilayer. *Physical Review Letters* **96** (8), 086805 (2006).
- 33 M. Edward & K. Mikito. The electronic properties of bilayer graphene. *Reports on Progress in Physics* **76** (5), 056503 (2013).
- 34 Y. Zhang, T.T. Tang, C. Girit, Z. Hao, M.C. Martin, A. Zettl, M.F. Crommie, Y.R. Shen & F. Wang. Direct observation of a widely tunable bandgap in bilayer graphene. *Nature* **459** (7248), 820-823 (2009).
- 35 K. Kechedzhi, V.I. Fal'ko, E. Mccann & B.L. Altshuler. Influence of trigonal warping on interference effects in bilayer graphene. *Physical Review Letters* **98** (17), 176806 (2007).
- 36 A.B. Kuzmenko, E. Van Heumen, F. Carbone & D. Van Der Marel. Universal optical conductance of graphite. *Physical Review Letters* **100** (11), 117401 (2008).
- 37 R.R. Nair, P. Blake, A.N. Grigorenko, K.S. Novoselov, T.J. Booth, T. Stauber, N.M.R. Peres & A.K. Geim. Fine Structure Constant Defines Visual Transparency of Graphene. *Science* **320** (5881), 1308 (2008).

- 38 R.R. Nair, P. Blake, A.N. Grigorenko, K.S. Novoselov, T.J. Booth, T. Stauber, N.M. Peres & A.K. Geim. Fine structure constant defines visual transparency of graphene (Supplementary Material). *Science* **320** (5881), 1308 (2008).
- 39 T. Ando, Y. Zheng & H. Suzuura. Dynamical Conductivity and Zero-Mode Anomaly in Honeycomb Lattices. *Journal of the Physical Society of Japan* **71** (5), 1318-1324 (2002).
- 40 K.F. Mak, J. Shan & T.F. Heinz. Seeing many-body effects in single- and few-layer graphene: observation of two-dimensional saddle-point excitons. *Physical Review Letters* **106** (4), 046401 (2011).
- 41 N.M.R. Peres. Colloquium: The transport properties of graphene: An introduction. *Reviews of Modern Physics* **82** (3), 2673-2700 (2010).
- 42 J. Horng, C.F. Chen, B. Geng, C. Girit, Y. Zhang, Z. Hao, H.A. Bechtel, M. Martin, A. Zettl, M.F. Crommie, Y.R. Shen & F. Wang. Drude conductivity of Dirac fermions in graphene. *Physical Review B* **83** (16), 165113 (2011).
- 43 K.F. Mak, L. Ju, F. Wang & T.F. Heinz. Optical spectroscopy of graphene: From the far infrared to the ultraviolet. *Solid State Communications* **152** (15), 1341-1349 (2012).
- 44 Z.Q. Li, E.A. Henriksen, Z. Jiang, Z. Hao, M.C. Martin, P. Kim, H.L. Stormer & D.N. Basov. Dirac charge dynamics in graphene by infrared spectroscopy. *Nature Physics* **4** (7), 532-535 (2008).
- 45 F. Wang, Y. Zhang, C. Tian, C. Girit, A. Zettl, M. Crommie & Y.R. Shen. Gate-Variable Optical Transitions in Graphene. *Science* **320** (5873), 206-209 (2008).
- 46 P. Kusch, S. Heeg, C. Lehmann, N.S. Müller, S. Wasserroth, A. Oikonomou, N. Clark, A. Vijayaraghavan & S. Reich. Quantum Nature of Plasmon-Enhanced Raman Scattering. *arXiv preprint arXiv:1503.03835* (2015).
- 47 B. Wang, X. Zhang, F.J. García-Vidal, X. Yuan & J. Teng. Strong Coupling of Surface Plasmon Polaritons in Monolayer Graphene Sheet Arrays. *Physical Review Letters* **109** (7), 073901 (2012).
- 48 R.R. Alfano & S.L. Shapiro. Optical Phonon Lifetime Measured Directly with Picosecond Pulses. *Physical Review Letters* **26** (20), 1247-1251 (1971).
- 49 D.N. Klyshko. Correlation between the Stokes and anti-Stokes components in inelastic scattering of light. *Soviet Journal of Quantum Electronics* **7** (6), 755 (1977).
- 50 K.C. Lee, B.J. Sussman, M.R. Sprague, P. Michelberger, K.F. Reim, J. Nunn, N.K. Langford, P.J. Bustard, D. Jaksch & I.A. Walmsley. Macroscopic non-classical states and terahertz quantum processing in room-temperature diamond. *Nature Photonics* **6** (1), 41-44 (2012).
- 51 A. Jorio, M. Kasperczyk, N. Clark, E. Neu, P. Maletinsky, A. Vijayaraghavan & L. Novotny. Optical-Phonon Resonances with Saddle-Point Excitons in Twisted-Bilayer Graphene. *Nano Letters* **14** (10), 5687-5692 (2014).
- 52 A. Gupta, G. Chen, P. Joshi, S. Tadigadapa & Eklund. Raman Scattering from High-Frequency Phonons in Supported n-Graphene Layer Films. *Nano Letters* **6** (12), 2667-2673 (2006).
- 53 R. Al-Jishi & G. Dresselhaus. Lattice-dynamical model for graphite. *Physical Review B* **26** (8), 4514-4522 (1982).
- 54 M.S. Dresselhaus, A. Jorio, M. Hofmann, G. Dresselhaus & R. Saito. Perspectives on Carbon Nanotubes and Graphene Raman Spectroscopy. *Nano Letters* **10** (3), 751-758 (2010).

- 55 S. Piscanec, M. Lazzeri, F. Mauri, A.C. Ferrari & J. Robertson. Kohn Anomalies and Electron-Phonon Interactions in Graphite. *Physical Review Letters* **93** (18), 185503 (2004).
- 56 A.C. Ferrari, J.C. Meyer, V. Scardaci, C. Casiraghi, M. Lazzeri, F. Mauri, S. Piscanec, D. Jiang, K.S. Novoselov, S. Roth & A.K. Geim. Raman spectrum of graphene and graphene layers. *Physical Review Letters* **97** (18), 187401 (2006).
- 57 Z.H. Ni, T. Yu, Y.H. Lu, Y.Y. Wang, Y.P. Feng & Z.X. Shen. Uniaxial Strain on Graphene: Raman Spectroscopy Study and Band-Gap Opening. *Acs Nano* **2** (11), 2301-2305 (2008).
- 58 L.G. Cancado, M.A. Pimenta, B.R. Neves, G. Medeiros-Ribeiro, T. Enoki, Y. Kobayashi, K. Takai, K. Fukui, M.S. Dresselhaus, R. Saito & A. Jorio. Anisotropy of the Raman spectra of nanographite ribbons. *Physical Review Letters* **93** (4), 047403 (2004).
- 59 R. Saito, A. Jorio, A.G. Souza Filho, G. Dresselhaus, M.S. Dresselhaus & M.A. Pimenta. Probing phonon dispersion relations of graphite by double resonance Raman scattering. *Physical Review Letters* **88** (2), 027401 (2002).
- 60 A.C. Ferrari. Raman spectroscopy of graphene and graphite: Disorder, electron-phonon coupling, doping and nonadiabatic effects. *Solid State Communications* **143** (1-2), 47-57 (2007).
- 61 A.A. Griffith. The Phenomena of Rupture and Flow in Solids. *Philosophical Transactions of the Royal Society of London. Series A* **221** 163-198 (1921).
- 62 Q.Z. Zhao, M.B. Nardelli & J. Bernholc. Ultimate strength of carbon nanotubes: A theoretical study. *Physical Review B* **65** (14), 144105 (2002).
- 63 T.J. Booth, P. Blake, R.R. Nair, D. Jiang, E.W. Hill, U. Bangert, A. Bleloch, M. Gass, K.S. Novoselov, M.I. Katsnelson & A.K. Geim. Macroscopic Graphene Membranes and Their Extraordinary Stiffness. *Nano Letters* **8** (8), 2442-2446 (2008).
- 64 J.J. Vlassak & W.D. Nix. A new bulge test technique for the determination of Young's modulus and Poisson's ratio of thin films. *Journal of Materials Research* **7** (12), 3242-3249 (1992).
- 65 S.P. Koenig, N.G. Boddeti, M.L. Dunn & J.S. Bunch. Ultrastrong adhesion of graphene membranes. *Nature Nanotechnology* **6** (9), 543-546 (2011).
- 66 H. Hencky. *Zeitschrift fuer Mathematik und Physik* **63** 311 (1915).
- 67 M.R. Begley & T.J. Mackin. Spherical indentation of freestanding circular thin films in the membrane regime. *Journal of the Mechanics and Physics of Solids* **52** (9), 2005-2023 (2004).
- 68 U. Komaragiri & M.R. Begley. The mechanical response of freestanding circular elastic films under point and pressure loads. *Journal of Applied Mechanics-Transactions of the Asme* **72** (2), 203-212 (2005).
- 69 K.T. Wan, S. Guo & D.A. Dillard. A theoretical and numerical study of a thin clamped circular film under an external load in the presence of a tensile residual stress. *Thin Solid Films* **425** (1-2), 150-162 (2003).
- 70 C. Lee, X.D. Wei, J.W. Kysar & J. Hone. Measurement of the elastic properties and intrinsic strength of monolayer graphene. *Science* **321** (5887), 385-388 (2008).
- 71 N.M. Bhatia & W. Nachbar. Finite indentation of an elastic membrane by a spherical indenter. *International Journal of Non-Linear Mechanics* **3** (3), 307-324 (1968).
- 72 J.S. Mitchell, C.A. Zorman, T. Kicher, S. Roy & M. Mehregany. Examination of bulge test for determining residual stress, Young's modulus, and Poisson's ratio of 3C-SiC thin films. *Journal of Aerospace Engineering* **16** (2), 46-54 (2003).

- 73 A. Castellanos-Gomez, V. Singh, H.S.J. Van Der Zant & G.A. Steele. Mechanics of freely-suspended ultrathin layered materials. *Annalen der Physik* **527** (1-2), 27-44 (2015).
- 74 J.S. Bunch & M.L. Dunn. Adhesion mechanics of graphene membranes. *Solid State Communications* **152** (15), 1359-1364 (2012).
- 75 Q.Y. Lin, Y.H. Zeng, D. Liu, G.Y. Jing, Z.M. Liao & D. Yu. Step-by-Step Fracture of Two-Layer Stacked Graphene Membranes. *Acs Nano* **8** (10), 10246-10251 (2014).
- 76 X. Wei, B. Fragneaud, C.A. Marianetti & J.W. Kysar. Nonlinear elastic behavior of graphene: Ab initio calculations to continuum description. *Physical Review B* **80** (20), 205407 (2009).
- 77 A. Politano & G. Chiarello. Probing the Young's modulus and Poisson's ratio in graphene/metal interfaces and graphite: a comparative study. *Nano Research* **8** (6), 1847-1856 (2015).
- 78 G.H. Lee, R.C. Cooper, S.J. An, S. Lee, A. Van Der Zande, N. Petrone, A.G. Hammerberg, C. Lee, B. Crawford, W. Oliver, J.W. Kysar & J. Hone. High-Strength Chemical-Vapor-Deposited Graphene and Grain Boundaries. *Science* **340** (6136), 1073-1076 (2013).
- 79 N. Clark, A. Oikonomou & A. Vijayaraghavan. Ultrafast quantitative nanomechanical mapping of suspended graphene. *physica status solidi (b)* **250** (12), 2672-2677 (2013).
- 80 J. Zhou & R. Huang. Internal lattice relaxation of single-layer graphene under in-plane deformation. *Journal of the Mechanics and Physics of Solids* **56** (4), 1609-1623 (2008).
- 81 C.D. Reddy, A. Ramasubramaniam, V.B. Shenoy & Y.W. Zhang. Edge elastic properties of defect-free single-layer graphene sheets. *Applied Physics Letters* **94** (10), 101904 (2009).
- 82 E. Cadelano, P.L. Palla, S. Giordano & L. Colombo. Nonlinear elasticity of monolayer graphene. *Physical Review Letters* **102** (23), 235502 (2009).
- 83 K.M. Fair, M.D. Arnold & M.J. Ford. Determination of the elastic properties of graphene by indentation and the validity of classical models of indentation. *Journal of Physics: Condensed Matter* **26** (1), 015307 (2014).
- 84 M. Arroyo & T. Belytschko. Finite crystal elasticity of carbon nanotubes based on the exponential Cauchy-Born rule. *Physical Review B* **69** (11), 115415 (2004).
- 85 E. Cadelano, P.L. Palla, S. Giordano & L. Colombo. Elastic properties of hydrogenated graphene. *Physical Review B* **82** (23), 235414 (2010).
- 86 K.N. Kudin, G.E. Scuseria & B.I. Yakobson. C₂F, BN, and C nanoshell elasticity from *ab initio* computations. *Physical Review B* **64** (23), 235406 (2001).
- 87 F. Liu, P. Ming & J. Li. Ab initio calculation of ideal strength and phonon instability of graphene under tension. *Physical Review B* **76** (6), 064120 (2007).
- 88 K.V. Zakharchenko, M.I. Katsnelson & A. Fasolino. Finite temperature lattice properties of graphene beyond the quasiharmonic approximation. *Physical Review Letters* **102** (4), 046808 (2009).
- 89 S. Bera, A. Arnold, F. Evers, R. Narayanan & P. Wölfle. Elastic properties of graphene flakes: Boundary effects and lattice vibrations. *Physical Review B* **82** (19), 195445 (2010).
- 90 K.H. Michel & B. Verberck. Theory of the elastic constants of graphite and graphene. *physica status solidi (b)* **245** (10), 2177-2180 (2008).
- 91 C.S. Ruiz-Vargas, H.L. Zhuang, P.Y. Huang, A.M. Van Der Zande, S. Garg, P.L. McEuen, D.A. Muller, R.G. Hennig & J. Park. Softened Elastic Response and Unzipping in Chemical Vapor Deposition Graphene Membranes. *Nano Letters* **11** (6), 2259-2263 (2011).

- 92 O.L. Blakslee. Elastic Constants of Compression-Annealed Pyrolytic Graphite. *Journal of Applied Physics* **41** (8), 3373 (1970).
- 93 L. Landau & E. Lifshitz. *Theory of Elasticity*. 3rd edn, 38-86 (Butterworth-Heinemann, 1959).
- 94 H.I. Rasool, C. Ophus, W.S. Klug, A. Zettl & J.K. Gimzewski. Measurement of the intrinsic strength of crystalline and polycrystalline graphene. *Nature Communications* **4** 2811 (2013).
- 95 X. Wei & J.W. Kysar. Experimental validation of multiscale modeling of indentation of suspended circular graphene membranes. *International Journal of Solids and Structures* **49** (22), 3201-3209 (2012).
- 96 C.Y. Chen, S. Rosenblatt, K.I. Bolotin, P. Kim, I. Kymissis, H.L. Stormer, T.F. Heinz & J. Hone. NEMS Applications of Graphene. *2009 Ieee International Electron Devices Meeting* 232-235 (2009).
- 97 M. Annamalai, S. Mathew, V. Viswanathan, C. Fang, D.S. Pickard & M. Palaniapan. Design, fabrication and Helium Ion Microscope patterning of suspended nanomechanical graphene structures for NEMS applications in *Solid-State Sensors, Actuators and Microsystems Conference (TRANSDUCERS), 2011 16th International*. doi: 10.1109/TRANSDUCERS.2011.5969824.
- 98 C. Chen & J. Hone. Graphene nanoelectromechanical systems. *Proceedings of the IEEE* **101** (7), 1766-1779 (2013).
- 99 A. Sakhaee-Pour, M.T. Ahmadian & R. Naghdabadi. Vibrational analysis of single-layered graphene sheets. *Nanotechnology* **19** (8), 085702 (2008).
- 100 C. Chen, S. Lee, V.V. Deshpande, G.H. Lee, M. Lekas, K. Shepard & J. Hone. Graphene mechanical oscillators with tunable frequency. *Nature Nanotechnology* **8** (12), 923-927 (2013).
- 101 A. Eichler, J. Moser, J. Chaste, M. Zdrojek, I. Wilson Rae & A. Bachtold. Nonlinear damping in mechanical resonators made from carbon nanotubes and graphene. *Nature Nanotechnology* **6** (6), 339-342 (2011).
- 102 A.M.V.D. Zande, R.A. Barton, J.S. Alden, C.S. Ruiz-Vargas, W.S. Whitney, P.H.Q. Pham, J. Park, J.M. Parpia, H.G. Craighead & P.L. Mceuen. Large-Scale Arrays of Single-Layer Graphene Resonators. *Nano Letters* **10** (12), 4869-4873 (2010).
- 103 X. Song, M. Oksanen, J. Li, P.J. Hakonen & M.A. Sillanpaa. Graphene optomechanics realized at microwave frequencies. *Physical Review Letters* **113** (2), 027404 (2014).
- 104 C. Chen, S. Rosenblatt, K.I. Bolotin, W. Kalb, P. Kim, I. Kymissis, H.L. Stormer, T.F. Heinz & J. Hone. Performance of monolayer graphene nanomechanical resonators with electrical readout. *Nature Nanotechnology* **4** (12), 861-867 (2009).
- 105 J.S. Bunch, A.M. Van Der Zande, S.S. Verbridge, I.W. Frank, D.M. Tanenbaum, J.M. Parpia, H.G. Craighead & P.L. Mceuen. Electromechanical Resonators from Graphene Sheets. *Science* **315** (5811), 490-493 (2007).
- 106 D. Garcia-Sanchez, A.M. Van Der Zande, A.S. Paulo, B. Lassagne, P.L. Mceuen & A. Bachtold. Imaging Mechanical Vibrations in Suspended Graphene Sheets. *Nano Letters* **8** (5), 1399-1403 (2008).
- 107 A. Sakhaee-Pour, M.T. Ahmadian & A. Vafai. Applications of single-layered graphene sheets as mass sensors and atomistic dust detectors. *Solid State Communications* **145** (4), 168-172 (2008).
- 108 R.A. Barton, B. Ilic, A.M. Van Der Zande, W.S. Whitney, P.L. Mceuen, J.M. Parpia & H.G. Craighead. High, Size-Dependent Quality Factor in an Array of Graphene Mechanical Resonators. *Nano Letters* **11** (3), 1232-1236 (2011).

- 109 J. Chaste, A. Eichler, J. Moser, G. Ceballos, R. Rurali & A. Bachtold. A nanomechanical mass sensor with yoctogram resolution. *Nature Nanotechnology* **7** (5), 301-304 (2012).
- 110 A.C. Ferrari, F. Bonaccorso, V. Fal'ko, K.S. Novoselov, S. Roche, P. Boggild, S. Borini, F.H.L. Koppens, V. Palermo, N. Pugno, J.A. Garrido, R. Sordan, A. Bianco, L. Ballerini, M. Prato, E. Lidorikis, J. Kivioja, C. Marinelli, T. Ryhanen, A. Morpurgo, J.N. Coleman, V. Nicolosi, L. Colombo, A. Fert, M. Garcia-Hernandez, A. Bachtold, G.F. Schneider, F. Guinea, C. Dekker, M. Barbone, Z. Sun, C. Galiotis, A.N. Grigorenko, G. Konstantatos, A. Kis, M. Katsnelson, L. Vandersypen, A. Loiseau, V. Morandi, D. Neumaier, E. Treossi, V. Pellegrini, M. Polini, A. Tredicucci, G.M. Williams, B. Hee Hong, J.-H. Ahn, J. Min Kim, H. Zirath, B.J. Van Wees, H. Van Der Zant, L. Occhipinti, A. Di Matteo, I.A. Kinloch, T. Seyller, E. Quesnel, X. Feng, K. Teo, N. Rupesinghe, P. Hakonen, S.R.T. Neil, Q. Tannock, T. Lofwander & J. Kinaret. Science and technology roadmap for graphene, related two-dimensional crystals, and hybrid systems. *Nanoscale* **7** (11), 4598-4810 (2015).
- 111 C.H. Lui, L. Liu, K.F. Mak, G.W. Flynn & T.F. Heinz. Ultraflat graphene. *Nature* **462** (7271), 339-341 (2009).
- 112 Y. Hernandez, V. Nicolosi, M. Lotya, F.M. Blighe, Z. Sun, S. De, I.T. Mcgovern, B. Holland, M. Byrne, Y.K. Gun'ko, J.J. Boland, P. Niraj, G. Duesberg, S. Krishnamurthy, R. Goodhue, J. Hutchison, V. Scardaci, A.C. Ferrari & J.N. Coleman. High-yield production of graphene by liquid-phase exfoliation of graphite. *Nature Nanotechnology* **3** (9), 563-568 (2008).
- 113 H.R. Thomas, S.P. Day, W.E. Woodruff, C. Vallés, R.J. Young, I.A. Kinloch, G.W. Morley, J.V. Hanna, N.R. Wilson & J.P. Rourke. Deoxygenation of Graphene Oxide: Reduction or Cleaning? *Chemistry of Materials* **25** (18), 3580-3588 (2013).
- 114 R. Muñoz & C. Gómez-Aleixandre. Review of CVD Synthesis of Graphene. *Chemical Vapor Deposition* **19** (10-11-12), 297-322 (2013).
- 115 M. Losurdo, M.M. Giangregorio, P. Capezzuto & G. Bruno. Graphene CVD growth on copper and nickel: role of hydrogen in kinetics and structure. *Physical Chemistry Chemical Physics* **13** (46), 20836-20843 (2011).
- 116 J.H. Lee, E.K. Lee, W.J. Joo, Y. Jang, B.S. Kim, J.Y. Lim, S.H. Choi, S.J. Ahn, J.R. Ahn, M.H. Park, C.W. Yang, B.L. Choi, S.W. Hwang & D. Whang. Wafer-Scale Growth of Single-Crystal Monolayer Graphene on Reusable Hydrogen-Terminated Germanium. *Science* **344** (6181), 286-289 (2014).
- 117 J. Kang, D. Shin, S. Bae & B.H. Hong. Graphene transfer: key for applications. *Nanoscale* **4** (18), 5527-5537 (2012).
- 118 S. Bae, H. Kim, Y. Lee, X. Xu, J.S. Park, Y. Zheng, J. Balakrishnan, T. Lei, H.R. Kim, Y.I. Song, Y.J. Kim, K.S. Kim, B. Ozyilmaz, J.H. Ahn, B.H. Hong & S. Iijima. Roll-to-roll production of 30-inch graphene films for transparent electrodes. *Nature Nanotechnology* **5** (8), 574-578 (2010).
- 119 P. Ruffieux, J. Cai, N.C. Plumb, L. Patthey, D. Prezzi, A. Ferretti, E. Molinari, X. Feng, K. Müllen, C.A. Pignedoli & R. Fasel. Electronic Structure of Atomically Precise Graphene Nanoribbons. *ACS Nano* **6** (8), 6930-6935 (2012).
- 120 J.M. Cai, P. Ruffieux, R. Jaafar, M. Bieri, T. Braun, S. Blankenburg, M. Muoth, A.P. Seitsonen, M. Saleh, X.L. Feng, K. Mullen & R. Fasel. Atomically precise bottom-up fabrication of graphene nanoribbons. *Nature* **466** (7305), 470-473 (2010).
- 121 I. Forbeaux, J.M. Themlin & J.M. Debever. Heteroepitaxial graphite on 6H-SiC(0001): Interface formation through conduction-band electronic structure. *Physical Review B* **58** (24), 16396-16406 (1998).
- 122 C. Virojanadara, M. Syväjarvi, R. Yakimova, L.I. Johansson, A.A. Zakharov & T. Balasubramanian. Homogeneous large-area graphene layer growth on 6H-SiC(0001). *Physical Review B* **78** (24), 245403 (2008).

- 123 Y.M. Lin, C. Dimitrakopoulos, K.A. Jenkins, D.B. Farmer, H.Y. Chiu, A. Grill & P. Avouris. 100-GHz Transistors from Wafer-Scale Epitaxial Graphene. *Science* **327** (5966), 662-662 (2010).
- 124 A. Tzalenchuk, S. Lara-Avila, A. Kalaboukhov, S. Paolillo, M. Syvajarvi, R. Yakimova, O. Kazakova, T.J. Janssen, V. Fal'ko & S. Kubatkin. Towards a quantum resistance standard based on epitaxial graphene. *Nature Nanotechnology* **5** (3), 186-189 (2010).
- 125 W. Kohn & Luttinger.Jm. New Mechanism for Superconductivity. *Physical Review Letters* **15** (12), 524 (1965).
- 126 T.M. Rice & G.K. Scott. New Mechanism for a Charge-Density-Wave Instability. *Physical Review Letters* **35** (2), 120-123 (1975).
- 127 P. Wing-Tat & D. Colm. A review and outlook for an anomaly of scanning tunnelling microscopy (STM): superlattices on graphite. *Journal of Physics D: Applied Physics* **38** (21), R329 (2005).
- 128 P. Moon & M. Koshino. Optical absorption in twisted bilayer graphene. *Physical Review B* **87** (20), 205404 (2013).
- 129 A. Luican, G. Li, A. Reina, J. Kong, R.R. Nair, K.S. Novoselov, A.K. Geim & E.Y. Andrei. Single-layer behavior and its breakdown in twisted graphene layers. *Physical Review Letters* **106** (12), 126802 (2011).
- 130 A. Reina, X. Jia, J. Ho, D. Nezich, H. Son, V. Bulovic, M.S. Dresselhaus & J. Kong. Large Area, Few-Layer Graphene Films on Arbitrary Substrates by Chemical Vapor Deposition. *Nano Letters* **9** (1), 30-35 (2009).
- 131 C.R. Woods, L. Britnell, A. Eckmann, R.S. Ma, J.C. Lu, H.M. Guo, X. Lin, G.L. Yu, Y. Cao, R.V. Gorbachev, A.V. Kretinin, J. Park, L.A. Ponomarenko, M.I. Katsnelson, Y.N. Gornostyrev, K. Watanabe, T. Taniguchi, C. Casiraghi, H.J. Gao, A.K. Geim & K.S. Novoselov. Commensurate-incommensurate transition in graphene on hexagonal boron nitride. *Nature Physics* **10** (6), 451-456 (2014).
- 132 J.M. Lopes Dos Santos, N.M. Peres & A.H. Castro Neto. Graphene bilayer with a twist: electronic structure. *Physical Review Letters* **99** (25), 256802 (2007).
- 133 A.O. Sboychakov, A.L. Rakhmanov, A.V. Rozhkov & F. Nori. Electronic spectrum of twisted bilayer graphene. *Physical Review B* **92** (7), 075402 (2015).
- 134 P. Moon & M. Koshino. Energy spectrum and quantum Hall effect in twisted bilayer graphene. *Physical Review B* **85** (19), 195458 (2012).
- 135 R.W. Havener, Y. Liang, L. Brown, L. Yang & J. Park. Van Hove Singularities and Excitonic Effects in the Optical Conductivity of Twisted Bilayer Graphene. *Nano Letters* **14** (6), 3353-3357 (2014).
- 136 T. Ohta, J.T. Robinson, P.J. Feibelman, A. Bostwick, E. Rotenberg & T.E. Beechem. Evidence for Interlayer Coupling and Moiré Periodic Potentials in Twisted Bilayer Graphene. *Physical Review Letters* **109** (18), 186807 (2012).
- 137 E. Suárez Morell, J.D. Correa, P. Vargas, M. Pacheco & Z. Barticevic. Flat bands in slightly twisted bilayer graphene: Tight-binding calculations. *Physical Review B* **82** (12), 121407 (2010).
- 138 R. Bistritzer & A.H. Macdonald. Moiré bands in twisted double-layer graphene. *Proceedings of the National Academy of Sciences* **108** (30), 12233-12237 (2011).
- 139 Y. Wang, Z. Ni, L. Liu, Y. Liu, C. Cong, T. Yu, X. Wang, D. Shen & Z. Shen. Stacking-Dependent Optical Conductivity of Bilayer Graphene. *Acs Nano* **4** (7), 4074-4080 (2010).

- 140 M.S. Dresselhaus, G. Dresselhaus & A. Jorio. *Group theory: application to the physics of condensed matter*. 1st edn, 97-110 (Springer Science & Business Media, 2007).
- 141 J. Campos-Delgado, G. Algara-Siller, C.N. Santos, U. Kaiser & J.P. Raskin. Twisted Bi-Layer Graphene: Microscopic Rainbows. *Small* **9** (19), 3247-3251 (2013).
- 142 K. Kim, S. Coh, L.Z. Tan, W. Regan, J.M. Yuk, E. Chatterjee, M.F. Crommie, M.L. Cohen, S.G. Louie & A. Zettl. Raman spectroscopy study of rotated double-layer graphene: misorientation-angle dependence of electronic structure. *Physical Review Letters* **108** (24), 246103 (2012).
- 143 Z. Ni, L. Liu, Y. Wang, Z. Zheng, L.J. Li, T. Yu & Z. Shen. G-band Raman double resonance in twisted bilayer graphene: Evidence of band splitting and folding. *Physical Review B* **80** (12), 125404 (2009).
- 144 V. Carozo, C.M. Almeida, B. Fragneaud, P.M. Bed e, M.V.O. Moutinho, J. Ribeiro-Soares, N.F. Andrade, A.G. Souza Filho, M.J.S. Matos, B. Wang, M. Terrones, R.B. Capaz, A. Jorio, C.A. Achete & L.G. Can ado. Resonance effects on the Raman spectra of graphene superlattices. *Physical Review B* **88** (8), 085401 (2013).
- 145 K. Sato, R. Saito, C. Cong, T. Yu & M.S. Dresselhaus. Zone folding effect in Raman G-band intensity of twisted bilayer graphene. *Physical Review B* **86** (12), 125414 (2012).
- 146 A. Jorio & L.G. Cancado. Raman spectroscopy of twisted bilayer graphene. *Solid State Communications* **175** 3-12 (2013).
- 147 V. Carozo, C.M. Almeida, E.H.M. Ferreira, L.G. Can ado, C.A. Achete & A. Jorio. Raman Signature of Graphene Superlattices. *Nano Letters* **11** (11), 4527-4534 (2011).
- 148 A. Righi, S.D. Costa, H. Chacham, C. Fantini, P. Venezuela, C. Magnuson, L. Colombo, W.S. Bacsa, R.S. Ruoff & M.A. Pimenta. Graphene Moir e patterns observed by umklapp double-resonance Raman scattering. *Physical Review B* **84** (24), 241409 (2011).
- 149 D.B. Miller. Device Requirements for Optical Interconnects to Silicon Chips. *Proceedings of the IEEE* **97** (7), 1166-1185 (2009).
- 150 S. Assefa, F. Xia, W.M.J. Green, C.L. Schow, A.V. Rlyakov & Y.A. Vlasov. CMOS-Integrated Optical Receivers for On-Chip Interconnects. *IEEE Journal of Selected Topics in Quantum Electronics* **16** (5), 1376-1385 (2010).
- 151 W. Bogaerts, R. Baets, P. Dumon, V. Wiaux, S. Beckx, D. Taillaert, B. Luyssaert, J.V. Campenhout, P. Bienstman & D.V. Thourhout. Nanophotonic waveguides in silicon-on-insulator fabricated with CMOS technology. *Journal of Lightwave Technology* **23** (1), 401-412 (2005).
- 152 G.T. Reed, G. Mashanovich, F.Y. Gardes & D.J. Thomson. Silicon optical modulators. *Nature Photonics* **4** (8), 518-526 (2010).
- 153 G. Li, X. Zheng, J. Yao, H. Thacker, I. Shubin, Y. Luo, K. Raj, J.E. Cunningham & A.V. Krishnamoorthy. 25Gb/s 1V-driving CMOS ring modulator with integrated thermal tuning. *Optics Express* **19** (21), 20435-20443 (2011).
- 154 Y. Tang, H.W. Chen, S. Jain, J.D. Peters, U. Westergren & J.E. Bowers. 50 Gb/s hybrid silicon traveling-wave electroabsorption modulator. *Optics Express* **19** (7), 5811-5816 (2011).
- 155 J.M. Liu. *Photonic Devices*. 1st edn, 164-189 (Cambridge University Press, 2005).
- 156 O. Schwelb. Transmission, group delay, and dispersion in single-ring optical resonators and add/drop filters-a tutorial overview. *Journal of Lightwave Technology* **22** (5), 1380-1394 (2004).

- 157 W. Bogaerts, P. De Heyn, T. Van Vaerenbergh, K. De Vos, S. Kumar Selvaraja, T. Claes, P. Dumon, P. Bienstman, D. Van Thourhout & R. Baets. Silicon microring resonators. *Laser & Photonics Reviews* **6** (1), 47-73 (2012).
- 158 M.A. Popovic, H.A. Haus & M.R. Watts. General approach to hitless switching and FSR extension resonators in integrated photonic circuits in *Optical Fiber Communication Conference, 2006 and the 2006 National Fiber Optic Engineers Conference. OFC 2006*. doi: 10.1109/OFC.2006.215550 (IEEE, 2006).
- 159 F.N. Xia, L. Sekaric & Y. Vlasov. Ultracompact optical buffers on a silicon chip. *Nature Photonics* **1** (1), 65-71 (2007).
- 160 K.D. Vos, I. Bartolozzi, E. Schacht, P. Bienstman & R. Baets. Silicon-on-Insulator microring resonator for sensitive and label-free biosensing. *Optics Express* **15** (12), 7610-7615 (2007).
- 161 V.M. Menon, W. Tong & S.R. Forrest. Control of quality factor and critical coupling in microring resonators through integration of a semiconductor optical amplifier. *IEEE Photonics Technology Letters* **16** (5), 1343-1345 (2004).
- 162 A. Yariv. Critical coupling and its control in optical waveguide-ring resonator systems. *IEEE Photonics Technology Letters* **14** (4), 483-485 (2002).
- 163 D.G. Rabus & M. Hamacher. MMI-coupled ring resonators in GaInAsP-InP. *IEEE Photonics Technology Letters* **13** (8), 812-814 (2001).
- 164 M.K. Park, J.S. Kee, J.Y. Quah, V. Netto, J. Song, Q. Fang, E.M. La Fosse & G.Q. Lo. Label-free aptamer sensor based on silicon microring resonators. *Sensors and Actuators B: Chemical* **176** 552-559 (2013).
- 165 M. Iqbal, M.A. Gleeson, B. Spaugh, F. Tybor, W.G. Gunn, M. Hochberg, T. Baehr-Jones, R.C. Bailey & L.C. Gunn. Label-Free Biosensor Arrays Based on Silicon Ring Resonators and High-Speed Optical Scanning Instrumentation. *IEEE Journal of Selected Topics in Quantum Electronics* **16** (3), 654-661 (2010).
- 166 C. Ciminelli, F. Dell'olio, D. Conteduca, C.M. Campanella & M.N. Armenise. High performance SOI microring resonator for biochemical sensing. *Optics & Laser Technology* **59** 60-67 (2014).
- 167 J.E. Moses & A.D. Moorhouse. The growing applications of click chemistry. *Chemical Society Reviews* **36** (8), 1249-1262 (2007).
- 168 H.Y. Chen, M. Hirtz, X. Deng, T. Laue, H. Fuchs & J. Lahann. Substrate-Independent Dip-Pen Nanolithography Based on Reactive Coatings. *Journal of the American Chemical Society* **132** (51), 18023-18025 (2010).
- 169 X. Zhao, J.M. Tsai, H. Cai, X.M. Ji, J. Zhou, M.H. Bao, Y.P. Huang, D.L. Kwong & A.Q. Liu. A nano-opto-mechanical pressure sensor via ring resonator. *Optics Express* **20** (8), 8535-8542 (2012).
- 170 K.I. Bolotin, K.J. Sikes, Z. Jiang, M. Klima, G. Fudenberg, J. Hone, P. Kim & H.L. Stormer. Ultrahigh electron mobility in suspended graphene. *Solid State Communications* **146** (9-10), 351-355 (2008).
- 171 G. Xing, H. Guo, X. Zhang, T.C. Sum & C.H.A. Huan. The Physics of ultrafast saturable absorption in graphene. *Optics Express* **18** (5), 4564-4573 (2010).
- 172 F. Bonaccorso, Z. Sun, T. Hasan & A.C. Ferrari. Graphene photonics and optoelectronics. *Nature Photonics* **4** (9), 611-622 (2010).
- 173 K. Kim, J.Y. Choi, T. Kim, S.H. Cho & H.J. Chung. A role for graphene in silicon-based semiconductor devices. *Nature* **479** (7373), 338-344 (2011).

- 174 T. Mueller, F.N.A. Xia & P. Avouris. Graphene photodetectors for high-speed optical communications. *Nature Photonics* **4** (5), 297-301 (2010).
- 175 M. Liu, X. Yin, E. Ulin-Avila, B. Geng, T. Zentgraf, L. Ju, F. Wang & X. Zhang. A graphene-based broadband optical modulator. *Nature* **474** (7349), 64-67 (2011).
- 176 H. Li, Y. Anugrah, S.J. Koester & M. Li. Optical absorption in graphene integrated on silicon waveguides. *Applied Physics Letters* **101** (11), 111110 (2012).
- 177 Q.L. Bao, H. Zhang, B. Wang, Z.H. Ni, C.H.Y.X. Lim, Y. Wang, D.Y. Tang & K.P. Loh. Broadband graphene polarizer. *Nature Photonics* **5** (7), 411-415 (2011).
- 178 Q. Bao, H. Zhang, Y. Wang, Z. Ni, Y. Yan, Z.X. Shen, K.P. Loh & D.Y. Tang. Atomic-Layer Graphene as a Saturable Absorber for Ultrafast Pulsed Lasers. *Advanced Functional Materials* **19** (19), 3077-3083 (2009).
- 179 K. Rai, T. Shinichi, T. Tai, W. Kaori, S. Satoru, H. Hiroki, N. Hirochika & Y. Koji. Characterization of Optical Absorption and Polarization Dependence of Single-Layer Graphene Integrated on a Silicon Wire Waveguide. *Japanese Journal of Applied Physics* **52** (6R), 060203 (2013).
- 180 I.F. Crowe, N. Clark, S. Hussein, B. Towlson, E. Whittaker, M.M. Milosevic, F.Y. Gardes, G.Z. Mashanovich, M.P. Halsall & A. Vijayaraghavan. Determination of the quasi-TE mode (in-plane) graphene linear absorption coefficient via integration with silicon-on-insulator racetrack cavity resonators. *Optics Express* **22** (15), 18625-18632 (2014).
- 181 P. Goodhew. General Introduction to Transmission Electron Microscopy (TEM) in R. Brydson. *Aberration-Corrected Analytical Transmission Electron Microscopy*, 1-17 (Wiley, 2011).
- 182 R. Egerton. *Physical Principles of Electron Microscopy: An Introduction to TEM, SEM, and AEM*. 2nd edn, 155-175 (Springer US, 2011).
- 183 P.M. Budd & P.J. Goodhew. *Light-element analysis in the transmission electron microscope, WEDX and EELS*. 3rd edn, 20-41 (Oxford University Press, 2000).
- 184 R. Brydson & N. Hondow. Electron Energy Loss Spectrometry and Energy Dispersive X-ray Analysis in R. Brydson. *Aberration-Corrected Analytical Transmission Electron Microscopy*, 163-210 (Wiley, 2011).
- 185 M. Kociak & O. Stephan. Mapping plasmons at the nanometer scale in an electron microscope. *Chemical Society Reviews* **43** (11), 3865-3883 (2014).
- 186 J. Verbeeck & S. Van Aert. Model based quantification of EELS spectra. *Ultramicroscopy* **101** (2-4), 207-224 (2004).
- 187 G. Bertoni & J. Verbeeck. Accuracy and precision in model based EELS quantification. *Ultramicroscopy* **108** (8), 782-790 (2008).
- 188 R.A. Schultz, M.C. Jensen & R.C. Bradt. Single-Crystal Cleavage of Brittle Materials. *International Journal of Fracture* **65** (4), 291-312 (1994).
- 189 L. Xuekun, Y. Minfeng, H. Hui & S.R. Rodney. Tailoring graphite with the goal of achieving single sheets. *Nanotechnology* **10** (3), 269 (1999).
- 190 P. Blake, E.W. Hill, A.H. Castro Neto, K.S. Novoselov, D. Jiang, R. Yang, T.J. Booth & A.K. Geim. Making graphene visible. *Applied Physics Letters* **91** (6), 063124 (2007).
- 191 F. Bonaccorso, A. Lombardo, T. Hasan, Z. Sun, L. Colombo & A.C. Ferrari. Production and processing of graphene and 2d crystals. *Materials Today* **15** (12), 564-589 (2012).

- 192 D. Belforti, B. Bovarnick & S. Blum. Highly Oriented Boron Nitride. *Nature* **190** (477), 901 (1961).
- 193 L.A. Ponomarenko, R. Yang, T.M. Mohiuddin, M.I. Katsnelson, K.S. Novoselov, S.V. Morozov, A.A. Zhukov, F. Schedin, E.W. Hill & A.K. Geim. Effect of a High- κ Environment on Charge Carrier Mobility in Graphene. *Physical Review Letters* **102** (20), 206603 (2009).
- 194 T. Taniguchi & K. Watanabe. Synthesis of high-purity boron nitride single crystals under high pressure by using Ba–BN solvent. *Journal of Crystal Growth* **303** (2), 525-529 (2007).
- 195 R.V. Gorbachev, I. Riaz, R.R. Nair, R. Jalil, L. Britnell, B.D. Belle, E.W. Hill, K.S. Novoselov, K. Watanabe, T. Taniguchi, A.K. Geim & P. Blake. Hunting for monolayer boron nitride: optical and Raman signatures. *Small* **7** (4), 465-468 (2011).
- 196 P. Nemes-Incze, Z. Osvath, K. Kamaras & L.P. Biro. Anomalies in thickness measurements of graphene and few layer graphite crystals by tapping mode atomic force microscopy. *Carbon* **46** (11), 1435-1442 (2008).
- 197 A.C. Ferrari & D.M. Basko. Raman spectroscopy as a versatile tool for studying the properties of graphene. *Nature Nanotechnology* **8** (4), 235-246 (2013).
- 198 A. Reina, H. Son, L. Jiao, B. Fan, M.S. Dresselhaus, Z. Liu & J. Kong. Transferring and Identification of Single- and Few-Layer Graphene on Arbitrary Substrates. *The Journal of Physical Chemistry C* **112** (46), 17741-17744 (2008).
- 199 X. Wang & Y. Shi. Fabrication Techniques of Graphene Nanostructures in G. Zhang & N. Manjooran. *Nanofabrication and its Application in Renewable Energy*, 1-30 (The Royal Society of Chemistry, 2014).
- 200 X. Li, W. Cai, J. An, S. Kim, J. Nah, D. Yang, R. Piner, A. Velamakanni, I. Jung, E. Tutuc, S.K. Banerjee, L. Colombo & R.S. Ruoff. Large-Area Synthesis of High-Quality and Uniform Graphene Films on Copper Foils. *Science* **324** (5932), 1312-1314 (2009).
- 201 X. Li, Y. Zhu, W. Cai, M. Borysiak, B. Han, D. Chen, R.D. Piner, L. Colombo & R.S. Ruoff. Transfer of Large-Area Graphene Films for High-Performance Transparent Conductive Electrodes. *Nano Letters* **9** (12), 4359-4363 (2009).
- 202 K.S. Kim, Y. Zhao, H. Jang, S.Y. Lee, J.M. Kim, K.S. Kim, J.H. Ahn, P. Kim, J.Y. Choi & B.H. Hong. Large-scale pattern growth of graphene films for stretchable transparent electrodes. *Nature* **457** (7230), 706-710 (2009).
- 203 J. Song, F.Y. Kam, R.Q. Png, W.L. Seah, J.M. Zhuo, G.K. Lim, P.K.H. Ho & L.L. Chua. A general method for transferring graphene onto soft surfaces. *Nature Nanotechnology* **8** (5), 356-362 (2013).
- 204 H. Li, J. Wu, X. Huang, Z. Yin, J. Liu & H. Zhang. A Universal, Rapid Method for Clean Transfer of Nanostructures onto Various Substrates. *ACS Nano* **8** (7), 6563-6570 (2014).
- 205 H.H. Kim, Y. Chung, E. Lee, S.K. Lee & K. Cho. Water-Free Transfer Method for CVD-Grown Graphene and Its Application to Flexible Air-Stable Graphene Transistors. *Advanced Materials* **26** (20), 3213-3217 (2014).
- 206 B. Aleman, W. Regan, S. Aloni, V. Altoe, N. Alem, C. Girit, B. Geng, L. Maserati, M. Crommie, F. Wang & A. Zettl. Transfer-free batch fabrication of large-area suspended graphene membranes. *ACS Nano* **4** (8), 4762-4768 (2010).
- 207 G. Deokar, J. Avila, I. Razado-Colambo, J.L. Codron, C. Boyaval, E. Galopin, M.C. Asensio & D. Vignaud. Towards high quality CVD graphene growth and transfer. *Carbon* **89** 82-92 (2015).

- 208 J. Kang, S. Hwang, J.H. Kim, M.H. Kim, J. Ryu, S.J. Seo, B.H. Hong, M.K. Kim & J.B. Choi. Efficient Transfer of Large-Area Graphene Films onto Rigid Substrates by Hot Pressing. *Acs Nano* **6** (6), 5360-5365 (2012).
- 209 Y. Wang, Y. Zheng, X. Xu, E. Dubuisson, Q. Bao, J. Lu & K.P. Loh. Electrochemical Delamination of CVD-Grown Graphene Film: Toward the Recyclable Use of Copper Catalyst. *Acs Nano* **5** (12), 9927-9933 (2011).
- 210 L. Gao, W. Ren, H. Xu, L. Jin, Z. Wang, T. Ma, L.P. Ma, Z. Zhang, Q. Fu, L.M. Peng, X. Bao & H.M. Cheng. Repeated growth and bubbling transfer of graphene with millimetre-size single-crystal grains using platinum. *Nature Communications* **3** 699 (2012).
- 211 L.A. Ponomarenko, A.K. Geim, A.A. Zhukov, R. Jalil, S.V. Morozov, K.S. Novoselov, I.V. Grigorieva, E.H. Hill, V.V. Cheianov, V.I. Fal'ko, K. Watanabe, T. Taniguchi & R.V. Gorbachev. Tunable metal-insulator transition in double-layer graphene heterostructures. *Nature Physics* **7** (12), 958-961 (2011).
- 212 A.S. Mayorov, R.V. Gorbachev, S.V. Morozov, L. Britnell, R. Jalil, L.A. Ponomarenko, P. Blake, K.S. Novoselov, K. Watanabe, T. Taniguchi & A.K. Geim. Micrometer-Scale Ballistic Transport in Encapsulated Graphene at Room Temperature. *Nano Letters* **11** (6), 2396-2399 (2011).
- 213 L. Wang, I. Meric, P.Y. Huang, Q. Gao, Y. Gao, H. Tran, T. Taniguchi, K. Watanabe, L.M. Campos, D.A. Muller, J. Guo, P. Kim, J. Hone, K.L. Shepard & C.R. Dean. One-Dimensional Electrical Contact to a Two-Dimensional Material. *Science* **342** (6158), 614-617 (2013).
- 214 F. Withers, O. Del Pozo-Zamudio, A. Mishchenko, A.P. Rooney, A. Gholinia, K. Watanabe, T. Taniguchi, S.J. Haigh, A.K. Geim, A.I. Tartakovskii & K.S. Novoselov. Light-emitting diodes by band-structure engineering in van der Waals heterostructures. *Nature Materials* **14** (3), 301-306 (2015).
- 215 S.J. Haigh, A. Gholinia, R. Jalil, S. Romani, L. Britnell, D.C. Elias, K.S. Novoselov, L.A. Ponomarenko, A.K. Geim & R. Gorbachev. Cross-sectional imaging of individual layers and buried interfaces of graphene-based heterostructures and superlattices (Supplementary Information). *Nature Materials* **11** (9), 764-767 (2012).
- 216 S.J. Haigh, A. Gholinia, R. Jalil, S. Romani, L. Britnell, D.C. Elias, K.S. Novoselov, L.A. Ponomarenko, A.K. Geim & R. Gorbachev. Cross-sectional imaging of individual layers and buried interfaces of graphene-based heterostructures and superlattices. *Nature Materials* **11** (9), 764-767 (2012).
- 217 R. Bistritzer & A.H. Macdonald. Moiré butterflies in twisted bilayer graphene. *Physical Review B* **84** (3), 035440 (2011).
- 218 J.R. Wallbank, A.A. Patel, M. Mucha-Kruczynski, A.K. Geim & V.I. Fal'ko. Generic miniband structure of graphene on a hexagonal substrate. *Physical Review B* **87** (24), 245408 (2013).
- 219 C.H. Park, L. Yang, Y.W. Son, M.L. Cohen & S.G. Louie. Anisotropic behaviours of massless Dirac fermions in graphene under periodic potentials. *Nature Physics* **4** (3), 213-217 (2008).
- 220 C.R. Dean, L. Wang, P. Maher, C. Forsythe, F. Ghahari, Y. Gao, J. Katoch, M. Ishigami, P. Moon, M. Koshino, T. Taniguchi, K. Watanabe, K.L. Shepard, J. Hone & P. Kim. Hofstadter's butterfly and the fractal quantum Hall effect in Moiré superlattices. *Nature* **497** (7451), 598-602 (2013).
- 221 L.A. Ponomarenko, R.V. Gorbachev, G.L. Yu, D.C. Elias, R. Jalil, A.A. Patel, A. Mishchenko, A.S. Mayorov, C.R. Woods, J.R. Wallbank, M. Mucha-Kruczynski, B.A. Piot, M. Potemski, I.V. Grigorieva, K.S. Novoselov, F. Guinea, V.I. Fal'ko & A.K. Geim. Cloning of Dirac fermions in graphene superlattices. *Nature* **497** (7451), 594-597 (2013).
- 222 Mishchenko, J.S. Tu, Caoy, R.V. Gorbachev, J.R. Wallbank, M.T. Greenaway, V.E. Morozov, S.V. Morozov, M.J. Zhu, S.L. Wong, Withers, C.R. Woods, Y.J. Kim, Watanabe,

- Taniguchi, E.E. Vdovin, Makarovskyo, T.M. Fromhold, V.I. Fal'ko, A.K. Geim, Eavesl & K.S. Novoselov. Twist-controlled resonant tunnelling in graphene/boron nitride/graphene heterostructures. *Nature Nanotechnology* **9** (10), 808-813 (2014).
- 223 C.C. Lu, Y.C. Lin, Z. Liu, C.H. Yeh, K. Suenaga & P.-W. Chiu. Twisting Bilayer Graphene Superlattices. *Acs Nano* **7** (3), 2587-2594 (2013).
- 224 J.T. Robinson, S.W. Schmucker, C.B. Diaconescu, J.P. Long, J.C. Culbertson, T. Ohta, A.L. Friedman & T.E. Beechem. Electronic Hybridization of Large-Area Stacked Graphene Films. *Acs Nano* **7** (1), 637-644 (2013).
- 225 L.A. Ponomarenko, A.K. Geim, A.A. Zhukov, R. Jalil, S.V. Morozov, K.S. Novoselov, I.V. Grigorieva, E.H. Hill, V.V. Cheianov, V.I. Fal'ko, K. Watanabe, T. Taniguchi & R.V. Gorbachev. Tunable metal-insulator transition in double-layer graphene heterostructures (Supplementary Information). *Nature Physics* **7** (12), 958-961 (2011).
- 226 K. Kim, V.I. Artyukhov, W. Regan, Y. Liu, M.F. Crommie, B.I. Yakobson & A. Zettl. Ripping Graphene: Preferred Directions. *Nano Letters* **12** (1), 293-297 (2012).
- 227 D. Sen, K.S. Novoselov, P.M. Reis & M.J. Buehler. Tearing Graphene Sheets From Adhesive Substrates Produces Tapered Nanoribbons. *Small* **6** (10), 1108-1116 (2010).
- 228 S. Neubeck, Y.M. You, Z.H. Ni, P. Blake, Z.X. Shen, A.K. Geim & K.S. Novoselov. Direct determination of the crystallographic orientation of graphene edges by atomic resolution imaging. *Applied Physics Letters* **97** (5), 053110 (2010).
- 229 C. Casiraghi, A. Hartschuh, H. Qian, S. Piscanec, C. Georgi, A. Fasoli, K.S. Novoselov, D.M. Basko & A.C. Ferrari. Raman Spectroscopy of Graphene Edges. *Nano Letters* **9** (4), 1433-1441 (2009).
- 230 M. Ishigami, J.H. Chen, W.G. Cullen, M.S. Fuhrer & E.D. Williams. Atomic Structure of Graphene on SiO₂. *Nano Letters* **7** (6), 1643-1648 (2007).
- 231 J. Yan & M.S. Fuhrer. Correlated charged impurity scattering in graphene. *Physical Review Letters* **107** (20), 206601 (2011).
- 232 E. Stolyarova, K.T. Rim, S. Ryu, J. Maultzsch, P. Kim, L.E. Brus, T.F. Heinz, M.S. Hybertsen & G.W. Flynn. High-resolution scanning tunneling microscopy imaging of mesoscopic graphene sheets on an insulating surface. *Proceedings of the National Academy of Sciences* **104** (22), 9209-9212 (2007).
- 233 R. Zan, C. Muryn, U. Bangert, P. Mattocks, P. Wincott, D. Vaughan, X. Li, L. Colombo, R.S. Ruoff, B. Hamilton & K.S. Novoselov. Scanning tunnelling microscopy of suspended graphene. *Nanoscale* **4** (10), 3065-3068 (2012).
- 234 J. Moser, A. Barreiro & A. Bachtold. Current-induced cleaning of graphene. *Applied Physics Letters* **91** (16), 163513 (2007).
- 235 A.M. Goossens, V.E. Calado, A. Barreiro, K. Watanabe, T. Taniguchi & L.M.K. Vandersypen. Mechanical cleaning of graphene. *Applied Physics Letters* **100** (7), 073110 (2012).
- 236 Z. Cheng, Q. Zhou, C. Wang, Q. Li, C. Wang & Y. Fang. Toward Intrinsic Graphene Surfaces: A Systematic Study on Thermal Annealing and Wet-Chemical Treatment of SiO₂-Supported Graphene Devices. *Nano Letters* **11** (2), 767-771 (2011).
- 237 M. Her, R. Beams & L. Novotny. Graphene transfer with reduced residue. *Physics Letters A* **377** (21-22), 1455-1458 (2013).
- 238 G. Algara-Siller, O. Lehtinen, A. Turchanin & U. Kaiser. Dry-cleaning of graphene. *Applied Physics Letters* **104** (15), 153115 (2014).

- 239 J.N. Longchamp, C. Escher & H.W. Fink. Ultraclean freestanding graphene by platinum-metal catalysis. *Journal of Vacuum Science & Technology B* **31** (2), 020605 (2013).
- 240 D.J. Tsao & J.Y. Ehrlich. Sources, Optics, and Laser Microfabrication Systems for Direct Writing and Projection Lithography in Y. S. Liu. *Laser Microfabrication*, 3-84 (Academic Press, 1989).
- 241 H. Ulrich, R.W. Wijnaendts-Van-Resandt, C. Rensch & W. Ehrensperger. Direct writing laser lithography for production of microstructures. *Microelectronic Engineering* **6** (1-4), 77-84 (1987).
- 242 K.R. Williams & R.S. Muller. Etch rates for micromachining processing. *Journal of Microelectromechanical Systems* **5** (4), 256-269 (1996).
- 243 K.R. Williams, K. Gupta & M. Wasilik. Etch rates for micromachining processing-Part II. *Journal of Microelectromechanical Systems* **12** (6), 761-778 (2003).
- 244 A. Oikonomou, N. Clark, S. Heeg, A. Kretinin, S. Varey, G. Yu & A. Vijayaraghavan. Scalable bottom-up assembly of suspended carbon nanotube and graphene devices by dielectrophoresis. *physica status solidi (RRL) – Rapid Research Letters* **9** (9), 539-543 (2015).
- 245 I. Barycka & I. Zobel. Silicon anisotropic etching in KOH-isopropanol etchant. *Sensors and Actuators A: Physical* **48** (3), 229-238 (1995).
- 246 H. Seidel, L. Csepregi, A. Heuberger & H. Baumgartel. Anisotropic Etching of Crystalline Silicon in Alkaline-Solutions .1. Orientation Dependence and Behavior of Passivation Layers. *Journal of the Electrochemical Society* **137** (11), 3612-3626 (1990).
- 247 O. Tabata, R. Asahi, H. Funabashi, K. Shimaoka & S. Sugiyama. Anisotropic etching of silicon in TMAH solutions. *Sensors and Actuators A: Physical* **34** (1), 51-57 (1992).
- 248 M. Shikida, K. Sato, K. Tokoro & D. Uchikawa. Differences in anisotropic etching properties of KOH and TMAH solutions. *Sensors and Actuators A: Physical* **80** (2), 179-188 (2000).
- 249 J. Yeom, Y. Wu, J.C. Selby & M.A. Shannon. Maximum achievable aspect ratio in deep reactive ion etching of silicon due to aspect ratio dependent transport and the microloading effect. *Journal of Vacuum Science & Technology B* **23** (6), 2319-2329 (2005).
- 250 A.L. Weisenhorn, P. Maivald, H.J. Butt & P.K. Hansma. Measuring adhesion, attraction, and repulsion between surfaces in liquids with an atomic-force microscope. *Physical Review B* **45** (19), 11226-11232 (1992).
- 251 M. Radmacher, R. Tillmann, M. Fritz & H. Gaub. From molecules to cells: imaging soft samples with the atomic force microscope. *Science* **257** (5078), 1900-1905 (1992).
- 252 M.R. Van Landingham. Review of instrumented indentation. *Journal of Research of the National Institute of Standards and Technology* **108** (4), 249-265 (2003).
- 253 S. Sundararajan & B. Bhushan. Development of AFM-based techniques to measure mechanical properties of nanoscale structures. *Sensors and Actuators A: Physical* **101** (3), 338-351 (2002).
- 254 D. Tranchida, S. Piccarolo & M. Soliman. Nanoscale mechanical characterization of polymers by AFM nanoindentations: Critical approach to the elastic characterization. *Macromolecules* **39** (13), 4547-4556 (2006).
- 255 S. Chowdhury & M.T. Laugier. The use of non-contact AFM with nanoindentation techniques for measuring mechanical properties of carbon nitride thin films. *Applied Surface Science* **233** (1-4), 219-226 (2004).

- 256 D.C. Lin, E.K. Dimitriadis & F. Horkay. Robust Strategies for Automated AFM Force Curve Analysis: I. Non-adhesive Indentation of Soft, Inhomogeneous Materials. *Journal of Biomechanical Engineering* **129** (3), 430-440 (2006).
- 257 T.G. Christopher, S.W. Gregory & M. Sverre. Determination of the spring constants of probes for force microscopy/spectroscopy. *Nanotechnology* **7** (3), 259 (1996).
- 258 J.E. Sader, J.W.M. Chon & P. Mulvaney. Calibration of rectangular atomic force microscope cantilevers. *Review of Scientific Instruments* **70** 3967 (1999).
- 259 J.W.M. Chon, P. Mulvaney & J.E. Sader. Experimental validation of theoretical models for the frequency response of atomic force microscope cantilever beams immersed in fluids. *Journal of Applied Physics* **87** (8), 3978-3988 (2000).
- 260 J.E. Sader. Frequency response of cantilever beams immersed in viscous fluids with applications to the atomic force microscope. *Journal of Applied Physics* **84** (1), 64-76 (1998).
- 261 J.E. Sader, I. Larson, P. Mulvaney & L.R. White. Method for the calibration of atomic force microscope cantilevers. *Review of Scientific Instruments* **66** (7), 3789-3798 (1995).
- 262 R. Levy & M. Maaloum. Measuring the spring constant of atomic force microscope cantilevers: thermal fluctuations and other methods. *Nanotechnology* **13** (1), 33-37 (2002).
- 263 H.J. Butt & M. Jaschke. Calculation of Thermal Noise in Atomic-Force Microscopy. *Nanotechnology* **6** (1), 1-7 (1995).
- 264 Y. Martin, C.C. Williams & H.K. Wickramasinghe. Atomic force microscope-force mapping and profiling on a sub 100-Å scale. *Journal of Applied Physics* **61** (10), 4723-4729 (1987).
- 265 M.E. Dokukin & I. Sokolov. Quantitative Mapping of the Elastic Modulus of Soft Materials with HarmoniX and Peak Force QNM AFM Modes. *Langmuir* **28** (46), 16060-16071 (2012).
- 266 T.J. Young, M.A. Monclus, T.L. Burnett, W.R. Broughton, S.L. Ogin & P.A. Smith. The use of the PeakForce (TM) quantitative nanomechanical mapping AFM-based method for high-resolution Young's modulus measurement of polymers. *Measurement Science & Technology* **22** (12), 125703 (2011).
- 267 J. Shi, Y. Hu, S. Hu, J. Ma & C. Su. Patent: Method and Apparatus of Using Peak Force Tapping Mode to Measure Physical Properties of a Sample. US 20120131702 A1 (2012).
- 268 L. Tapaszto, G. Dobrik, P. Lambin & L.P. Biro. Tailoring the atomic structure of graphene nanoribbons by scanning tunnelling microscope lithography. *Nature Nanotechnology* **3** (7), 397-401 (2008).
- 269 I.S. Byun, D. Yoon, J.S. Choi, I. Hwang, D.H. Lee, M.J. Lee, T. Kawai, Y.W. Son, Q. Jia, H. Cheong & B.H. Park. Nanoscale Lithography on Monolayer Graphene Using Hydrogenation and Oxidation. *Acs Nano* **5** (8), 6417-6424 (2011).
- 270 K.S. Novoselov, Z. Jiang, Y. Zhang, S.V. Morozov, H.L. Stormer, U. Zeitler, J.C. Maan, G.S. Boebinger, P. Kim & A.K. Geim. Room-Temperature Quantum Hall Effect in Graphene. *Science* **315** (5817), 1379-1379 (2007).
- 271 M.Y. Han, J.C. Brant & P. Kim. Electron Transport in Disordered Graphene Nanoribbons. *Physical Review Letters* **104** (5), 056801 (2010).
- 272 L.A. Ponomarenko, F. Schedin, M.I. Katsnelson, R. Yang, E.W. Hill, K.S. Novoselov & A.K. Geim. Chaotic Dirac Billiard in Graphene Quantum Dots. *Science* **320** (5874), 356-358 (2008).

- 273 Y. Cao, S. Dong, S. Liu, Z. Liu & X. Guo. Toward functional molecular devices based on graphene-molecule junctions. *Angewandte Chemie International Edition English* **52** (14), 3906-3910 (2013).
- 274 C.W. Marquardt, S. Grunder, A. Blaszczyk, S. Dehm, F. Hennrich, H. Von Lohneysen, M. Mayor & R. Krupke. Electroluminescence from a single nanotube-molecule-nanotube junction. *Nature Nanotechnology* **5** (12), 863-867 (2010).
- 275 B. Cord, J. Yang, H.G. Duan, D.C. Joy, J. Klingfus & K.K. Berggren. Limiting factors in sub-10 nm scanning-electron-beam lithography. *Journal of Vacuum Science & Technology B* **27** (6), 2616-2621 (2009).
- 276 A.L. Koh, D.W. McComb, S.A. Maier, H.Y. Low & J.K.W. Yang. Sub-10 nm patterning of gold nanostructures on silicon-nitride membranes for plasmon mapping with electron energy-loss spectroscopy. *Journal of Vacuum Science & Technology B* **28** (6), C6O45-C46O49 (2010).
- 277 W. Chen & H. Ahmed. Fabrication of 5–7 nm wide etched lines in silicon using 100 keV electron-beam lithography and polymethylmethacrylate resist. *Applied Physics Letters* **62** (13), 1499-1501 (1993).
- 278 C. Vieu, F. Carcenac, A. Pépin, Y. Chen, M. Mejias, A. Lebib, L. Manin-Ferlazzo, L. Couraud & H. Launois. Electron beam lithography: resolution limits and applications. *Applied Surface Science* **164** (1–4), 111-117 (2000).
- 279 W.C. Hu, K. Sarveswaran, M. Lieberman & G.H. Bernstein. Sub-10 nm electron beam lithography using cold development of poly(methylmethacrylate). *Journal of Vacuum Science & Technology B* **22** (4), 1711-1716 (2004).
- 280 J.K.W. Yang, B. Cord, H.G. Duan, K.K. Berggren, J. Klingfus, S.W. Nam, K.B. Kim & M.J. Rooks. Understanding of hydrogen silsesquioxane electron resist for sub-5-nm-half-pitch lithography. *Journal of Vacuum Science & Technology B* **27** (6), 2622-2627 (2009).
- 281 J.K.W. Yang & K.K. Berggren. Using high-contrast salty development of hydrogen silsesquioxane for sub-10-nm half-pitch lithography. *Journal of Vacuum Science & Technology B* **25** (6), 2025-2029 (2007).
- 282 Y. Cao, S.H. Dong, S. Liu, L. He, L. Gan, X.M. Yu, M.L. Steigerwald, X.S. Wu, Z.F. Liu & X.F. Guo. Building High-Throughput Molecular Junctions Using Indented Graphene Point Contacts. *Angewandte Chemie-International Edition* **51** (49), 12228-12232 (2012).
- 283 B.S. Archanjo, A.P. Barboza, B.R. Neves, L.M. Malard, E.H. Ferreira, J.C. Brant, E.S. Alves, F. Plentz, V. Carozo, B. Fragneaud, I.O. Maciel, C.M. Almeida, A. Jorio & C.A. Achete. The use of a Ga⁺ focused ion beam to modify graphene for device applications. *Nanotechnology* **23** (25), 255305 (2012).
- 284 M.C. Lemme, D.C. Bell, J.R. Williams, L.A. Stern, B.W.H. Baugher, P. Jarillo-Herrero & C.M. Marcus. Etching of Graphene Devices with a Helium Ion Beam. *Acs Nano* **3** (9), 2674-2676 (2009).
- 285 B.S. Archanjo, B. Fragneaud, L. Gustavo Cançado, D. Winston, F. Miao, C. Alberto Achete & G. Medeiros-Ribeiro. Graphene nanoribbon superlattices fabricated via He ion lithography. *Applied Physics Letters* **104** (19), 193114 (2014).
- 286 O. Lehtinen, J. Kotakoski, A.V. Krasheninnikov, A. Tolvanen, K. Nordlund & J. Keinonen. Effects of ion bombardment on a two-dimensional target: Atomistic simulations of graphene irradiation. *Physical Review B* **81** (15), 153401 (2010).
- 287 A.N. Abbas, G. Liu, B. Liu, L. Zhang, H. Liu, D. Ohlberg, W. Wu & C. Zhou. Patterning, characterization, and chemical sensing applications of graphene nanoribbon arrays down to 5 nm using helium ion beam lithography. *Acs Nano* **8** (2), 1538-1546 (2014).

- 288 J. Buchheim, R.M. Wyss, I. Shorubalko & H.G. Park. Understanding the interaction between energetic ions and freestanding graphene towards practical 2D perforation. *Nanoscale* **8** (15), 8345-8354 (2016).
- 289 B. Song, G.F. Schneider, Q. Xu, G. Pandraud, C. Dekker & H. Zandbergen. Atomic-Scale Electron-Beam Sculpting of Near-Defect-Free Graphene Nanostructures. *Nano Letters* **11** (6), 2247-2250 (2011).
- 290 S. Garaj, W. Hubbard, A. Reina, J. Kong, D. Branton & J.A. Golovchenko. Graphene as a subnanometre trans-electrode membrane. *Nature* **467** (7312), 190-193 (2010).
- 291 Y. Lu, C.A. Merchant, M. Drndic & A.T.C. Johnson. In Situ Electronic Characterization of Graphene Nanoconstrictions Fabricated in a Transmission Electron Microscope. *Nano Letters* **11** (12), 5184-5188 (2011).
- 292 B. Sommer, J. Sonntag, A. Ganczarczyk, D. Braam, G. Prinz, A. Lorke & M. Geller. Electron-beam induced nano-etching of suspended graphene. *Scientific Reports* **5** 7781 (2015).
- 293 A. Zobelli, A. Gloter, C.P. Ewels & C. Colliex. Shaping single walled nanotubes with an electron beam. *Physical Review B* **77** (4), 045410 (2008).
- 294 C. Jin, H. Lan, L. Peng, K. Suenaga & S. Iijima. Deriving Carbon Atomic Chains from Graphene. *Physical Review Letters* **102** (20), 205501 (2009).
- 295 Z.J. Qi, J.A. Rodríguez-Manzo, A.R. Botello-Méndez, S.J. Hong, E.A. Stach, Y.W. Park, J.C. Charlier, M. Drndić & A.T.C. Johnson. Correlating Atomic Structure and Transport in Suspended Graphene Nanoribbons. *Nano Letters* **14** (8), 4238-4244 (2014).
- 296 F. Prins, A. Barreiro, J.W. Ruitenber, J.S. Seldenthuis, N. Aliaga-Alcalde, L.M.K. Vandersypen & H.S.J. Van Der Zant. Room-Temperature Gating of Molecular Junctions Using Few-Layer Graphene Nanogap Electrodes. *Nano Letters* **11** (11), 4607-4611 (2011).
- 297 V. Gupta, N. Madaan, D.S. Jensen, S.C. Kunzler & M.R. Linford. Hydrogen Plasma Treatment of Silicon Dioxide for Improved Silane Deposition. *Langmuir* **29** (11), 3604-3609 (2013).
- 298 Z. Li, Y. Wang, A. Kozbial, G. Shenoy, F. Zhou, R. Mcginley, P. Ireland, B. Morganstein, A. Kunkel, S.P. Surwade, L. Li & H. Liu. Effect of airborne contaminants on the wettability of supported graphene and graphite. *Nature Materials* **12** (10), 925-931 (2013).
- 299 H. Schroder, E. Obermeier, A. Horn & G.K.M. Wachutka. Convex corner undercutting of {100} silicon in anisotropic KOH etching: the new step-flow model of 3-D structuring and first simulation results. *Journal of Microelectromechanical Systems* **10** (1), 88-97 (2001).
- 300 HyperSpy: multi-dimensional data analysis toolbox v0.81 *doi:10.5281/zenodo.54004* (2015).
- 301 P. Trebbia & N. Bonnet. EELS elemental mapping with unconventional methods. I. Theoretical basis: image analysis with multivariate statistics and entropy concepts. *Ultramicroscopy* **34** (3), 165-178 (1990).
- 302 P. Cueva, R. Hovden, J.A. Mundy, H.L. Xin & D.A. Muller. Data Processing for Atomic Resolution Electron Energy Loss Spectroscopy. *Microscopy and Microanalysis* **18** (04), 667-675 (2012).
- 303 F. Wang, R. Egerton & M. Malac. Fourier-ratio deconvolution techniques for electron energy-loss spectroscopy (EELS). *Ultramicroscopy* **109** (10), 1245-1249 (2009).
- 304 R.F. Egerton & M. Malac. Improved background-fitting algorithms for ionization edges in electron energy-loss spectra. *Ultramicroscopy* **92** (2), 47-56 (2002).

- 305 C. Lee, X.D. Wei, J.W. Kysar & J. Hone. Measurement of the elastic properties and intrinsic strength of monolayer graphene (Supplementary Material). *Science* **321** (5887), 385-388 (2008).
- 306 C.L. Wong, M. Annamalai, Z.Q. Wang & M. Palaniapan. Characterization of nanomechanical graphene drum structures. *Journal of Micromechanics and Microengineering* **20** (11), 115029 (2010).
- 307 M.B.B.S. Larsen, D.M.A. Mackenzie, J.M. Caridad, P. Bøggild & T.J. Booth. Transfer induced compressive strain in graphene: Evidence from Raman spectroscopic mapping. *Microelectronic Engineering* **121** 113-117 (2014).
- 308 T. Kawai, S. Okada, Y. Miyamoto & H. Hiura. Self-redirection of tearing edges in graphene: Tight-binding molecular dynamics simulations. *Physical Review B* **80** (3), 033401 (2009).
- 309 A. Jorio, M. Kasperczyk, N. Clark, E. Neu, P. Maletinsky, A. Vijayaraghavan & L. Novotny. Stokes and anti-Stokes Raman spectra of the high-energy C–C stretching modes in graphene and diamond. *physica status solidi (b)* **252** (11), 2380-2384 (2015).